Investigation of AlN/GaN Superlattices and their Application to Group III Nitride Devices

Von der Fakultät für Elektrotechnik und Informationstechnik
der Rheinisch-Westfälischen Technischen Hochschule Aachen
zur Erlangung des akademischen Grades
einer Doktorin der Naturwissenschaften genehmigte Dissertation

vorgelegt von

Ada Wille, M.Sc.

aus Braunschweig

Berichter: Univ.-Prof. Dr.-Ing. Andrei Vescan
Univ.-Prof. Dr.-Ing. Rainer Waser

Tag der Mündlichen Prüfung: 2. Februar 2017

Contents

Chapter 1

Introduction

Group-III nitrides have been in the focus of research for many years and possess great potential in many application fields to boost performance and efficiency of devices. The white GaN-based LED already outperformed long established lighting technologies such as incandescent light bulbs or energy-saving lamps regarding energy consumption, lifetime and cost efficiency. This evolution was honored with the Nobel Prize in physics in 2014 awarded to Isamu Akasaki, Hiroshi Amano and Shuji Nakamura [1]. Heterostructure field effect transistors (HFET) based on group-III nitrides are also at the edge to surpass the performance of devices based on Si and SiC. Due to the inherent polarization of group-III nitrides determined by their crystal structure, carriers are accumulated in the transistor channel without doping [2]. Especially in the RF (radio frequency) and high-power regimes, GaN-based technology benefits from the large band gap, high breakdown voltages, large saturation velocities and high carrier mobility [3]. Also optical devices such as distributed Bragg reflectors (DBR) [4] are realized and new concepts for electro-optic modulators [5], [6] are investigated in group-III nitrides and pave the way towards new technologies like ultra-fast inter-chip communication.

Despite their great success, group-III nitride heterostructures suffer from a major drawback which is the occurrence of large stress leading to straining and relaxation of the material. This is unwanted because defects are formed which deteriorate the crystal quality. Also the material surface can roughen or the material can crack. The large amount of stress in nitride epitaxy originates from large differences in lattice parameters between the binary compounds GaN, AlN and InN [7]. The lattice mismatch between GaN and AlN is 2.4 % [7], which is very large compared to GaAs and AlAs (-0.14 % [8]). This causes relaxation processes which affect material properties like the band gap energy [9]. Especially ternary alloys as AlGaN, InGaN and AlInN pose a challenge to process control because stress, strain and process parameter fluctuations can cause the composition to vary. If relaxation starts in ternary alloys and the lattice parameter is changed gradually, the energy barrier for the incorporation of certain atomic species into the solid phase can be lowered or increased. This causes the composition of ternary alloys to change during the relaxation process and is termed as compositional pulling [10], [11].

Binary materials as GaN or AlN are much more stable and robust regarding their epitaxial processes. Compositional pulling cannot occur for these materials. To combine the robustness

of binary materials with the enhanced design possibilities of ternary compounds, superlattices (SL) can be used. Very thin alternating layers of GaN and AlN on the nm-scale form an effective AlGaN solid solution replacing classical ternary AlGaN. In this way, SL form a virtual alloy. SL exhibit a much higher quality and are significantly more stable compared to their respective ternary materials. Furthermore, SL can introduce new relaxation mechanisms, enable strain engineering and introduce novel electro-optic properties while the degree of freedom of ternary alloys regarding parameter design is maintained. In group-III nitrides, SL have already been studied and the results are very promising. SL have been successfully used in GaN-on-Si technology to impede layer cracking [12], [13]. They have been employed in LED technology as electron blocking layers to reduce droop [14], [15]. Also nitride-based solar cells were improved with the help of group-III nitride SL [16]. Nevertheless, the underlying strain managing mechanisms have been investigated only in part and further studies are necessary to exploit the full potential of SL in group-III nitrides.

This thesis will concentrate on the investigation and application of AlN/GaN-SL. After the theoretical background of group-III nitrides, their fabrication with MOVPE, the concept of strain in hetero epitaxy and SL are elucidated, an epitaxial process for AlN/GaN-SL of superior layer quality will be developed (chapter 3). Also the strain managing potential of SL will be exploited to finally prove that the performance of SL can surpass the one of ternary alloys (chapter 3.2). In the following, AlN/GaN-SL will be incorporated into existing devices like HFET (chapter 4.1) and DBR (chapter 4.2). It will be demonstrated that the incorporation of AlN/GaN-SL into HFET leads to increased carrier mobility and increased linearity in transistor performance. In DBR, the SL enable crack-free structures by the introduction of new relaxation mechanisms in contrast to those of conventional AlGaN. A thorough analysis of the SL-DBR strain state will be given. Beyond this great potential, SL also enable the design of completely new devices. In chapter 4.3, a new electro-optic modulator based on AlN/GaN-SL will be presented. The invention of this new modulator concept ("TuneDBR", inventors Ada Wille and Holger Kalisch) was filed for patent by RWTH Aachen University (incl. PCT application). The modulation principle will be elucidated and modulated reflectance spectra of test structures will be shown including an analysis of the gained results via simulation. A final conclusion and an outlook will be given in chapter 5.

Chapter 2

Group III Nitrides: Theory and Characterization

2.1 Group III Nitrides

This chapter will cover the basic properties of group III nitrides, their deposition by metal-organic vapor phase epitaxy (MOVPE) on sapphire substrates and the role and evolution of defects and strain in the epitaxial layers. Further information on structural, optical and electronic properties is given in references [7], [17] and [18].

2.1.1 Basic Properties of Group III Nitrides

Group III nitrides are compound semiconductors (CS) which crystallize in the wurtzite structure (α-phase). A metastable zincblende structure is also existent (β-phase) [17]. The crystal structure with the elementary cell is depicted in figure 2.1. The coordination geometry of every atom is tetrahedral with one of the metal-nitrogen bonds oriented in c-direction ($< 0001 >$). Their space group $P6_3mc$, which lacks inversion symmetry and has a polar axis in $< 0001 >$ direction, leads to pyroelectricity manifesting in a macroscopic spontaneous polarization of the CS crystal. As an example, this polarization is used in heterostructure field effect transistors (HFET) to create two-dimensional electron gases (2DEG). This makes modulation doping, used in classical III-V material like GaAs, unnecessary [19]. On the other hand, polarization leads to tilted quantum wells in c-plane LED and the occurrence of the quantum confined stark effect (QCSE) which decreases the internal quantum efficiency [18]. The polar axis also leads to the fact that the [0001] direction and the $[000\bar{1}]$ direction are not equivalent. Therefore an epitaxial film can either be metal-face ([0001] is the growth direction) or nitrogen-face ($[000\bar{1}]$ is the growth direction). The two top surfaces resulting from these two crystal orientations differ in surface atom species (metal or nitrogen) and number of surface states [17]. With MOVPE (cmp. chapter 2.1.2), metal-face crystals are typically formed. Depending on the pretreatment of the substrate, nitrogen-face crystal growth is also possible with MOVPE.

The three most important binary compounds in group III nitrides are GaN, AlN and InN.

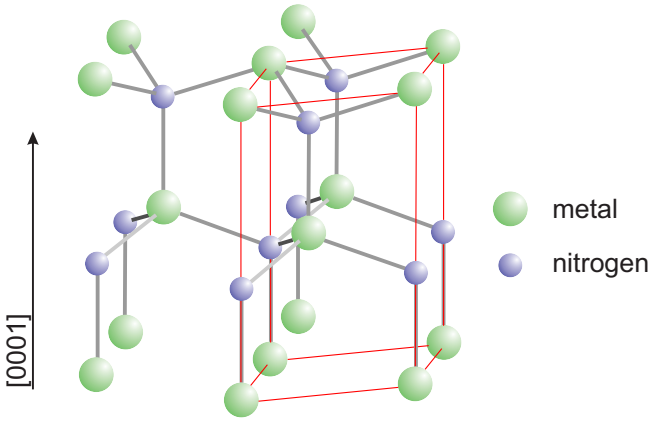

Figure 2.1: Wurtzite crystal lattice with metal (green) and nitrogen (blue) atomic species.

These materials differ strongly in lattice parameters and bandgap energies. The dependence of bandgap energies on the lattice parameter is depicted in figure 2.2. With 6.25 eV [7], AlN has the largest bandgap, followed by GaN (3.51 eV [7]) and InN (0.78 eV [7]). The bandgap energies of their ternary and quaternary alloys can be interpolated by Vegard's law extended with corresponding bowing parameters. This wide range from 6.25 to 0.78 eV covers the whole visible spectrum and also UV and infrared wavelengths. As the bandgap is also of direct nature [20], group III-nitrides are very suitable for optical applications such as LED, LASER and photovoltaics.

The refractive index is very important for the design of these optical devices. However, measured refractive index values for group III nitrides differ if several publications are compared [21], [22], [23]. This can be attributed to the strong influence of strain on the optical parameters and differences in material quality, fabrication and measurement techniques. The refractive index of GaN is real for wavelengths larger than 360 nm. For shorter wavelengths, the material absorbs light which leads to a non-zero extinction coefficient and a complex refractive index. The refractive index of AlN is real in the whole visible and near-UV wavelength regime. In general, the refractive index of GaN near the band edge is around 2.8 and decreases with longer wavelengths to approximately 2.4 [21], [22]. AlN has a lower refractive index from approximately 2.2 at 300 nm down to approximately 2.0 [21], [22]. The refractive index of InN is even lower (1.7 at 400 nm) with a large extinction coefficient for wavelength shorter than 1590 nm [23].

Group III nitrides can be doped with silicon to create n-type conductivity and magnesium to create p-type conductivity. The magnesium acceptor suffers from high activation energies (0.26 eV [24]), complex formation with hydrogen and compensation by unintentionally doped (uid) n-type background doping originating from the growth procedure, which makes p-doping in group III nitrides challenging [25]. N-type conductivity is much easier to gain. Only for alloys with high Al content and pure AlN, n-type doping becomes less effective because of a deeper donator level with increasing Al content [26], [27]. Group III nitrides are also very suited for high-power and high-frequency applications due to their large breakdown voltage, good thermal conductivity compared to silicon and large electron velocities in combination with high electron concentrations [3].

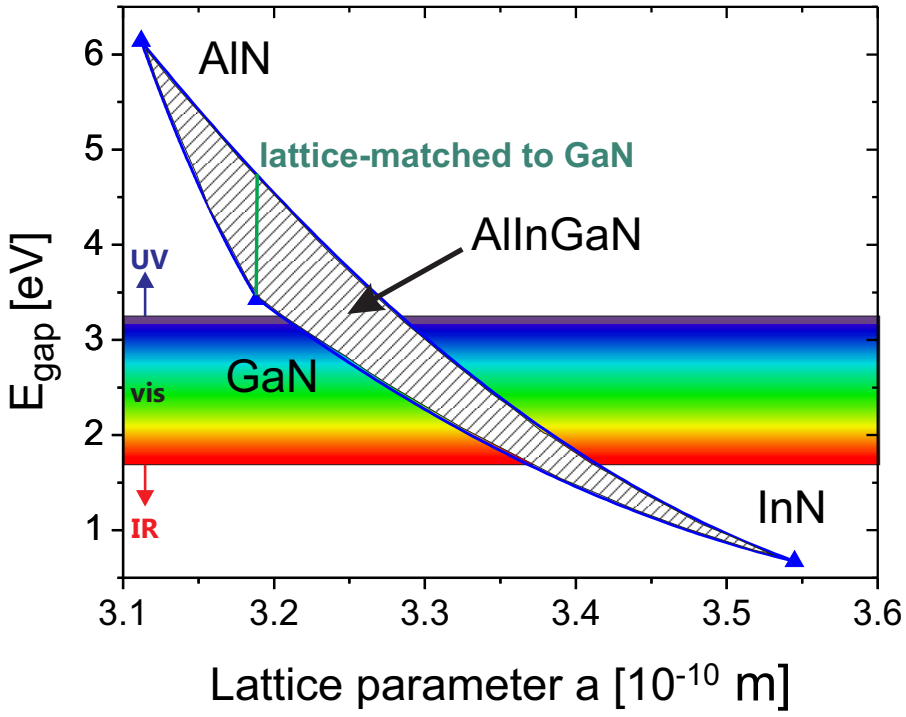

Figure 2.2: Bandgap energies of group III-nitride materials versus their lattice parameter. The colored area shows the visible spectrum of the band gap energy.

2.1.2 Growth of Group III Nitrides with Metal-Organic Vapor Phase Epitaxy (MOVPE)

A fast and production-compatible technique to deposit crystalline layers of group III-nitrides is MOVPE (also known as metal-organic chemical vapor deposition, MOCVD). In this epitaxial process, metal-organic precursors, such as trimethylgallium (TMGa), trimethylaluminium (TMAl) and trimethylindium (TMIn), are used to deliver the group III component of the semiconductor material. These metal-organic compounds are provided in a stainless steel container called bubbler. The working principle of a bubbler is shown in figure 2.3. Carrier gas (hydrogen or nitrogen) is directed into the bubbler unit and, depending on the vapor pressure, a certain amount of precursor is mixed with the carrier gas which is then transported out of the bubbler. As a precursor for nitrogen, ammonia (NH_3) is used. These precursors are transported into a reactor chamber with well defined temperature, pressure and gas flows in which the heated substrate is located as depicted in figure 2.3. The temperature can be controlled with an RF coil with internal cooling which inductively heats the susceptor. The temperature measurement is conducted using a pyrometer on the lower side of the substrate holder. This measured temperature value is the basis of the reactor temperature set point feedback loop. As an additional temperature measurement, a LayTec in-situ tool [28] is mounted on top of the reactor chamber which enables a direct emissivity-corrected, pyrometric measurement of the substrate temperature. In the reaction chamber, the MO precursors and ammonia are mixed

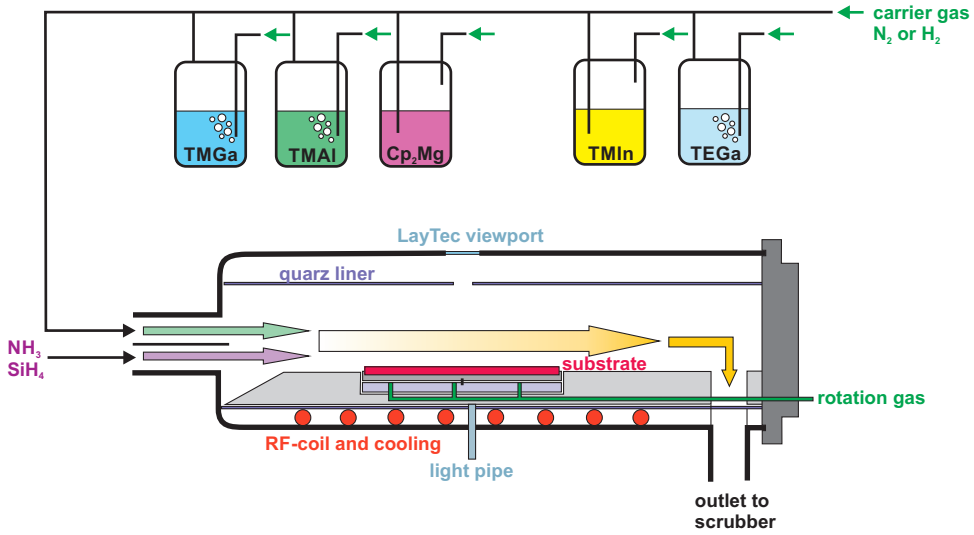

Figure 2.3: Schematic of a horizontal flow MOVPE reactor.

and gas-phase adducts such as $[(CH_3)_3MNH_3]$ are formed where M denotes the metal atom (Ga, Al or In). A surface adduct is then generated close to the substrate by elimination of CH_4. With further elimination of CH_4 and H_2, the binary nitride compound MN is formed directly on the substrate surface [17], [29]. Side products of the precursor reaction are transported to the outlet side of the reactor chamber by horizontal carrier gas flows, a scrubber system neutralizes the excess of alkaline ammonia. The precursor reaction time is slow compared to the drift velocity in the reactor chamber. This results in different reaction states at the upstream substrate side compared to the downstream side. To compensate for this effect, the substrate is rotated with a gas foil rotation system.

Due to the lack of GaN or AlN substrates in sufficient quality, group III nitrides are fabricated in a hetero-epitaxial process mainly on sapphire (Al_2O_3), silicon or silicon carbide (SiC) wafers. Sapphire substrates have a rhombohedral symmetry which allows for epitaxy of hexagonal materials [17]. They are widely used due to their high thermal and chemical stability, broad availability, high structural quality and low cost [17]. Sapphire is also transparent up to 8.8 eV which can be beneficial for the fabrication of optoelectronic devices. SiC substrates are mainly used for high-power and microwave devices because of their better thermal conductivity compared with sapphire and their availability as p- and n-type doped substrates [17]. The lattice mismatch of SiC to AlN is also very small, which makes heteroepitaxy less challenging [17]. Silicon substrates are explored due to cost issues, availability in large diameters and if an integration of the device into CMOS technology is anticipated [30], [31]. Direct epitaxy of GaN on Si is not possible due to the formation of an eutectic phase. This process is called meltback etching [32]. This can be circumvented by insertion of a low-temperature AlN layer between Si substrate and GaN layers [32]. Due to large differences in thermal expansion coefficients between Si and group III nitrides, strain engineering is also a very important aspect for epitaxy on Si(111) [32].

To deposit group III-nitrides hetero-epitaxially on sapphire, a low-temperature nucleation step is necessary. The nucleation on sapphire can be conducted using either GaN or AlN. In

the following the AlN nucleation and subsequent buffer growth is described as it is used in this thesis. An AlN nucleation in combination with an AlN buffer is advantageous as the resulting sapphire-AlN-interface is insulating while the sapphire-GaN-interface is conductive [33], [34]. The conductivity of the GaN nucleation layer is generated by oxygen atoms, which diffuse out of the sapphire substrate and are incorporated into the subsequent semiconductor layer. In GaN, oxygen forms a shallow donor which is ionized at room temperature. In AlN, oxygen forms a deep donor which is not ionized at room temperature and therefore leads to an insulating interface. In the nucleation step, small irregular AlN crystallites are formed on the substrate surface due to limited diffusion length of the surface species [35] and the higher surface formation energy of AlN compared to sapphire [36]. The orientation of the crystallites (Al-face or N-face) is mainly determined by TMAl or NH_3 preflow prior to the nucleation growth process [37]. In a subsequent annealing step, discontinuous grain growth and surface roughening occurs [38]. The annealing temperature is generally the growth temperature of the following high-temperature buffer layer. In the initial growth phase of the high-temperature AlN buffer, nuclei favored by geometric selection grow faster than other nuclei and form trapezoid crystals which then start to coalesce in an epitaxial lateral overgrowth (ELOG) mode. After this, a stable growth front establishes and a high-temperature AlN buffer layer of 300 nm thickness is deposited to shield the following GaN buffer from the unintentionally oxygen-doped nucleation layer [17], [39]. With the GaN layer of 1-3 μm thickness, the buffer layer stack is completed and growth of functional layers, such as layers for HFET, LED or distributed Bragg reflectors (DBR) stacks, can be pursued.

2.1.3 Defects and Strain in Group III Nitride Heterostructures

As previously described in chapter 2.1.2, the lack of native substrates makes it necessary to deposit group III nitrides on foreign substrates as sapphire, silicon or silicon carbide. With this heteroepitaxial approach, strain and defects occur due to differences in crystal structure, lattice parameter and thermal expansion coefficients between substrate and material. In addition, also the formation of heterojunctions can lead to evolution of defects and strain. This chapter will introduce the most important defects in group III nitrides and the concept of strain in heteroepitaxial processes.

Point Defects Point defects are zero-dimensional and occur in group III nitrides as vacancies and impurities. A vacancy denotes a missing atom in the crystal lattice. For group III nitrides, this can be a nitrogen or a metal atom (Ga, Al, In). The donor type nitrogen vacancy V_N has very high formation energies for n-type GaN. As undoped GaN always shows n-type behavior, the formation of V_N is very unlikely [40]. The gallium vacancy V_{Ga} has a much lower formation energy in n-type GaN, acts as an acceptor and might be partly responsible for yellow luminescence (YL) which is a very broad parasitic emission in the yellow spectral range [41]. Interstitials or antisites generally do not occur in group III nitrides because of too high formation energies but impurities such as carbon or oxygen are very common [40]. The impu-

rity atoms can occupy either a metal or a nitrogen lattice site but there is always a dominant configuration. For oxygen, this is the incorporation on a nitrogen site (O_N) and carbon is also most likely placed on a nitrogen site (C_N). O_N acts as a shallow donor and is responsible for the n-type conductivity in undoped GaN [40]. C_N forms a deep acceptor and is responsible for yellow luminescence together with the afore mentioned gallium vacancy [41].

Dislocations Dislocations are one-dimensional crystal defects. This means that the crystal is distorted along a line. There are two basic dislocation types. The first on is an edge dislocation (fig. 2.4 left), the second is a screw dislocation (fig. 2.4 right). A dislocation is defined by the line element **s** and the Burgers vector **b**. The Burgers vector denotes the lattice displacement between the ideal and defect-containing crystal, which is always a translation vector of the crystal lattice. The line element is the tangential unit vector of the dislocation line [42]. For screw dislocations, the line element is always parallel to the Burgers vector while for edge dislocations, Burgers vector and line element are oriented perpendicular to each other. If the correlation between line element and Burgers vector is neither parallel nor perpendicular, the dislocation is a combination of edge- and screw-type and is called mixed dislocation. If the angle between Burgers vector and line element is even changing along the dislocation line, the dislocation type is called prismatic [42]. Dislocations with Burgers vectors which are no translation vectors of the crystal lattice are also existent. This dislocation type is called partial dislocation [42].

The line element indicates the propagation direction of the dislocation in a crystal. If an epitaxial layer stack is considered, e.g a sapphire substrate with AlN and GaN buffer on top, dislocations mostly propagate in the growth direction or perpendicular to the growth direction. Dislocations propagating in growth direction can thread through interfaces between different materials, e.g. AlN and GaN, and are called threading dislocations (TD). In the case of group III nitrides on sapphire, the most common growth direction is the [0001]-direction for which the growth plane is c-plane. The most dominant TD in c-plane MOVPE GaN are edge dislocations with $\mathbf{b} = 1/3 < 11\bar{2}0 >$, mixed dislocations with $\mathbf{b} = 1/3 < 11\bar{2}3 >$ and screw dislocations with $\mathbf{b} =< 0001 >$ [43], [44], [45]. The majority of TD are edge and mixed dislocations, while there are only 2 % screw TD [43]. Dislocations which propagate in in-plane directions, which means parallel to material interfaces, are called misfit dislocations (MD) because they can accommodate lattice misfit between two layers. MD in c-plane MOVPE GaN have a Burgers vector of $\mathbf{b} = 1/3 < 11\bar{2}0 >$ and a line element of $\mathbf{s} =< 1\bar{1}00 >$ [46], [47], [48].

Movement of Dislocations Dislocations are not immobile and can move in the crystal by two mechanisms, slip and climb. Slip occurs always in a specific slip system (a slip plane and a slip direction) which depend on the crystal symmetry, the driving forces and the dislocation type. The normal of the slip plane m is defined by the Burgers vector and the line element with

$$m = \mathbf{s} \times \mathbf{b} \tag{2.1}$$

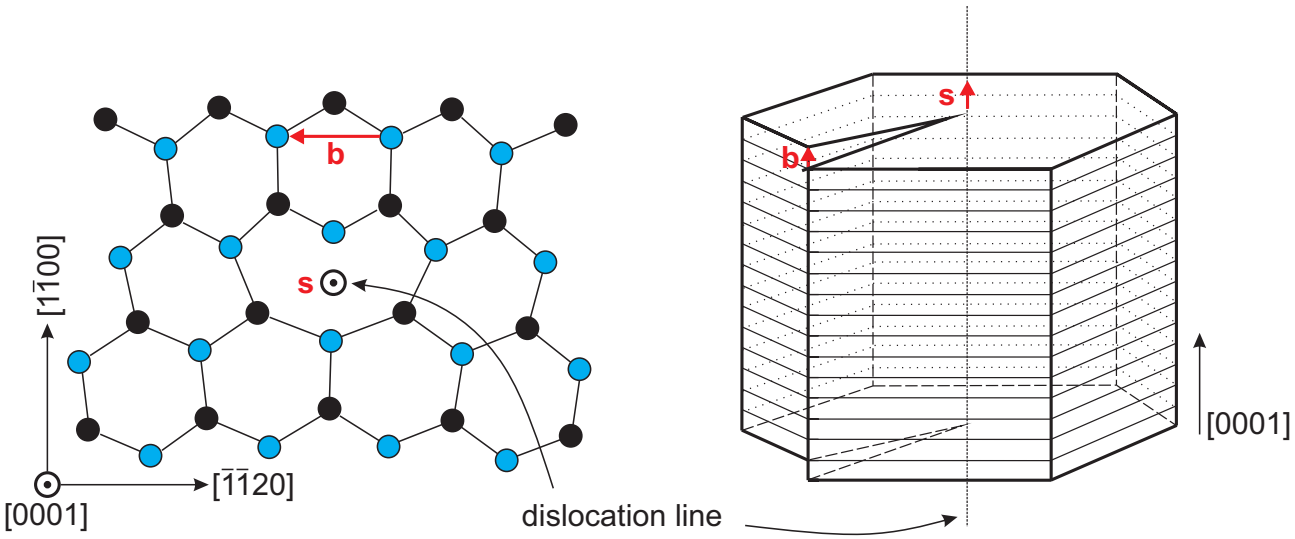

Figure 2.4: Left side: Edge dislocation in hexagonal GaN with Burgers vector $\boldsymbol{b} = 1/3[11\bar{2}0]$*, after[45]. Right side: Screw dislocation in a hexagonal lattice with* $\boldsymbol{b} = [0001]$.

This implies that screw dislocations with parallel Burgers vector and line element do not have a defined slip system and can change their slip plane. Prismatic dislocations are immobile because the slip plane would change along the dislocation line [42].

Edge and mixed dislocations have a defined slip system. In most cases, the dominant slip plane is the close-packed plane because the inter-atomic spacing is smallest which results in a very small Peierls force. The Peierls force can be understood as a frictional force between the two sheared crystal planes [48], [42]. These slip systems are called primary slip systems. For hexagonal crystals like group III nitrides, the close-packed plane is the basal (0001) plane and the resulting primary slip system is $\{0001\} < 11\bar{2}0 >$ which is depicted in figure 2.5 (a) [48]. The primary slip system often remains inactive due to geometric considerations concerning dislocation type and driving forces or non-ideal c/a-ratios < 1.63. Such ratios lead to non-close-packed basal planes and therefore increased Peierls forces in the primary slip system. For theses cases, slip can also occur on secondary slip systems [48]. In the wurtzite structure, the secondary slip systems comprise the prismatic and pyramidal planes as slip planes. The resulting secondary slip systems are depicted in figure 2.5 (b)-(f). While (b) and (c) show slip via prismatic planes, the slip systems using pyramidal slip planes are shown in (d), (e) and (f) of figure 2.5.

The second mechanism for dislocation motion is climb. Dislocation climb is a diffusion-related mechanism which implies a higher climb probability at elevated temperatures as in MOVPE processes. The dislocation absorbs or emits point defects like vacancies which generates a movement. In this way, even edge or mixed dislocations are able to leave their slip plane and also prismatic dislocations are able to move via this mechanism. Climb is classified as non-conservative dislocation motion as the number of point defects and therefore the volume of the crystal changes [42].

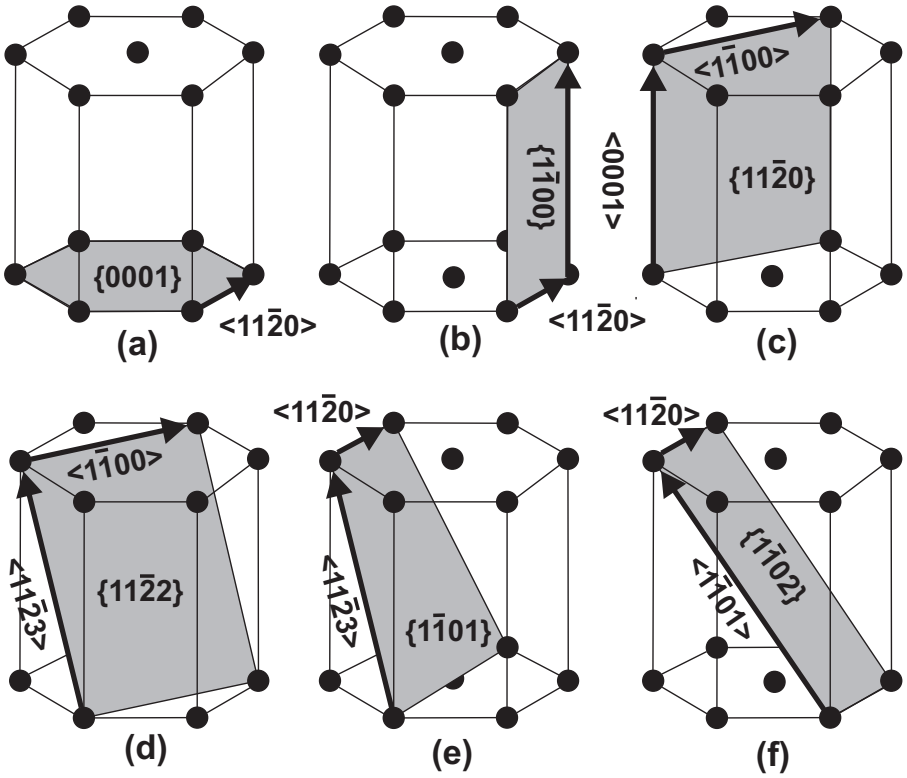

Figure 2.5: Slip systems in group III nitrides. (a) primary slip system, (b) - (f) secondary slip systems, after [48].

Generation and Movement of MD The driving force of every dislocation motion or formation is always a stress field σ in the crystal, which can have various origins and manifests as compressive or tensile strain ϵ governed by Hooke's law $\sigma = E\epsilon$ with the Young's modulus E. If an epitaxial process is considered, there are several important mechanisms induced by stress which take place right at the beginning of layer growth. The first mechanism is the generation of MD at the layer/substrate interface. The lattice mismatch Δa is defined as

$$\Delta a = \frac{a_{layer} - a_{subs}}{a_{subs}}. \tag{2.2}$$

For AlN on sapphire, the lattice mismatch is $\Delta a = 34.6$ %, which is extremely large [49], [37]. Therefore epitaxial growth of AlN on sapphire can only take place if the crystal lattices are rotated 30 degrees against each other which reduces the lattice mismatch to -13.2 %. This remaining mismatch is still very large and would induce a high level of stress. Eight $\{11\bar{2}0\}$ planes in AlN match nine $\{11\bar{2}0\}$ planes in sapphire so every ninth $\{11\bar{2}0\}$ sapphire plane is terminated with an misfit edge dislocation. The 8-to-9 arrangement results in a MD spacing of 2 nm and is energetically much more favorable than straining even one monolayer of the AlN compressively to match every $\{11\bar{2}0\}$ AlN plane with a corresponding sapphire plane [50]. For other material combinations than AlN on sapphire, MD generation may start much later when an already thick layer of epitaxial material has been deposited on the substrate. This can either be caused by a smaller lattice mismatch of epilayer and substrate and therefore less induced strain or by higher MD formation energy. The point at which MD generation becomes

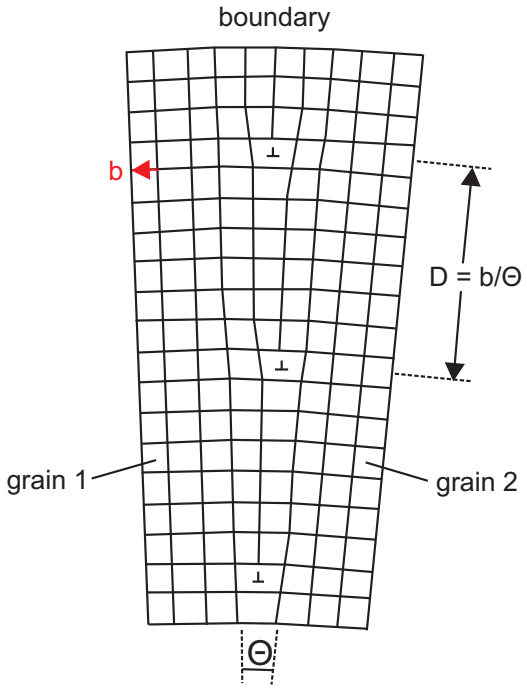

Figure 2.6: Top view on a LAGB in a cubic system with Burgers vector **b**, *twist angle of the crystallites* Θ *and the resulting dislocation spacing D, after [42].*

energetically more favorable than straining the material is called the critical layer thickness and can be calculated after the Matthews-Blakeslee model [51], [52]. The critical layer thickness is the starting point for the relaxation process. During which, the in-plane strain of the epitaxial layer acts a the driving force to overcome the counteracting Peierls force. Slip systems are activated and the crystal planes are sheared which produces and moves MD. By the generation and rearrangement of MD, the in-plane strain is relaxed and the driving force for further MD generation becomes zero.

Generation of TD During Coalescence The second mechanism described here is the formation of TD in the nucleation procedure. Small AlN crystallites are formed on the sapphire surface instead of a 2D AlN film as described in section 2.1.2. The growing AlN islands coalesce at some stage of the process. The crystallites are not perfectly aligned but slightly twisted and tilted against each other. This twist and tilt has to be accommodated during the coalescence process. Accommodation by strain is again energetically unfavorable and TD at the island boundaries are generated. These TD are edge type and can arrange periodically in $\{1\bar{2}10\}$ planes [44]. This periodical arrangement of TD is called low-angle grain boundary (LAGB) and is displayed for a cubic system in figure 2.6. In contrast to high-angle grain boundaries, the twist angle of the two crystallites is smaller than 15° and crystal planes are continuous. This implies that the material is still single-crystalline [42]. Besides the formation of LAGB, a certain amount of TD is annihilated during the coalescence process which is accompanied by a growth mode change from island to 2D layer growth [53]. The annihilation process also leads to a more random-like distribution of dislocations in the material because not all dislocations originating from the coalescence process are continued.

Generation of TD by Annihilation of Stacking Faults Another source of randomly distributed TD in the epitaxial material can be the annihilation of stacking faults [44]. Basal-plane stacking faults are distortions in the ABABABAB stacking order of the wurtzite hcp lattice in <0001> direction. For group III nitrides every layer A, B or C consists of metal-nitrogen bilayer. Figure 2.7 shows the ABAB stacking order of a hcp lattice on the top which is similar to the wurtzite crystal structure and the ABCABC fcc stacking order in <111> direction on the bottom which resembles the zincblende structure, which is closely related to wurtzite. In the case of basal-plane stacking faults, one or more A or B layers of the hcp lattice are displaced to form a C layer as in the fcc lattice which results in a stacking order like ABABCBCB. This introduces small zincblende units into the wurtzite lattice. This process is most prominent in GaN as the formation energy for stacking faults is lowest for GaN followed by InN and is highest for AlN [54]. Stacking faults in GaN are often generated during the initial state of layer growth. Some stacking faults are removed by formation of partial dislocations with Burgers vectors of $1/6 < 02\bar{2}3 >$ which occurs during subsequent growth. Two of these newly generated partial dislocations can react and form a regular edge or mixed dislocation with Burgers vectors of $1/3 < 11\bar{2}0 >$, $1/3 < 11\bar{2}3 >$, $1/3 < 11\overline{23} >$ [44].

Further Mechanisms for Strain Relaxation Besides the mechanisms described above, there are other ones that can come into action if strain has to be relieved in a crystal. The following mechanisms do not necessarily take place at the beginning of layer growth. They occur whenever stress is large and the continued formation of strained material becomes energetically unfavorable. Generally, all mechanism involve the formation of defects. This is why the relaxation process in most cases is undesirable, as an increase in defect density decreases the crystal quality of the layer. Due to the change in strain state during relaxation, the incorporation rate of Al, Ga or In for subsequent layer growth can be higher or lower due to differences in atomic radii. As a result, the layer composition of ternary or quaternary alloys can change during growth due to the relaxation process which is known as compositional pulling effect [55], [10].

V-pits can be formed to relieve strain. This mechanism only takes place at high dislocation densities which increases the formation energy of additional MD due to the inherent strain fields of dislocations [48]. Unfavorable growth conditions promote the formation of V-pits as other crystal facets than the (0001) plane have to be formed [56]. A schematic drawing of an opening V-pit in InGaN is shown in figure 2.8. The V-pit originates at a TD and the opening facets are the six $\{10\bar{1}0\}$ planes, which are arranged in an inverted hexagonal pyramid [57]. V-pits are often observed in InGaN/GaN MQW structures.

For tensile strain, layer-cracking is often observed even at the initial state of the relaxation process when the activation of dislocation glide is difficult because only biaxial stress states as produced by lattice mismatch without a shear component are present [58]. Layer cracking can also occur during cool-down of the sample if the thermal expansion coefficient mismatch between layer and substrate introduces additional strain [59]. This can only be avoided by changing the composition of the material and therefore changing the thermal expansion coefficient mismatch or by introducing stress of opposing direction into the sample in a way that after cool-down

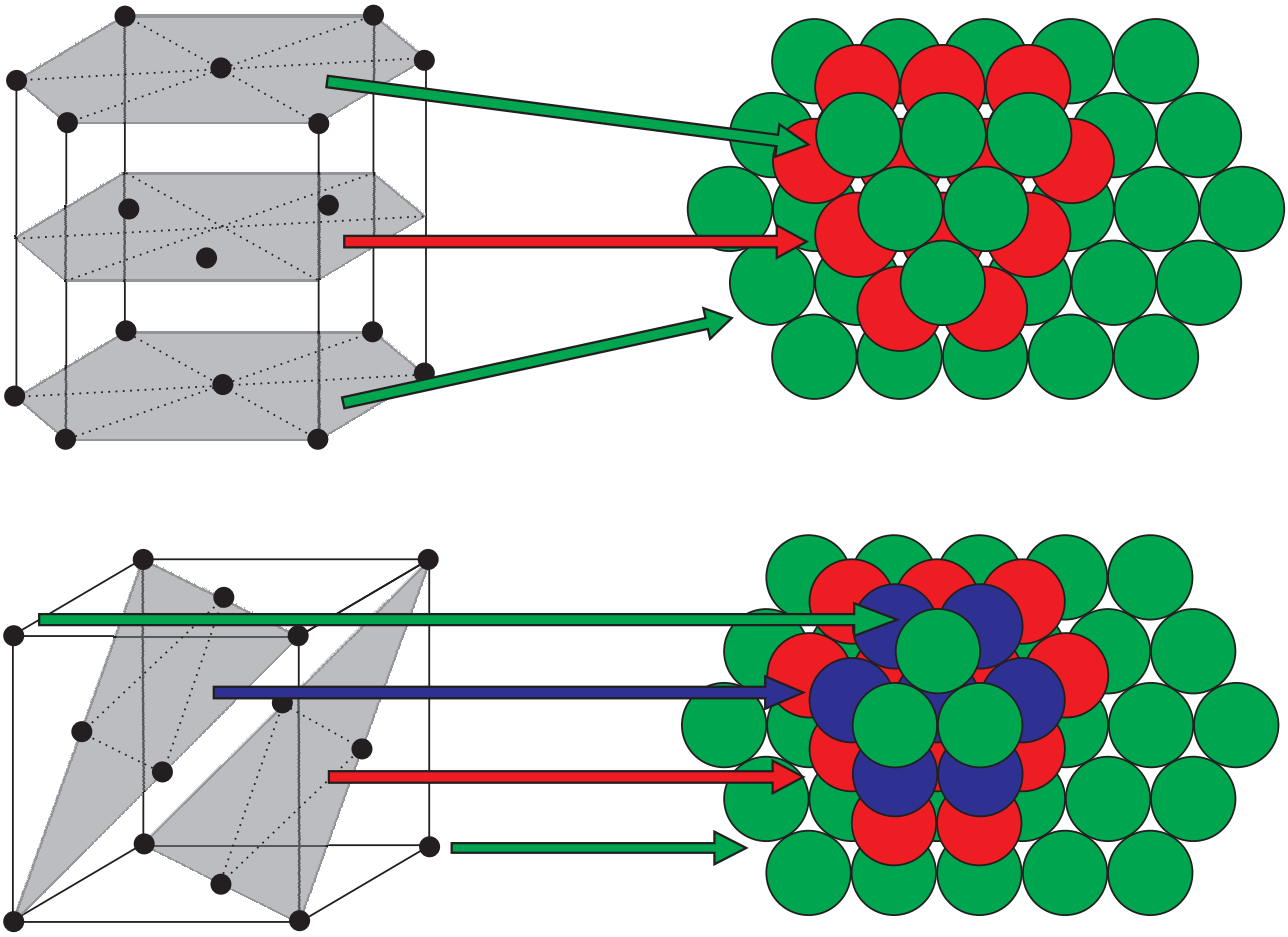

Figure 2.7: Top: stacking order of hcp lattice. The first and third layer (both in green) are crystallographically equivalent. Bottom: stacking order of fcc lattice. The first (green) and third (blue) layer are not equivalent. Only the atoms of the fourth layer (again in green) occupy the same lattice sites as the fist layer. In conclusion, hcp (wurtzite) and fcc (zincblende) can be converted into each other by a change in stacking order.

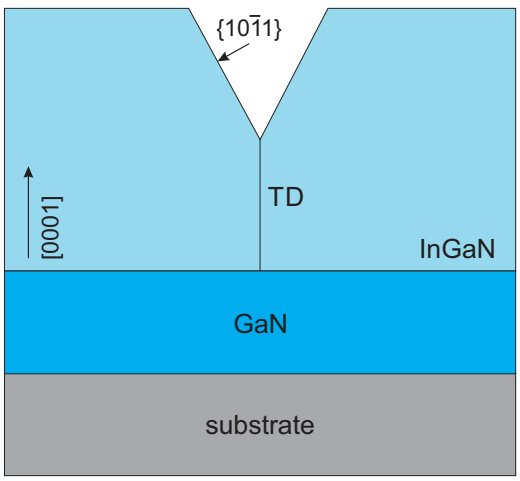

Figure 2.8: V-pit in an epitaxial layer stack. A TD denotes the origin of the V-pit.

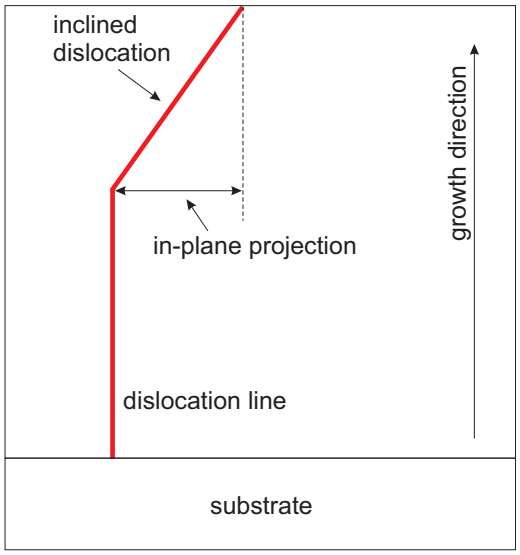

Figure 2.9: Strain relieve mechanism utilizing inclined dislocations. The in-plane projection of the tilted dislocation part acts as a MD segment and can relieve strain.

the resulting strain is sufficiently small.

Another relaxation process is the inclination of TD. This process is described by the Romanov-Speck model [60]. Generally, TD are not able to relieve further in-plane strain during their propagation through the material. By inclination of edge TD towards the $< 1\bar{1}00 >$ directions, TD can act as a MD segment with the length of the in-plane projection as depicted in figure 2.9. Dislocation inclination does not include formation of dislocations and can even utilize existent dislocation types which typically do not contribute to relaxation. But as the inclination mechanism of the dislocations is climb, the dislocation motion is nonconservative and involves the formation of point defects.

Strain and relaxation do not only influence the defect structure of a material. As the bond lengths in the crystal are changed, the periodic potential in the lattice is also altered. As a consequence, the bandgap energy is a function of the strain state of a layer [9]. The length of the dipoles in the polar axis are elongated or shortened which affects the dipole momentum and the resulting macroscopic polarization. This additional polarization, which has to be added to the inherent spontaneous polarization ($\vec{P}_{sp}$) in the unstrained material, is called piezoelectric polarization ($\vec{P}_{pz}$). The total polarization of a group III nitride layer ($\vec{P}_{tot}$) can be expressed as

$$\vec{P}_{tot} = \vec{P}_{sp} + \vec{P}_{pz} \tag{2.3}$$

The piezoelectric polarization can be positive or negative compared to the spontaneous polarization depending on whether the strain is compressive or tensile. For metal-face layers grown in [0001] direction, the spontaneous polarization has negative values and points to the substrate from nitrogen to metal atoms along the long bond in $[000\bar{1}]$ direction. Tensily strained top layers generate a $\vec{P}_{pz}$ component parallel to $\vec{P}_{sp}$ and compressively strained layers an antiparallel component [2].

2.2 Superlattices (SL)

Superlattices (SL) are artificial materials which consist of a repeating sequence of two layers with different properties due to doping or composition. The latter are called compositional superlattices (SL) and contain a sequence of two distinct alternating materials with different band gap energies as shown in figure 2.10 for a GaN/AlN-SL. The material with the smaller bandgap forms a quantum well, while the material with the higher bandgap acts as the barrier material. SL are called symmetrical if both materials feature the same layer thicknesses. Asymmetrical SL are also possible. In the latter case, the thickness ratio can be described by the volume fraction of one of the SL materials devided by the the total volume of the SL. An AlN/GaN-SL with 1 nm thick AlN layers and 3 nm GaN layers would for example feature an AlN volume fraction of 25 %. This value can be thought of as an effective AlN content if a comparison to ternary AlGaN layers with a specific Al content is anticipated. For a symmetrical AlN/GaN-SL, the effective AlN content would be 50 %.

The wells and barriers of group III nitride SL are tilted due to the polarization differences. If the period of the SL is shorter than the electron mean free path, the neighboring wavefunctions of the quantum wells can overlap and, similar to the periodic potential of atoms in a crystal lattice, minibands can develop [61], [62]. Miniband formation offers the possibility to precisely tailor electrical and optical properties of SL which derive from the artificial crystal structure according to the Kronig-Penney-Model. For every material combination used in a SL with a certain difference in band gap energies, a limit in barrier thickness exists up to which the wavefunction overlap from well to well is large enough for minibands to evolve. If minibands are created, the optical properties are governed by the transition E_1 from the lowest confined electron state to the highest confined hole state. For barrier thicknesses exceeding this limit, the wavefunctions in the wells do not overlap and the optical properties of the SL can be approximated with the properties of a homogeneous alloy formed out of barrier and well materials with the same volume ratio [63] (e.g. the properties of an AlN/GaN-SL with layer thicknesses of 1 nm for GaN and 1 nm for AlN, can be approximated with the properties of $Al_{0.5}Ga_{0.5}N$). For AlN/GaN-SL, miniband formation is quite unlikely. Due to the large conduction band offset between GaN and AlN of 1.56 eV [64], carriers in GaN exhibit strong confinement and the wavefunction decays over short length scale in AlN. Hsu et al. determined a penetration depth of 0.3 nm for wavefunction located in GaN confined by an AlN barrier [65]. With this value, the rough approximation can be made that the AlN barrier thickness should be below 0.6 nm to allow an overlap of the wavefunction of adjacent GaN wells.

The growth of such SL structures in the group III nitride system can be performed by MOVPE. This can be challenging as the growth times of thin layers become very short in comparison to the ramping times between growth steps (50 s growth time vs. 1-2 minutes ramping times). This leads to a pronounced influence of interface quality on the whole SL structure. The individual layers of SL can consist of binary, ternary and also quaternary alloys. With increasing number of atomic species in the alloy, the epitaxial process becomes more challenging. A higher degree of freedom in composition can lead to compositional pulling

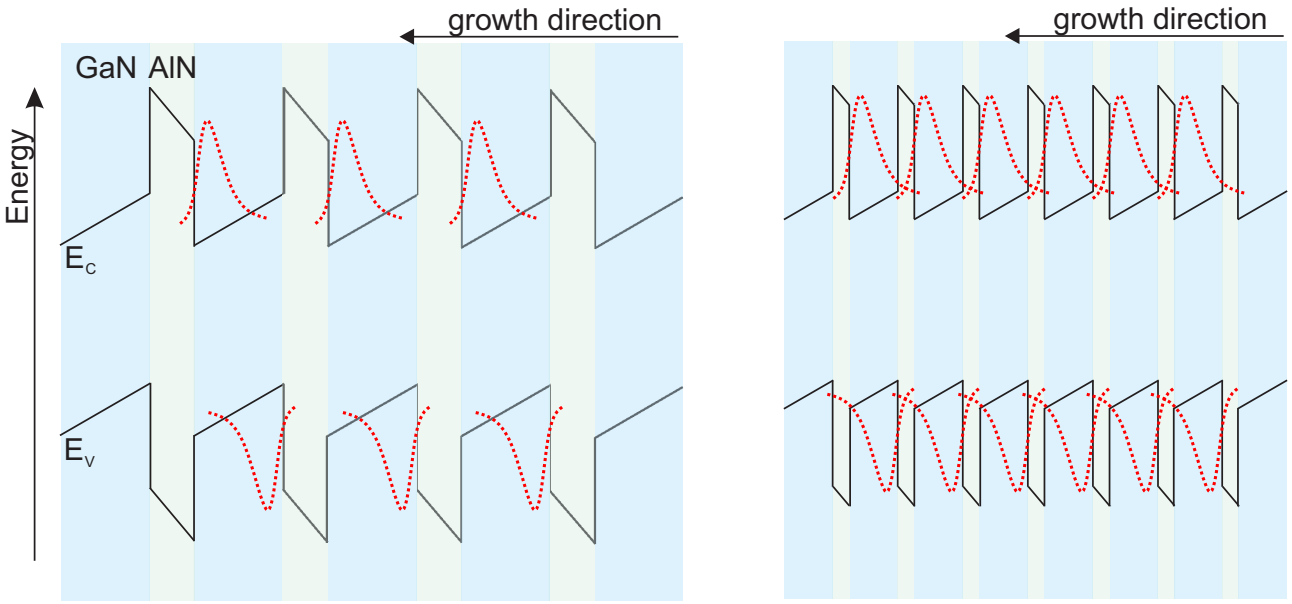

Figure 2.10: Band diagram of a GaN/AlN-SL. The wavefunctions for electrons and holes are shown in dotted red lines. On the left, the layer thicknesses are large and the carriers are confined in the GaN layers. On the right, the layer thicknesses are much smaller ($d_{AlN} < 0.6nm$). The wavefunctions overlap and subbands can develop.

effects [10], [11]. This is undesirable as growth rate (and as a consequence layer thickness), band gap energy and strain state are also changed with composition. These effects would lead to distortions in the periodic potential of the SL which implies nonuniform material properties of the SL. Therefore, this thesis will concentrate on SL composed of the binary materials AlN and GaN.

In the literature, it is evident that SL are able to manage or even relieve large amounts of strain as AlN/GaN-SL and AlGaN/GaN-SL are already applied in GaN-on-Si(111) epitaxy instead of the standard AlGaN staircase to obtain crack-free GaN buffers [12], [13]. AlGaN/GaN-SL are also used as electron blocking layers (EBL) in LED structures as the lower strain of the SL leads to a lower piezoelectric polarization difference at the MQW-EBL interface which promotes EBL performance and reduces droop [14], [15]. InGaN/GaN-SL were furthermore applied as absorption layers in solar cells. Due to the strain-managing properties of the SL, phase separation and defect formation in InGaN layers with high In content were suppressed. This reduces the possibility of shunt resistance paths and promotes carrier separation [16]. Despite of these impressive results, there is still a lack of understanding concerning the critical layer thicknesses and relaxation mechanisms for SL. The following paragraphs will try to give an overview over the current state of the understanding of strain distribution and relaxation mechanisms in SL and identify pending tasks and challenges:

To evaluate the strain state of SL can be quite complicated compared to conventional bi- or trilayer stacks. The strain state is determined mainly by the substrate lattice parameter a_{subs} and the in-situ lattice parameters of the two SL materials a_{SL1} and a_{SL2}. The term substrate refers in this context to the layer (assumed rigid) on which the SL epitaxy is performed. This could literally be a substrate like sapphire, Si, AlN or even GaN or the topmost layer of a buffer

structure such as GaN/AlN/sapphire (cmp. chapter 2.1.2). For the SL materials SL1 and SL2, five general scenarios are possible regarding the in-plane lattice paramters:

- Type 1: $a_{subs} < a_{SL1} < a_{SL2}$. This combination should induce compressive stress in both SL materials. In the nitride material system, this could be represented by an GaN/InGaN-SL deposited on an AlGaN buffer.
- Type 2: $a_{subs} = a_{SL1} < a_{SL2}$. In this case, the SL1 layers are likely to be free of stress while the SL2 layers should exhibit compressive stress. This set-up could be represented by and GaN/InGaN-SL deposited on a GaN buffer.
- Type 3: $a_{SL1} < a_{subs} < a_{SL2}$. This intermediate combination should induce tensile stress in the SL1 layers and compressive stress in the SL2 layers. An AlN/GaN-SL deposited on an AlGaN buffer would lead to this configuration.
- Type 4: $a_{SL1} < a_{SL2} = a_{subs}$. In this case, the SL2 layers are likely to be free of stress, while the SL1 layers should exhibit tensile stress. This is represented by AlN/GaN-SL deposited on GaN buffers as investigated in this thesis.
- Type 5: $a_{SL1} < a_{SL2} < a_{subs}$: This combination should induce tensile stress in both SL materials. AlN/AlGaN-SL deposited on a GaN buffer would create this scenario.

According to Hookes law, the induced stress should lead to strain in the designated layers. For types 1 and 5, this would lead to a completely compressively or tensily strained SL. The two SL materials would exhibit a different value of strain but the strain type (tensile or compressive) would be the same for the whole SL. Types 2 and 4 would generate a more complex strain state. One of the SL materials would be strained (type 2: compressively, type 4: tensily) and the other one should theoretically be free of strain. Type 3 would even create a strain state with alternating strain types. All these considerations only hold for SL without any relaxation. If relaxation is present, the problem becomes even more complicated. One question which has to be clarified concerns the onset of relaxation. As explained in chapter 2.1.3, the critical layer thickness, calculated after the Matthews-Blakeslee model, is generally the starting point for the relaxation process. As the strain state of SL is not uniform, it is unclear if relaxation might occur at smaller or larger layer thicknesses than the Matthews-Blakeslee model predicts. Also the relaxation process could be much more complicated. SL contain large numbers of interfaces at which dislocations could be generated, stopped or redirected. Layer cracking or even delamination might also be a scenario. For types 1 and 2, the situation could be comparable to uniform layers treated in the Matthews-Blakeslee model because the strain type is the same and both in-plane lattice parameters tend to relax in the same direction. For types 2, 3 and 4, this seems unlikely as the strained layers which encounter a driving force for relaxation are alternated with layers which exhibit no strain (i.e. no driving force for relaxation) or which even feel a driving force in the opposite direction (type 3).

Three relaxation mechanisms for SL were reported in literature:

- coherent relaxation via MD formation only at the SL/buffer interface which induces strain of opposite direction in the second SL material and is comparable to relaxation occurring in a bilayer stack [66]
- crack formation [66], [67]
- staircase pattern of TD [68]

Einfeld et al. [66] were able to demonstrate a combined relaxation mechanism for AlGaN/GaN-SL deposited on a GaN (this corresponds to a case 4 SL). During the early stages of relaxation, the strain was relaxed via MD generation at the SL/substrate interface. This does not only relieve the tensile strain in the AlGaN barriers but also induces compressive strain in the GaN wells which was identified by a blue-shift of the GaN well photoluminescence peak. This is only possible up to a certain point at which additional compressive strain in the GaN wells becomes unfavorable. At this point, crack formation occurred. Another relaxation mechanism in SL was observed by Cherns et al. [68]. They investigated $Al_{0.5}GaN_{0.5}/GaN - SL$ deposited on $Al_{0.45}Ga_{0.55}N$ (which correspond to case 3) and found a staircase pattern of TD relieving the compressive strain in the GaN wells similar to the dislocation inclination process described in the Romanov-Speck model.

The onset of relaxation in SL has also been discussed in the literature. Most groups investigated the relaxation onset as a function of the effective material content (e.g. AlN fraction in AlN/GaN-SL) while the overall SL layer thickness was fixed [66], [46]. This makes it quite difficult to compare the properties of SL with their respective alloys and clarify if and how SL can handle higher strain than homogeneous alloys. Several reasons why SL should feature a delayed relaxation onset compared to homogeneously alloyed layers have been proposed: Reduced TD densities (generated by TD termination at interfaces in the SL) could suppress crack nucleation (material defects as TD could act as crack nucleation sites [66]). Defects such as cracks have to thread through lesser strained, unstrained or even differently strained (compressive vs. tensile) layers which is energetically unfavorable. Defects might also encounter periodically changing formation energy in a SL which could also impede their formation [66]. In this context, it seems difficult to precisely predict the behavior of a random SL under stress and further analysis is still necessary. Nevertheless, the theoretical considerations given above are very promising. SL might be able to overcome the limitations of ternary or quaternary alloys induced by relaxation phenomena. This of special importance for group III nitrides where explicit control over the strain state and relaxation process of layers is crucial.

Although the concept of strain engineering with SL is very interesting and also promising, SL can also be used for other applications. Because of the periodic valence band oscillations, SL are useful for Mg-doped structures. The high ionization energy of Mg (0.26 eV [24]) prohibits efficient p-type doping in group III nitrides. With the valence band oscillation in the SL structure, the acceptor level of Mg can locally be dragged under the Fermi level [69], [70]. The

high internal strain also affects nonlinear optical properties as the Pockels effect. AlGaN/GaN SL are found to have electro-optic coefficients ten times larger than bulk GaN [71].

Altogether, SL open up great possibilities to further engineer and optimize material properties for the designated applications. Nevertheless, fundamental research is still necessary to fully understand the behavior of group III nitride SL in heteroepitaxy. SL could serve as an alternative to ternary or quaternary layers if drawbacks like compositional pulling or crystal quality are circumvented and the strain state can be controlled successfully.

2.3 Characterization Methods

2.3.1 X-ray Diffraction

X-ray diffraction is a powerful method to gain information about composition, strain state and crystal quality of epitaxial group III nitride layers. During the measurement, X-rays are diffracted at the crystal lattice planes according to the Bragg condition [43]. Depending on the angle of diffraction θ and lattice plane spacing d_{hkl}, constructive or destructive interference occurs. The diffraction experiment converts each set of two-dimensional lattice planes from real space into a point reflex in reciprocal space. The sum of all point reflexes from different sets of lattice planes form a three-dimensional point lattice in the reciprocal space. Real and reciprocal space are correlated inversely by Fourier transformations. Further information on the theoretical background of X-ray diffraction can be found in the paper by Moram et al. [43].

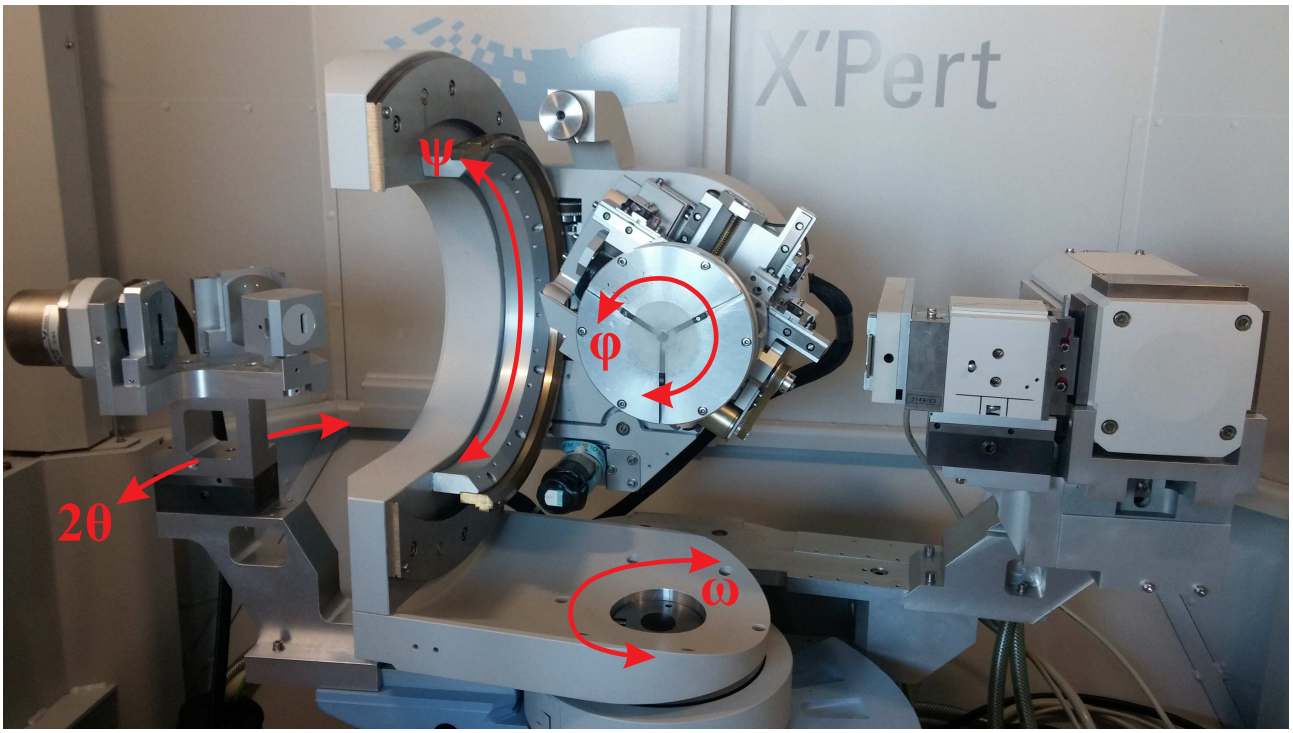

Figure 2.11: Panalytical X'Pert MRD XRD with a four-circle goniometer with rotation angles ω, 2θ, φ and ψ.

The sample under investigation is mounted on a four-circle goniometer as shown in figure 2.11. This enables rotation of the sample in four independent directions: omega (ω, angle between sample surface and fixed incident beam), theta (θ, angle between diffracted beam and crystal lattice plane), phi (φ , azimuthal angle) and psi (ψ, polar angle). A line-focused X-ray beam is directed onto the sample surface. The diffracted beam is detected either directly with the open detector (OD or RC) or with an additional triple-axis analyzer crystal (TA) for higher angular resolution. In the given geometry, 2θ is also called the diffraction angle between incident and diffracted beam.

To obtain information about the crystal quality of a sample, rocking curve scans are utilized. In this method, the goniometer is set to specific angles so that the Bragg condition is

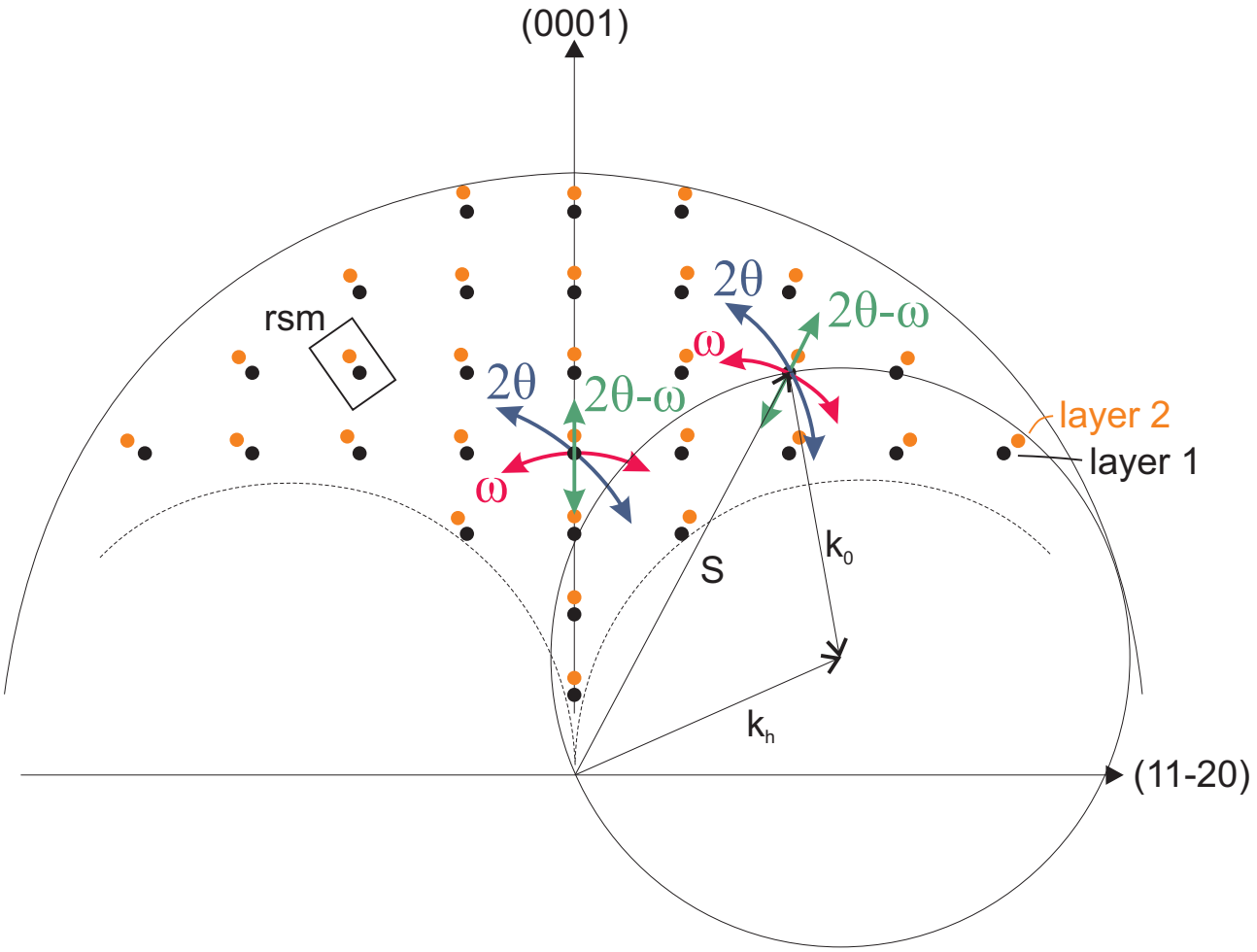

Figure 2.12: Reciprocal space for a bilayer sample with diffraction peaks for layer 1 shown in black and in orange for layer 2. The scan directions in the reciprocal lattice for symmetric and asymmetric diffraction conditions are shown. A typical area of a reciprocal space map is depicted. The reciprocal space under the dotted semicircles can not be accessed with a standard four-circle goniometer because the sample blocks the X-ray beam.

fulfilled. The sample is then "rocked" back and forth in omega direction, in and out of the Bragg condition. The direction of the RC omega scan in reciprocal space for symmetric (000l) and asymmetric (hkil) diffraction conditions is depicted in figure 2.12 (red arrows). The schematic drawing shows the diffraction peaks for a bilayer sample (layer 1 and layer 2) in reciprocal space. The scan direction of omega scans is always perpendicular to the scattering vector **S** which is determined by the incident and diffracted beams $\mathbf{k}_0$ and $\mathbf{k}_h$ with $\mathbf{S} = \mathbf{k}_h - \mathbf{k}_0$.

The detected peak has a specific width, which can be characterized with the full-width-at-half-maximum (FWHM) value. This figure indicates the crystal quality, as defects broaden the peaks representing a deviation from the ideal crystal lattice. Other broadening factors as sample size, instrumental broadening, limited correlation length and wafer curvature are also present and have to be taken into account [43]. Rocking curve scans also yield information concerning dislocation types present in the sample. The lattice distortion of a dislocation, which is responsible for dislocation-related peak broadening, is described by the Burgers vector as previously explained in chapter 2.1.3. This is a non-isotropic phenomenon as the Burgers vector has a specific direction, which depends on the dislocation type (screw, edge, mixed)

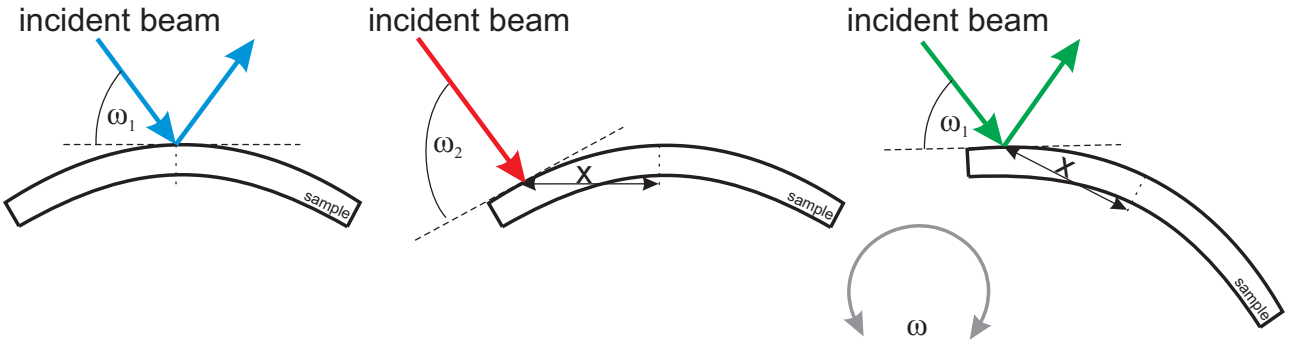

Figure 2.13: Curvature measurement with XRD. Left: sample with correct diffraction geometry. Middle: the sample has been moved in x-direction and due to the curvature the diffraction condition is not fulfilled anymore. Right: The sample has been rotated in ω and the correct diffraction geometry is regained. The curvature radius can now be concluded with displacement in x-direction and the rotation angle in ω.

and the crystal structure. Dislocations with Burgers vectors in c-direction (<0001>) lead to broadening of X-ray diffraction reflexes (hkil) with $l \neq 0$. Dislocations with Burgers vectors in in-plane direction (<hki0>) lead to broadening of reflexes with $h, k, i \neq 0$. Burgers vectors with in-plane and c-direction projections lead to broadening of all reflexes. By comparison of FWHM values of different reflexes, the dominant Burgers vector direction can be concluded.

Rocking curve scans are also useful to determine the curvature radius of a wafer (under the assumption that the substrate is flat and the relation of crystal lattice and sample surface is laterally constant) . In a curved wafer, the lattice planes parallel to the surface are not strictly planar but slightly curved according to the curvature of the wafer. This implies that the effective ω value of a diffraction condition depends on the x-y position on the wafer. The measurement set-up is depicted in figure 2.13. To fulfill the Bragg condition, the angle ω between incident beam and sample surface has to be set to a specific value. This is shown with the blue incident beam on the left. If the curved sample is now moved in x-direction, the surface bends away which changes ω (red incident beam in the middle of figure 2.13). To again fulfill the diffraction condition, the sample has to be rotated in ω to match the specific value. This is shown on the right with the green X-ray beam. In this way, the diffraction condition at the wafer edge (right) is fulfilled for a different ω_{eff} as in the wafer center (blue). The curvature radius R can then be calculated with $R = x/sin(\Delta\omega)$ with the distance between the measurement points x and $\Delta\omega = \omega_2 - \omega_1$. By mapping the effective ω values over the wafer, the curvature type and radius can be calculated.

As described in section 2.1.3, strain is a very important parameter in epitaxially grown thin-film structures. X-ray diffraction yields information about the strain state of crystalline layers via lattice parameter measurements. In this measurement technique, a part of the reciprocal space is scanned by repeated 2θ-ω-scans (2θ and ω are moved simultaneously during the scan, the scan direction is depicted in fig. 2.12) with increasing offset in ω. The scanned area is a map of the reciprocal space (reciprocal space map, rsm) and should be selected in a manner that the reflexes (e.g. $(10\bar{1}5)$) of all layers in the multilayer sample under investigation are included. This means that a certain area around one of the diffraction peaks in figure 2.12 is

mapped. From rsm, it is possible to calculate the lattice parameters of a layer as the exact diffraction angles ω and 2θ of a reflex are recorded. In this thesis, the (0002), (0004), $(10\bar{1}5)$ and $(20\bar{2}4)$ reflexes are used to determine the c-lattice parameter and the $(10\bar{1}5)$ and $(20\bar{2}4)$ reflexes are used to access the a-lattice parameter.

With rsm, it is also possible to directly derive whether a layer is pseudomorphically grown or not. The lattice parameters a and c in real space are connected to the coordinates of the reciprocal space by:

$$\mathbf{Q_x} \propto \frac{1}{a} \tag{2.4}$$

$$\mathbf{Q_z} \propto \frac{1}{c} \tag{2.5}$$

This implies that if the reciprocal space coordinates Q_x of two layers are the same, the lattice parameters a of both layers are equal. In the case of a layer heteroepitaxially deposited on another layer, pseudomorphic growth of the upper layer on the underlying layer can be concluded. If the reciprocal space coordinates are not the same, the heteroepitaxially deposited layer has a different in-plane lattice parameter a than the underlying layer. In this case, relaxation of the heteroepitaxial layer is present. If the composition of the heteroepitaxial layer is known, the relaxation grade can be determined by comparing measured and bulk lattice parameter values.

If the strain state of a multilayer sample is known, a 2θ-ω scan of the (0002) reflex can give additional information concerning the composition and thickness of individual layers. Due to the nature of the (0002) reflex, all layer peaks have the Q_x coordinate zero, regardless of their a-lattice parameter. This implies that a (0002) 2θ-ω scan includes peaks from all layers in the sample, if the scan range is wide enough. For epitaxial layer stacks grown in c-direction, all interfaces and the sample surface are parallel to the (0002) planes and can therefore affect the (0002) 2θ-ω scan. At the interfaces, the X-ray beam is partially reflected and for different incident angles, fringe peaks are forming due to interference effects. Theses fringe peaks are called Pendellösung fringes. The thickness d of the layer under investigation is directly related to the spacing of the fringe peaks $\delta\omega$ by [43]:

$$\delta\omega = \frac{\lambda \cdot \sin(\epsilon)}{d \sin(2\theta)} \tag{2.6}$$

The angle ϵ denotes the angle between sample surface and diffracted beam while 2θ is the average 2θ value for the fringe peaks. If the strain state of a ternary layer is known, the composition is also accessible from 2θ-ω scans because for every lattice parameter, there is only one possible ternary composition. For quaternary layers, it is not possible to determine the composition with XRD because the third group III atom species introduces an additional degree of freedom. For such layers, other methods as secondary ion mass spectrometry (SIMS) or Rutherford backscattering spectrometry (RBS) are necessary to access the composition.

2.3.2 Atomic Force Microscopy

With atomic force microscopy (AFM), the surface morphology of a sample can be investigated. The height resolution reaches values in the Ångström regime. The lateral resolution is in the micrometer range.

During the measurement, a probe tip mounted on a cantilever is moved in proximity to the sample surface. Figure 2.14 shows the schematic set-up of the AFM. The probe tip has a tip radius in the range of tens to hundreds of nm, which determines the lateral resolution. The cantilever is excited with its resonance frequency. Due to interaction of tip and sample atoms, the oscillation of the cantilever is damped. This interaction is based on the attractive Van-der-Waals forces and repulsive overlapping of electron orbitals (Pauli repulsion) resulting in the Lennard-Jones potential [72]. The attractive interaction (r^{-6}) and the repulsive interaction (r^{-12}) are highly sensitive on the distance r of the two interaction partners tip and sample. The oscillation is recorded with a laser beam which is directed on the cantilever and then reflected into a photodetector. With a controller, the height of the tip with respect to the sample is permanently readjusted to a constant damping set-point. In this way, the tip follows the surface topography of the sample, which can then be recorded and depicted.

With AFM, the surface morphology of epitaxial layers can be judged. It is possible to distinguish between 3D and 2D growth modes. The first one shows pronounced height differences while the latter shows characteristic step flow patterns with step heights of approximately one elementary cell as visible in figure 2.15. The step heights measured in fig. 2.15 are between 0.4 and 0.75 nm, which is in the range of the theoretical c-lattice parameter of GaN. The roughness is a very good measure for the epitaxial quality. To quantify the roughness of a surface, the root mean square (rms) of the height distribution is used in most cases. As an example, this value should be below 1 nm for buffer surfaces. The depicted GaN buffer in figure 2.15 exhibits an rms value of 0.4 nm.

In this thesis a DME DualScope AFM with a DS 95 scanner and C-26 digital-controller is used.

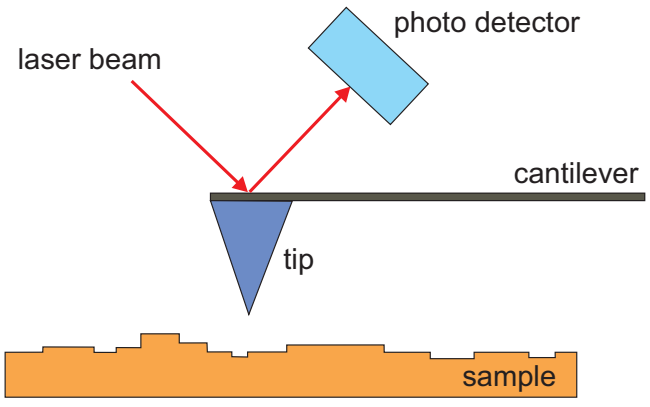

Figure 2.14: Measurement principle of AFM.

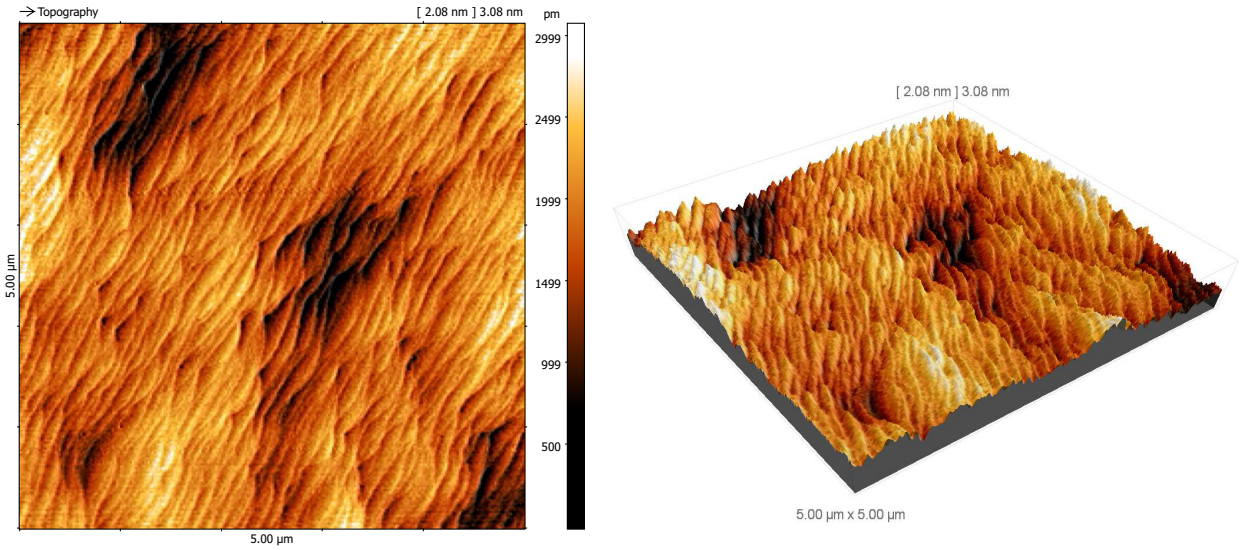

Figure 2.15: AFM image of a standard GaN buffer in standard 2D presentation on the left. The 3D picture is shown on the right.

2.3.3 Optical Reflectometry

With white-light reflectometry, layer thicknesses, refractive indices or wavelength-sensitive reflectance can be determined. The sample is illuminated with white light perpendicular to the sample surface as depicted in figure 2.16. According to Fresnel's formulas, the light is partly reflected, transmitted or absorbed. The reflected light intensity is detected with a spectrometer. Constructive or destructive interference occurs depending on layer thickness, refractive index and incident wavelength. If the layer thickness is known, the refractive index of the layer can be determined and vice versa. It is also possible to examine multiple layers by using a model which is fitted to the measured reflectance data. The reflectance of mirrors like distributed Bragg reflectors (DBR) can be directly measured with the reflectometer. In this thesis, a Sentech FTP advanced white light reflectometer is used with a spectral range from 230 - 840 nm.

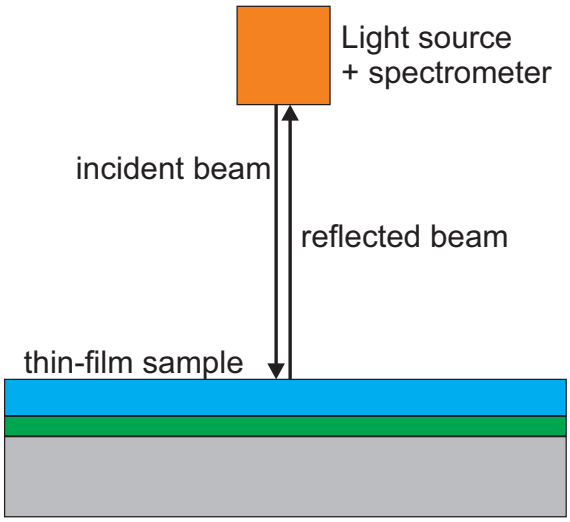

Figure 2.16: Measurement set-up of a white-light reflectometer.

Chapter 3

Deposition of AlN/GaN-SL Structures with MOVPE

This chapter will cover the basic MOVPE process for AlN/GaN-SL and the structural characterization of the resulting layer stacks. The influence of process parameters on the crystal quality of the SL is investigated. Also the strain managing capabilities of AlN/GaN-SL are explored and the critical thickness and the relaxation mechanism are determined. In the last section, a resonant tunneling diode (RTD) fabricated on the basis of the developed SL deposition conditions is explored to finally prove the high structural quality of the AlN/GaN-SL deposited with MOVPE.

3.1 Optimization of Growth Parameters for AlN/GaN-SL

To obtain high-quality SL, the growth parameters have to be evaluated very carefully. The growth rates should be comparably low to be able to precisely deposit the very thin individual layers of the SL (1-8 nm). High interface quality and layer thickness homogeneity are also necessary to obtain laterally uniform material properties. In the case of AlN/GaN-SL, the binary materials GaN and AlN have to be deposited in an alternating sequence. As GaN and AlN require quite different growth conditions, the deposition of the SL can be pursued in two ways: Either GaN and AlN are deposited at their respective ideal growth conditions which includes ramping steps between the individual layers or GaN and AlN layers are deposited at the same but non-ideal growth conditions without any ramping steps. The first approach seems to lead to high-quality individual layers in the first place. However, the ideal growth conditions for GaN and AlN are very different. While GaN should be deposited at higher reactor pressures above 300 mbar [73], AlN needs a very low pressure around 30 mbar to prevent parasitic gas phase reactions of TMAl [74]. The typical growth surface temperature (monitored with the in-situ LayTec tool) of GaN ranges from $1020°C$ to $1090°C$ for the used MOCVD system while AlN is deposited at remarkably higher growth surface temperatures around $1250°C$. Already the differences in reactor pressure and temperature account for ramping times of one to two

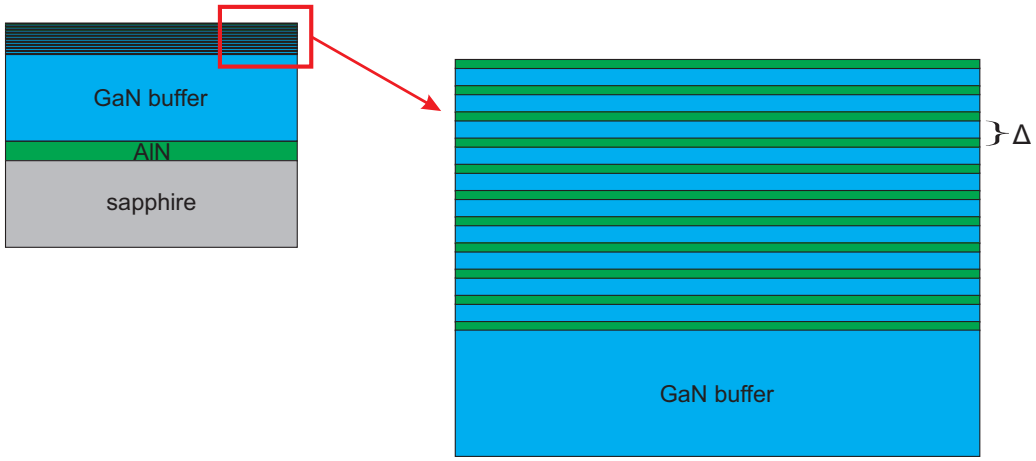

Figure 3.1: Schematic layer stack of a SL sample. The SL is deposited on a GaN/AlN buffer stack on a sapphire substrate. The enlarged SL region is shown on the right consisting of AlN and GaN layers. The thickness of one AlN/GaN period Δ is marked on the right.

minutes between GaN and AlN growth. This is very long compared to growth times around one minute or less for each individual layer. During the ramping steps, the sample surface can be destabilized by parasitic hydrogen etching [75]. To avoid these critical ramping steps, the deposition of both binary materials at the same conditions is pursued in this thesis.

In a first step, growth conditions which allow depositing both GaN and AlN in an acceptable quality have to be found. To study various parameters, test structures were used comprising an AlN/GaN-SL deposited on a standard buffer structure on sapphire substrate (cmp. chapter 2.1.2). Figure 3.1 shows a schematic structure of the samples. At first, the impact of the reactor pressure is investigated. In general, the reactor pressure needs to be kept more in the AlN- than in the GaN-compatible range to prevent the parasitic gas phase reactions of TMAl mentioned before.

In figure 3.2, (0002)-2θ-ω-scans of three 15-fold AlN/GaN-SL samples are depicted which were deposited at different reactor pressures of 75, 100 and 125 mbar (all samples were deposited at 1060°). The (0002) 2θ-ω-scans comprise diffraction peaks from the SL and diffraction peaks from the underlying GaN and AlN buffer layers (cmp. fig. 3.1). The diffraction peak originating from the AlN buffer is located at higher angles than the GaN buffer diffraction peak because both buffer layers are nearly fully relaxed and the c lattice constant of AlN is smaller then the c lattice constant of GaN (cmp. sec. 2.3.1). The SL causes multiple diffraction peaks. The zero-order SL-peak (marked with "0. SL" in fig. 3.2) is located between the GaN and AlN diffraction peaks as the AlN/GaN-SL represents a virtual AlGaN alloy. Pendellösung fringes at the zero-order SL peak refer to the interfaces of the SL to adjacent layers and their spacing is related to the overall layer thickness of the SL. The higher-order SL peaks (first-order SL are marked with "1. SL" in fig. 3.2) are connected to the interfaces in the SL (between GaN and AlN). Their spacing to the neighboring SL peak of higher or lower order is related to the thickness of the bilayer Δ (cmp. fig. 3.1). The appearance of higher-order SL peaks is a measure for the interface quality and the uniformity of Δ_{SL} throughout the whole SL layer. With higher-order peaks present in the 2θ-ω-scan, the layer thicknesses of GaN and AlN in the

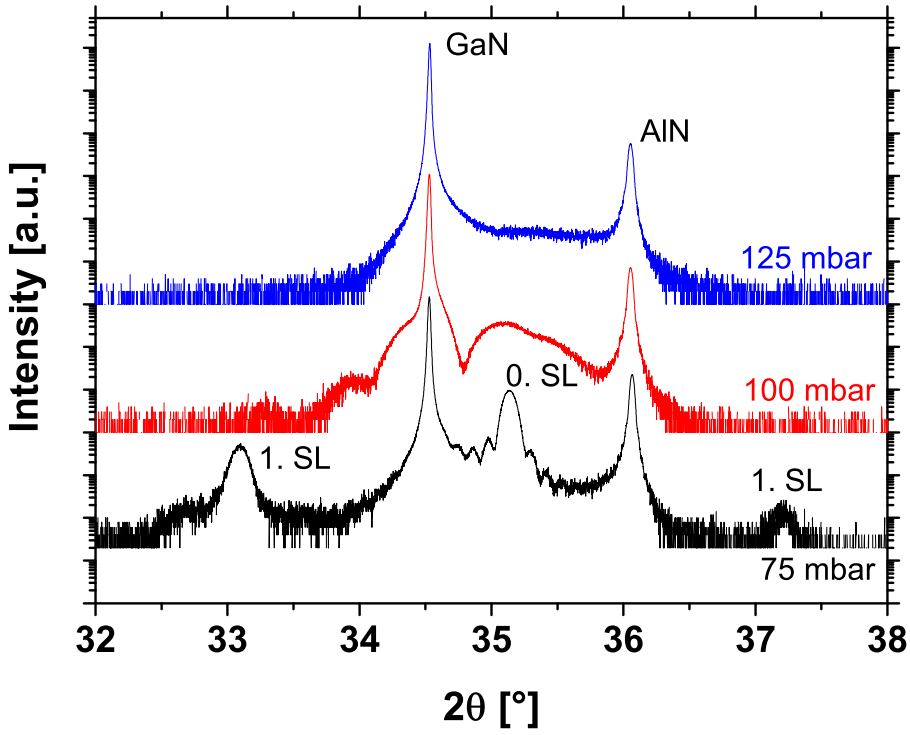

Figure 3.2: (0002) 2θ-ω-scans of three SL samples deposited at 75, 100 and 125 mbar. The graphs have been displaced on the intensity axis for better visibility.

SL can be evaluated by fitting a simulation of the scan to the measured data.

The (0002) 2θ-ω-scan of the SL deposited at 75 mbar shows Pendellösung fringes and also first-order SL peaks (at 33° and 37.5°). This proves good interface and crystal quality of the fabricated sample. If the reactor pressure during SL growth is increased to 100 mbar (red graph in fig. 3.2), the first-order peaks and Pendellösung fringes vanish from the scan. Only a very broad zero-order SL peak is visible. If the pressure is further increased to 125 mbar, no diffraction features from the SL can be found in the 2θ-ω-scan (blue graph in fig. 3.2). This behavior is presumably related to the inadequate reactor pressure for AlN MOVPE growth. It was already elucidated that AlN growth is only possible at low reactor pressures. At reactor pressures of 100 mbar or above, the AlN layer and interface quality is affected as the SL interface features vanish from the 2θ-ω-scans. This might be caused by parasitic prereactions of TMAl in the gas phase [74]. In summary, it can be concluded that SL growth is only possible at reactor pressures below 100 mbar. As a standard reactor pressure, 75 mbar is chosen for SL growth.

Regarding the growth surface temperature, GaN deposition is not possible at temperatures as high as $1250°C$ because of the aforementioned hydrogen etching. The growth surface temperature is therefore chosen in a temperature regime typical for GaN growth which is between $1000°C$ and $1100°C$ [37]. Growth surface temperatures from $1053°C$ to $1073°C$ were tested to evaluate if layer degradation occurs.

Figure 3.3 shows the LayTec in-situ reflectivity signal at 605 nm of four 15-fold SL samples deposited at different temperatures and 75 mbar. The x-axis displays the time during deposi-

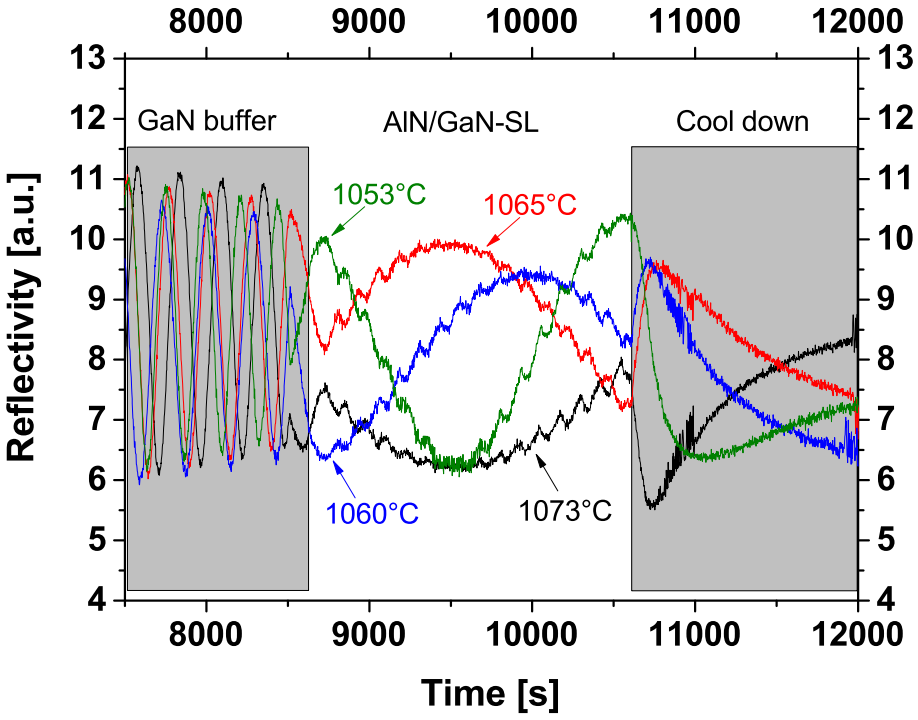

Figure 3.3: LayTec in-situ reflectivity signal at 605 nm of four SL samples during growth at different growth surface temperatures and 75 mbar.

tion. For clarity, the preceding GaN buffer deposition and following cool-down steps are shown grayed out. The reflectivity signals show a slow oscillation of which only one or two maxima or minima are visible in the graph. This oscillation is related to the growth rate of the whole SL stack. The appereance of this slow oscillation depends only on the exact GaN buffer thickness and the phase of interference and is not related to the SL layer quality. It can be seen that the oscillation frequency is not constant for the four samples. While the SL deposited at 1060°C (blue graph) and 1065°C (red graph) show a very similar oscillation frequency, the frequency is higher for the SL deposited at 1053°C. This implies that the growth rate at 1053°C is higher than at 1060°C. At a deposition temperature of 1073°C, a much lower oscillation frequency can be observed which translates into a much slower growth rate.

All four reflectivity signals show a second, much shorter oscillation. This oscillation corresponds to the alternating deposition of AlN and GaN during SL growth and indicates good interface quality in the SL. As a standard growth surface temperature, 1060°C is chosen for SL growth, as no reduction in interface quality was observed in the tested temperature regime and the sample exhibits an intermediate growth rate.

As already described in chapter 2.2, the growth times of the individual AlN and GaN layers in the SL become very short due to the low layer thicknesses around 1 to 3 nm. Critical ramping steps have already been avoided but there is another constraint for ultra-thin layer deposition: The growth times should be at least one order of magnitude larger than the response/switching time of the valves and the gas residence time in the MOVPE system which are in the range of one second. With the growth rates used for buffer structures this can not be achieved. For

	TMGa flow [sccm]	TMAl flow [sccm]	NH_3 flow [sccm]	V/III GaN	V/III AlN
GaN buffer	15	0	1500	1015	-
AlN/GaN-SL	6-10	24-42	1000	1690-1015	2130-1220

Table 3.1: Precursor flows of buffer and SL growth conditions

the GaN buffer, a growth rate around 1.8 μm is used which is realized by precursor flows of 15 sccm TMGa and 1500 sccm NH_3 resulting in a V/III ratio of 1016. Such a high growth rate would lead to a deposition time of 6 seconds for a 3 nm thick GaN layer. As this would be in the same order of magnitude as the valve response and residence time, the growth rate has to be lowered for successful SL deposition. On the other hand, it is always desirable to use the highest possible growth rate due to efficiency considerations concerning the runtime of the MOVPE system. Therefore, it is necessary to optimize the growth rate during SL growth to obtain a rate which is as slow as necessary and as high as possible.

To obtain such low growth rates compared to buffer growth conditions, the V/III ratios for AlN and GaN growth need to be increased and the overall precursor supply has to be lowered. As a starting point for a V/III ratio variation, 2130 was chosen for AlN growth and 1690 for GaN growth which was realized with TMGa and TMAl flows of 6 and 24 sccm and an ammonia flow of 1000 sccm. The ammonia flow was reduced to 1000 sccm for SL growth compared to the buffer conditions of 1500 sccm. The precursor flows of buffer and SL growth are summarized in table 3.1 The resulting growth times for 3 nm GaN and 1 nm AlN layers at these conditions are around 50 s each. The V/III ratio was then reduced by an increase of the group III precursor flow with constant ammonia flow to investigate the influence of the AlN and GaN growth rates on the SL quality and test if slightly higher growth rates (and resulting shorter growth times) still yield satisfying results. The 18-fold SL was deposited at 75 mbar and a growth surface temperature of $1060°C$ and with anticipated layer thicknesses of 3 nm for GaN and 1.3 nm for AlN in the SL. Figure 3.4 shows the GaN growth rate in the SL with respect to the V/III ratio. It can be clearly seen that the growth rate increases with decreasing V/III ratio. The values of the growth rate range from 0.06 to 0.19 nm/s. This leads to deposition times of 50 s for 3 nm GaN at a growth rate of 0.06 nm/s down to 15 s for 3 nm GaN at a growth rate of 0.19 nm/s. In this way, the growth rate is determined by the group III flow which is the expected behavior in MOVPE.

Figure 3.5 shows the AlN growth rate for V/III ratios varied from 2130 to 1220. The growth rate stays constant at 0.026 nm/s and shows no increase as for GaN. This behavior might originate from the previously described parasitic gas phase prereactions of TMAl, which can lead to decreased precursor efficiency. According to Lobanova et al. [74], this phenomenon is expected to worsen at reduced V/III ratios. This could lead to a constant growth rate as the additional precursor does not contribute to the growth process but is already consumed by parasitic prereactions. Lobanova et al. suggest a decreased reactor pressure to prevent these prereactions also at reduced V/III ratios. To test this hypothesis, an additional SL was fabricated at a reduced reactor pressure of 50 mbar. This sample exhibited massive particle

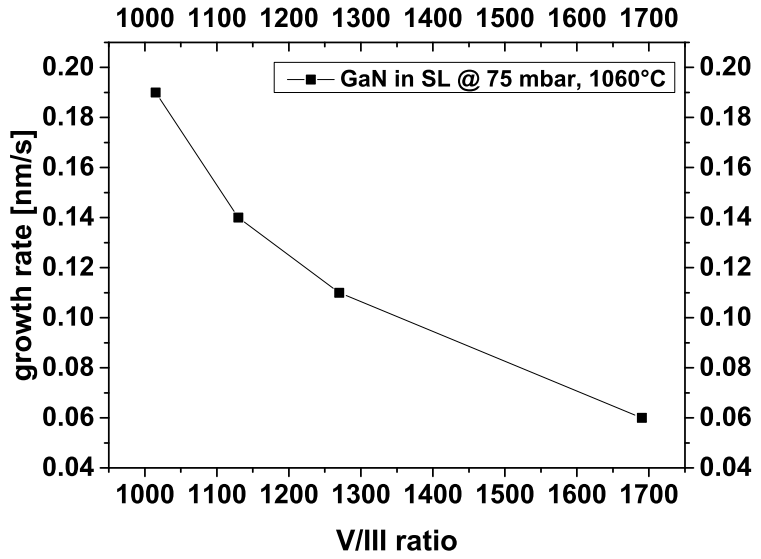

Figure 3.4: Growth rate of GaN in the SL plotted versus V/III ratio with constant ammonia flow.

formation in the gas phase, so no SL growth was possible. An additional increase of the growth surface temperature from 1060°C to 1080°C hindered the particle formation and a growth rate of 0.066 nm/s was possible at a V/III ratio of 1220 (red star in figure 3.5).

To investigate the crystal quality of the samples, (0002) 2θ-ω-scans were collected from the samples (figure 3.6). All samples exhibit Pendellösung fringes and higher-order SL peaks which proves successful SL deposition and also implies good interface quality. With decreasing V/III ratio, the zero-order SL peak moves towards the GaN peak and away from the AlN peak. This can be attributed to the increased GaN growth rate in combination with the constant AlN growth rate (cmp. fig 3.4 and 3.5), which results in a decreased AlN fraction in the SL in analogy with AlGaN with a reduced Al content. One can also see that the zero-order SL peak becomes narrower and features higher intensity compared to the GaN peak. This is related to the thicker overall layer thickness of the SL layer caused by the increased GaN growth rate. This is also confirmed by the decreasing spacing of the higher-order SL peaks which implies a higher thickness of the GaN/AlN bilayer repeat Δ. A fit of the XRD scan yields an increase of the SL layer thickness from 81 nm to 206 nm.

In summary, it was possible to successfully deposit SL at all tested growth rates. For higher growth rates, parasitic prereactions of TMAl occurred and SL deposition was only possible at reduced reactor pressure and increased growth temperatures. For the following experiments, the lowest growth rates at V/III ratios of 2130 (AlN) and 1690 (GaN) were chosen as standard growth rates (GaN: 0.06 nm/s, AlN: 0.026 nm/s). These conditions eliminate the problem of parasitic prereactions and the reduced MOVPE runtime efficiency is neglected for the fundamental experiments carried out in this work. Nevertheless, it was shown that SL deposition is possible at higher growth rates. This is of great importance for implementation of SL into devices. Therefore, the topic of enhanced growth rates will be considered again for SL-DBR growth described in section 4.2.

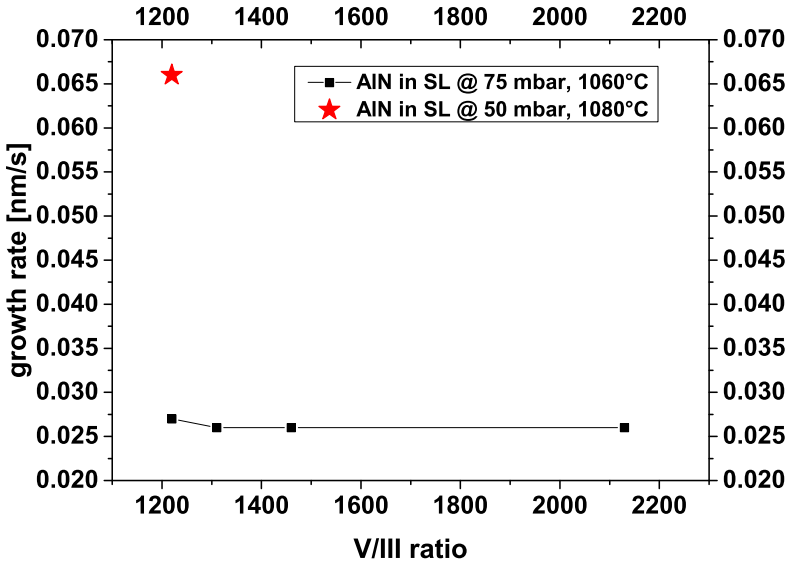

Figure 3.5: Growth rate of AlN in the SL plotted versus V/III ratio with constant ammonia flow.

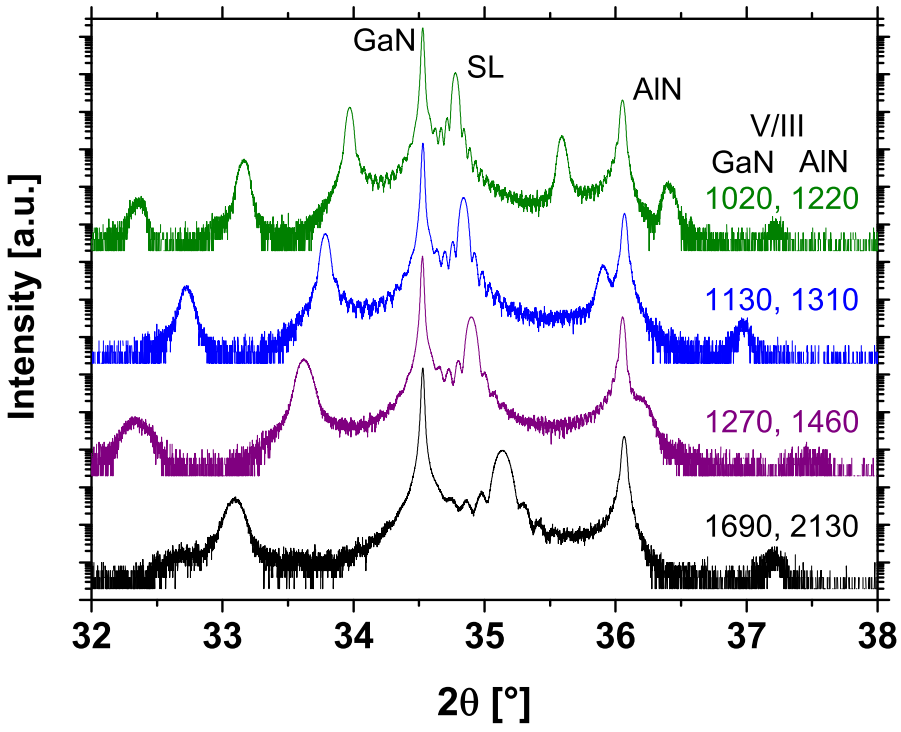

Figure 3.6: (0002) 2θ-ω-scans of 18-fold SL marked with the V/III ratios (NH_3 = const.) of GaN and AlN during SL growth. The graphs have been displaced on the intensity axis for better visibility.

3.2 Determination of Critical Thickness of AlN/GaN-SL

To investigate the strain management quality of AlN/GaN-SL, the critical thickness of such SL was determined. Five SL samples with increasing number of bilayer n_{SL} and thus increasing layer thickness were fabricated and analyzed with AFM and HR-XRD. The samples were deposited at standard conditions of 75 mbar, 1060°C, V/III ratios of 2130 for AlN and 1690 for GaN (cmp. sec. 3.1). The thicknesses of AlN and GaN layers in the SL were chosen to be $d_{AlN} = 1.3\ nm$ and $d_{GaN} = 3\ nm$, respectively. The whole SL structure was deposited on a relaxed GaN buffer (cmp. sec. 2.1.2). Special attention was paid to the layer thickness of the thin AlN layers of the SL. The critical thickness, at which relaxation starts, for a thin AlN layer between two thick GaN layers is around 3 nm [46]. This is why the layer thickness of AlN in the SL d_{AlN} was chosen to 1.3 nm which is far below this limit to prevent individual relaxation of the AlN layers. To increase the layer thickness of the SL d_{SL}, the number of bilayer repeats n_{SL} was gradually increased. In this manner 7-, 10-, 15-, 18- and 20-fold SL were fabricated. Every SL stack was terminated with an additional AlN layer of 1.3 nm. This results in a slightly decreasing effective Al content in the SL (x_{AlN}) with increasing layer thickness. The SL layer thickness of every sample was determined with (0002) 2θ-ω scans. The scans of the 15-, 18- and 20-fold sample are shown in figure 3.7. One can see that all scans show Pendellösung fringes indicating good crystal quality with exception of the 20-fold SL sample. The SL layer thicknesses for the 7-, 10-, 15- and 18-fold samples were extracted from the (0002) 2θ-ω scans by fitting a simulation of the scan to the measured data with the layer thickness as fitting parameter. The simulated scans are shown for the 15- and 18-fold sample in fig. 3.7 as thin lines. Very good agreement between simulation and measurement was achieved for all four samples. The layer thicknesses of the individual AlN and GaN layers match very well the anticipated layer thicknesses of 1.3 nm for AlN and 3 nm for GaN. Under the assumption of constant growth rates, the layer thickness of the lower-quality 20-fold SL sample was extrapolated. The AlN fraction of this sample was calculated using averaged values for AlN and GaN thickness. Table 3.2 summarizes the samples, their layer thicknesses extracted from XRD and resulting AlN fractions.

To investigate the strain state of the SL samples, reciprocal space maps (rsm) of the $(10\bar{1}5)$ and $(20\bar{2}4)$ reflexes were recorded. For the samples with 7-, 10- and 15-fold SL, the Q_x coordinate of SL zero-order and underlying GaN buffer layer peak was the same for the $(10\bar{1}5)$

n_{SL}	d_{AlN} [nm]	d_{GaN} [nm]	d_{SL} [nm]	strain state	x_{AlN} [%]
7	1.35	3.43	33	pseudomorphic	31.03
10	1.29	2.75	42	pseudomorphic	34.04
15	1.28	3.04	64	pseudomorphic	30.99
18	1.33	2.98	79	beginning relaxation	32.02
20	-	-	90	relaxed (58 %)	31

Table 3.2: Number of repetitions of AlN/GaN bilayers in the SL with the achieved layer thicknesses and AlN fraction

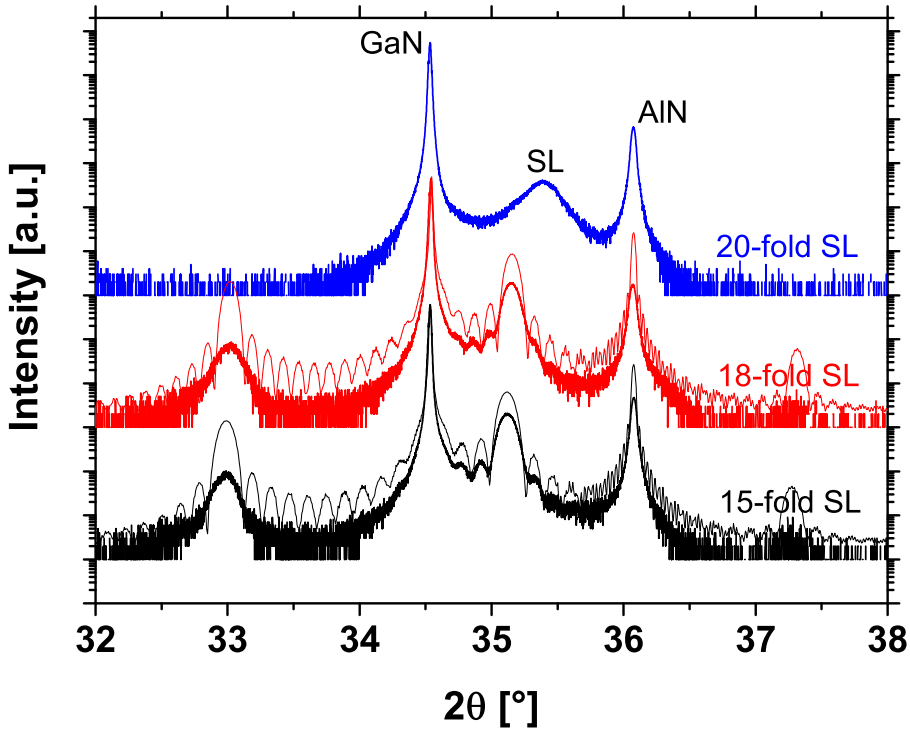

Figure 3.7: (0002) 2θ-ω-scans for 15-, 18- and 20-fold SL. The graphs have been displaced on the intensity axis for better visibility. For the 15- and 18-fold sample, the simulated 2θ-ω-scans are also depicted (thin lines).

and $(20\bar{2}4)$ reflexes. This indicates pseudomorphic growth of the SL on the GaN buffer. The 18-fold sample showed the same Q_x coordinate of SL and GaN buffer only in the $(10\bar{1}5)$ reflex. The Q_x coordinated differed for the $(20\bar{2}4)$ reflex, marking the onset of relaxation at a SL layer thickness of 79 nm which denotes the critical layer thickness. The 20-fold sample showed clear relaxation for both reflexes from the GaN buffer peak towards the AlN buffer peak indicating that tensile stress of the SL induced by the AlN films was responsible for the relaxation process. Figure 3.8 shows a merged rsm of the 15- and 20-fold sample. It can clearly be seen that the SL peak of the 20-fold sample is shifted to the right in the direction of the bulk AlN in-plane lattice constant. From figure 3.8, it also becomes clear that the SL peak of the 20-fold sample features lower intensity and is smeared out compared to the diffraction peak obtained from the 15-fold SL. This might be related to a decrease in crystal quality by defect generation due to the relaxation process. This hypothesis is confirmed by the lack of the afore mentioned Pendellösung fringes in the (0002) 2θ-ω-scan of the 20-fold sample (fig. 3.7).

Judging the grade of relaxation is quite difficult in the case of this SL. For ternary AlGaN layers, one would measure the Al content with a (0002) 2θ-ω-scan, calculate the resulting bulk in-plane a-lattice parameter with Vegard's law [76] and compare this result with the actual lattice parameter of the relaxed layer. With this technique, an a lattice parameter equal to the a-lattice parameter of the substrate layer would denote a relaxation grade of 0 % while an a-lattice parameter equal to the calculated in-plane lattice parameter would denote 100 % relaxation. In a first approximation, the SL was assumed to behave like a homogeneous AlGaN

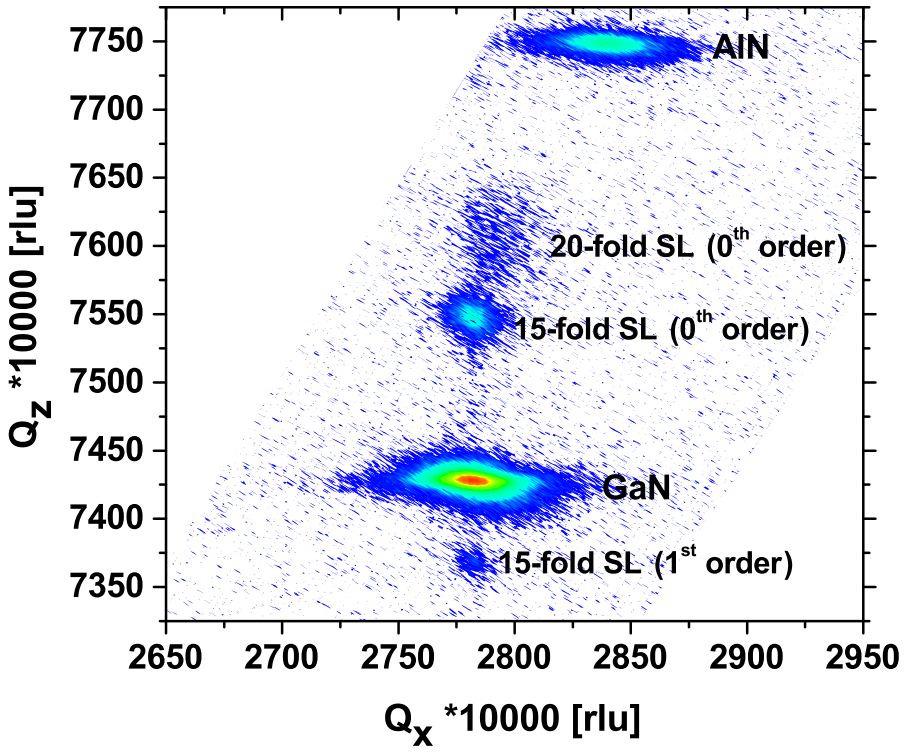

Figure 3.8: Merged rsm of the $(10\bar{1}5)$ *reflex for the 15- and 20-fold SL sample.*

layer with an Al content of 31 % (equal to the AlN fraction of the 20-fold sample). The a-lattice parameter is then calculated after Vegard's law with an AlN lattice parameter of 0.3112 nm [7] and a GaN lattice parameter of 0.3194 nm determined with rsm of the GaN buffer reflex from the 20-fold sample. The resulting in-plane lattice parameter is 0.31686 nm. The lattice parameter of the 20-fold SL was measured to be 0.31792 nm. With respect to the lattice constant of the underlying GaN buffer, a relaxation grade of 58 % can be derived for the 20-fold sample. This value might exhibit a severe error as the determination of the SL lattice parameter with XRD is very imprecise due to the low diffraction intensity. It is not clear if the applied relaxation model is valid for a SL which will be investigated in the following.

The surface of all samples was characterized by AFM. Figure 3.9 shows the AFM graphs for all five samples. The surfaces of the 7-, 10-, 15- and 18-fold SL samples show a terrace-like structure with slightly increasing terrace area for increasing SL layer thickness. The 20-fold sample shows a network of micro cracks. The majority of the cracks seem overgrown which indicates a cracking during the epitaxial process and not during cool-down (illustrated in fig. 3.10). This matches with the theoretical understanding of the relaxation process, in which further growth of strained material becomes energetically unfavorable when the critical thickness is exceeded and defect generation occurs accompanied by subsequent deposition of relaxed material. The occurrence of micro-cracks explains the reduced intensity in the $(10\bar{1}5)$ rsm as well as the lack of Pendellösung fringes in the (0002) 2θ-ω scan and proves the assumption that a decrease in crystal quality is responsible for this behavior. In this way, micro-cracking can be identified as the major relaxation mechanism for AlN/GaN-SL with an effective AlN

fraction of 32 %.

To judge the strain-engineering properties of SL, the obtained critical thickness for the AlN/GaN-SL of 79 nm is compared to the critical thickness of a ternary AlGaN layer with an Al content similar to the AlN fraction of the SL under investigation. Ambacher et al. calculated the critical thickness of AlGaN layers grown on relaxed GaN buffers for various compositions [19]. They compared critical thicknesses derived from the Matthews-Blakeslee model with the values obtained by a model suggested by Fisher et al. and with experimental values. For an Al content of 32 %, the critical thickness was calculated to be below 10 nm with the Matthews-Blakeslee model, around 20 nm for the model by Fisher et al. and the experimental values yielded a critical thickness of approximately 60 nm. This is considerably lower than the 79 nm determined for the AlN/GaN-SL. It does not become fully clear what causes the higher critical thickness of the AlN/GaN-SL compared to AlGaN.

Bykhovski et al. [46] suggest that in AlN/GaN-SL the strain is distributed equally between the GaN and AlN layers and that the unrelaxed strain in symmetrical SL (equal layer thickness for AlN and GaN) can be halved in comparison to a single AlN layer sandwiched between GaN layers. This does not seem to apply for the samples investigated in this thesis. The reciprocal space map clearly shows that the SL as a whole is grown pseudomorphically on GaN until the critical thickness is reached. This means that both, AlN and GaN, layers have an a-lattice parameter equal to the in-plane GaN buffer lattice parameter. If that is the case, the GaN layers in the SL have to be unstrained and the AlN layers are fully strained which is contradicting the theory of equally distributed strain. This disagreement can be attributed to the fact that Bykhovski et al. proposed their theory on the basis of calculations for free-standing SL while the current samples are deposited on a GaN buffer which changes the strain state dramatically.

Kandaswamy et al. [67] also investigated the strain relaxation in AlN/GaN-SL grown by plasma assisted molecular beam epitaxy (PAMBE). They found that the SL relaxed to an equal final strain state regardless of the buffer structure (GaN-on-sapphire compared with AlN-on-sapphire) by formation of MD. But in contrast to the samples described in this thesis, the relaxation started already in the first SL period. From in-plane lattice parameter measurements by RHEED, Kandaswamy et al. concluded three-dimensional growth during the initial stage of AlN deposition in the SL, which could explain the immediate onset of the relaxation process. The relaxation mechanism of MD generation also differs from the cracking observed for the samples in this thesis. This could be the case due to the very different growth conditions of PAMBE compared to MOVPE. Those might influence the formation energy of defects as MD. Also the individual layer thickness of AlN in the SL deposited by Kandaswamy et al. was 3 nm which is exactly the value for which relaxation of single AlN layers sandwiched between GaN layers by MD generation is enabled [46]. As already described above, all SL samples in this thesis feature an AlN layer thickness in the SL around 1.3 nm to prohibit the direct relaxation by MD generation. This makes the relaxation mechanism described by Kandaswamy et al. very unlikely to apply for the samples described here.

Einfeld et al. [66] found a two-step relaxation mechanism for their MBE-grown AlGaN/GaN-

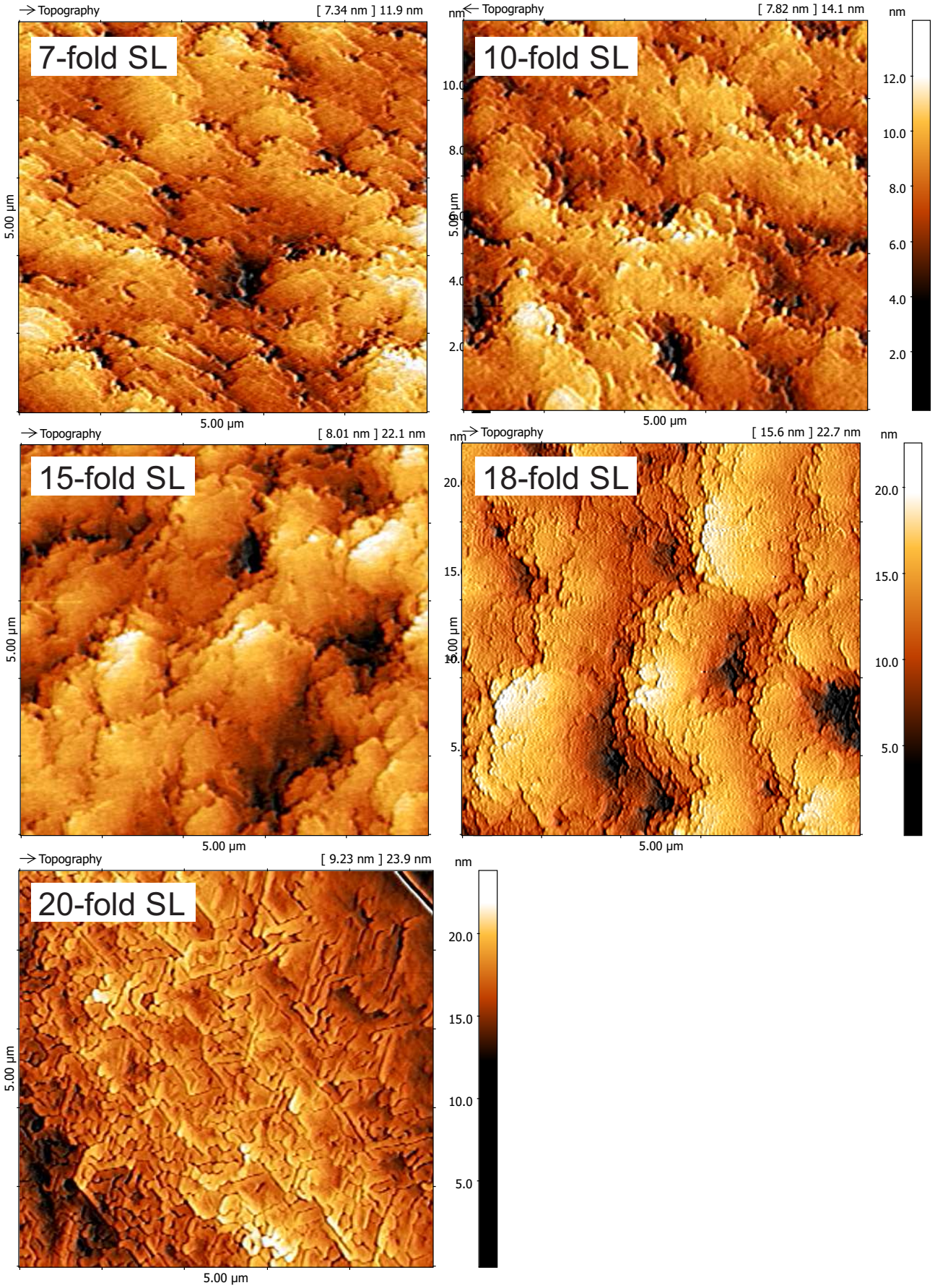

Figure 3.9: AFM images of 7-, 10-, 15-, 18- and 20-fold SL samples. (An FFT filter was applied to the raw data to exclude parasitic oscillations.)

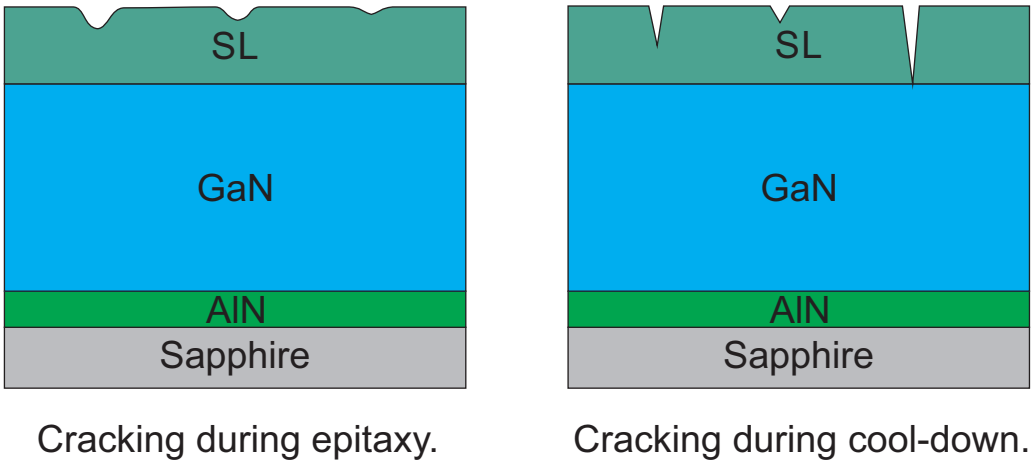

Figure 3.10: Schematic illustration of layer cracking during epitaxy (left) and cooldown (right). For cracking occurring already during epitaxy, the cracks are overgrown and form surface undulations. In the case of cracking during cool-down, the cracks are not overgrown.

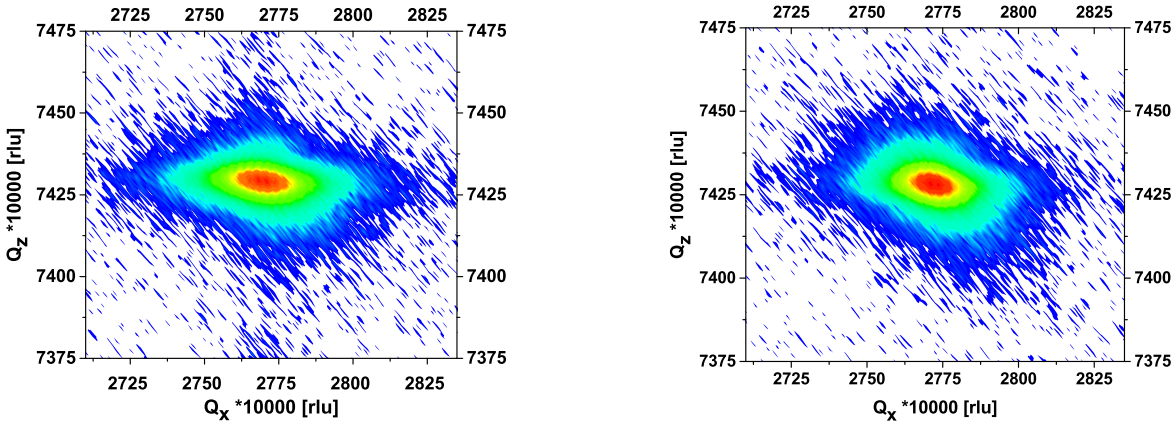

(a) *(b)*

Figure 3.11: Enlarged $(10\bar{1}5)$ *GaN reflex for the 15-fold (a) and 20-fold (b) SL samples.*

SL which comprises MD generation at the SL/buffer interface including the introduction of compressive strain in the GaN layers of the SL followed by layer cracking which stopped additional compressive straining of the GaN layers. The performed measurements identify compressive strain in the GaN films of the SL. However, comparing the shape of the GaN reflexes in the $(10\bar{1}5)$ rsm from the 15- and 20-fold sample, a very slight difference Δ might be observable (cmp. enlarged in figure 3.11). The GaN reflex of the 20-fold SL sample (right) shows slightly enhanced intensity towards the lower right corner in comparison to the 15-fold sample. Compressively strained GaN would be located to the bottom right of the unstrained GaN reflex, as the a-lattice parameter becomes smaller (= larger Q_x-value) and, due to volume conservation, the c-lattice parameter becomes larger (= smaller Q_z-value). This difference is very small and the feature is not very pronounced which could be attributed to very low compressive strain and/or to the very small volume fraction of GaN in the SL compared to the GaN buffer. Further measurements would be necessary to exactly determine the strain state of the SL-GaN layers. From the obtained XRD data, compressive strain can not be excluded for the GaN layers.

Nevertheless, layer cracking seems to be the dominant relaxation mechanism for AlN/GaN-SL investigated in this work. With this assumption, the increased critical layer thickness compared to AlGaN might occur by a higher crack formation energy due to the unstrained GaN layers of the SL. This can be explained as follows: To generate a crack in tensily strained AlN, a certain formation energy is necessary. This formation energy is supplied if the tensile strain is large. If the crack does not only thread through AlN but also through unstrained GaN, as it is the case in an AlN/GaN-SL, the formation energy has to increase because cracking of unstrained GaN is energetically unfavorable. In the case of tensily strained AlGaN, the strain is distributed homogeneously in the whole layer, comparable to the individual AlN layer. There are no areas in the AlGaN layer in which cracking is energetically unfavorable. In this way, the critical thickness of an AlN/GaN-SL might be enhanced in comparison to AlGaN if layer cracking is the only available relaxation mechanism. This agrees well with the assumption that the energy release rate should drop rapidly if cracks have to pass unstrained or compressively strained GaN as proposed by Einfeld et al. [66].

3.3 Resonant Tunneling Diode Based on SL

To test the interface and layer quality of the SL, a resonant tunneling diode (RTD) was fabricated. RTD rely on the principle that the current flow is dominated by tunneling processes through two high-bandgap barrier layers. Between the barrier layers, a quantum well is formed with a lower-bandgap material. For good layer qualities, discrete energy levels form in the quantum well. When a voltage is applied to the structure, the conduction band of the contact layer on one side of the barriers is lifted with respect to the conduction band of the contact layer on the other side of the barriers. The energy levels in the quantum well are positioned at intermediate levels. With increasing voltage, the tunneling probability increases and so does the current every time the conduction band (CB) of the contact layer aligns with the discrete energy levels of the quantum well. For further increased voltages, the energy levels are not aligned anymore and the tunneling probability is reduced. This manifests in a drop in current although the voltage was increased in this voltage interval. If the CB approaches the next energy level of the QW, the current again starts to increase. The current drop translates to a negative differential resistance (NDR) in this voltage interval [77].

In figure 3.12, the layer stack of the deposited RTD is displayed. The underlying GaN buffer was doped with Si ($7 \cdot 10^{18}\ cm^{-3}$). Then two AlN barriers with an nominally undoped GaN in between were deposited with a V/III ratio of 2130 (AlN) and 1690 (GaN) at 75 mbar reactor pressure and a growth surface temperature of $1060°C$, which all denote the previously developed SL standard conditions. The layer thicknesses of AlN and GaN layers are the same compared to the previously deposited SL (i.e. 1.3 nm AlN and 3 nm GaN). After the upper AlN barrier growth the surface was stabilized by a constant TMGa and ammonia flow during the ramping step of temperature, pressure and flows from SL growth conditions back to those of GaN buffer growth. When the GaN buffer conditions were reached, silane was added to the gas phase to again realize a Si doping ($7 \cdot 10^{18}\ cm^{-3}$) and the upper n-GaN layer was deposited with a thickness of approximately 300 nm. With a recess etch and an ohmic contact, the underlying n-GaN is contacted. With the same metal stack, the upper n-GaN is accessed. The mesa side wall was passivated employing a 50 nm thick SiN layer.

Figure 3.13 shows a simulation of the conduction band edge of the fabricated structure at zero bias obtained with a 1D Poisson solver [78]. The left side denotes the sample surface while the GaN buffer is located on the right side in figure 3.13. In the GaN buffer, a 2DEG is formed at the heterointerface towards the first AlN barrier. The lowest energy level E_1 of the 2DEG is marked. The GaN well is located between the two AlN barriers. The two lowest energy levels in this quantum well E_1 (red) and E_2 (blue) are marked. To measure the NDR, negative bias is applied to the n-GaN buffer, injecting electrons into the active zone. The NDR is expected to occur when the E_1 level of the 2DEG aligns with the E_1 level of the GaN well (and at higher bias with E_2). From figure 3.13, one can see that approximately 0.9 V is necessary to align the E_1 level of the 2DEG with the E_1 level in the quantum well.

In figure 3.15, the current density measured at room temperature is plotted versus the applied voltage. Beyond 0.5 V the current density drops clearly showing NDR. In contrast to

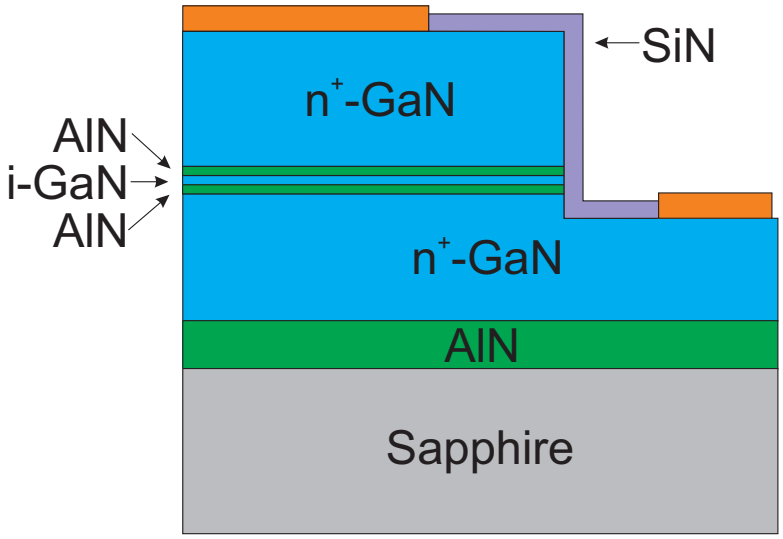

Figure 3.12: Schematic layer stack of the RTD. Two ohmic contacts are applied to the top and bottom $n^+ - GaN$ layers.

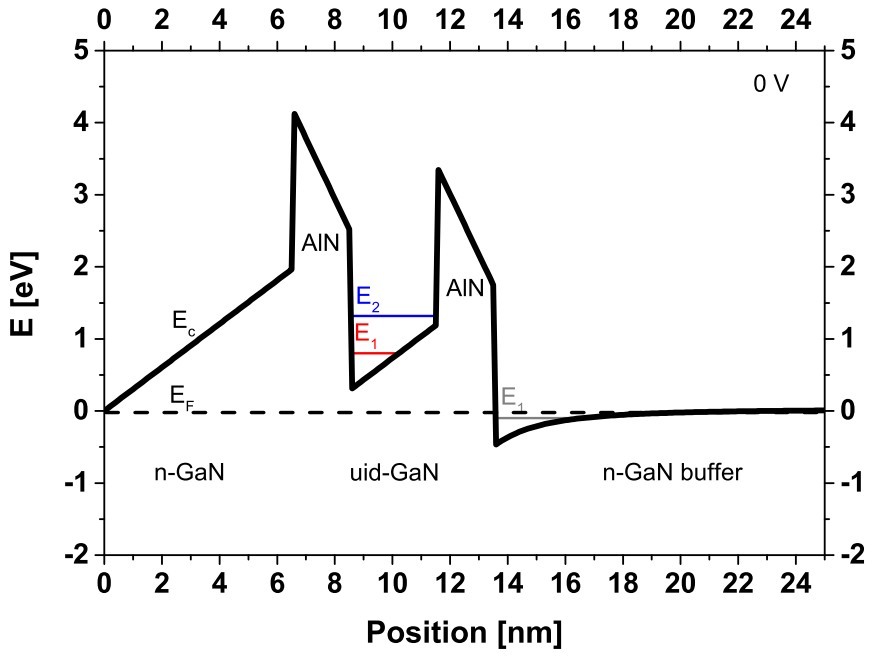

Figure 3.13: Simulated conduction band edge of the RTD structure. The energy levels in the GaN well E_1 and E_2 are marked. The E_1 level of the 2DEG forming in the GaN buffer below the lower AlN barrier is also depicted.

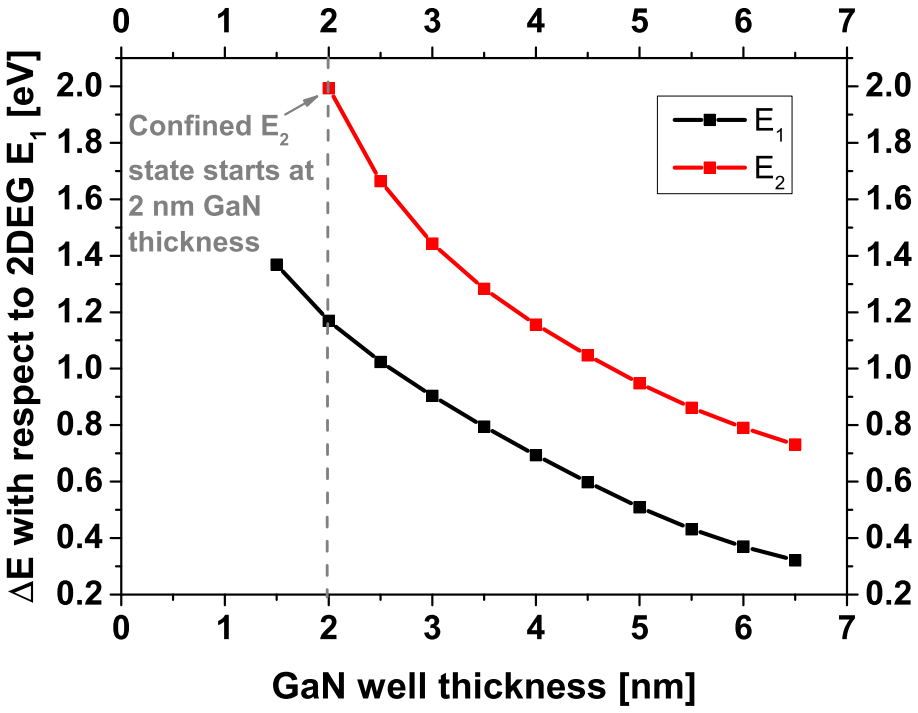

Figure 3.14: Dependence of the energy difference between the first or second confined state of the well and the 2DEG on the GaN well thickness (simulation).

the simulation, the NDR does not occur at 0.9 but at 0.5 V. This is a reasonable deviation, as the CB was simulated for the unbiased case which represents the band structure for the biased case only in part. An applied bias does not solely alter the CB energy. Bend and tilt of the CB are also influenced which affects the shape of 2DEG and GaN quantum well. Additionally, the CB was simulated using bulk n-GaN as boundary condition at the upper and lower surface of the device. In the biased device, contact potentials have to be considered instead. All this changes the position of the energy levels. Also the layer thicknesses in the sample change the position of the energy levels. Exemplarily, the dependence of the energy difference ΔE between the first or second energy level in the well (E_1 and E_2) and the 2DEG energy level on the GaN well thickness was simulated. The results are depicted in figure 3.14. At a well thickness of 3 nm, the ΔE is 0.9 eV as already determined in the previous simulation (cmp. fig. 3.13). For thicker GaN wells, the ΔE of the E_1 levels rapidly decreases towards the measured 0.5 eV which is reached at a well thickness of 5 nm. A thickness variation of 2 nm compared to the measured thickness of 3 nm is reasonable for ultra-thin layer growth in the used MOVPE system on a 2 inch wafer. The layer thicknesses of the RTD were determined via a reference sample (because the RTD well is to thin to be measured with HR-XRD) which also might introduce small thickness deviations. Therefore, the assumption that a deviation in the GaN well thickness caused the voltage difference in RTD onset between measurement and simulation together with a discrepancy between unbiased and biased band structure is well-founded.

The successful realization of the RTD again highlights the good crystal quality of the SL layers and the favorable growth conditions developed for SL deposition. This result is even more

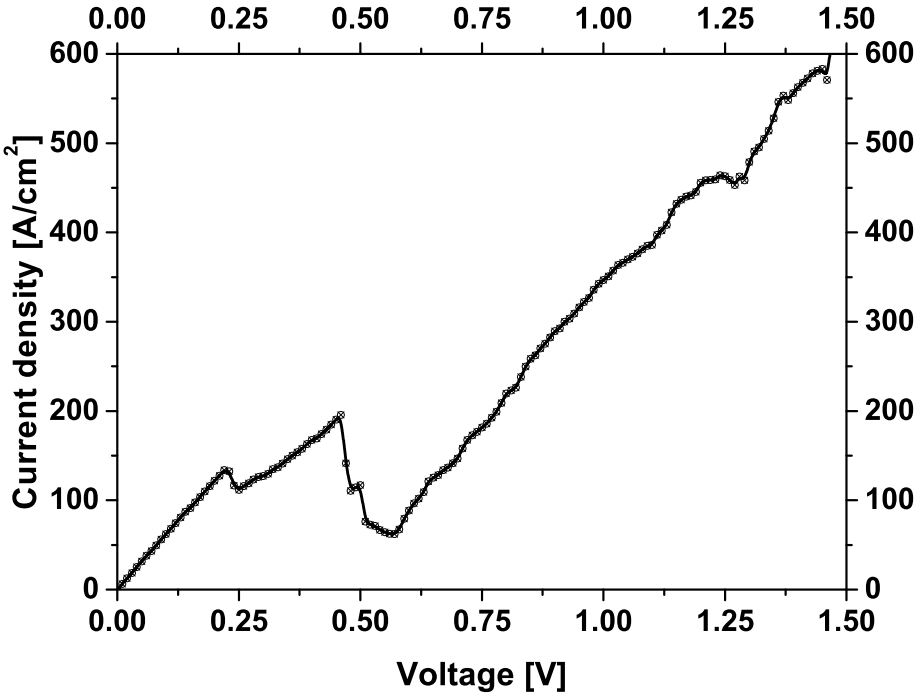

Figure 3.15: Current density versus applied voltage for the RTD. NDR is clearly visible at 0.5 V.

important if it is considered that only very few reports on nitride-based RTD can be found in the literature. GaN RTD have been demonstrated by MBE growth [79] [80]. MOVPE-grown RTD already showed NDR but the results were not reproducible for which the crystal quality and surface quality was blamed [81]. Only very recent results show the successful realization of GaN-based RTD via MOVPE [82].

Chapter 4

Applications of AlN/GaN-SL in Group III Nitride Devices

After developing a deposition process for AlN/GaN-SL and investigating the fundamental behavior under tensile stress, the SL are now implemented in devices. Chapter 4.1 covers the application of SL to heterostructure field effect transistors (HFET) which results in a multi-channel approach and is used to engineer the carrier mobility. In chapter 4.2, the concept of SL is implemented into distributed Bragg reflectors (DBR) which helps to prohibit crack formation. Finally, chapter 4.3 will introduce a new electro-optic modulator concept on the basis of nitride SL.

4.1 The SL Heterostructure Field Effect Transistor

4.1.1 HFET in Group III Nitrides

Heterostructure field effect transistors use the inherent polarization of group III nitrides to generate two-dimensional electron gases as channel medium [2]. For this, a barrier material with a higher bandgap has to be deposited on a GaN buffer to form a heterojunction. Barrier materials like AlGaN, AlInN or AlInGaN are suitable to achieve this. To even further increase the conduction band offset, a thin AlN spike is inserted at the heterointerface. A typical AlGaN/GaN HFET stack is depicted in figure 4.1.

The barrier material is grown pseudomorphically on the 90 % relaxed GaN buffer. This means that barrier and buffer have spontaneous and piezoelectric (lattice-matched barriers excluded) polarization components. In figure 4.1, both total polarizations of AlGaN barrier and GaN buffer point downwards antiparallel to the growth direction. Polarization leads to surface or interface charges σ_S. For unstrained or tensily strained layers, the (0001) surface has a negative charge and the $(000\overline{1})$ backside surface has a positive one. Therefore σ_{S1} and σ_{S3} are negative and σ_{S2} and σ_{S4} are positive. If the negatively charged (0001) surface of the GaN buffer and the positively charged $(000\overline{1})$ surface of the barrier material are in contact, the resulting interface charge σ_I is the difference of both surface charges σ_{S2} and σ_{S3}. For

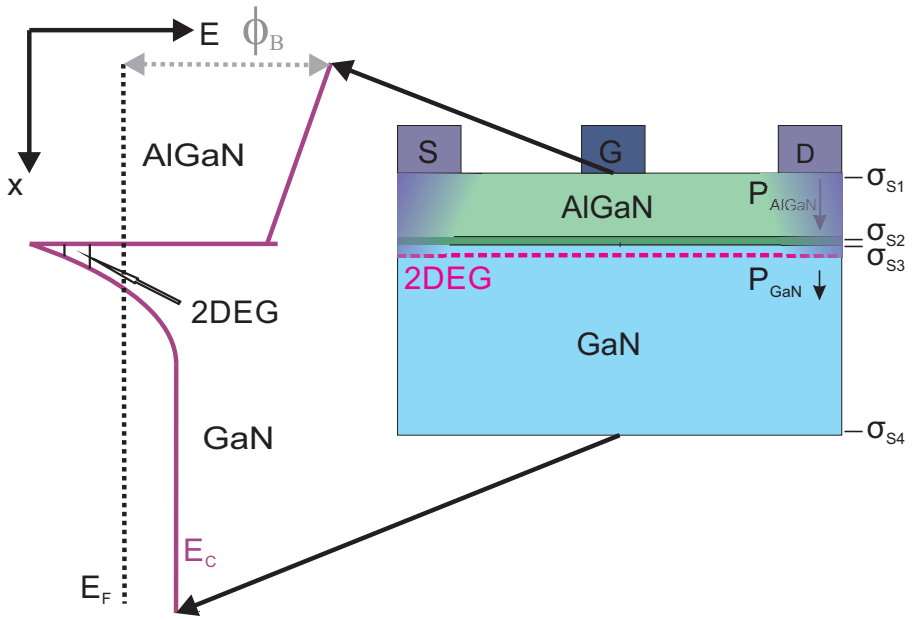

Figure 4.1: Layer stack of an AlGaN/GaN HFET. The corresponding conduction band is shown on the left side.

Al-containing, tensily strained barriers, the absolute value of the total polarization is always larger than for a nearly relaxed GaN buffer. This means that the interface charge σ_I is positive which promotes 2DEG accumulation at heterointerface. The resulting triangular potential well in GaN directly at the heterointerface is depicted in the CB band diagram of figure 4.1.

In the 2DEG, electrons can move parallel to the heterointerface but are confined perpendicular to it. The electron sheet carrier concentration in the 2DEG depends on the value of the interface charge and is therefore directly related to the polarization difference between buffer and barrier material and the barrier thickness. The sheet carrier density in the 2DEG is described by the following equation [2]:

$$n_s(x) = \frac{+\sigma_I(x)}{e} - \left(\frac{\epsilon_0\epsilon(x)}{e^2 d}\right)[e\phi_B(x) + E_F(x) - \Delta E_C(x)] \tag{4.1}$$

with the interface charge $\sigma_I(x)$, the barrier thickness d, the Schottky barrier height $\phi_B(x)$, the Fermienergy $E_F(x)$ and the conduction band offset $\Delta E_C(x)$. The Schottky barrier height (ϕ_B) at the barrier top surface also affects the carrier concentration. For a decreasing ϕ_B, the CB including the potential well is lowered with respect to the Fermi level which increases the electron concentration of the 2DEG. An increase of ϕ_B lifts the conduction band which leads to a smaller well and a reduced electron concentration. When the conduction band is lifted even further, the minimum of the potential well rises above the Fermi level resulting in a fully depleted 2DEG. Also, a voltage can be applied to the structure via a Schottky gate contact. This voltage V_{GS} lifts or decreases the CB with respect to ϕ_B. With ohmic contacts generated to the 2DEG and the control of its carrier concentration via the gate contact, 2DEG can be used as transistor channels in HFET [2]. For a standard AlGaN/GaN HFET, there is always a non-vanishing sheet carrier concentration at zero gate-source bias. The threshold voltage V_{GS} at which the

conduction band is sufficiently lifted and the 2DEG is depleted, is negative. This behavior is called normally-on or depletion-mode (d-mode). It is also possible to achieve normally-off or enhancement-mode (e-mode) behavior for nitride HFET. This can be accomplished by various approaches such as polarization engineering to change the interface charge σ_I, gate-recess etching to lower the barrier thickness b, replacement of standard gate metallization to affect ϕ_B, bandgap engineering to alter the conduction band offset ΔE_C, introduction of a gate insulator to increase ϵ or the introduction of a backbarrier which again changes σ_I [83].

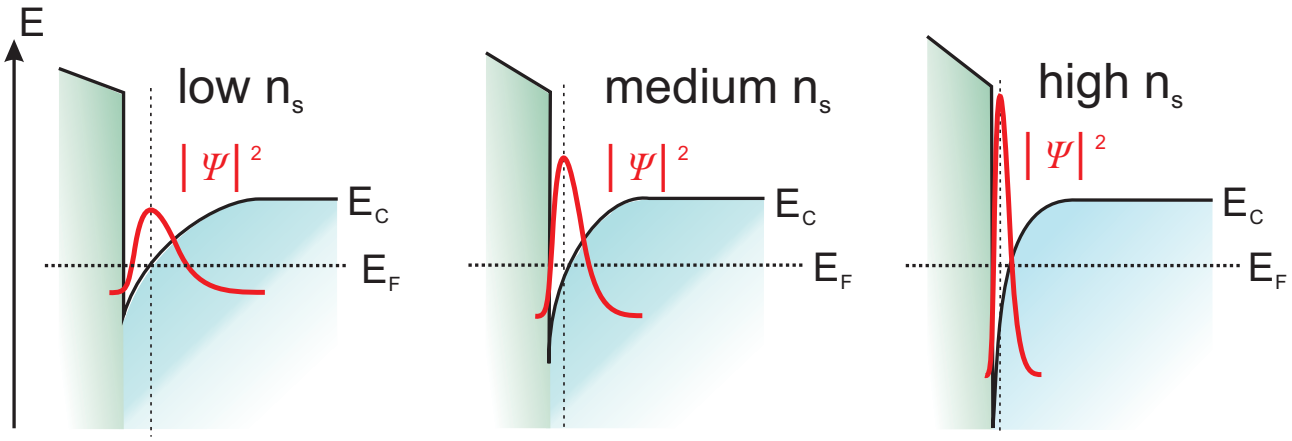

Figure 4.2: Simplified schematic of an AlGaN/GaN heterointerface with 2DEG and the probability density function $|\Psi^2|$ of the carriers. The polarization difference increases from left to right leading to higher sheet carrier concentrations in the 2DEG

Electrons in a 2DEG move parallel to the interface. Due to their confined 2D-like states the probability of a scattering process with defects or phonons is dramatically reduced compared to that of quasi-free electrons in bulk material [2]. As the interaction volume of electrons with the crystal is only reduced but not eliminated, there are still several limitations in mobility. According to Gurusinghe et al. [84], the four major scattering mechanisms in 2DEG are phonon, ionized impurity, defect and interface scattering which are explained in the following. Depending on the sheet carrier concentration, the potential well is not only deeper or shallower but also changes its shape. Hence, the probability density function of the 2DEG electrons is altered. For low sheet carrier concentrations ($< 7 \cdot 10^{12}\ cm^{-2}$), the potential well is relatively shallow and broad. This case is depicted in figure 4.2 on the left. The shape of the quantum well leads to a broad probability density function $|\Psi^2|$ for the carriers, low confinement and an increased interaction with the crystal lattice. This promotes the influence of crystal defects as point defects (impurities, vacancies, interstitials) or dislocations. In this case, the term impurity does not only include classic impurities like carbon or oxygen but also vacancies as from both defect types, a similar scattering mechanism is generated. Both defect types can also occur in a neutral and a charged state. The effect generated by neutral impurities is very small and can be neglected. Only ionized impurities have a notable influence on the mobility. Scattering from dislocations mainly refers to TD which penetrate the heterointerface and the adjacent 2DEG. The dislocation line is negatively charged and can therefore be treated in a similar way as ionized impurities with the difference that dislocations generate a one-dimensional charge along the dislocation line and not a point charge.

At medium sheet carrier concentrations ($\approx 7 \cdot 10^{12}\ cm^{-2}$), the well is deeper and narrower as shown in the middle of figure 4.2. This increases the electron confinement which in turn reduces the influence of defects and therefore increases carrier mobility. As the sheet carrier concentration is further increased ($> 7 \cdot 10^{12}\ cm^{-2}$) which is shown in figure 4.2 on the right, the well becomes even deeper and narrower. This increases the confinement but also moves the electrons closer to the heterointerface [85]. Interface scattering now plays a major role and reduces the mobility. The interface roughness causes a spatial variation of the wavefunction and the resulting energy levels in the 2DEG which generates a local scattering potential. The important measure for interface roughness is not only the structural height variation (roughness) which is generally described by the rms values obtained for example by AFM (cmp. chapter 2.3.2) but also the lateral extent of the variation. The latter can be described with the auto correlation length. The higher the auto correlation length, the higher the mobility because with larger auto correlation length, the points of large interface displacement move away from each other and are therefore fewer if a constant interface area is considered [84]. In some publications, alloy scattering is also mentioned as a reason for mobility degradation in the high carrier concentration regime [65], [86]. Alloy scattering describes the spatial variation of the scattering potential, e.g. due to inhomogeneously distributed Al atoms in a ternary AlGaN barrier [87], [88]. With the AlN spike at the heterointerface, alloy scattering can be inhibited. Due to the higher ΔE_C of the AlN spike/GaN buffer interface, the electrons are more confined and their wavefunction decays exponentially whithin 0.3 nm in the AlN [65]. This results in a zero probability density of the electrons in the ternary AlGaN barrier. The AlN spike is binary and therefore cannot cause any alloy scattering. As a result, alloy scattering can be neglected if an AlN spike is used which is the case for all devices shown in this thesis.

Phonon scattering is present throughout the whole carrier concentration regime and can only be suppressed by lowered temperatures. Scattering at acoustic phonons is an elastic process and can be observed as deformation potential scattering and piezoelectric scattering. The effect of piezoelectric scattering on the mobility of nitride HFET is very small and can be neglected. The deformation potential scattering is only dominant at temperatures below 150 K. At or above room temperature, the inelastic scattering at LO phonons is present and becomes stronger at higher sheet carrier concentrations as the effective 3D carrier concentration is also increased which leads to enhanced phonon lifetimes [89].

For every scattering process, a reduced electron mobility can be derived under the assumption that the currently investigated scattering process is dominant in the sample. To obtain the combined mobility with all scattering mechanisms considered, Matthiessen's rule is applied [90] and the combined mobility can be written as:

$$\frac{1}{\mu_{combined}} = \frac{1}{\mu_{ionimp}} + \frac{1}{\mu_{disl}} + \frac{1}{\mu_{int}} + \frac{1}{\mu_{LOph}} \tag{4.2}$$

This formula is only correct if the scattering mechanisms are independent of each other which is valid in first approximation for group III nitrides. The formula also elucidates that the contribution of a certain scattering process is only significant if the mobility reduction due to the

specific process is at least comparable to all other scattering mechanisms present in the sample. Even high dislocation densities of 10^{11} cm^{-2} only lead to a reduced mobility of 4000 cm^2/Vs [84] in the low carrier concentration regime. This mobility value is considerably higher than standard nitride HFET mobilities. Therefore, dislocations do not limit the mobility at low carrier concentrations. Instead, scattering by ionized impurities acts as the dominating scattering mechanism. In the high carrier concentration regime, scattering due to interface roughness generally limits the mobility. The influence of phonon scattering is smaller but in the same order of magnitude. This means that LO-phonon scattering can become the limiting scattering mechanism for high carrier concentrations if the contribution of interface scattering is small. The highest mobility can be achieved at medium carrier concentration around $6 \cdot 10^{12}$ cm^{-2} when the increasing carrier confinement already reduces ionized impurity scattering but the distance between 2DEG and interface is still large enough to diminish interface roughness scattering. The general behavior of the mobility for carrier concentrations from $4.5 \cdot 10^{12}$ cm^{-2} to $1.4 \cdot 10^{13}$ cm^{-2} is summarized in figure 4.3 for a standard AlGaN/GaN HFET. The depicted data was collected from a standard single-channel AlGaN/GaN HFET with an AlN spike (1.3 nm). The deposition and fabrication of this single-channel HFET will be explained in the following chapter 4.1.3.

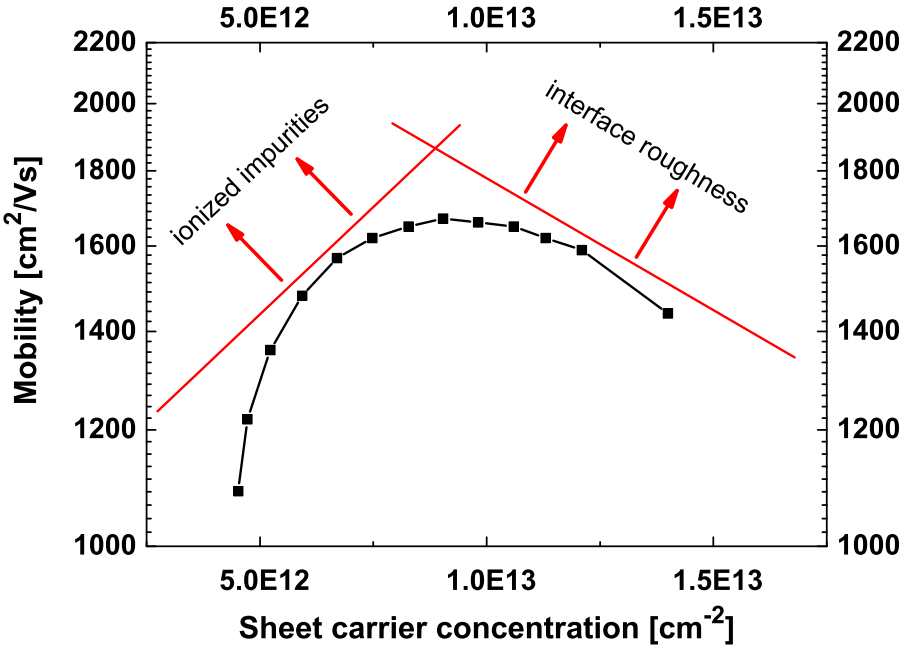

Figure 4.3: Mobility of a standard AlGaN/GaN HFET for varying carrier concentrations.

4.1.2 Concept of the SL-HFET

In the last chapter, the working principle of nitride HFET was elucidated. But it also became clear that the mobility of 2DEG carriers still has some constraints. While the mobility limitation in the low carrier concentration regime is related to the crystal quality and hence could be

overcome by reducing the defect density, the limitation in the high carrier concentration regime is an inherent property of 2DEG because the heterointerface is necessary to create the 2DEG and an interface itself can be regarded as a defect irrespective of its perfection. This manifests itself as an intrinsic problem as large carrier concentrations are needed for high-power applications or RF switches.

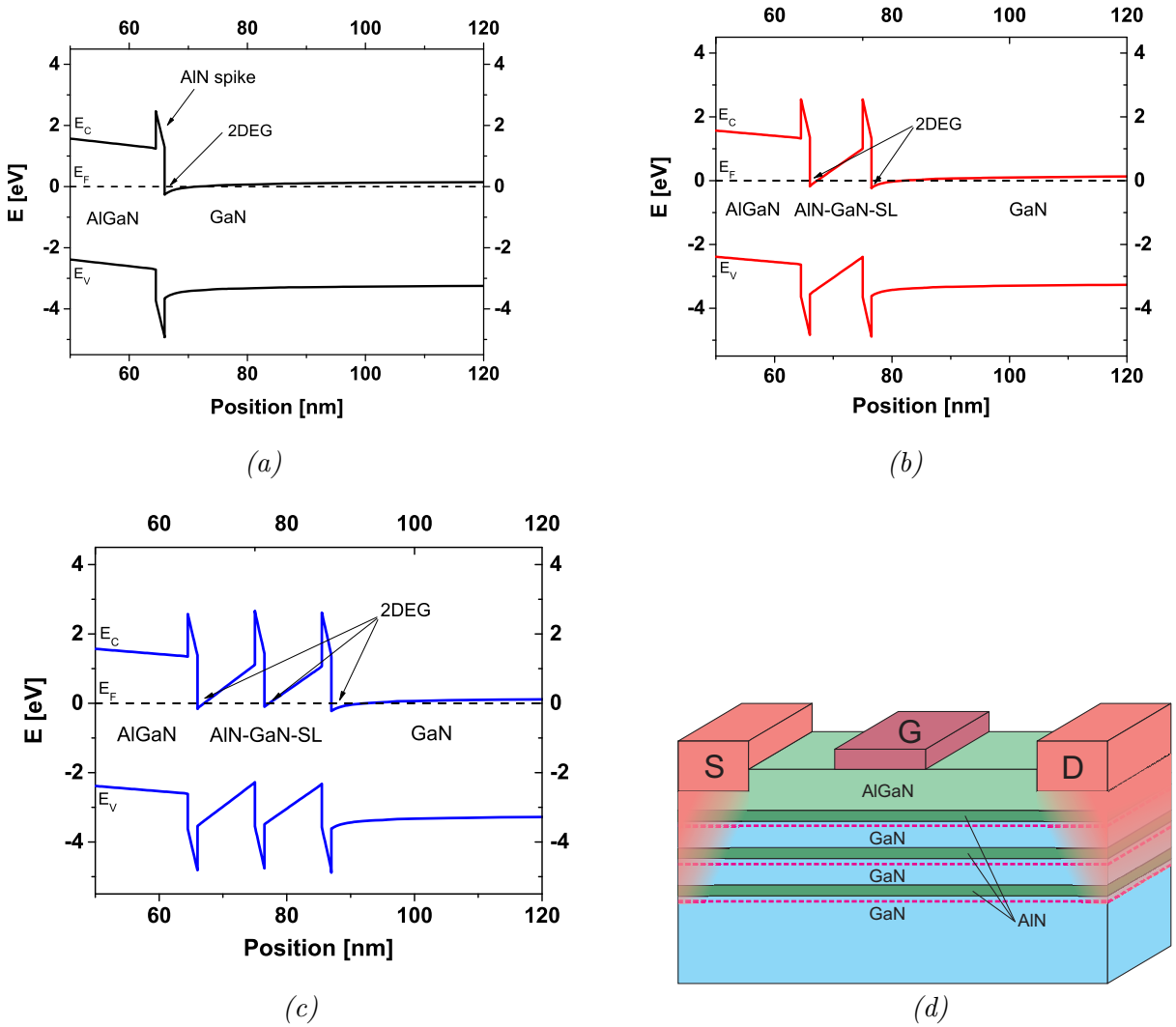

Figure 4.4: Bandstructures of SL-HFET with one (a), two (b) and three (c) parallel 2DEG. The schematic device layout is show for the triple-channel HFET (d).

One possible approach to solve this problem is the integration of SL into HFET. In this way, multiple parallel 2DEG can be realized. The basic idea of this concept is that the carrier concentration in HFET at zero gate-source voltage is determined by the polarization difference between barrier and buffer as equation 4.1 indicates. When all these carriers are accumulated in one 2DEG, the carrier concentration is comparably high. But if the constant amount of carriers is distributed into several parallel 2DEG, the carrier concentration in every single 2DEG is lower. The lower carrier concentration moves the centroid of the the electron wavefunction away from the heterointerface which reduces interface scattering and hence enhances mobility.

Figure 4.4 shows the simulated band diagrams of a standard AlGaN/GaN HFET with AlN spike (a), a double-channel structure with two parallel 2DEG (b) and a triple-channel

structure with three parallel 2DEG (c). The band diagrams were simulated with Synopsis TCAD at zero gate-source bias. Figure 4.4d shows the cross section of a triple-channel HFET. In the simulated band diagrams, the wells forming the 2DEG are clearly visible. There are two 2DEG present in the double-channel structure and three in the triple-channel one in contrast to the standard single-channel HFET (fig. 4.4a). All 2DEG are populated with carriers, as the conduction band crosses the Fermi level. Due to the sample geometry, the upper 2DEG of the double-channel structure and the upper two 2DEG of the triple-channel one feature a backbarrier-like structure due to the SL below. Figure 4.5 shows a schematic drawing of the 2DEG shape with and without backbarriers. The underlying AlN of the SL tilts the conduction band upwards due to the polarization difference between AlN and GaN. This conduction band tilting enhances the confinement of the electrons in the upper two 2DEG which should decrease the interaction volume of electrons with the crystal lattice and should therefore reduce ionized-impurity scattering.

The overall carrier concentration present in each device (single- or multichannel HFET) is determined by the polarization difference between AlGaN barrier and GaN buffer and the thickness of the AlGaN barrier. Therefore, the overall carrier concentration of single- and multichannel HFET is expected to be same as the same AlGaN barrier is used for all samples. From this fact, in a first order approximation it can be expected that the maximum drain current is the same for all samples regardless of their number of 2DEG channels. Only a successful mobility improvement can increase the maximum drain current to a certain extent, as the resulting higher saturation velocity of 2DEG electrons allows for higher currents.

From the schematic in figure 4.4d, it also becomes clear that the structure which generates the parallel 2DEG has to be very thin (in the nm range) to be effectively controllable via the gate. In general, a ratio of gate length and barrier thickness greater than 6 is necessary for the gate to maintain control over the channel [91]. If the aspect ratio is smaller, the material thickness, which has to be depleted, becomes too high and the threshold voltage V_{th} would decrease dramatically. V_{th} becomes strongly drain voltage dependent due to drain induced barrier lowering (DIBL). This significantly increases output conductance degrading RF properties like gain and power added efficiency [92]. This is circumvented with very thin AlN/GaN-SL structures. They combine excellent material quality with high ΔE_C and ΔP to generate 2DEG and low layer thicknesses.

Such multi-channel approaches have already been pursued by other groups. Their goal was not only an improvement of carrier mobility which was supposed to lead to higher drain currents [93] but also a reduction of self-heating effects by ultra-fast phonon decay [89] and lowering of access resistance accompanied by higher linearity [94]. Despite great progress, most groups did not combine epitaxial stack design with full processing and characterization options and none of the groups investigated structures with more than two parallel 2DEG channels. In most cases, the two parallel channels were either very close to each other which rather generated a uniformly distributed carrier concentration in the structure than realizing discrete 2DEG and is detrimental to carrier confinement [89]. In other publications, the 2DEG were

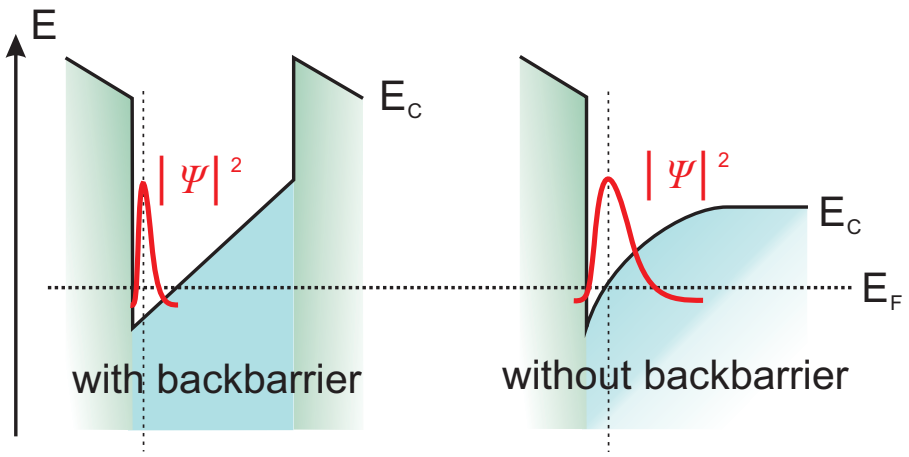

Figure 4.5: AlN/GaN/AlN heterojunction (as used in the SL) on the left shows higher carrier confinement than an AlN/GaN buffer hetero junction shown on the right.

separated by more than 30 nm of material which results in reduced controllability via the gate and low population of the lower channel [95],[96]. Palacios et al. showed that the low population of the lower 2DEG can be compensated by proper structure design which in this case included a graded AlGaN barrier between the two channels with decreasing Al fraction towards the upper channel accompanied by AlN spikes [94]. However, this group did not pursue a normal double-channel HFET design and etched away the upper channel in the gate region to successfully tailor the source access resistance. Zhang et al. used a promising intermediate distance of parallel 2DEG of 7 nm distance for their AlInN/AlN/GaN/AlN/GaN structures but they performed only un-gated Hall measurements and did not process complete HFET devices [93]. Nevertheless, Zhang et al. were able to show that a double-channel structure improved the mobility (1430 cm^2/Vs) compared to a single-channel device (1090 cm^2/Vs) at large carrier concentrations $> 1 \cdot 10^{13}$ cm^2/Vs. All previous results are very promising regarding the multi-channel concept but a thorough characterization of all aspects is still lacking. In the following chapter, the multi-channel approach will be investigated on devices with up to three parallel 2DEG and a complete HFET characterization including DC, AC, RF and power gain properties is aspired.

4.1.3 Mobility Improvement by Multiple Parallel Channels

To investigate the concept of multiple channels for mobility improvement, three transistor structures were fabricated. The schematic layer stacks of all samples are shown in figure 4.6. The first sample is a standard AlGaN/GaN HFET with a single 2DEG at the AlN spike/GaN buffer interface. This sample is referred to as single-channel. The second sample is a double-channel structure in which an additional GaN layer and a second AlN spike were inserted between barrier and buffer. The third sample is designed as a triple-channel structure in which two repetitions of GaN and AlN are realized (cmp. figure 4.4d (a)). The GaN and AlN layers between barrier and buffer represent a short-period AlN/GaN-SL. The layer thickness of GaN in the SL was 8.5 nm and 1.3 nm for AlN. The AlGaN top barrier had a thickness of 9.5 nm with

34 % Al content. All values were obtained by fitting of HR-XRD measurements. The layers were deposited at a growth surface temperature of 1080°C, the reactor pressure was 50 mbar and the V/III ratio 1220 for AlN growth and 1015 for GaN growth. The AlGaN barrier was grown at the same conditions by opening the TMGa and TMAl runlines at the same time. These samples were processed into transistor devices with a gate length of 2 μm and a width of 100 μm.

For the source and drain contacts, a Ti/Al/Ni/Au stack in combination with a recess etch (by inductively coupled reactive ion etching) was used. A recess depth of 7 nm was applied to the single-channel sample to support ohmic contact formation. For the double-channel and the triple-channel samples, the recess depths were increased to 21 and 28 nm, respectively, to account for the larger layer thickness of the SL and to enable ohmic contact formation vertically for the lowest 2DEG and laterally for the upper ones. The metal stack was evaporated on rotated and slightly tilted samples. This enhances metal deposition on the side flanks of the ohmic recess which improves the ohmic contact to the 2DEG. Contact resistances around 1 Ωmm were realized. To investigate the carrier concentration, structures for gated Hall [97], [98] and capacitance-voltage measurements were also fabricated.

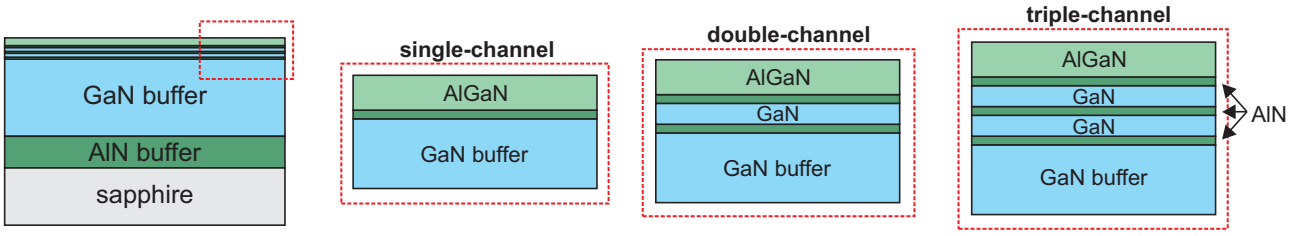

Figure 4.6: Layer stacks of the multi-channel samples. The buffer structure of all three samples is shown on the left. The three layer stacks on the right only depict the topmost layers of the samples

Gated Hall measurements allow to characterize the mobility of a sample with respect to the carrier concentration (controlled by the gate-source voltage). As in this case multiple channels are measured in a parallel arrangement, the obtained carrier concentration is the total carrier concentration in the device and the measured mobility represents an averaged value of all carriers participating in transport. Figure 4.7 shows the measured mobility values for single-, double- and triple-channel transistors. It is obvious that the mobility is rising with an increasing number of parallel 2DEG, if the same overall carrier concentration in considered. At a carrier concentration of $7.5 \cdot 10^{12}$ cm^{-2}, the mobility was increased from 1690 cm^2/Vs for the single-channel device to 1900 cm^2/Vs for the triple-channel one which is consistent with the results obtained by Zhang et al. [93]. In the high carrier concentration regime, the increase in mobility can be attributed to the distribution of the carriers in the parallel 2DEG. In consequence of this carrier distribution, the lesser populated individual 2DEG lead to an increased distance of the carriers to the interfaces which reduces interface scattering. It is also possible that reduced scattering at LO phonons contributes to the enhanced mobility. Due to the carrier distribution, the effective 3D carrier concentration is reduced because the same number of electrons is now located in a larger crystal volume. This can reduce the phonon lifetime and therefore diminish this scattering mechanism [89]. In the low carrier concentration

regime, the mobility is also enhanced. This can be explained by the backbarrier effect of the SL structure mentioned before (cmp. figure 4.5). In addition, this effect leads to higher mobility in the upper two 2DEG compared to the lowest one. For the double-channel structure, this is true only for the upper 2DEG. The mobility improvement due to the backbarrier effect seems slightly stronger than the increase due to the reduced interface scattering. This conclusion can be derived from the fact that the maximum of the mobility is shifted to smaller carrier concentrations with increasing number of parallel 2DEG. At a sheet carrier concentration of $6 \cdot 10^{12}\ cm^{-2}$, an additional peak is visible in the mobility characteristic of the double- and triple-channel HFET. This peak was reproducible for all tested devices of both process cycles. The origin of this peak is speculative but in the literature, reports on a plasmon-hot phonon resonance occurring in double-channel HFET at the same carrier concentration can be found [99], [100]. This resonance can result in ultra-fast LO-phonon decay and can therefore locally reduce their scattering contribution.

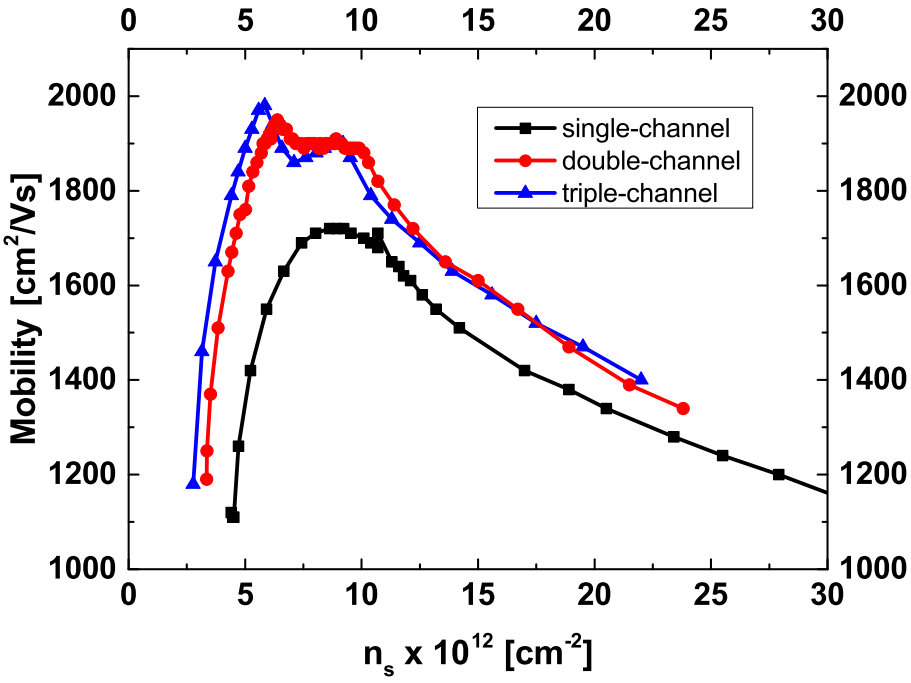

Figure 4.7: Gated Hall measurements of single-, double- and triple-channel HFET.

4.1.4 Characterization of the SL-HFET

DC- and CV-Characterization

The transfer characteristic of single-, double- and triple channel HFET are shown in figure 4.8. The semi-logarithmic scale on the left reveals an abrupt pinch-off for all three samples with drain-leakage currents below $1 \cdot 10^{-4}\ mA/mm$. This proves the applicability of the thin AlN/GaN-SL to nitride HFET. With the linear scale on the right, the maximum drain current ($I_{D,max}$) of single-, double and triple-channel HFET can be compared. With increasing channel number, the maximum drain current increases from 723 mA/mm over 760 mA/mm to 781

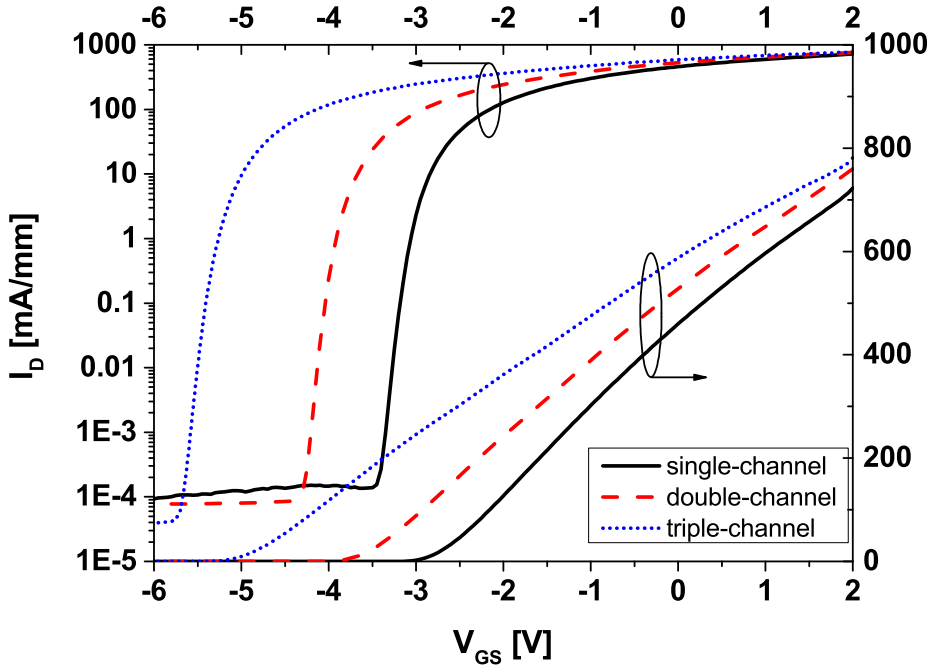

Figure 4.8: Drain current of single- (black solid lines), double- (red dashed lines) and triple-channel HFET (blue dotted lines) in semi-log scale on the left axis and linear scale on the right axis.

mA/mm at $V_{GS} = 2\ V$. Although this increase is notable, the maximum drain current remains in the same order of magnitude. This proves the previously made assumption that in a first order approximation the maximum drain current is constant for all three samples as it depends only on the overall carrier concentration determined by barrier composition and thickness (equal for all three samples). The slight but notable increase of $I_{D,max}$ can be attributed to the improved mobility of the double- and triple-channel HFET design.

The transconductance profiles for all three devices (single-, double- and triple-channel) are depicted in figure 4.9. The single-channel device (plotted in black squares) shows a conventional DC HFET behavior with normally-on characteristic. The maximum transconductance is $g_{m,max}$ = 178 mS/mm and the transistor can be pinched off with a gate-source voltage slightly smaller than -3 V. For the double-channel device (red circles), the transconductance deviates from the trend of the single-channel. It shows two peaks, separated by a voltage difference of 1.5 V (caused by the two parallel 2DEG channels present in this device). The upper channel can be correlated with the maximum g_m at -1 V gate-source voltage and the lower channel with the maximum g_m at -2.5 V.

The double-channel device pinches off at -4 V. The difference in pinch-off voltage of approximately 1 V between single- and double-channel HFET corresponds to the bias difference of the first and second maximum in the double-channel transconductance graph. The maximum transconductance of the double-channel transistor also differs from the value of the single-channel device. Only 156 mS/mm are reached within the maximum at -2.5 V gate-source voltage. The transconductance peak correlated with the upper channel ($V_{GS} = -1\ V$) is even lower with 148 mS/mm. Although the maximum transconductance is reduced for the

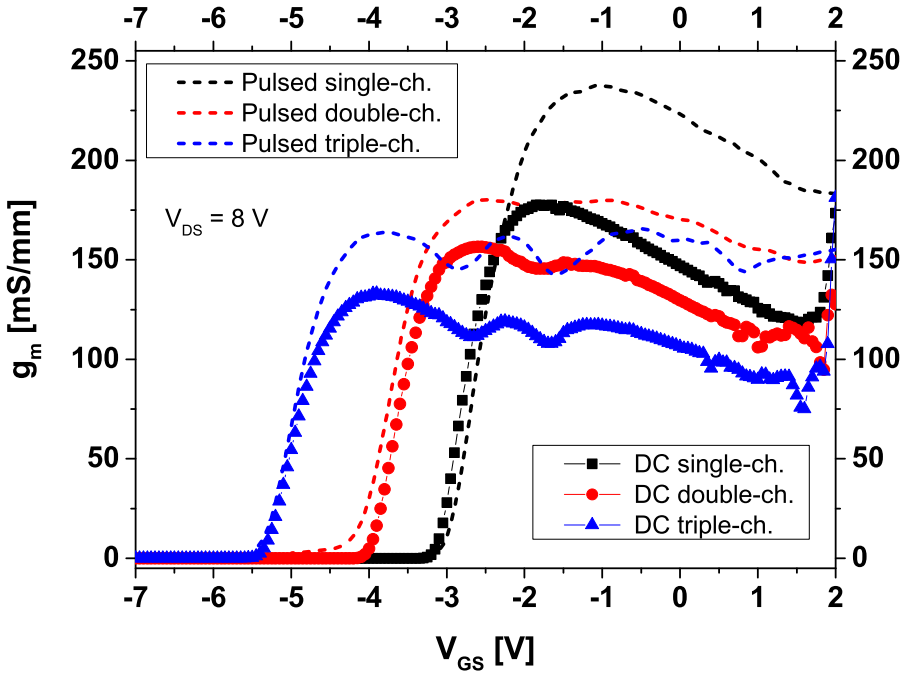

Figure 4.9: Transfer characteristics for single-, double- and triple-channel HFET measured at a drain-source voltage of 8 V.

double-channel device, the integrated area under the transconductance graph (representing the maximum drain current $I_{D,max}$) is nearly constant because of its broader shape. This again confirms the equal number of electrons present in the devices when all channels are in the on-state. The transconductance of the uppermost channel therefore decreases with increasing channel number due to a lower carrier concentration in this channel.

The triple-channel HFET (blue triangles) follows the previously described trends. The transconductance characteristic features three local maxima corresponding to the three parallel 2DEG in this sample. The first one is again located at -1 V gate-source voltage. This maximum can be correlated with the upper channel. The second maximum is located at -2 V gate-source voltage and can be assigned to the middle channel. The third maximum occurs at a gate-source voltage of -4 V and corresponds to the lower channel. While the first two maxima show a voltage difference of 1 V, the second and third maxima exhibit a distance of 2 V. The absolute value of the pinch-off voltage is even further increased to -5.4 V, which is -1.4 V lower than for the double-channel device. From the maxima spacing between 1 and 2 V and the increasing pinch-off voltage with channel number, it can be concluded that approximately -1 to -2 V are needed to deplete one bilayer repeat (GaN + AlN) of the SL incl. the 2DEG depending on the respective carrier concentration in the 2DEG. A more thorough analysis of the depletion behavior will be given in the following when capacitance-voltage measurements of the devices are analyzed.

The maximum transconductance of the triple-channel HFET is again located in the peak attributed to the lower channel and reaches 133 mS/mm. The transconductance peaks of the

middle and upper channel reach 119 mS/mm and 117 mS/mm, respectively. The transconductance graph exhibits a very broad characteristic compared to the double- and single-channel structure which leads to a very linear behavior over more than 4 V ($-4 \leq V_{GS} \leq 0$). This feature can even be further promoted by increasing the number of channels with a simultaneous reduction of the GaN layer thickness in the SL. To prove this, an four-channel HFET with a reduced GaN thickness in the SL (3 nm) and from a different epitaxial series was processed and investigated. The sample is not fully comparable to the previously characterized single-, double- and triple-channel HFET, but the effect of more channels in closer proximity to each other can be demonstrated. The sample was grown at the standard SL conditions from chapter 3.1. In figure 4.10, the transconductance characteristic of the four-channel device is shown. Its transconductance profile is even more linearized compared to the triple-channel HFET. Such observed broad and linear transconductance characteristics are very suitable for the amplification of large signals in a class A or AB configuration, as the V_{GS} amplitude can be much larger without leaving the optimal constant transconductance regime.

All DC g_m characteristics in figure 4.9 show pronounced g_m compression at positive gate-source voltages. This can either be related to self-heating effects or enhanced scattering processes at high sheet carrier concentrations. To investigate the g_m compression in depth, pulsed transfer characteristics were obtained from all devices with pulse times of 2 μs which excludes self-heating effects. The pulsed transfer characteristic of the single-channel HFET still shows g_m compression which can now be solely attributed to enhanced scattering at high sheet carrier concentrations. The double-channel device shows only a small amount of g_m compression while this effect has completely vanished for the triple-channel HFET. This can be attributed to the reduced interface and phonon scattering of the multi-channel concept which is even more inhibited for an increasing number of parallel channels. It also confirms the gated Hall results which also suggested a reduction of interface and phonon scattering in the high sheet carrier concentration regime for the multi-channel devices.

Capacitance voltage measurements (C-V) are carried out for the double- and triple-channel structures to investigate the carrier distribution in the channels. The capacitance was measured at gate voltages from +1 to -8 V (to) and -8 to +1 V (back) at 100, 400, 700 and 1000 kHz on large-area diodes (d = 100 μm). For the double-channel structure, the C-V results are depicted in figure 4.11a. For a sweep direction from positive to negative gate voltages, the first drop in capacitance occurs at -1 V and can be assigned to the depletion of the upper channel. At -4.5 V, a second decrease in capacitance can be observed which can be correlated with the depletion of the lower 2DEG. The measurement shows no hysteresis which leads to the conclusion that no electrically active traps with emission time constants between 0.01 ms (measurement at 100 kHz) and 1 μs (measurement at 1000 kHz) are present in the device.

Calculated capacitance values with the given layer thicknesses and dielectric constants of $\varepsilon_r(GaN) = 10.28$ [101], $\varepsilon_r(AlN) = 10.31$ [101] and $\varepsilon_r(AlGaN) = 10.38$ [101] are compared to the measured data. They show reasonable values in the same order of magnitude which are slightly higher than the measured ones which can be attributed to layer thickness deviations and

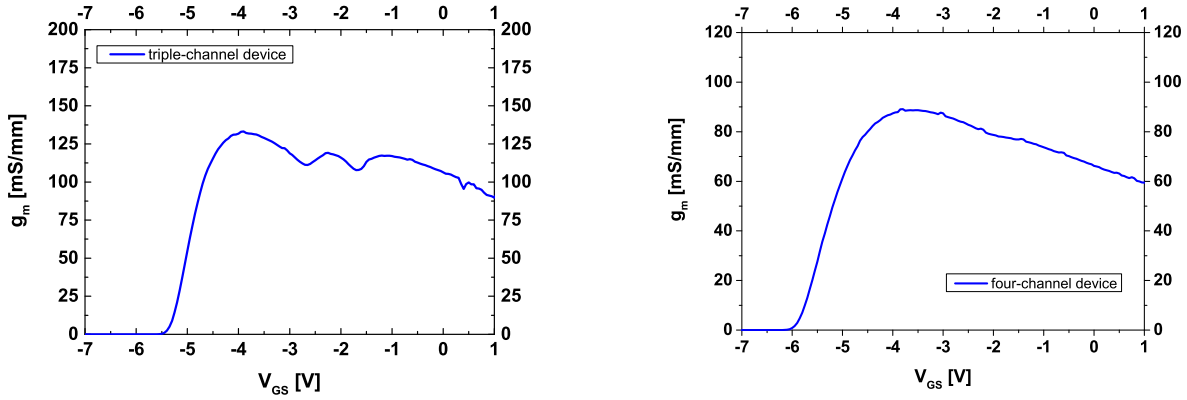

(a) *(b)*

Figure 4.10: Left: Transconductance characteristic of the triple-channel device with 10 nm spacing between each 2DEG. The three discrete maxima are clearly visible. Right: Transconductance characteristic of a four-channel structure with a spacing of only 4.3 nm between the individual 2DEG. There are no individual maxima visible and g_m is smoothed and even more linearized compared to the triple-channel device.

different dielectric constants of the deposited material. For the undepleted case, a capacitance of 664 nF/cm^2 was calculated while a value of 580 nF/cm^2 was measured. The calculated capacitance for a depleted upper channel is 396 nF/cm^2 which is again higher than the measured value (350 nF/cm^2) which also is attributed to layer thickness and dielectric constant deviations.

Via an integration of the C-V curve measured at 100 kHz, the carrier concentration in the upper and lower 2DEG was accessed. For the upper 2DEG the capacitance was integrated from -1.5 V to 0 V yielding a sheet carrier concentration of $4.81 \cdot 10^{12}$ cm^{-2}. The sheet carrier concentration in the lower 2DEG was determined by the integrated capacitance from -4.5 V to -1.5 V. This resulted in a sheet carrier concentration of $5.7 \cdot 10^{12}$ cm^{-2} which is higher than the one of the upper 2DEG. The overall sheet carrier concentration can in conclusion be determined to be $1.05 \cdot 10^{13}$ cm^{-2}.

It must also be noted that the sheet carrier concentration in both 2DEG may not be ideal to achieve the maximum mobility improvement. Figure 4.7 shows that the highest mobility for a single 2DEG is achieved at carrier concentrations between $6 \cdot 10^{12}$ cm^{-2} and $1 \cdot 10^{13}$ cm^{-2}, which is slightly above the sheet carrier concentration in the upper 2DEG. Therefore, scattering at ionized impurities might be enhanced for the upper channel which, on the other hand, could already be compensated by the better carrier confinement due to the backbarrier structure of the SL. Simulations showed that the carrier distribution between upper and lower 2DEG can be influenced by the GaN layer thickness in the SL. This means that a GaN layer thickness variation can clarify if further optimization of the mobility is possible.

The extracted distribution of carrier concentration in the 2DEG is depicted in figure 4.11c. Two peaks are visible representing two separate 2DEG. The extracted distance between the two 2DEG is 10 nm which correlates well with the layer thicknesses obtained by XRD measurements (1.3 nm AlN + 8.5 nm GaN).

Figure 4.11b shows the C-V data of the triple channel-device. In contrast to the results

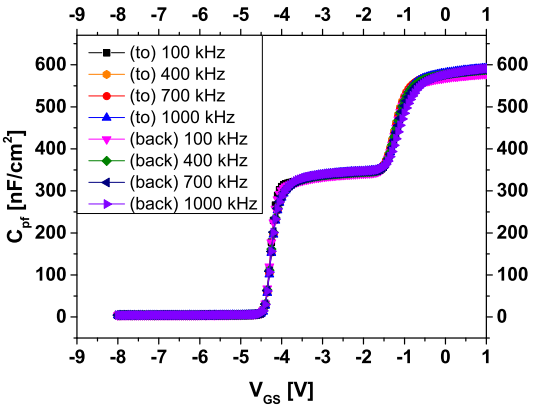

(a) C-V results of double-channel device

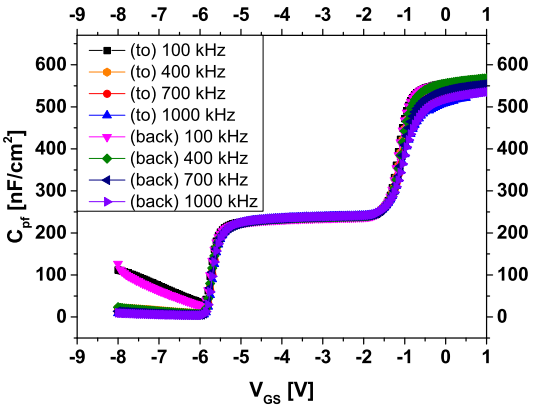

(b) C-V results of triple-channel device

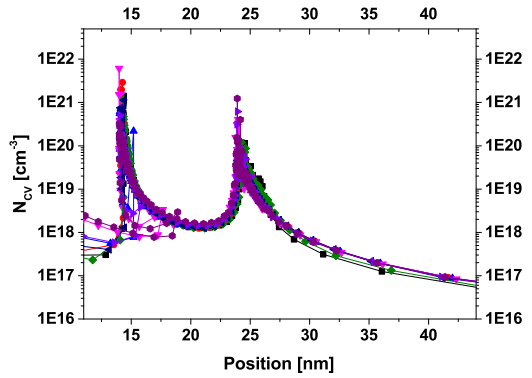

(c) Carrier concentration of double-channel device

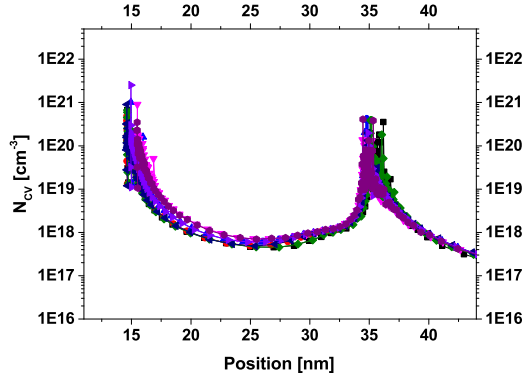

(d) Carrier concentration of triple-channel device

Figure 4.11: Capacitance voltage measurements of double- and triple-channel devices and the extracted carrier concentrations.

from the double-channel device, the number of capacitance steps does not match the number of 2DEG in the device. Only two capacitance drops at -1 V and -5.5 V are visible. This is also visualized in the extracted carrier concentration pictured in figure 4.11d. The distance of the carrier maxima is approximately 20 nm although the real spacing of the 2DEGs is 10 nm. The step connected to the middle 2DEG at the position of 25 nm is missing. Another difference between the double- and triple-channel devices can be found in the values of the capacitance drops. For the triple-channel sample, the first capacitance drop is larger than the second one while the behavior is exactly opposite for the double-channel device. Because a simulation of the band structure of the triple channel sample still yields the highest sheet carrier concentration in the lower 2DEG (in comparison to the middle and upper 2DEG), the higher capacitance drop at -1 V can only be explained by a simultaneous depletion of the upper and middle 2DEG. This fact is in contradiction to the measured transfer characteristics which showed three peaks indicating individual depletion of all three 2DEG. The reason for this behavior can be found in the differing contact layout and measurement conditions of C-V and transfer characteristic measurements. As already mentioned, C-V measurements are obtained from large-area diodes ($d = 100\ \mu m$). This induces a very uniform potential distribution under the Schottky contact which resembles the gate in a transistor geometry. Transfer characteristics are measured at

structures with comparably short gate length ($L_g = 2\ \mu m$) which, in combination with the applied drain-source voltage of $V_{DS} = 10\ V$, leads to a short-channel behavior. This means that due to the asymmetric potential distribution during the transfer characteristic measurement, the conduction band edge of the middle 2DEG is pulled down and a simultaneous depletion together with the upper 2DEG is hindered.

This effect can be visualized by transfer characteristics measured at decreasing V_{DS} which is shown in figure 4.12a. The transconductance at $V_{DS} = 10\ V$ shows three local maxima. If the drain-source voltage is decreased to 1.5 V, the transconductance peaks of the upper and middle 2DEG move closer together while the peak of the lower 2DEG is enhanced. At $V_{DS} = 0.5\ V$, the peaks of upper and middle 2DEG coalesce which leaves only two transconductance peaks for the triple-channel device similar to the results of the C-V measurement. By simulating the bandstructure of the triple-channel device and extracting the intersection at the second channel for $V_{GS} = -2.5\ V$ and $V_{DS} = 8\ V$ or $0\ V$, the measurement conditions for transfer and C-V characteristics are reproduced, respectively. The simulations shown in figure 4.12b exhibit significant differences in the conduction band energy when applying an external V_{DS} bias. By taking a closer look at the gate-drain region, a lower conduction band energy is noticed when biasing with $V_{DS} = 10\ V$ which is known as drain induced barrier lowering (DIBL). This will lead to accumulation of carriers in the middle channel which will rise to an extra capacitance step (i.e. separate depletion of the middle and upper channel) in the transfer characteristic.

The simultaneous depletion of upper and middle channel is also confirmed if calculated capacitances are compared to the measured values: The calculated capacitance value for depleted upper and middle channel and populated lower channel is 282 nF/cm^2 and the measured capacitance for this state is around 250 nF/cm^2 (plateau between -1 and -5 V in fig. 4.11b). The two values show good agreement with the same deviation as the calculated and measured capacitances did for the double-channel device. This again proves that at the capacitance plateau between -1 and -5 V in fig. 4.11b the upper and middle channel are already depleted.

The sheet carrier concentration of the triple-channel device is again accessed by integration of the measured C-V data. As the upper and middle channel are depleted simultaneously, only the combined sheet carrier concentration of both channels can be determined yielding $4.49 \cdot 10^{12}\ cm^{-2}$ (-1.55 to 0 V). The lower channel is populated with a concentration of $6.02 \cdot 10^{12}\ cm^{-2}$ which results in an overall sheet carrier concentration of $1.05 \cdot 10^{13}\ cm^{-2}$.

RF Characterization

To investigate the RF performance of the multichannel HFET, S-parameter measurements were performed. Devices with 1 μm gate length and a gate-drain distance of 2.5 μm were utilized. At a drain-source voltage of 10 V, S-parameters were measured as a function of V_{GS} up to 50 GHz. The extracted transit frequency (f_T) and the maximum oscillation frequency (f_{max}) are shown in figure 4.13. The maximum values decreases with increasing number of 2DEG from 18 GHz for the single-channel over 14.5 to 13.3 GHz for the double- and triple-channel transistors. A similar behavior can be observed for f_{max}. The decrease of f_T and f_{max} for the double- and

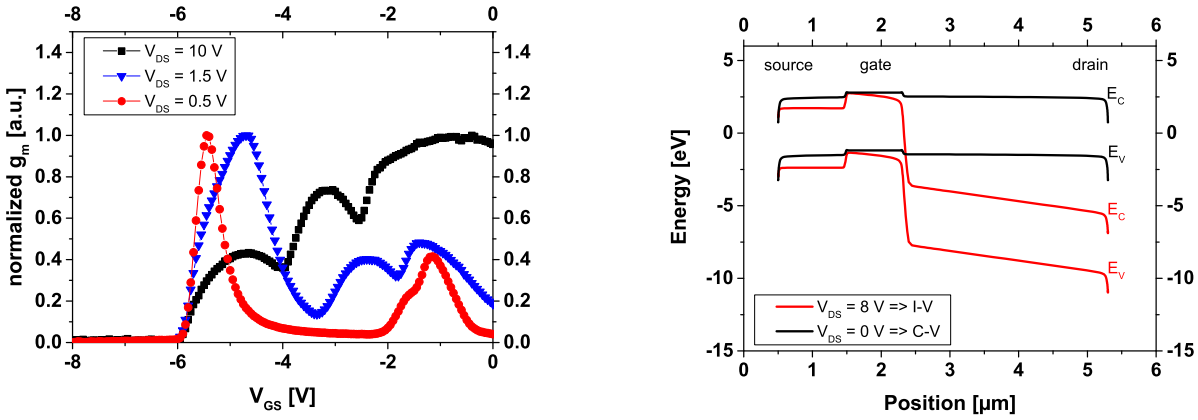

(a) *(b)*

Figure 4.12: Left: normalized transconductance of the triple-channel device measured at different source-drain voltages. Right: Simulated band structure from source to drain of the middle channel with and without applied V_{DS}.

triple-channel device seems reasonable as the maximum g_m decreases with a higher number of 2DEG channels.

When the measured f_T is compared to roughly estimated f_T values calculated with the formula

$$f_T = \frac{g_m}{2\pi \cdot C_{gs}} \; valid \; for \; C_{gd} << C_{gs} \tag{4.3}$$

at the respective gate bias points, the decrease of the measured f_T values is surprising by large. Table 4.1 shows the calculated f_T values from DC and CV measurements. The 3 GHz difference in f_T for the single-channel device originates from the fact that for the calculated values, C_{gs} and g_m are taken from low frequency measurements $\leq 1\ MHz$ and C_{gs} is measured at $V_{DS} = 0\ V$ while the measured f_T is measured at $V_{DS} = 10\ V$. Despite of this deviation, it is obvious that the calculated transit frequency increases with rising number of 2DEG in the devices whereas measured values decrease with increasing channel number. This leads to the conclusion that the shrinking g_m values for double- and triple-channel structures are not dominating the behavior of f_T. The calculated increase of the maximum f_T with the number of 2DEG can instead be attributed to the decrease of the gate-source capacitance C_{gs} due to the larger distance between the lowest 2DEG and the gate contact. As the changing g_m values do not dominate the calculated f_T characteristic, it seems likely than the measured f_T values are neither governed by the drop of g_m.

Sample	V_{GS} [V]	f_T [GHz] measured	f_T [GHz] calculated
Single-channel	-1.4	18.0	15.0
Double-channel	-2.8	14.5	16.0
Triple-channel	-3.6	13.3	19.5

Table 4.1: Comparison between the measured and calculated f_T for single-, double- and triple-channel HFET at the respective gate-source voltages.

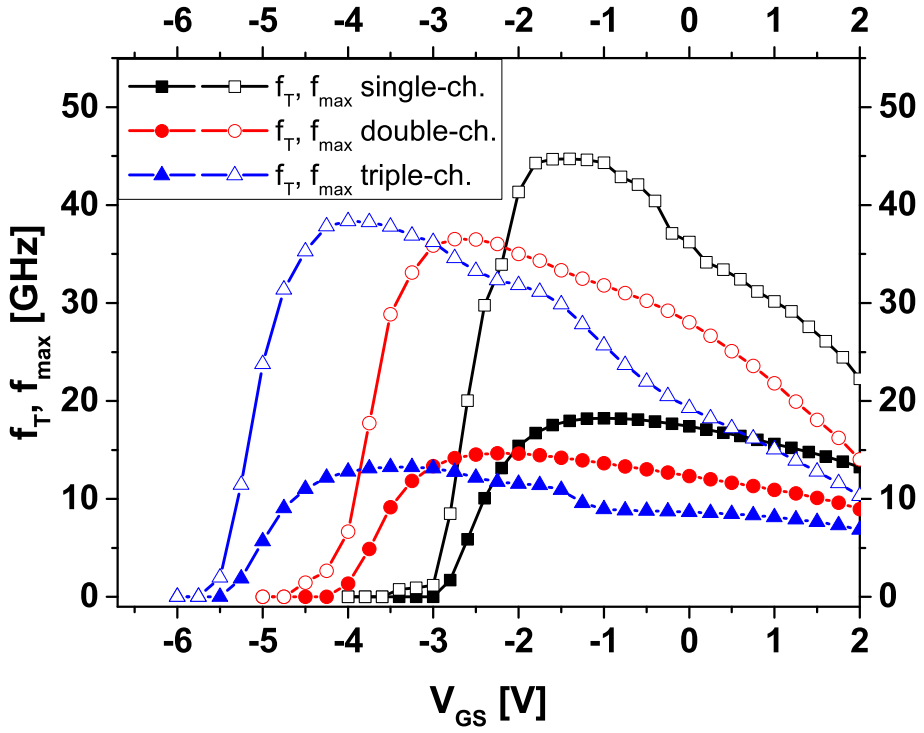

Figure 4.13: f_T (full symbols) and f_{max} (open symbols) for single-, double- and triple-channel devices measured at $V_{DS} = 10\ V$.

A possible candidate to explain the divergent trend of measured and calculated f_T is the gate-drain capacitance C_{gd} (assumed to be negligible in equation 4.3). In a standard single-channel HFET, this capacitance is located between the gate metal and the undepleted part of the pinched-off 2DEG channel under the drain contact. This results in a very small capacitance as the comparably large distance (2.5 μm) between gate and drain contact denotes the effective thickness of the capacitance in the equivalent-circuit diagram. For a double- or triple-channel HFET, the situation is different. The gate-drain capacitance is now represented by a parallel configuration of capacitances between the gate metal and the undepleted part of the upper and lower 2DEG for the double-channel device or even upper, middle and lower 2DEG for the triple-channel device. This results in a much larger parasitic C_{gd} for multichannel HFET which degrades RF performance. With a large C_{gd}, equation 4.3 is no longer true and equation 4.4 has to be considered instead.

$$f_T = \frac{g_m}{2\pi(C_{gs} + C_{gd})} \tag{4.4}$$

The equivalent circuit diagram corresponding to equation 4.4 is depicted in figure 4.14. The current amplification $|\underline{h}_{21}|$ of this equivalent circuit diagram was simulated using SPICE [102] with previously measured values for C_{gs} and g_m. C_{gd} was varied until the simulated current amplification matched the measured data. The results are shown in figure 4.15. The current amplification $|\underline{h}_{21}|$ was modeled for $C_{gd} = 0.012 \cdot C_{gs}$ (green graph) which would satisfy the approximation of $C_{gd} \ll C_{gs}$ but does not fit the measured data. An assumed gate-drain capacitance of $C_{gd} = 0.12 \cdot C_{gs}$ (red graph) matches the measured data of the triple-channel

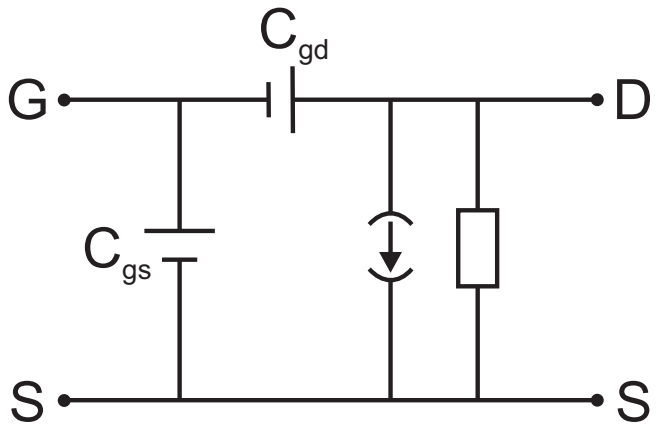

Figure 4.14: Equivalent circuit diagram of a standard transistor with C_{gs} and C_{gd}

device well. This allows the conclusion that the degradation of f_T and f_{max} can be attributed to the increasing C_{gd}.

Figure 4.16 shows the maximum available gain (MAG) extracted at 2 GHz and $V_{DS} = 10\ V$ for the single-, double- and triple-channel devices. With increasing number of 2DEG, the MAG profile becomes wider and more linear. For the triple-channel structure, a linear MAG profile can be realized for drain-source voltages from -5 to +1 V while the single-channel structure yields a linear behavior only from -2 to +1 V. The maximum gain varies from 17.5 dB for the single-channel device to 16 dB for the double- and triple-channel transistor. The deviation of the maximum gain is very small if all three samples are compared which makes the expansion of the MAG profile even more promising. The MAG profile proves that the highly linear properties from DC measurements also translate into the RF properties of the devices and larger RF input signals could be applied.

To further investigate the suitability of multi-channel HFET for highly linear amplifiers, the large-signal power amplification properties were investigated with load-pull measurements. Figure 4.17 shows the output power plotted versus the input power at 2 GHz. It is obvious that the power gain is highest for the single-channel device and decreases gradually for double- and triple-channel geometries which can be attributed to the lower g_m values for double- and triple-channel structures. For small input power levels, the output power shows a linear dependency. This is displayed in figure 4.17 by linear fits (solid lines) of the graphs. This linear fit represents the behavior of an ideal amplifier. Actual devices show a divergent characteristic. At higher input power values, the output power does not follow the linear behavior anymore due to varying g_m, trapping of carriers, hot-electron effects, self-heating and eventually saturation. The point at which the actual output power has decreased by 1 dB below the linear extrapolation is called 1dB-compression point and is a measure for the linearity of a power amplifier. The 1dB-compression points are marked in figure 4.17 with dashed lines and it directly becomes clear that they are shifted to higher input power levels for the double- and triple-channel HFET. This implies a higher degree of linearity in power amplification for double- and triple-channel devices which makes these devices very interesting for highly linear amplifiers.

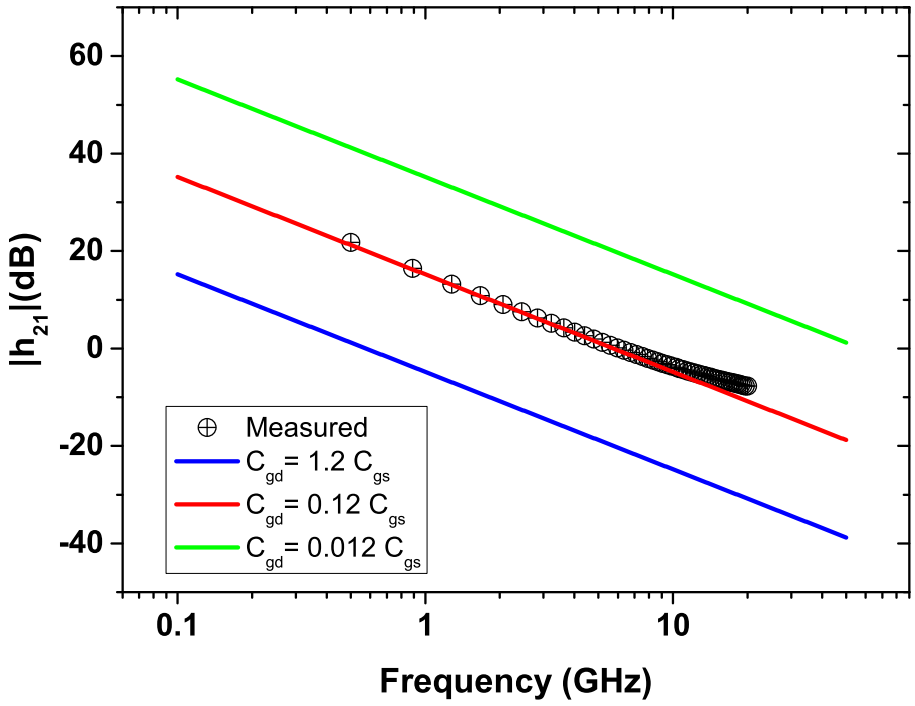

Figure 4.15: Comparison of measured current amplification of the triple-channel device with models representing a varying influence of C_{gd}.

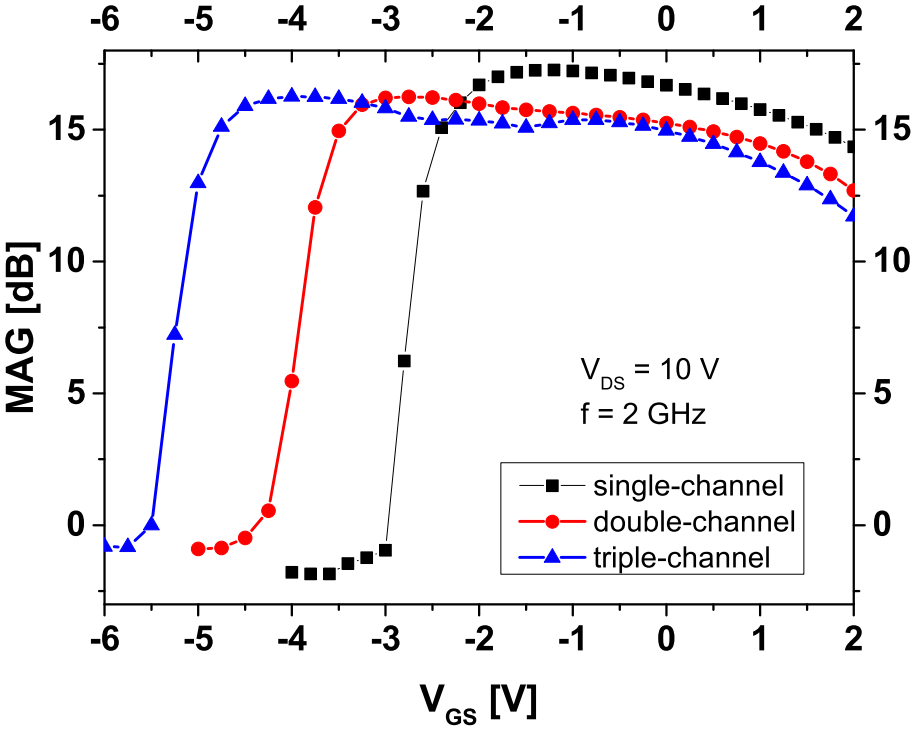

Figure 4.16: Maximum available gain (MAG) for single-, double- and triple-channel devices obtained at $V_{DS} = 10\ V$ and 2 GHz operating frequency.

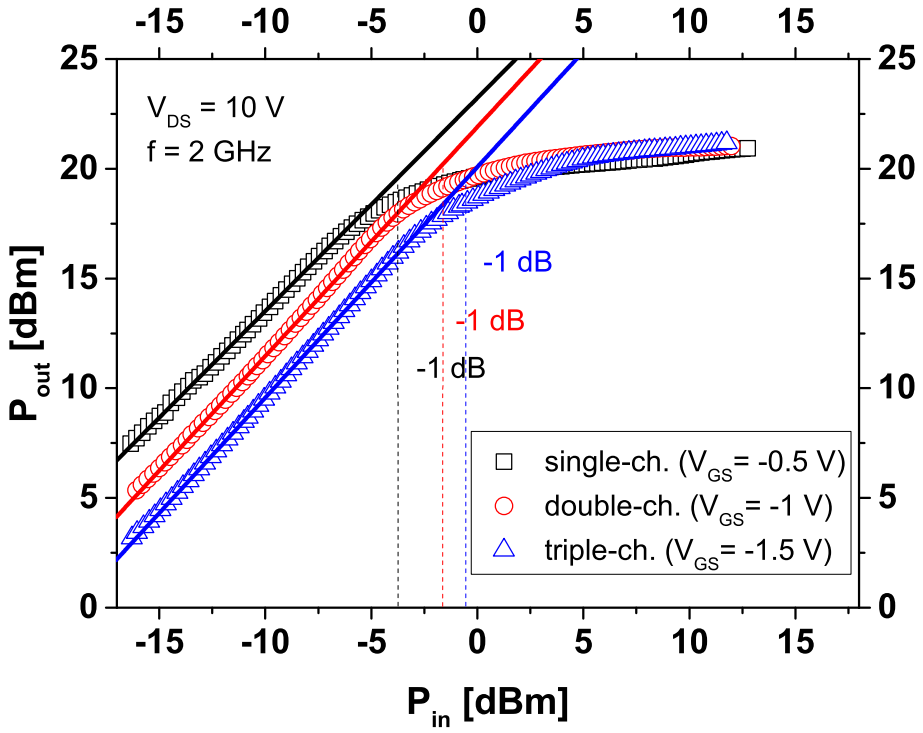

Figure 4.17: Power sweep (symbols) for single-, double- and triple-channel devices with linear extrapolations (lines) and marked 1 dB compression points (dashed lines).

4.2 The SL Distributed Bragg Reflector

4.2.1 DBR in Group III Nitrides

Distributed Bragg reflectors (DBR) are wavelength-sensitive mirrors [103]. The reflectance reaches values close to 100 % for incident wavelengths in the so called stopband. For wavelengths outside the stopband range, the reflectance is very low. A schematic structure of a DBR is depicted in figure 4.18

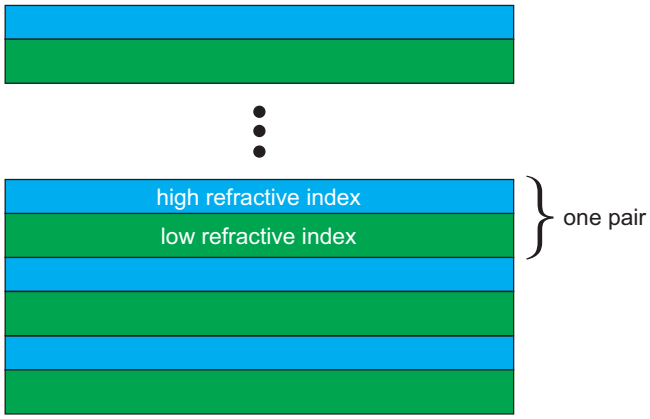

Figure 4.18: Schematic layer stack of a DBR.

DBR consist of two materials. For the ideal case, both materials are 100 % transparent i.e. exhibit no absorption at the stopband wavelength. One material has a high refractive index and the second a low refractive index. The two materials are deposited alternating on top of each other creating a structure with modulated refractive index. One double layer, containing one layer of each material, denotes one DBR pair.

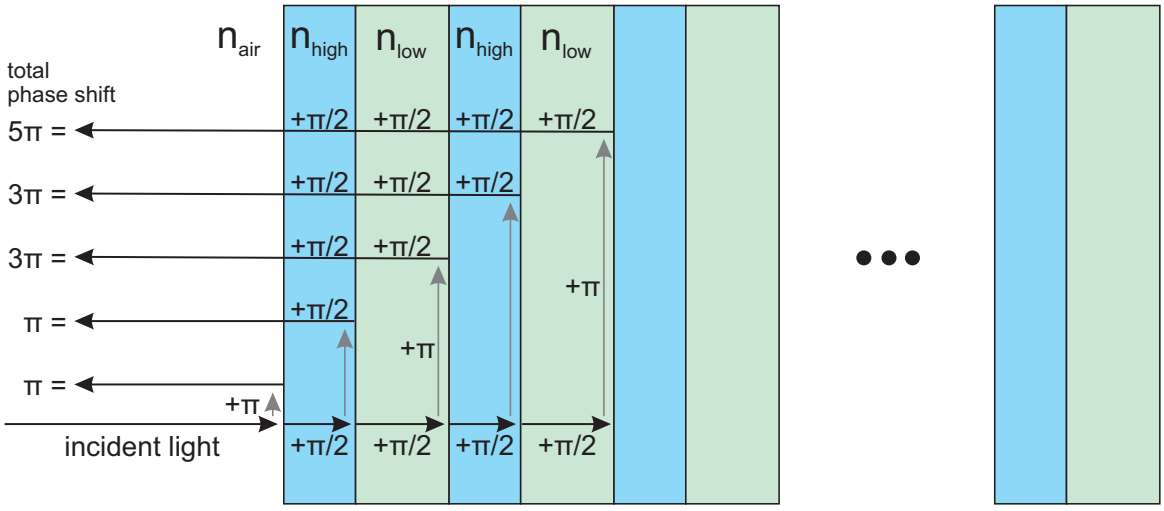

Figure 4.19: Schematic working principle of a DBR. For clarity, the reflected beams are shifted upwards, marked with grey arrows.

The reflectance of the DBR is based on multiple reflection processes and constructive interference at the interfaces between low- and high-index layers. Figure 4.19 shows a DBR structure under normal light incidence. Every layer has the optical thickness of a quarter of

the stopband wavelength $\lambda/4$ which corresponds to a phase shift of $\pi/2$. The incident beam is partly reflected and transmitted at each interface according to Fresnel's formulas [104]. For dielectric materials with zero extinction coefficient and normal light incidence, the reflected and transmitted quantities of the electric field can be calculated as follows:

$$\frac{E_{0r}}{E_{0e}} = r = \frac{n_1 - n_2}{n_1 + n_2} \tag{4.5}$$

$$\frac{E_{0t}}{E_{0e}} = t = \frac{2n_1}{n_1 + n_2} \tag{4.6}$$

According to equation 4.5, at the interface from low (n_1) to high refractive index (n_2), a phase shift of π takes place ($r < 0$), whereas at the interface from high to low refractive index, no phase shift is present ($r > 0$) [105]. As a result, the phase shift of all reflected beams is an uneven multiple of π which implies that all reflected beams are in phase and interfere constructively. Even multiple reflection conserve this phase relation. The reflectance of a DBR strongly depends on the number of pairs N. By increasing N, additional interfaces which partly reflect the incident light are appended to the DBR structure. This increases the reflection coefficient of the whole structure. As a drawback, more pairs N also increase the structure complexity and the overall material thickness the light interacts with. This implies increased absorption and scattering losses due to interface imperfections and at specific pair number N, no further improvement of the DBR reflectance is possible by adding more pairs. In some material systems, addition of further pairs may be difficult due to fabrication-related issues. DBR fabricated with MOVPE (cmp. section 2.1.2) are often limited in pair number N due to strain (cmp. section 2.1.3).

The reflectance of the DBR also depends on the difference in refractive index Δn of the two materials. By increasing this difference, the reflectance of the DBR can be effectively enhanced. The refractive index is a material-specific property and follows directly out of the complex permittivity of the material [61]. Therefore the material choice for high- and low-index layers is extremely important. The reflectivity of an ideal DBR under normal incidence can be calculated with a simplified formula after [106]:

$$R = \left[\frac{n_0(n_2)^{2N} - n_s(n_1)^{2N}}{n_0(n_2)^{2N} + n_s(n_1)^{2N}}\right]^2 \tag{4.7}$$

where n_0 is the refractive index of the surrounding medium, n_1 and n_2 are the refractive indices of high- and low-index DBR materials. n_s denotes the refractive index of the substrate and N the number of DBR pairs.

Suitable materials for DBR have low absorption in the stopband wavelength. For the UV and visible wavelength range, semiconducting wide band gap materials like group III nitrides [4] or dielectric materials like metal oxides [107], [108] as well as metalloid oxides [109] and nitrides [110] are suitable. Group III nitrides are very interesting for DBR fabrication as solid state lasers in the UV, blue and green wavelength regime are based on theses materials. These laser devices are often realized as vertical cavity surface emitting lasers (VCSEL) which consist

of a bottom DBR, an active region in which photons are generated and a top DBR. A major disadvantage of group III nitride DBR is the relatively small refractive index variation between AlN, GaN and InN. Additionally, the most promising material combinations with largest index contrast cannot be deposited epitaxially because of too large stress. As a consequence, generally more than 30 nitride DBR pairs have to be deposited to reach reflectivities above 99 %. The refractive indices of the materials at 400 nm are approximately 2.13 for AlN, 2.55 for GaN and 1.7 for InN (strong absorption) [23][22][21]. Refractive indices of the alloys can be interpolated with formulas given in references [22] and [21].

Commonly used material combinations are AlN/GaN, AlGaN/GaN and AlInN/GaN [111]. AlInN with 18 % In is lattice-matched to GaN (cmp. 2.2). This composition used in an AlInN/GaN DBR leads to a strain-free DBR layer stack. However, Δn of this material system (7.5 %) is quite small compared to AlN/GaN DBR (20 %)[111]. Therefore, more than 50 pairs are needed to obtain reflectance values for the DBR larger than 99.9 % [111]. Another issue is the fact that due to the low Gibbs free energy of formation of InN compared to AlN and GaN, In-containing alloys can not be deposited with hydrogen as carrier gas. Furthermore, hydrogen is also a product of the group III nitride formation reaction and a high partial pressure of hydrogen drives the equilibrium of the formation reaction to the educt side [75]. Nitrogen as carrier gas has to be used instead which in return is not beneficial for GaN deposition [17]. Also In-containing alloys have to be deposited at low growth temperatures in the range of $700 - 800°C$ and GaN epitaxy should be carried out at $1050 - 1070°C$ (cmp. chapter 3.1. To account for the very different optimal growth parameters for AlInN and GaN, ramping steps between every layer have to be included which often hamper interface quality.

AlGaN/GaN DBR structures are much more undemanding concerning growth parameters. Yet stress, which is not an issue in the lattice-matched AlInN/GaN system, is the major challenge for AlGaN/GaN structures. The theoretical critical layer thickness of AlGaN on GaN rapidly decreases with increasing Al content and is approximately 15 nm for $Al_{0.2}Ga_{0.8}N$ [46] (cmp. chapter 3.2). To obtain sufficiently large Δn for AlGaN/GaN DBR, the Al content has to be larger than 40 % which further reduces the critical thickness of AlGaN on GaN and makes it impossible to grow AlGaN layers reaching an optical thickness of $\lambda/4$ ($\lambda = 400\ nm \Rightarrow \frac{\lambda}{4n} = 40\ nm$ AlGaN with $n = 2.5$) for stopband wavelengths in the near-UV or visible regime. Nevertheless AlGaN/GaN DBR with high Al content can be manufactured if strain managing measures are taken. Possible approaches are Al-containing buffers or prelayers, which shift the pseudomorphic lattice constant of the DBR stack from GaN in the direction of AlN [112] [113], or AlN interlayers [112].

4.2.2 Concept of the SL-DBR

The last chapter discussed some approaches to overcome the strain-related issues in AlGaN/GaN DBR such as Al-containing buffers or AlN interlayers. An alternative approach to manage strain in DBR structure is the use of of AlN/GaN-SL. As described in section 2.2, AlN/GaN-SL denote a virtual AlGaN alloy and are capable of effectively managing stress. In chapter 3.2, the critical thickness of these SL was already demonstrated to be much higher than the critical thickness of AlGaN with a comparable Al content. This makes it very promising to investigate the application of AlN/GaN-SL in AlGaN/GaN-DBR. The used SL period thickness around 4 nm is two orders of magnitude smaller than the wavelength in the near-UV or visible range ($300 - 700$ nm). These small layer thicknesses ensure that the individual layers of the SL do not lead to a significant interaction with visible or near-UV light. Instead, the AlN/GaN-SL can be treated as an effective medium for electromagnetic waves. In this way, AlN/GaN-SL can replace the low-index AlGaN in AlGaN/GaN-DBR. GaN remains as the high-index material and alternates with the SL.

Figure 4.20 shows a schematic of a possible sample geometry. The left side shows a standard AlGaN/GaN-DBR and the right side the new SL-DBR in which the low-index layer is formed by an AlN/GaN-SL. The SL-DBR structure leads to the occurrence of two different periodicities in one structure. One is the periodicity of the DBR with a periodic repetition length Δ_{DBR} (around 100 nm) which is the combined layer thickness of one AlN/GaN-SL layer (low-index) and one GaN layer (high-index). The other, much shorter, periodicity is the one of the AlN/GaN-SL and is defined as the combined layer thickness of one AlN and one GaN layer Δ_{SL} (around 4 nm) forming the AlN/GaN-SL, in analogy with the previous chapters 3.1 and 4.1.

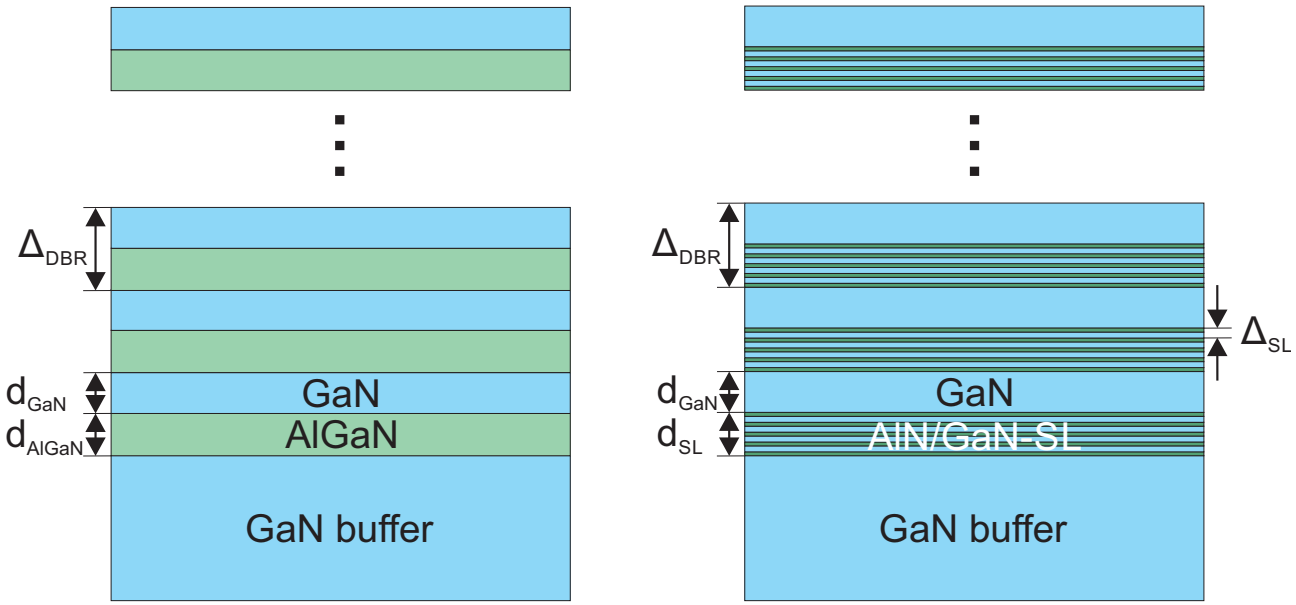

Figure 4.20: Left: standard AlGaN/GaN DBR. AlGaN denotes the low-index and GaN the high-index material. Right: SL-DBR with an AlN/GaN-SL as low-index and GaN as high-index material. The periodic lengths of DBR (Δ_{DBR}) and SL (Δ_{SL}) are marked and the layer thicknesses d_i of AlGaN, SL and GaN are defined.

The last chapter elucidated that every layer of a DBR has to have the optical thickness

of a quarter of the designated stopband wavelength. This is also true for the AlN/GaN-SL. In the case of AlGaN, the refractive index can be interpolated between the binary compounds AlN and GaN [21], [22]. A linear interpolation after the effective medium theory (EMT) of the refractive index poses a good approximation for AlGaN for wavelength well away from its absorption edge. To clarify if this is also valid for AlN/GaN-SL, the refractive indices obtained by EMT calculations were compared to Floquet mode simulations (carried out at the chair of Integrated Photonics of RWTH Aachen University). The results showed very good agreement when the layer thicknesses of the individual AlN and GaN layers in the SL were chosen to be much smaller than the wavelength for which the refractive index is considered. Therefore, the assumption seems valid that the refractive index of AlN/GaN-SL can be interpolated linearly between AlN and GaN for DBR design. This hypothesis is also affirmed by Rodak et al. who successfully fabricated SL-DBR designed under the assumption of equal refractive indices for SL and AlGaN with the same averaged Al content [114]. Figure 4.21 shows the calculated refractive index data for AlN/GaN-SL with varying effective Al content. On the basis of these data, SL-DBR design is conducted.

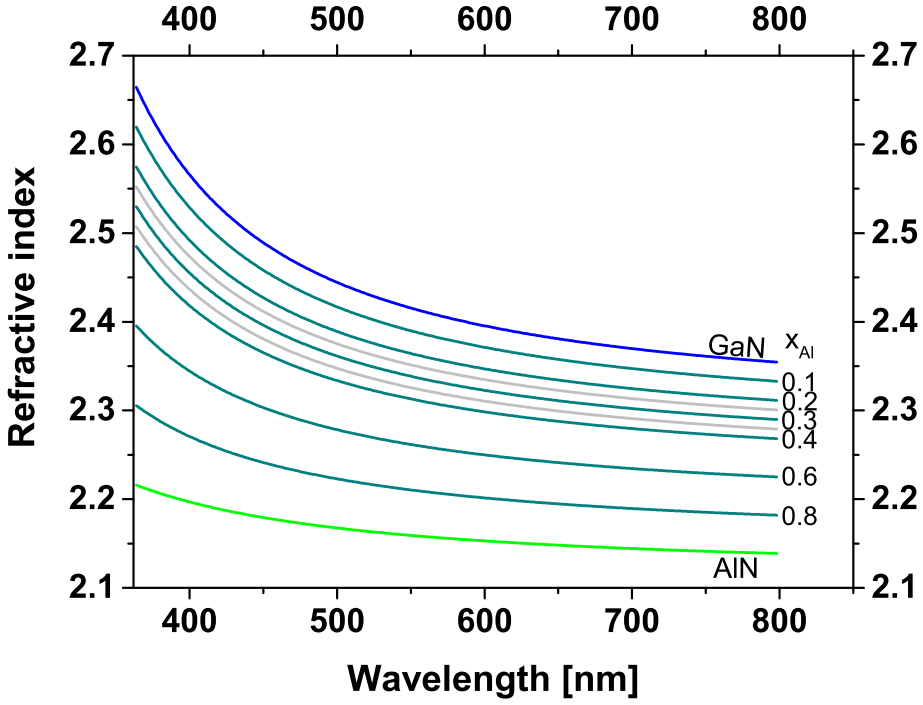

Figure 4.21: Refractive index of GaN, AlN and AlN/GaN-SL calculated with EMT. Refractive index data for GaN and AlN are taken from [115].

To obtain an optical contrast to the adjacent high-index GaN layers and boundary conditions required for a DBR, it is necessary to start and end the SL stack with an AlN layer. Finally, to adjust the layer thickness of the SL d_{SL} to match the quarter wavelength condition, the repetition number of the AlN-GaN sequence N is adjusted to fulfill the condition

$$d_{SL} = \frac{\lambda}{4n} = N\Delta_{SL} + d_{AlN,SL} \tag{4.8}$$

where $d_{AlN,SL}$ denotes the layer thickness of the thin AlN layers used in the SL and n is the calculated refractive index of the SL. In order to fine-tune the SL layer thickness, it is of course possible to vary the GaN and AlN layer thicknesses in the SL. This can be performed either by maintaining a constant ratio of AlN and GaN, which does not affect the refractive index, or the ratio is varied and the change in refractive index has to be taken into account.

Other groups also used SL for strain engineering in nitride-based DBR. Nakada et al. used an AlGaN/GaN-SL prior to AlGaN/GaN-DBR growth. In contrast to the standard GaN buffer, this underlying layer stack exhibits an a-lattice parameter smaller than that of GaN, which reduces the tensile strain in the low-index AlGaN layers of the DBR [116]. However, a comparison with an AlGaN layer instead of the SL layer is lacking so it was not possible to derive any conclusion concerning the strain managing properties of the SL. Huang et al. used AlN/GaN-SL in the quarter wavelengths stack of an AlN/GaN-DBR. They substituted every sixths low-index AlN layer with an AlN/GaN-SL layer with an effective AlN content of 50 % to hinder crack formation [117]. With 3 - 5 nm, the individual GaN and AlN layers in the SL were slightly thicker than the SL explored in this thesis. Therefore, only 5.5 periods were necessary to reach the quarter wavelength thickness. In this study, it was not explored if AlGaN instead of AlN/GaN-SL could yield the same result. Rodak et al. in general used a similar approach as pursued in this thesis. They used an AlN/GaN-SL as the low-index layer in DBR. GaN serves as the high-index layer [114]. The layer thicknesses in the SL were 10.4 nm for AlN and 0.94 nm for GaN. This implies an effective AlN content in the SL around 90 %. 25 DBR pairs were successfully deposited using this approach. The samples only showed cracks within a few mm at the wafer edge. The wafer center remained uncracked. Reflectivities of 96 % were measured. SEM images showed V-defects in the DBR structure. This indicates that relaxation processes might be present in the DBR samples. Yet, no XRD data ware shown, which would enable a thorough evaluation of the strain state in the samples. Altogether, it can be stated that the use of SL in DBR growth is very promising but a detailed analysis of strain evolution and distribution is still lacking for such samples. In the following, such an analysis will be prepared.

4.2.3 Fabrication and Structural Characterization of SL-DBR

To investigate the concept of the SL-DBR, a 10-pair DBR with AlN/GaN-SL as low-index layer is deposited on a standard GaN buffer with AlN nucleation and buffer on 2" sapphire substrate (cmp. chapter 2.1.2). The deposition of the SL-DBR was carried out at standard SL-growth conditions, namely 1060°C, 75 mbar and a V/III ratio of 1220 for AlN growth and 1015 for GaN growth (cmp. chapter 3.1). The SL featured 6 pairs of AlN and GaN concluded with an additional AlN layer. The stopband wavelength was aimed to be around 370 nm. The resulting sample surface showed no cracks or other defects visible to the naked eye.

A structure with only 10 DBR pairs is pursued to account for the long growth times in MOVPE. The growth time of one DBR pair is approximately 30 min with the growth conditions and stopband wavelength given above. The total growth time of the overall structure, including

heating, nucleation, buffer layer and cooling steps, adds up to 7-8 hours. The same structure could be realized on a shorter timescale in a production type MOVPE system. Due to the reactor limitations of the R&D MOVPE system, test structures with only 10 DBR pairs are mainly explored in this thesis. 10 DBR pairs are expected to deliver only a comparably low reflectivity. In AlN/GaN-DBR, reflectivities of 99 % were reached with 35 pairs and 16 pairs led to a reflectivity of 93 % [113]. As the refractive index contrast is lower between AlN/GaN-SL and GaN, reflectivities of considerably less than 93 % are expected. With formula 4.7 and refractive indices of 2.7 for GaN and 2.5 for the SL, a reflectivity of 72 % is predicted with 10 DBR pairs.

The reflectivity spectrum of the sample described above is depicted in figure 4.22. This spectrum was taken 6.5 mm from the wafer center in the direction of the wafer edge (this is necessary due to a thickness inhomogeneity caused by the MOVPE reactor type). For all samples investigated in this thesis, the radial position yielding the highest reflectivity in the stopband was chosen for evaluation. The reflectivity of the SL-DBR is quite low over the whole wavelength rage and shows a periodic oscillation between 10 and 30 % with exception of region between 350 and 400 nm. In this wavelength regime, the reflectivity features a sharp peak which is the stopband of the SL-DBR. The maximum reflectivity of this peak is 74 % located at 366 nm with a stopband width of 16 nm. This deviates only 2 % from the calculated value which seems very precise if one considers the high sensitivity of the formula on refractive index values in combination with the only interpolated n_{SL}. The narrow stopband width of only 16 nm is caused by the low refractive index contrast in group III nitrides.

Experimental results from several groups are summarized in the paper from Carlin et al. [111]. Compared to these data, a maximum reflectivity around 75 % with 10 pairs is ranked acceptable for nitride-based DBR. The reflectivity data from our sample are even slightly higher than the given data of AlGaN/GaN-DBR but this can be attributed to the very small stopband wavelength close to the absorption edge of GaN for the SL-DBR sample. This increases the refractive index contrast. The graph in red (in fig. 4.22) shows the reflectivity spectrum of a buffer structure (sapphire substrate, AlN, GaN) comparable to the one in the SL-DBR sample. The reflectivity of the buffer structure shows no stopband peak but also periodic oscillations between 400 and 800 nm. By comparison of the two graphs, it becomes clear that the modulation observed for the SL-DBR on the long-wavelength side of the stopband peak originates from the buffer structure. Between 550 and 800 nm, the reflectivity graphs of SL-DBR (black) and buffer structure (red) look quite identical and only the oscillation frequency of the buffer structure is higher. This could be related to differences in layer thicknesses. Between 400 and 550 nm, the spectra for SL-DBR and buffer structure look more different. This can be attributed to a convolution of DBR reflectivity ripples from the adjacent stopband with the thickness-related oscillation from the buffer for the SL-DBR structure. The node at approximately 530 nm is also related to the layer thicknesses in the buffer stack. A simulational analysis of the reflectivity will be given at the end of this chapter.

The AFM image of the sample, displayed in figure 4.23, reveals a stepflow pattern similar

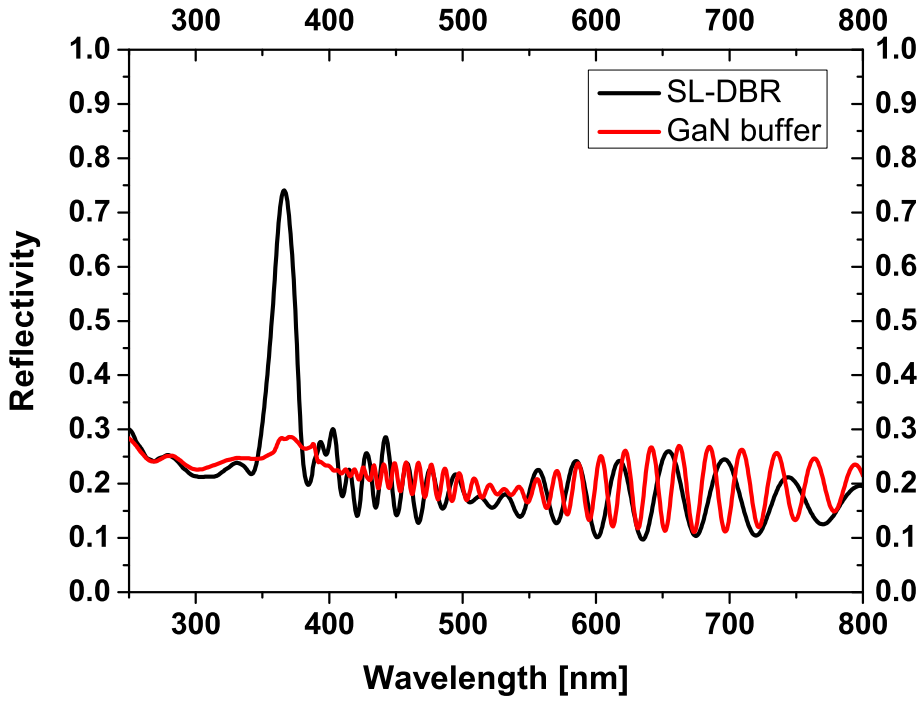

Figure 4.22: Reflectivity spectrum of a 10-pair SL-DBR (black) in comparison to the reflectivity spectrum of a standard GaN buffer (red).

to a GaN buffer surface. But in the case of the DBR, the terrace edges are not as strictly aligned parallel to the wafer offcut as it is the case for a GaN buffer. The average step height is in the range of 0.32 nm. This is similar to GaN buffer samples and is in the range of the c lattice parameter of the material (if the error of the AFM height measurement is taken into account). The average terrace width is around 185 nm. This is significantly larger than for a GaN buffer structure for which values around 100 nm are reached. It agrees well with the AFM results obtained from the single SL structures (cmp. chapter 3.1), which showed a strong terrace formation with widths in the μm regime. The SL-DBR surface, which is a GaN surface as this is the topmost layer, combines the characteristics of GaN and SL, resulting in stepflow pattern with increased terrace width. The average root mean square roughness value (rms) of the SL-DBR sample is 2.1 nm. This is notably higher than for GaN buffers (< 1 nm) but still very smooth. AlGaN/GaN-DBR fabricated by Nakada et al. show rms roughness values in the same range [116].

A (0002) 2θ-ω-scan of the SL-DBR sample is depicted in figure 4.24. The interpretation of the scan is similar to (0002) 2θ-ω-scans of single SL-layers as discussed in chapter 3.1, but the scan is not only a convolution of contributions from SL period thickness Δ_{SL} and SL layer thickness d_{SL}. The XRD data also contains features reflecting the periodicity of the DBR. The GaN and AlN buffer layer peaks are marked with "GaN" and "AlN". The peaks from the SL layers have a very large separation related to the small periodic length Δ_{SL} and are marked in figure 4.24 with "Δ_{SL}". The periodicity of the DBR manifests in various peaks of small spacing caused by the larger periodic length Δ_{DBR}. The number of visible peaks from a superlattice is

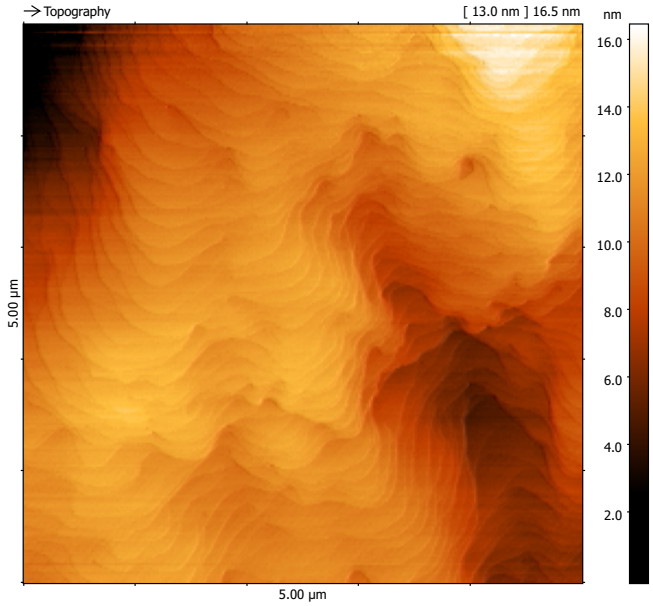

Figure 4.23: AFM graph of the SL-DBR surface. (An FFT filter was applied to the raw data to exclude parasitic oscillations.)

a measure for its interface quality and exactness of layer thickness. The scan shows multiple peaks for the AlN/GaN-SL and the SL/GaN-DBR, as the latter is also a superlattice with longer periodicity. Therefore, it can be concluded that the complex structure of the SL-DBR was successfully realized. The peak spacing is related only to the period thickness Δ_{SL} and Δ_{DBR}. The individual layer thicknesses can therefore not be extracted directly from the data. In this case, a simulation is necessary in which the layer thicknesses are adjusted to match the measured data. In the Epitaxy software (version 4.1, ©PANalytical B.V.), a complete layer model of the sample is generated. To every layer, a specific thickness, composition and relaxation grade is assigned. SL can also be specified in the model. As only binary layers are present in the sample, the composition of every layer remains constant and the strain state can be determined from HR-XRD rsm. To fit the layer thickness to the measurement, a reasonable starting point is necessary for which generally the anticipated layer thickness is used. As already explained, the peak spacing is inversely related to the periodic thicknesses Δ_{SL} and Δ_{DBR}. The angular position of the peaks can be optimized by changing the effective AlN content of SL or DBR with constant periodic thickness. In the first place, the layer thicknesses of AlN and GaN in the SL have to be adjusted in such a way that the angular position of the zero-order SL peak is correct. This is performed by adjusting the AlN and GaN thicknesses of the SL (while a constant Δ_{SL} is maintained). In the next step, the periodic thickness of the SL (Δ_{SL}) is varied (while the AlN-to-GaN ratio in the SL is maintained) to match the peak spacing of the SL peaks. At this stage, the effective AlN content in the SL is fixed because the number of SL-pairs in combination with the fitted Δ_{SL} defines the SL thickness d_{SL} and the effective AlN content in the SL. In a third step, the peaks related to the DBR periodicity are fitted by varying the thickness of the high-index GaN layer d_{GaN}. Now the spacing and angular position are changed at the same time because varying d_{GaN} while maintaining a constant d_{SL} changes the effective AlN content of one DBR pair and simultaneously the period thickness

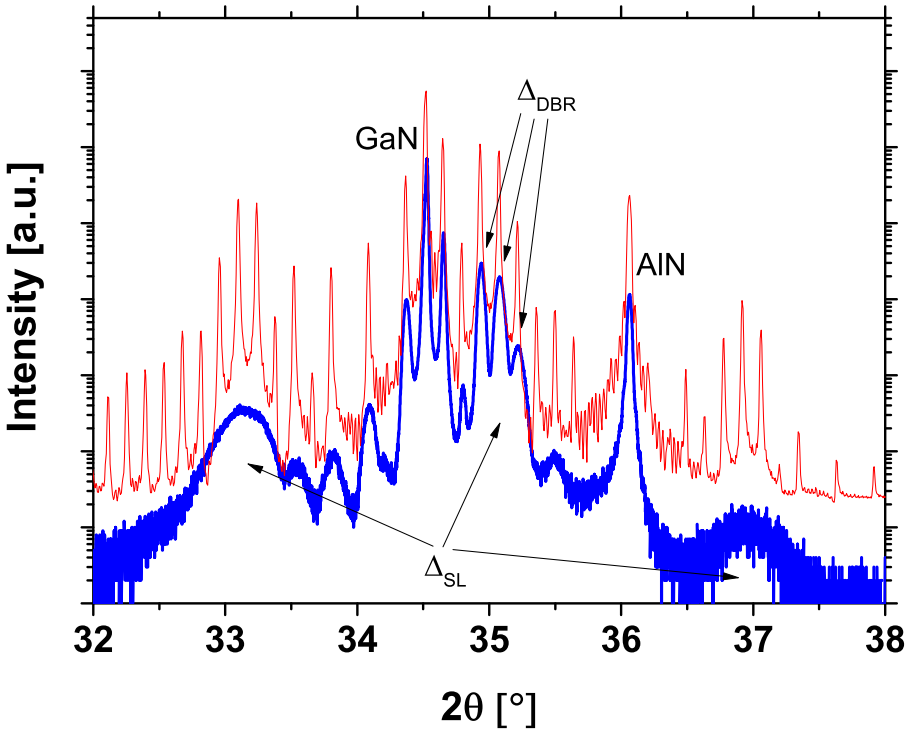

Figure 4.24: (0002) 2θ-ω-scan of the SL-DBR (blue) and the corresponding simulation (red, shifted to higher intensity values for better visibility) to extract the layer thicknesses.

Δ_{DBR}. If the agreement between measurement and simulation is not satisfying, the procedure can be repeated several times. In general, this should not be necessary because the method is not iterative but if one of the starting values is deviating strongly from the real thickness, the method can be misleading.

Figure 4.25 shows the rsm of the SL-DBR. It can directly be seen that the DBR has the same Q_x coordinate as the underlying GaN buffer and is therefore grown pseudomorphically. No relaxation is present in the DBR stack. With this information, the fit of the 2θ-ω-scan can be executed according to the method described above. The resulting layer thicknesses are 33.7 nm for the high-index GaN (d_{GaN}) and 28.6 nm for the low-index SL (d_{SL}) with a resulting periodic DBR length of 62 nm (ΔDBR). The latter is formed by 6 GaN layers of 3.3 nm thickness and 7 AlN layers which have a thickness of 1.25 nm. This leads to a periodic length for the SL of 4.55 nm (Δ_{SL}) and results in an AlN content of 26 % in the SL. This is a quite high effective Al content for a nitride DBR structure and one could expect relaxation features like layer cracking which is actually not present for this sample. This gives rise to the question on the mechanism by which the SL structure is able to manage such high Al concentrations. This will be covered in the following section 4.2.4.

The reflectance spectra of the SL-DBR were simulated with FreeSnell [118]. The refractive index data for AlN was taken from reference [119] (370-800 nm) and reference [120] (300-370 nm). For GaN data, reference [121] (370-800 nm) and reference [120] (300-370 nm) were used. For GaN, the onset of absorption was corrected from 370 nm to 364 nm to match the

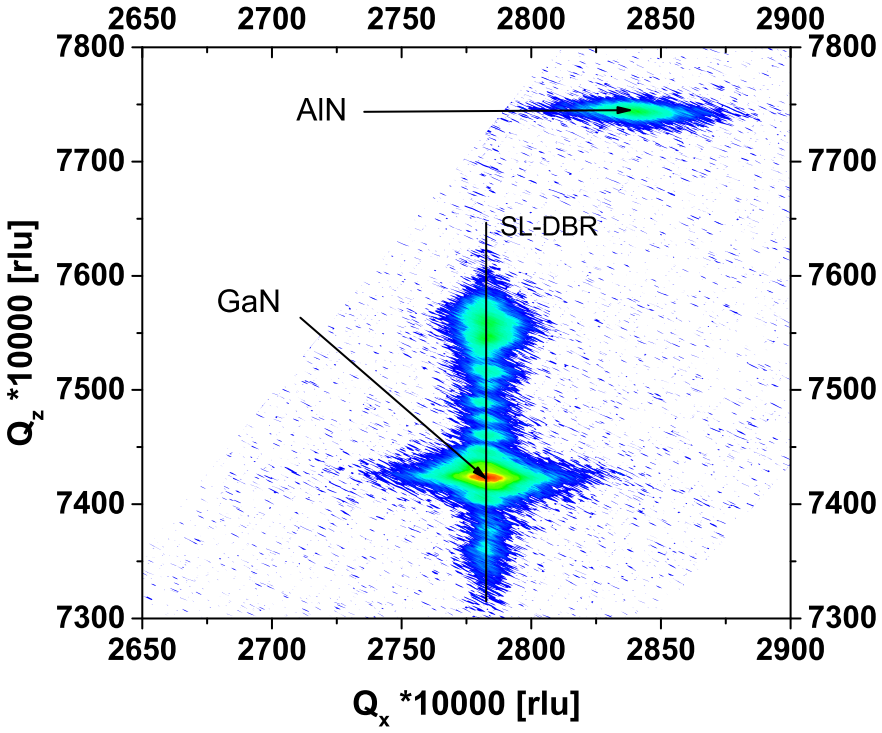

Figure 4.25: $(10\bar{1}5)$ *rsm of the SL-DBR.*

measured data. Figure 4.26 shows the simulated reflectivity of the SL-DBR and the underlying GaN buffer structure. To create a stopband peak, the thickness of the SL (d_{SL}) had to be corrected from the measured 28.6 nm (HR-XRD evaluation) to 36.07 nm which matches the quarter wavelength condition for the measured stopband wavelength of 366 nm with the interpolated refractive index for $Al_{0.26}Ga_{0.74}N$ (EMT approximation for the SL). With the measured SL thickness of 28.6 nm no stopband peak could be generated in the simulation at all. With this thickness correction, the spectra match the measured data very well. This leads to the conclusion that the AlN/GaN-SL creates a larger optical thickness than provided by the refractive index obtained from EMT. To match the quarter wavelength condition at 366 nm with a 28.6 nm thick layer, a refractive index of 3.2 would be necessary. This would make the SL the high-index and GaN the low-index layer which is very implausible. It is much more probable that electrons are present in the SL due to the polarization discontinuity which generate a different phase shift than π possibly combined with a slight increase of n.

On the right side of the stopband peak, the convolved oscillations of DBR and buffer material resemble the measurement very well. The stopband peak itself is also very similar to the measurement. The simulated maximum reflectance denotes 72 % which is the same value obtained from equation 4.7 and is very close to the measured maximum reflectance of 74 % (cmp. fig. 4.22). The matching of results from equation 4.7 and simulation is reasonable as both are based on Fresnel's formulas. On the left side of the stopband peak, a slight deviation between simulation and measurement can be noted. This is presumably related to deviations in absorption between the refractive index data obtained from literature (references [119], [120],

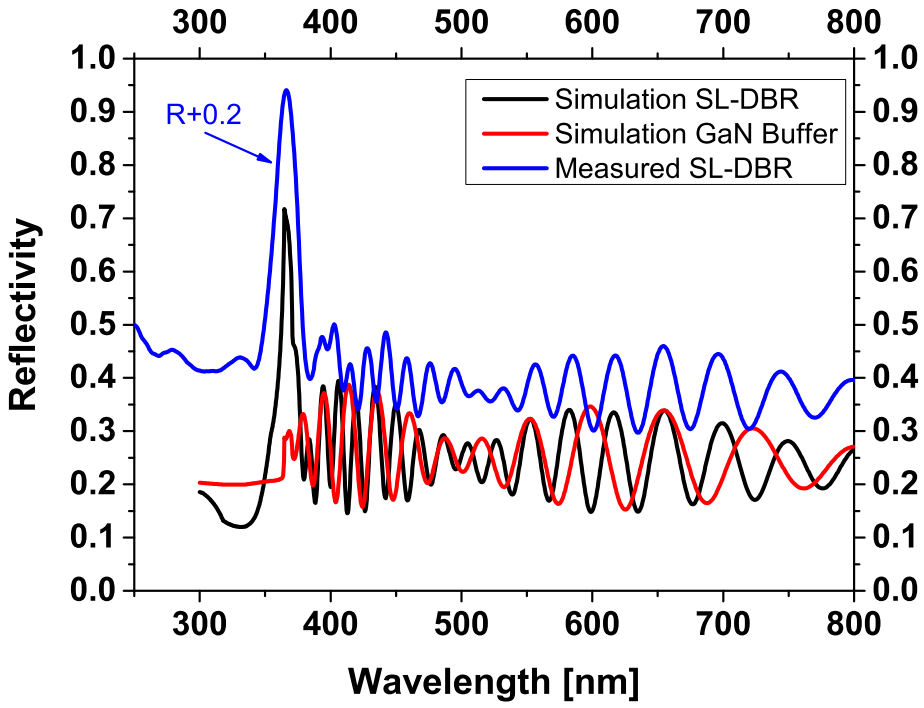

Figure 4.26: Simulated reflectance spectra of the previously investigated SL-DBR (black) and the buffer structure (red) in comparison to the measured spectrum (blue, shifted vertically for better visibility, cmp. fig. 4.22).

[121]) and the deposited epitaxial material in the sample. Especially, the modeling of absorption in the AlN/GaN-SL with EMT might be incorrect. With EMT, the absorption sets in at the band edge of the material, which is around 310 nm for $Al_{0.26}Ga_{0.74}N$. The absorption behavior of AlN/GaN-SL might deviate from the respective ternary AlGaN alloy due to the GaN wells formed in the SL. Therefore it can be concluded that the complex refractive index of SL can only by modeled by EMT for wavelengths at which no absorption or electrons are present. The simulation of the buffer reflectance (red graph) also matches the measurement. In general, the behavior of the SL-DBR could successfully be simulated.

It was also investigated whether the reflectivity scales with the number of DBR pairs. At the same standard conditions, two SL-DBR were deposited with a stopband at 370 nm. The samples also exhibit an AlN content of 26 % in the SL. One SL-DBR with 10 DBR pairs and another sample with 15 DBR pairs. The maximum reflectivity was measured and compared with calculated reflectivities for various DBR pair numbers as well as various refractive index contrasts Δn. The reflectivity was calculated with equation 4.7. With the refractive index of the surrounding medium assumed to be air ($n_0 = 1$) and the refractive indices of GaN and SL for $n_1 = n_{GaN}$ and $n_2 = n_{SL}$ and a GaN buffer as substrate ($n_s = n_{GaN}$) the equation now writes as:

$$R = \left[\frac{(n_{SL})^{2N} - n_{GaN}(n_{GaN})^{2N}}{(n_{SL})^{2N} + n_{GaN}(n_{GaN})^{2N}}\right]^2 \tag{4.9}$$

The refractive index of the SL was interpolated between GaN and AlN according to the EMT.

In figure 4.27, the results of this calculation are depicted. The blue curves show the calculated reflectivity plotted versus the number of DBR pairs for various Δn. The red circles are the two SL-DBR samples with 10 and 15 DBR pairs. The reflectivity values of the samples correspond to a Δn around 6 % which matches the $\Delta n/n$ of AlGaN/GaN DBR with 34 % Al content in the AlGaN layers (already critical for pseudomorphic growth) [111]. This shows that the refractive index contrast in SL-DBR is not hampered in comparison to standard AlGaN/GaN-DBR. The reflectivity increase of the measured samples also matches the predicted reflectivity increment from the formula given above. Therefore it can be expected that the reflectivity of a SL-DBR can be scaled in the same manner as for AlGaN/GaN DBR.

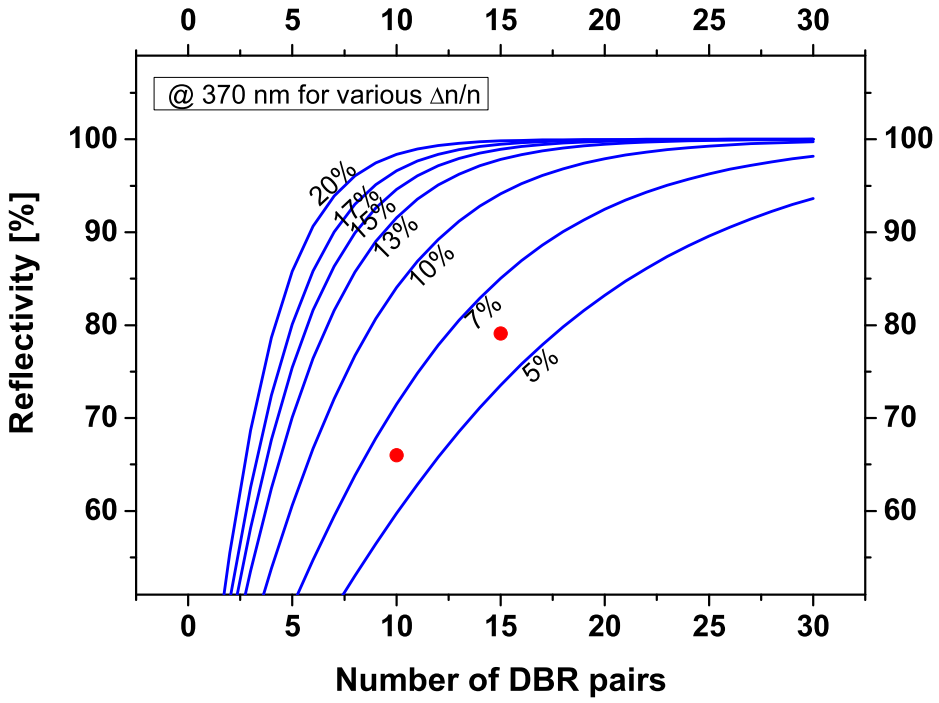

Figure 4.27: Calculated reflectivity vs. DBR pair number for various $\Delta n/n$ (blue curves) and maximum reflectivities of two SL-DBR samples with 10 and 15 DBR pairs (red circles)

4.2.4 Strain State of SL-DBR

To further investigate the strain managing properties of the SL-DBR concept, 10-pair SL-DBR samples were fabricated with increasing SL thickness d_{SL}. The thickness of the SL was increased by raising the number of periods in the SL. In the first SL-DBR sample described above, a 6-fold SL served as the low index layer. To increase d_{SL}, 7- and 8-fold SL were used while the period length in the SL Δ_{SL} was approximately constant for all samples. These samples feature as expected a degraded reflectivity of 67 % for the sample with a 7-fold SL and 55 % for the sample with a 8-fold SL as low-index layers, because the increasing SL thickness does not fulfill the quarter wavelength condition of a DBR. The aim of these samples is solely to investigate the effect of large SL thickness accompanied by an increased overall AlN content in the DBR

on the strain state of the structure. Table 4.2 summarizes the layer thicknesses and effective Al contents of all samples. The SL thicknesses of the samples with 7- and 8-fold SL as low-index layers were determined to 35 nm and 39 nm, respectively. Due to process fluctuations, the sample with the 7-fold SL exhibits a slightly increased AlN content of 27.8 % instead of 26 %. Despite of this fact and the higher SL thickness, the sample shows pseudomorphic growth as depicted in the rsm in figure 4.28. From figure 4.29, it can be seen that even the sample with an 8-fold SL as low index-layer has been grown pseudomorphically.

Sample	d_{SL} [nm]	Δ_{SL} [nm]	x_{Al} [%]
6-fold SL	29	4.55	26
7-fold SL	35	4.81	27.8
8-fold SL	39	4.75	26
more Al (7-fold SL)	33	-	42

Table 4.2: SL-thickness d_{SL}, periodic length of the SL Δ_{SL} and effective Al content x_{Al} of the four samples. It was not possible to evaluate Δ_{SL} for the sample with more Al due to missing Pendellösung oscillations.

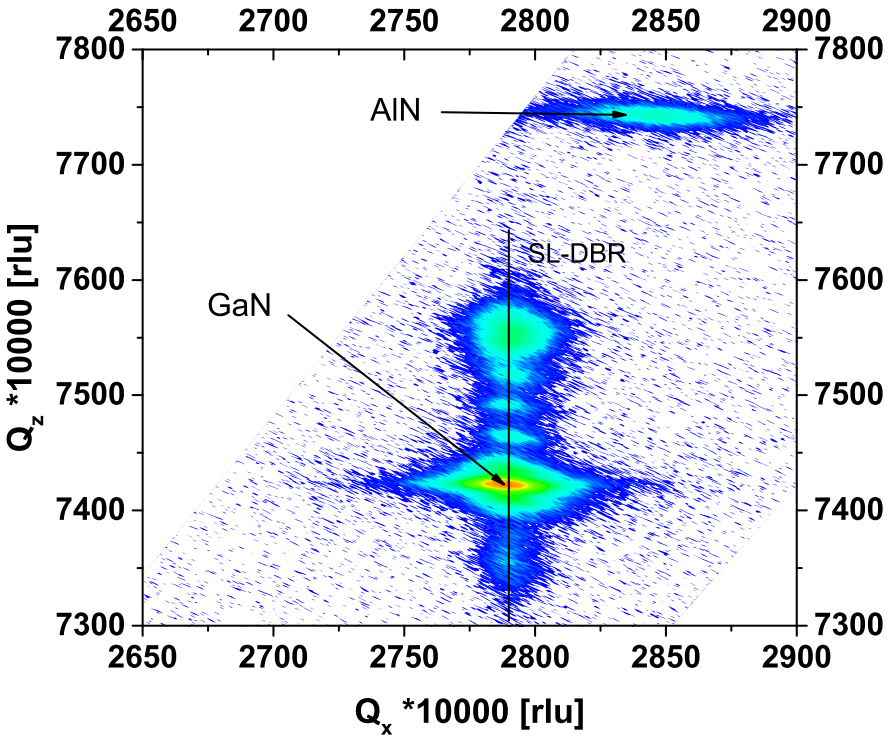

Figure 4.28: $(10\bar{1}5)$ *rsm of the SL-DBR with a 7-fold SL as low-index layer.*

As no relaxation is present in those three samples, an additional SL-DBR ("more Al") with increased AlN content was fabricated. The low-index layer is formed by a 7-fold SL, but the deposition times for the AlN layers in the SL were increased and the ones for GaN reduced. This resulted in a SL thickness around 33 nm and an effective AlN content in the SL layers of approximately 42 %. It was difficult to evaluate the SL thickness and AlN content because

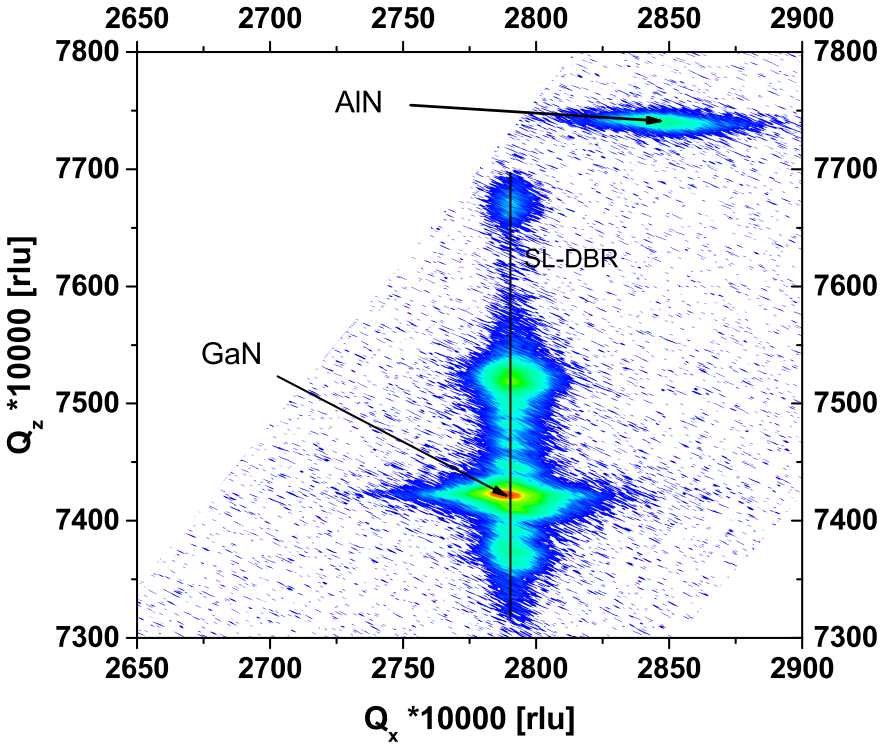

Figure 4.29: $(10\bar{1}5)$ *rsm of the SL-DBR with an 8-fold SL as low-index layer.*

the 2θ-ω-scans of the (0002) reflex did not show very distinct features and was challenging to fit. This is a first hint that relaxation may be present which is affirmed by the rsm obtained from this sample. The scan is depicted in figure 4.30. This sample shows clear relaxation of the SL-DBR stack from the pseudomorphic position at the GaN buffer coordinates towards the lattice parameters of AlN. Therefore the in-plane stress which caused this relaxation process has been of tensile nature. The whole SL-DBR stack, including the GaN layers, seem to relax to smaller a lattice parameters. This implies that all GaN layers in the DBR stack are now compressively strained. In analogy with chapter 3.2, in which the unstrained GaN layers in the SL are supposed to increase the formation energy of cracks, the energy which is necessary to compressively strain the GaN might be able to delay the relaxation process. On the other hand, it also is obvious that for the non-cracked but relaxed SL-DBR, a different relaxation mechanism comes into action compared to that of single SL layers which relaxed by layer cracking only (cmp. chapter 3.2).

The surface of the relaxed sample shows a completely different morphology. The AFM graph belonging to this sample is depicted in figure 4.31. In direct comparison with figure 4.23, it stands out that the surface shows a different step structure. The surface steps are no longer oriented parallel to the substrate offcut and exhibit a more island-like shape. The step edge is not straight but shows a wavy profile. Furthermore, the step heights exhibit a much higher variation. Step heights from 0.256 nm (which correlates with step heights in the afore mentioned pseudomorphic SL-DBR sample) up to 2.42 nm are observed in this measurement.

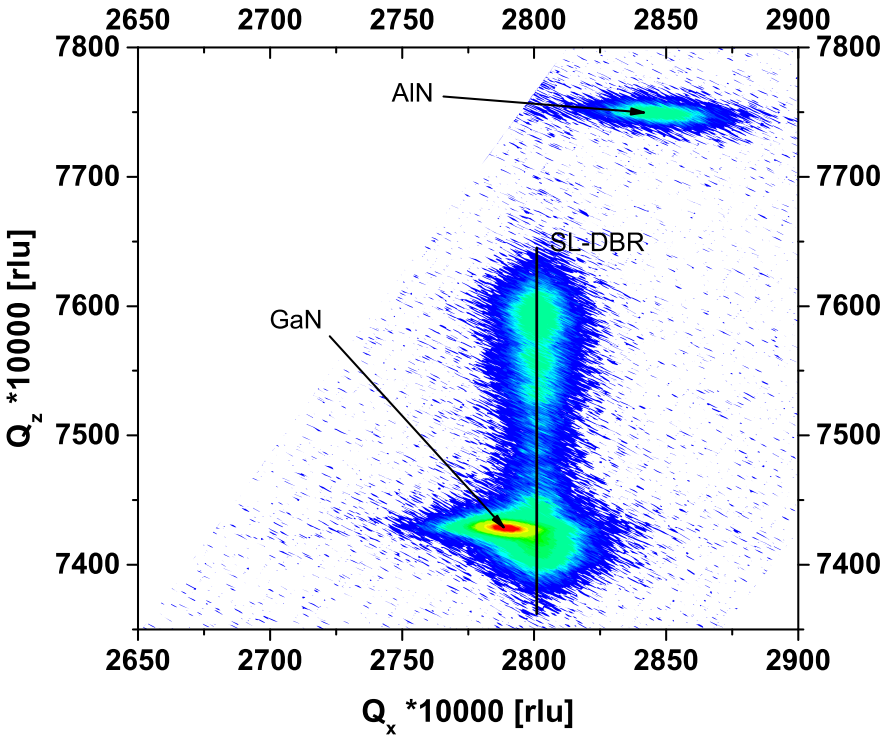

Figure 4.30: $(10\bar{1}5)$ *rsm of a SL-DBR with an enhanced AlN content in the 7-fold low-index SL layers (Q_x values were shifted to correct a measurement error).*

The terrace area is also increased. This sample shows a tendency of accumulating smaller steps into large steps.

Curvature Measurements

Curvature measurements were carried out to further investigate the strain state of SL-DBR samples. The curvature was measured ex-situ with X-ray diffraction. As described in chapter 2.3.1, rocking curves were obtained from several positions on the wafer. Figure 4.32 shows the measurement principle: The sample holder can be rotated in ϕ and translated in x- and y-direction. At $\phi = 0°$, a ψ-scan is carried out to eliminate any misorientation perpendicular to the X-ray beam. Misorientation parallel to the X-ray beam can be neglected because only differences of ω will be used to determine the curvature and not the values itself. Then a rocking curve is measured in the wafer center marked with "0" in figure 4.32. The ω-value of this peak denotes the reference angle for measurements at the current angle ϕ. Now the sample is moved in x-direction to obtain rocking curves at the positions 1, 2, 3 and 4 marked in figure 4.32. As explained in chapter 2.3.1, the ω-values deviate from the value at position 0 for a curved wafer. If the values from position 1 and 2 are larger than the value from position 0 and the values from position 3 and 4 smaller, the wafer exhibits a bowl-like curvature, i.e. a concave shape. If the values from position 1 and 2 are smaller than the value from position 0 and the values from position 3 and 4 larger, the wafer exhibits a mound-like curvature, i. e. a convex form. The

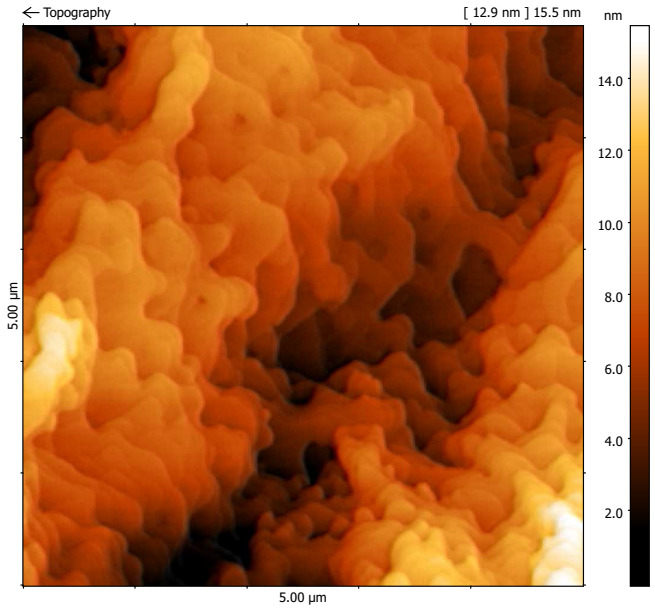

Figure 4.31: AFM graph of the SL-DBR with increased AlN fraction in the low-index SL layer. (An FFT filter was applied to the raw data to exclude parasitic tip oscillations.)

curvature radius R can then be calculated with distance x between the measurement position and the position 0:

$$R = \frac{x}{sin(\omega_i - \omega_0)} \tag{4.10}$$

The vertical displacement of the wafer from a flat surface d_v at position x can be calculated with the follwing formulas:

$$d_v = R + \sqrt{R^2 - x^2} \; for \; convex \; shape \tag{4.11}$$

$$d_v = R - \sqrt{R^2 - x^2} \; for \; concave \; shape \tag{4.12}$$

A non-constant curvature radius is detected by the two measurement points on each side of position 0. This procedure is then repeated for several angles ϕ to detect elliptical or cylindrical wafer curvature. Figure 4.32 also shows the measurement setup for $\phi = 22.5°$. The x- and y-axis are also rotated in ϕ. Therefore, the sample now has to be moved in a combination of x- and y-axis to reach the positions 1, 2, 3, and 4. For the measurements presented here, the curvature was measured at $\phi = 0°, 22.5°, 45°, 67.5°, 90°, 112.5°, 135°$ and $157.5°$ with a spacing of 1 cm between each adjacent position 0 - 4.

Figure 4.33 shows the vertical displacement of the wafer edge in relation to the wafer center. Negative values mean that the wafer edges are lower than the wafer center which denotes a convex curvature. Positive displacement values represent a concave wafer curvature. The wafer flat is always oriented at 180°. For measurement positions 2 and 3, a distance of 10 mm to the wafer center is chosen. Measurement positions 1 and 4 are located 20 mm away from the wafer center. Values in between are interpolated by the contour plot. From this measurement setup results an edge exclusion of 5 mm.

In figure 4.33a, the shape of a sapphire substrate as used for all sample types is shown. The

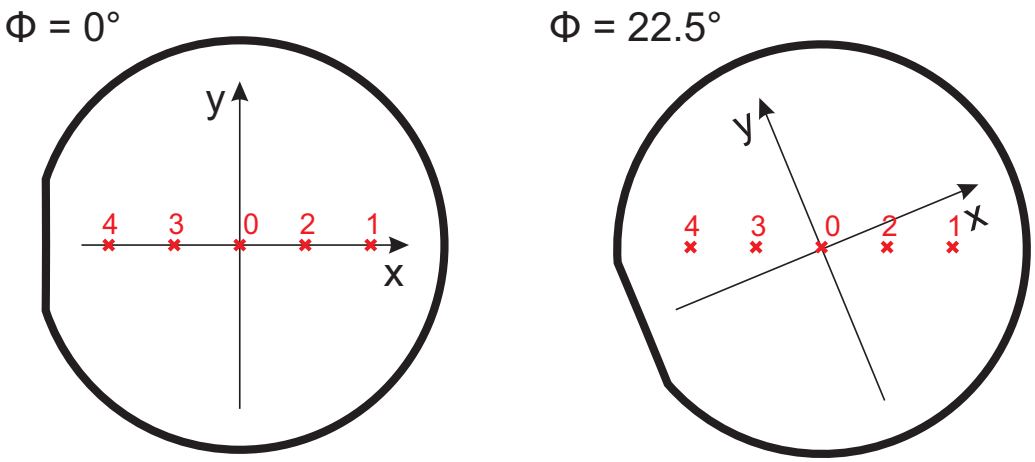

Figure 4.32: Measurement principle to determine the wafer curvature by XRD. Two angles, $\phi = 0°$ and $\phi = 22.5°$, are shown exemplarily.

wafer edge (20 mm from center) shows a very slight displacement of 3.5 μm in comparison to the wafer center. As the specifications of the supplier guarantee bow of less than 10 μm, this value is reasonable. The displacement is also of positive nature, which leads to a concave wafer shape. For a 2-inch wafer, the measured displacement corresponds to an inverse curvature radius of 0.0174 1/m. The substrate curvature is caused by residual stress incorporated during ingot fabrication. After dicing, the stress translates into strain i.e. curvature. It is notable that the curvature is not completely spherical but shows a slight cylindrical shape with an axis of minimum curvature parallel to the wafer flat. Along this axis, the inverse curvature radius is much smaller and denotes $8.29 \cdot 10^{-4}$ 1/m.

The resulting curvature of a GaN buffer deposited on such a sapphire substrate is shown in figure 4.33b. One can directly see that the strain state changed dramatically. The displacement is now negative which denotes a convex wafer shape. The change from concave to convex curvature can be attributed to the compressively stressed GaN buffer which relaxes and strains the sapphire substrate as illustrated in figure 4.34. The maximum displacement is -21.2 μm 20 mm away from the wafer center. This corresponds to a inverse curvature radius of 0.1059 1/m. Again the curvature is not strictly spherical but with cylindrical component. For the GaN buffer, this shape is much more pronounced in comparison to the bare sapphire substrate. The axis of minimum curvature is now aligned approximately perpendicular to the wafer flat (the angular resolution in the measurement was 22.5°) and has an inverse curvature radius of 0.0743 1/m which is smaller than the 0.1059 1/m measured perpendicular to this axis. Nevertheless, the inverse radii are still large compared to the values obtained from the sapphire substrate. The non-spherical part of the curvature has to have a different origin than the one of the sapphire substrate as the direction of minimum curvature changed about 90° which can not be explained by the 30° crystal rotation between sapphire and group III nitrides.

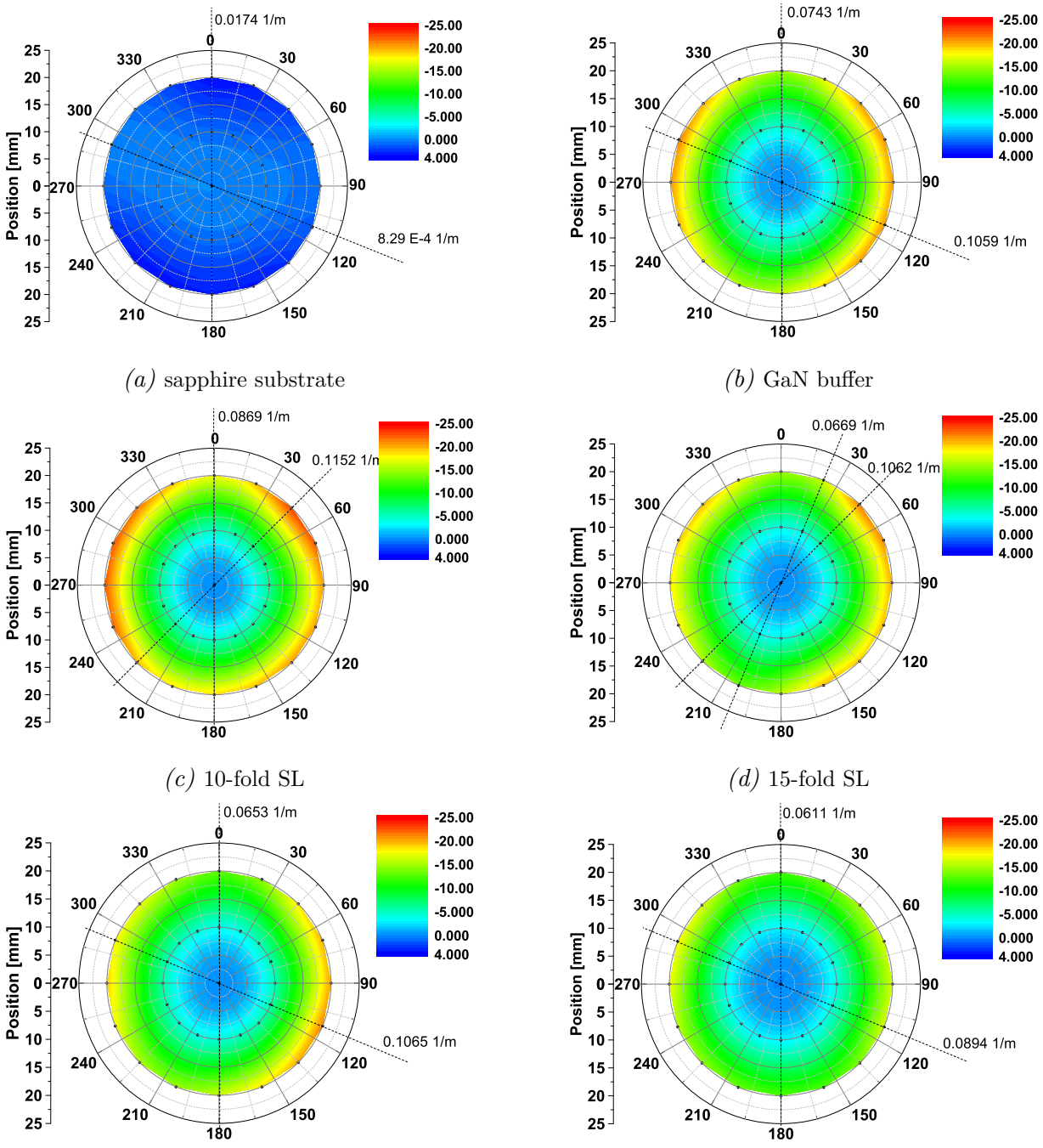

(a) sapphire substrate

(b) GaN buffer

(c) 10-fold SL

(d) 15-fold SL

(e) 23-fold SL

(f) SL-DBR (10 pairs)

Figure 4.33: Displacement of the wafer edge in µm in relation to the wafer center for the sapphire substrate, GaN buffer, SL samples and SL-DBR. Inverse curvature radii are given along the dotted axes. The wafer flat is always oriented at 180°.

According to Moram et al. [43], the curvature deviates from the strictly spherical shape if higher stresses are present due to a trigonal distortion of the elementary cell. This seems to apply for the samples in this measurement. Figure 4.33c shows the curvature data for a 10-fold AlN/GaN-SL. The strain state looks similar to the one of the previously analyzed GaN buffer. The sample also shows convex curvature with a cylindrical component. The axis of minimum curvature is again oriented perpendicular to the wafer flat and exhibits an inverse curvature radius of 0.0869 1/m. The largest inverse curvature radius detected is 0.1152 1/m. This value was detected at 45° and not perpendicular to the axis of minimum curvature but the displacement distribution in figure 4.33c looks similar to that of the investigated GaN buffer (fig. 4.33b). The inverse radii of the 10-fold SL are larger compared to those obtained from the GaN buffer. This is counter-intuitive as the AlN/GaN-SL should introduce tensile strain into the sample as depicted in figure 4.34 on the right. The introduction of the SL in the layer stack would decrease the curvature because it acts against the compressive strain from the underlying GaN buffer. It is difficult to explain this unexpected behavior of the investigated sample as no statistics were collected for theses curvature measurements. Thus, it is impossible to judge if the deviation of curvature between 10-fold SL and GaN buffer is significant or lies well within a typical variation. An analysis of the buffer growth conditions of both samples revealed that the underlying GaN buffer of the 10-fold SL sample was deposited at a $5°C$ lower growth temperature than the GaN buffer sample. This results in an increased buffer layer thickness of 2.315 μm for the 10-fold SL sample. A larger thickness could induce more compressive strain than present in the GaN buffer sample. Even if a part of this larger compressive strain is already compensated by the tensile strain of the 10-fold SL layer on top, the resulting convex curvature might still be larger than the one of the GaN buffer sample. This argumentation is of course highly speculative and a statistical analysis of the curvature of an adequate number of GaN buffer and SL samples would be necessary.

In figure 4.33d, the curvature state of a 15-fold SL sample is depicted. In comparison to the 10-fold SL, the convex curvature looks less pronounced but the cylindrical component is still visible. The axis of minimum curvature is also oriented approximately perpendicular to the wafer flat and shows an inverse curvature radius of 0.0669 1/m. The maximum curvature exhibits an inverse radius of 0.1062 1/m. These values are slightly smaller than the ones of the 10-fold SL sample which can be attributed to the increased tensile strain introduced by the larger SL layer thickness counteracting the convex shape. A 23-fold SL (figure 4.33e) affirms this observation. The inverse radii are very similar as for the 15-fold SL (0.0653 and 0.1065 1/m) while the overall convex shape with a cylindrical component still persists but looks a little less pronounced. This again confirms that an AlN/GaN-SL behaves like an AlGaN alloy being tensily strained on GaN.

Figure 4.33f now shows the curvature of a full SL-DBR with 10 pairs. The curvature is less pronounced compared to the SL samples but the reduction of inversed curvature radii is quite small. The measured inverse radii are 0.0611 and 0.0894 1/m which is in the same order of magnitude as for the SL samples. This result is quite astonishing as the SL-DBR structure

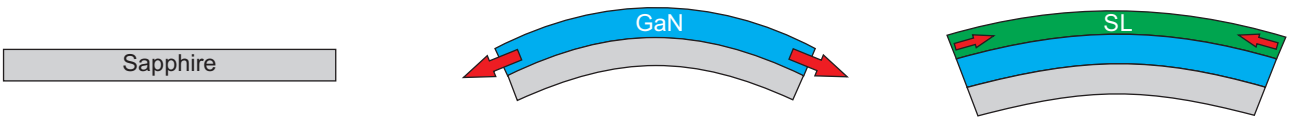

Figure 4.34: Curvature type of the bare sapphire substrate (left), a GaN buffer deposited on sapphire (middle) and a SL/GaN buffer stack on sapphire (right). The AlN nucleation and buffer layers are neglected as they do not change the direction of curvature. The red arrows mark the direction of strain which is caused by the partial relaxation of stress.

contains much more AlN than one SL layer stack. One would expect a much smaller curvature as the sample should be flattened by the tensile strain from the thick SL-DBR stack. As both samples are fully pseudomorphic, the tensile stress from the AlN has to be relieved in a different mechanism than manifesting in strain/curvature. The assumption that the strain leads to different relief mechanisms for a SL-DBR than for an AlN/GaN-SL seems likely.

TEM Analysis

TEM images were obtained from a 10-pair SL-DBR by Frank Heyroth in the group of Prof. Georg Schmidt (Martin-Luther University Halle, Germany) using a Jeol microscope at 200 kV to investigate the layer and structure of the SL-DBR. The TEM sample was prepared parallel to the a-plane $(11\bar{2}0)$. In this way, dislocations with Burgers vectors of $1/3 < 11\bar{2}0 >$ should be visible in the TEM image. TEM images of a 5-fold AlN/GaN-SL were taken by Koji Yoshitsugu in the group of Prof. Uraoka (Nara Institute of Science and Technology, Japan) using a Jeol JEM-3100FEF microscope at 300 kV and a resolution of 0.19 nm. Figure 4.35a shows the layer stack of a SL-DBR. Three AlN/GaN-SL stacks are visible sandwiched between the high-index GaN layers. Every AlN layer (bright) in the SL can be clearly distinguished from the surrounding GaN (dark). This confirms the XRD results in which both periodicities Δ_{DBR} and Δ_{SL} were be observed in (0002) 2θ-ω-scans. Figure 4.35b shows an AlN/GaN-SL in a larger magnification. The atomic planes are visible in this picture. The AlN layers in bright contrast show a very flat and smooth lower interface to GaN (dark), while the upper interface looks irregular. As the growth direction points from bottom to top, this means that the GaN-to-AlN interface is atomically flat and of high quality while the AlN-to-GaN interface exhibits a higher roughness.

The whole layer stack of the 10 pair SL-DBR is depicted in figure 4.36. At the bottom line of the picture, the AlN buffer layer is visible. It shows a large number of TD which in most cases terminate at the AlN-to-GaN interface. Few of the TD propagate through the GaN buffer and reach the SL-DBR structure in the upper region of figure 4.36. As the magnification of this TEM image is lower, only the DBR period is visible. The resolution is too coarse to distinguish the thin AlN and GaN layers within the SL. All TD show a remarkable propagation behavior in the SL-DBR structure. The TD bend when they reach the SL-DBR. The magnified inset in figure 4.36 shows a TD bending into the in-plane direction at the GaN buffer/SL interface. The TD then moves parallel to the interface for approximately 150 nm and finally kinks back into the c-direction. After that, the TD propagates through the AlN/GaN-SL and the top GaN

high-index layer of the DBR without further kinking. At the next interface, which is again a GaN-to-SL interface, the process is repeated. As a result, the TD moves in a staircase pattern through the DBR structure which results in an effective inclination angle. It can be observed that all dislocations bend when they reach the SL-DBR region. Some are redirected into a flatter, others into a steeper effective inclination angle. In general, two inclination angles can be observed in figure 4.36. The TD either incline 30° or 60° to the left or right. For the TD inclining only 30° away from the c-direction, the propagation length parallel to the interfaces looks shorter. This can be explained by the crystallographically equivalent directions in the wurtzite lattice and even allows to identify the crystallographic direction into which the TD bend:

Figure 4.37 depicts a hexagonal lattice in a top view on the left. In this graph, the c-plane is parallel to the paper plane and the a-plane is perpendicular. If now a TD propagates in c-direction (out of the paper plane) and bends at the GaN-SL interface into the $< 11\bar{2}0 >$ directions, there are six crystallographically equivalent directions marked with blue arrows. If now a side view (fig. 4.37 right) of this constellation in the intersecting a-plane is considered, as it is prepared in the TEM image, two of the inclination directions (marked with thin blue arrows) would result in disappearing TD because the TD inclines out of the prepared TEM specimen. The other four directions (marked with thick blue arrows) would result in a TD inclined to the left or right side at one specific angle. This constellation does not lead to the observed result (all TD inclined, two characteristic angles). The observed inclination pattern is only realized if the TD are assumed to incline into the $< 1\bar{1}00 >$ directions marked with green arrows. Now the thin green arrows mark bend directions which result in a larger inclination angle projection in the side view and the thick green arrows mark bend directions resulting in a smaller inclination angle projection in the side view. In this way, the TEM image only shows the a-plane projection of the real in-plane propagation lengths which is different for the various crystallographically equivalent $< 1\bar{1}00 >$ directions (compare thin and thick green arrows). Other directions than $< 11\bar{2}0 >$ or $< 1\bar{1}00 >$ would result in three different inclination angle projections. In conclusion, it can be derived that the TD bend from the $< 0001 >$ direction into the $< 1\bar{1}00 >$ directions when reaching a SL layer.

Chapter 2.1.3 explains that a bending of TD can relax in-plane strain according to the Romanov-Speck model. This may also be true for the TD in the SL-DBR samples and would explain the lack of difference in strain state between a single SL layer (23-fold) and a full SL-DBR stack as observed with the curvature measurements discussed above. In chapter 3.2, the major relaxation mechanism of AlN/GaN-SL layers was identified to be layer cracking. This obviously did not occur for the SL-DBR samples so the staircase movement of TD is a promising candidate to explain why SL-DBR growth does not accumulate additional strain in the layers. In contrast to the before mentioned Romanov-Speck model (cmp. chapter 2.1.3), in which the dislocations incline at a constant angle to relieve in-plane strain, the SL-DBR samples show a staircase movement. The TD either moves perpendicular or parallel to the interfaces which leads to the effective inclination angles described above.

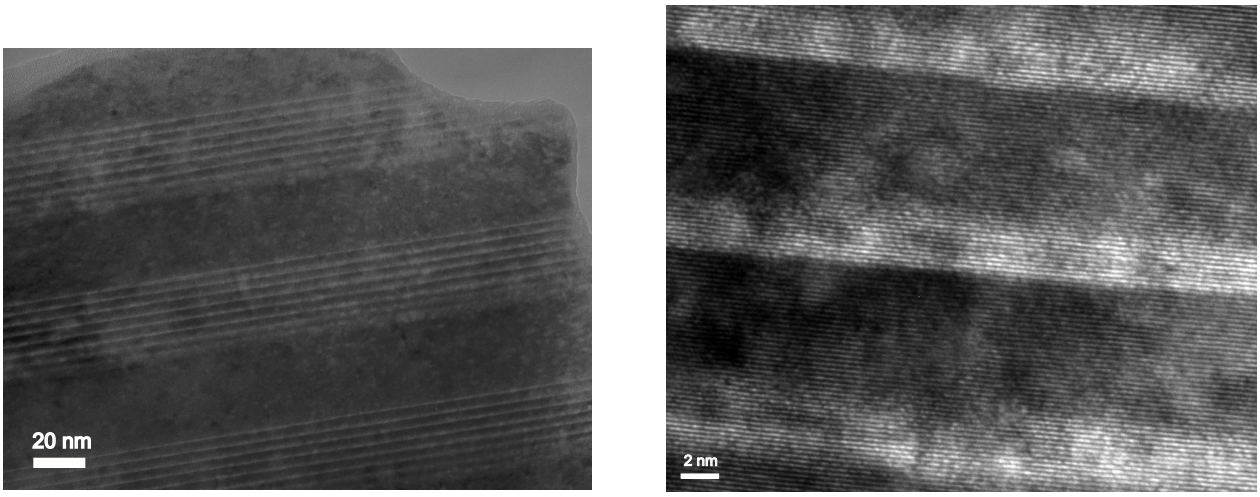

(a) (b)

Figure 4.35: Left: TEM image of a SL-DBR. The quarter wavelength layers of GaN (high-index) and AlN/GaN-SL (low-index) are clearly visible (Heyroth et al.). Right: TEM image of the AlN/GaN-SL (Yoshitsugu et al.).

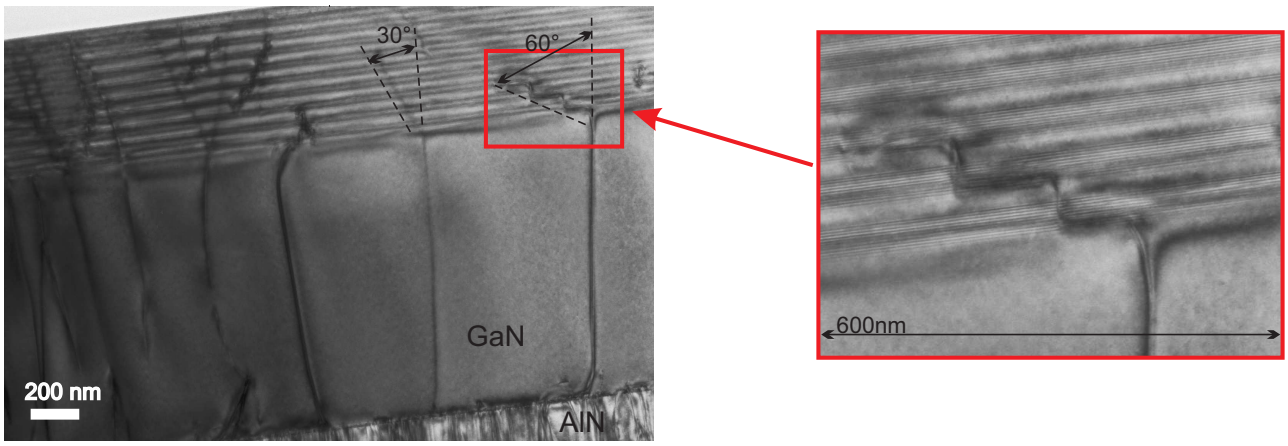

Figure 4.36: TEM image of the complete 10 pair SL-DBR stack (Heyroth et al.) with marked bend angles.

A staircase movement was already observed by Cherns et al. [68] for AlGaN/GaN MQW. But in their samples, the AlGaN/GaN MQW was deposited on an AlGaN buffer layer which means that the AlGaN in the MQW was lightly tensily strained and the GaN in the MQW exhibited compressive strain. Also the staircase pattern occurred on a much smaller scale. The AlGaN layers had a thickness of 10.5 nm and the GaN layer thickness was varied between 1.5 and 3.5 nm. In agreement with the previously gained findings here, the in-plane direction in which the TD bend was identified to be $< 1\bar{1}00 >$ for the samples from Cherns et al. The group also identified climb as the mechanism with which the TD are able to leave the c-direction because no appropriate slip system exists for TD with $\mathbf{b} = 1/3 < 11\bar{2}0 >$. The compressive strain is relieved by the TD climb because the inserted half plane associated with the TD is reduced in its extent. For TD propagating in c-direction, the additional half plane is inserted on one side of the dislocation line. If the TD bends into the in-plane direction, the half plane is then either below or above the dislocation line. If this happens at a heterointerface, it implies that either the layer below or the layer above the TD contains an additional half plane of

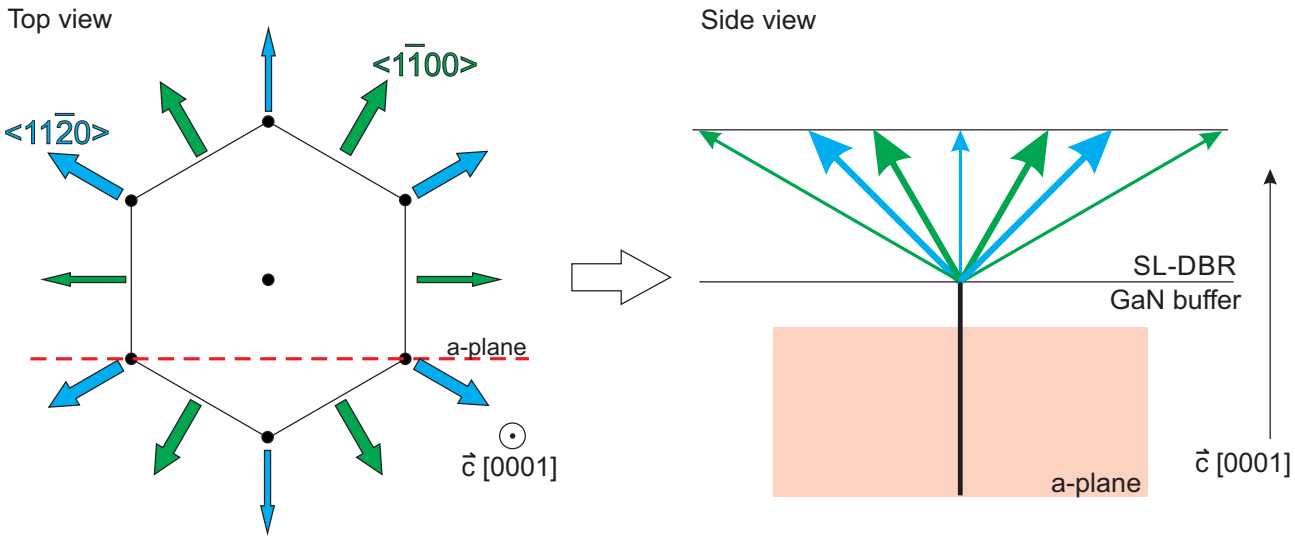

Figure 4.37: Possible bend directions in a hexagonal lattice (left) and the resulting side view (right). Crystallographically equivalent directions are marked in the same color.

atoms. It is evident that this additional half plane can accommodate lattice mismatch at least partially. The mechanism for compressive strain relief is depicted in figure 4.38 on the left. Figure 4.38*a* shows an unbent TD in a compressively strained AlGaN/GaN-MQW. The half plane of the TD is depicted on the left of the dislocation line. When this is compared to figure 4.38*b*, it can be seen that the staircase pattern of the TD reduces the extent of the dislocation half plane, which in turn relieves compressive strain in the MQW. It must be noted that figures 4.38*a* and *b* cannot represent the same sample before and after the relaxation process. The staircase pattern of the TD already evolves during the MQW growth. Figure 4.38*a* is only given for comparison with 4.38*b* and can be considered as a similar sample with slightly lesser strain in the MQW which still allows relaxation-free growth.

To release compressive strain in GaN, as it is the case for the samples from Cherns et al., the additional half plane is located below the dislocation line. This means that the inserted half plane does not extend into the compressively strained GaN and acts like a MD. As this process is driven by climb, which is diffusion-based, it can only take place at sufficiently high temperatures in close proximity to the growth front which denotes a reservoir for the atom species diffusing to and away from the TD. Farther away from the growing surface, the TD freezes and becomes immobile due to the lack of supply of diffusing atoms and suitable slip systems. This also limits the in-plane propagation length of the TD: During the in-plane propagation of the TD, the sample is still growing in c-direction which moves the growth surface away from the in-plane segment of the TD. This process slows down the in-plane propagation until it finally stops and can only be continued at interfaces closer to the growth surface. As a result, a staircase pattern evolves.

A diffusion-based process also implies that it does not necessarily have to take place in the moment in which the considered volume solidifies from the gas phase. The bending of TD can also rearrange after the growth front already moved on a little. This allows the bending also to occur even if the individual strained layers do not exceed the critical thickness. After some

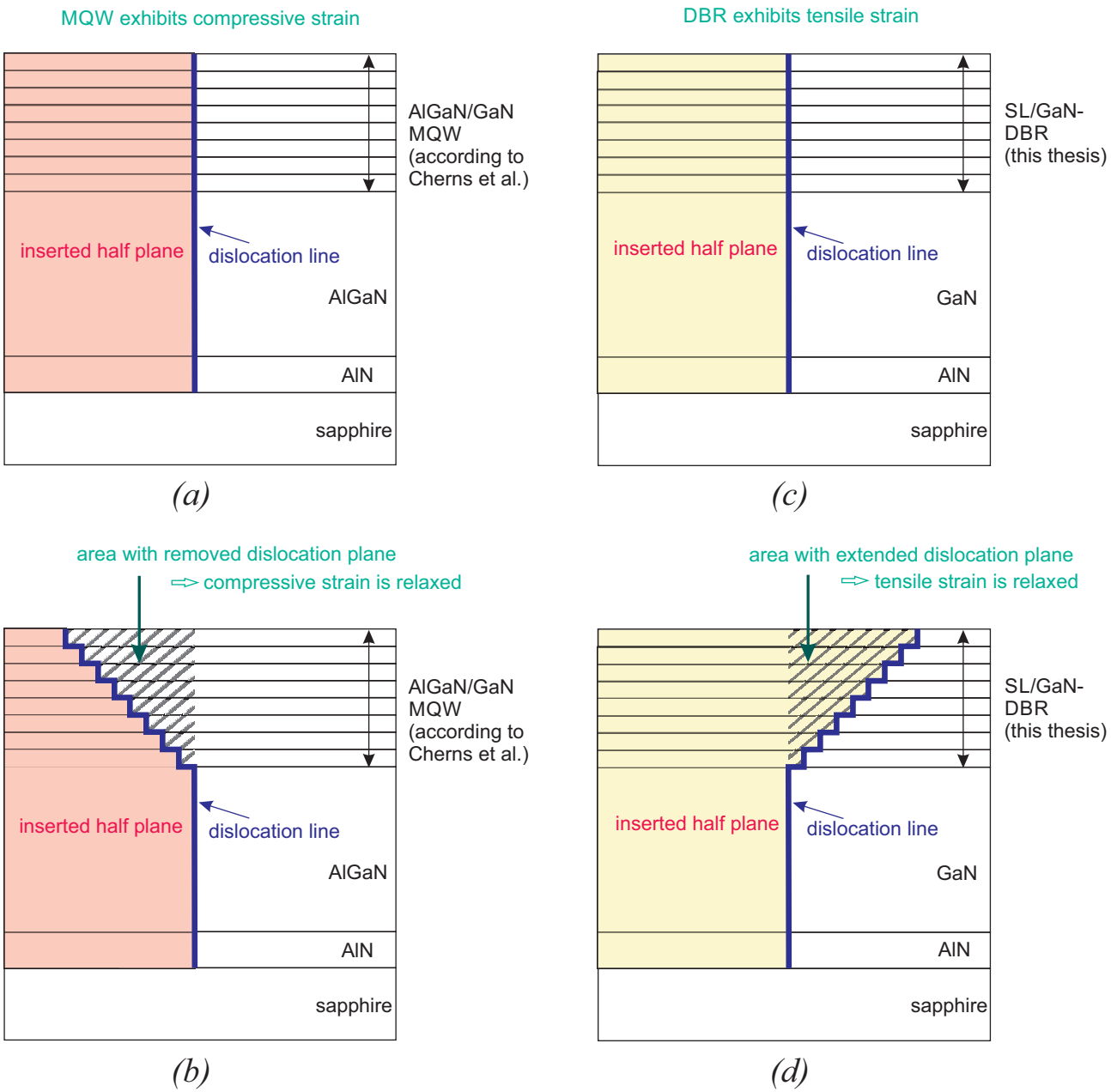

Figure 4.38: Schematic drawing of relaxation process via dislocation climb for compressive (b) and tensile strain (d) compared to samples with no dislocation climb present ((a) and (c)).

of the strained layers (for the work of Cherns et al., these are the compressively strained GaN layers) are deposited, their strain can add and facilitate the bending of TD [68]. Due to its diffusion-based nature, the bending process might be influenced by the growth temperature and the growth rate (determines how fast the surface moves away from the interface at which TD bending happens). The staircase pattern leads to the fact that only a small volume fraction in the SL-DBR is actually partly relaxed, namely the small part below every horizontal section of a TD. This seems to be sufficient to hinder crack formation in the structure. On the other hand, the volume seems to be small enough to not influence the rsm, according to which the strain state is fully pseudomorphic.

In contrast to the results from Cherns et al., the SL-DBR samples investigated here are tensily strained. But the relaxation mechanism seems also be able to relax tensile strain as depicted on the right side of figure 4.38. In this case, the additional half plane is located in the layer above the bent dislocation line. For the SL-DBR samples, this is the tensily strained AlN/GaN-SL. With the evolving staircase pattern of the TD, the half plane extends (cmp. figs. 4.38*c* and 4.38*d*) and the additional atoms act as a misfit segment relaxing the tensily strained SL.

Still the question remains why for the compressively strained AlGaN/GaN MQW from Cherns et al., the TD bend between the thin layers of the MQW and for the samples discussed here, bending only occurs on the larger quarter wavelength scale of the DBR and not on the one of the AlN/GaN-SL. The energy barrier to force the TD into the in-plane direction at every AlN/GaN interface in the SL apparently cannot be overcome. This could either be due to a higher energy barrier for the AlN/GaN-SL in comparison to the AlGaN/GaN MQW or lesser strain in the SL. The latter does not seem very likely as in these samples pure AlN is deposited on GaN whereas Cherns et al. used GaN on $Al_{0.50}Ga_{0.50}N$. This results in a less pronounced lattice mismatch while the layer thicknesses of the strained layers were comparable. It leads to the possibility of a higher energy barrier for the diffusion-based climb process of the SL-DBR samples and only the accumulated strain of a whole SL quarter wavelength layer would be able to force the TD into the in-plane direction. This could originate from different self-diffusion coefficients in GaN and AlN. Up to now, no comparable data of self-diffusion coefficients could be found for these materials. Ambacher et al. investigated the self-diffusion of GaN [122] and concluded that the diffusion is dominated by nitrogen vacancy diffusion and the breaking of the Ga-to-N bond. As the bond strength of Al-to-N is higher ($E_B = 2.88\ eV$ [2]) than that of the Ga-to-N bond ($E_B = 2.20\ eV$ [2]), this should result in a lower diffusivity of nitrogen in AlN than in GaN. This could lead to a higher energy barrier for TD bending if the additional half plane has to extend into the AlN-containing AlN/GaN-SL. This explanation is, of course, highly speculative and further research should be focused on this issue in order to improve the interface quality of the AlN/GaN-SL. With experiments like the introduction of growth interruptions and the use of higher or lower growth rates in combination with a TEM analysis the dislocation bending could be investigated more thoroughly.

4.2.5 Aspects of Growth Rate Scaling for SL-DBR Fabrication

In chapter 3.1, the influence of the growth rate on the structural properties of AlN/GaN-SL was examined. This chapter will investigate if the results from AlN/GaN-SL regarding the growth rate are applicable to SL-DBR structures. The standard growth conditions require growth times around one minute for every GaN or AlN layer in the SL. These times are added according to the targeted layer thickness of the SL low-index layer. The growth time of the high-index GaN layer also scales with the chosen growth conditions as they are the same for high-index GaN and low-index SL. In summary, growth times around 30 minutes per DBR pair are reached if stopband wavelengths in the blue to green spectral region are chosen. This is quite long as about 30 to 40 DBR pairs are necessary if a reflectivity greater than 99 % is required. In this manner, any growth time reduction is an advantage for SL-DBR fabrication, especially if an industrial production is envisioned.

The two highest precursor flows from chapter 3.1 were tested in 10-pair SL-DBR stacks. The first DBR was deposited using a V/III ratio of 1130 (GaN) and 1310 (AlN). This is realized by increasing the TMAl and TMGa flows from 24 sccm and 6 sccm (reference sample, 24/6) to 39 sccm and 9 sccm (sample 39/9). The growth conditions of all samples are summarized in table 4.3. The growth time for one DBR pair was reduced to 20 minutes at theses conditions. A second DBR was fabricated using V/III ratios of 1020 (GaN) and 1220 (AlN) which are realized by 42 sccm TMAl and 10 sccm TMGa flow (sample 42/10). At these precursor flows, the growth time of one DBR pair was further reduced to 17 minutes. Both samples were successfully fabricated without any visible surface cracks. The sample with 42 sccm and 10 sccm even reached a record reflectivity of 79.5 % for a 10-pair DBR (not shown here).

Sample	TMAl flow [sccm]	TMGa flow [sccm]	t_{growth} [s/DBR pair]	$x_{AlN}(SL)$ [%]
24/6	24	6	30	26
39/9	39	9	20	35
42/10	42	10	17	41

Table 4.3: group III precursor flows, growth times per DBR pair and AlN content in the SL for the three samples discussed in this chapter.

To judge the crystal and interface quality of the SL-DBR at higher growth rates, 2θ-ω scans are utilized in analogy with the analysis of SL in chapter 3.1. Figure 4.39 shows the (0002) 2θ-ω-scans of the two DBR samples (39/9: red and 42/10: blue) and a reference SL-DBR deposited at standard conditions (24/6: black). Higher-order peaks are visible for both increased growth rates to the same extent as for the reference sample. The scans show comparable intensities of SL-DBR peaks in relation to the GaN and AlN peaks. From that, it can be concluded that the crystal quality and interface roughness of the SL-DBR are not hampered by the increased growth rates as this would manifest in a decreased diffraction intensity. Due to the increased growth rates, the growth times of the individual layers in the SL become very short (around 20 seconds) which makes it even more challenging to adjust the epitaxial recipe to precisely obtain the required layer thicknesses. In the case of the discussed samples, the GaN layer

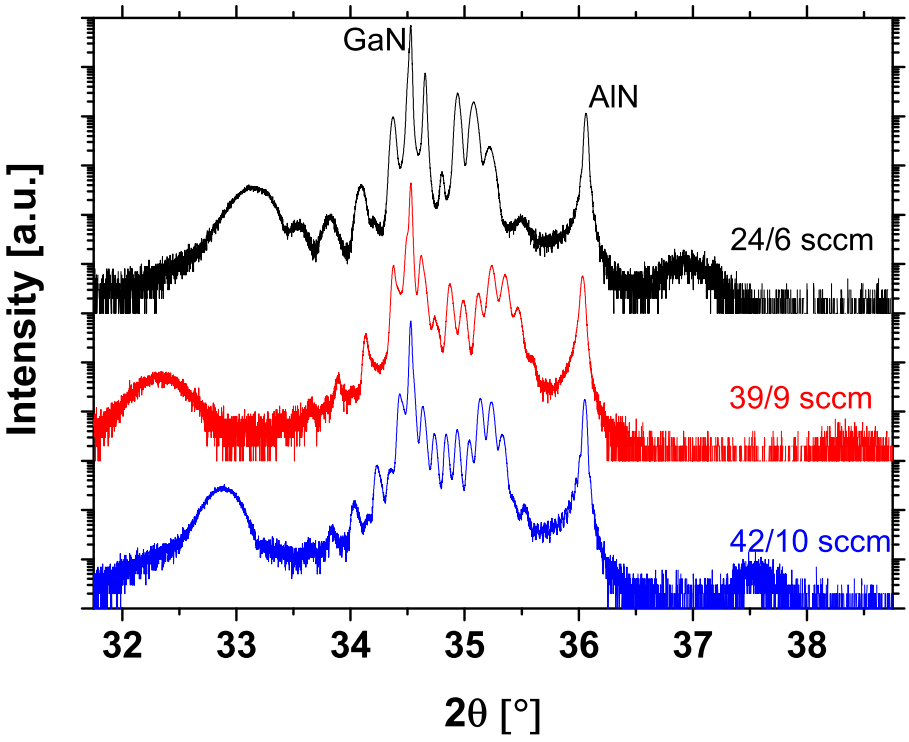

Figure 4.39: (0002) 2θ-ω-scan of 10-pair SL-DBR structures. The flows during DBR growth were 39 sccm for AlN and 9 sccm for GaN (red curve) and 42 sccm for AlN and 10 sccm for GaN (blue curve). As a reference, the black curve shows the 2θ-ω-scan of a SL-DBR deposited at standard conditions (24/6). The three curves are displaced vertically for clarification.

thickness in the SL was targeted to around 3 nm but only 2.7 nm (39/9 sccm) and 1.9 nm (42/10 sccm) were realized. This manifests in an increased effective Al content of SL and also the whole SL-DBR structure. While the reference SL-DBR (24/6) contains 26 % AlN in the SL, the samples with enhanced growth rates exhibit AlN concentrations in the SL of 35 % (39/9 sccm) and 41 % (42/10 sccm). The recipe design of all samples in this thesis relies on the assumption that the layer thickness scales approximately linearly with growth time, i.e. that the growth rate is constant during layer growth. From the deviation in layer thicknesses, it can be concluded that this might not be true for the initial stages of growth and could cause thickness deviations for very thin layers deposited at very high growth rates (e.g. sample 39/9 and 42/10).

Rsm are collected from the samples to analyze the strain state of the SL-DBR with higher growth rates. Figure 4.40 shows the $(10\bar{1}5)$ rsm of the sample 39/9. The vertical line marks the Q_x position of the SL-DBR stack. A slight displacement of the SL-DBR peaks to the right side of the GaN buffer peak can be observed. If the a-lattice parameters of GaN buffer and SL-DBR stack are compared for this sample, only a minute deviation can be detected: The SL-DBR stack exhibits an a-lattice parameter of 0.31922 nm and the GaN buffer 0.31955 nm. This deviation is so small that the sample might even be termed as pseudomorphic because the measurement error for lattice parameters with HR-XRD is in the range of the deviation. Because the $(20\bar{2}4)$ rsm was also analyzed and yielded the same deviation, a very small amount of relaxation seems

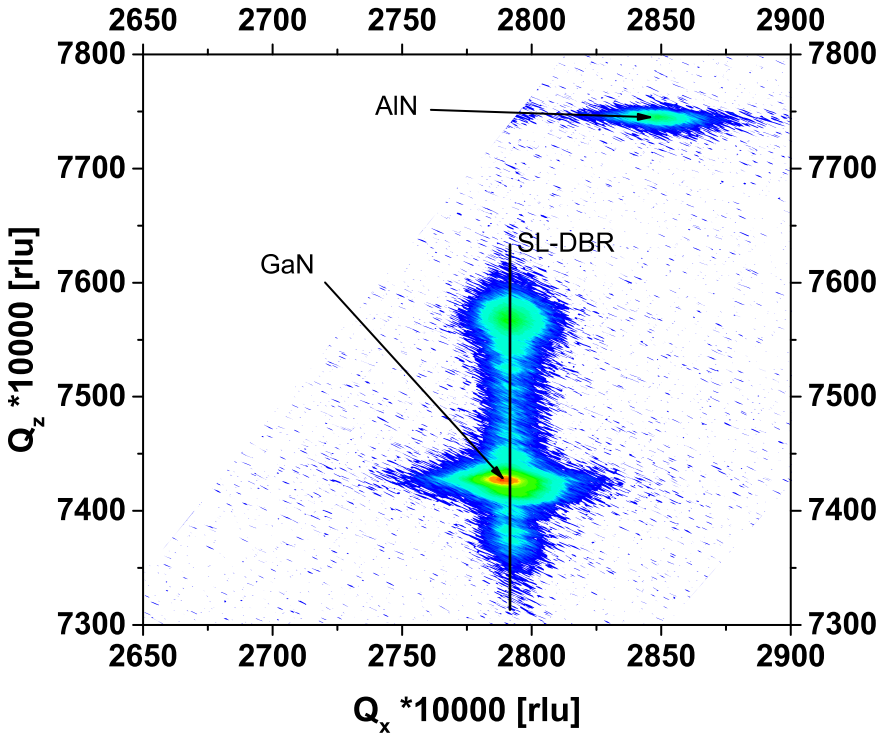

Figure 4.40: $(10\bar{1}5)$ *rsm of a 10-pair SL-DBR growth with 39 sccm (AlN) and 9 sccm (GaN). The vertical line marks the* Q_x *coordinate of the SL-DBR stack.*

to be present in sample 39/9 in contrast to the SL-DBR deposited at standard growth rates (24/6). The $(10\bar{1}5)$ rsm of the SL-DBR with the highest growth rates (42/10) is shown in figure 4.41. The vertical line again marks the Q_x coordinate of the DBR stack. This sample shows clear relaxation. The lattice parameters of GaN buffer and SL-DBR were extracted and are 0.31762 nm for the SL-DBR and 0.31842 nm for the underlying GaN buffer. These values deviate more strongly than for the previous sample indicating a higher degree of relaxation. A more detailed analysis of the relaxation mechanism including further TEM studies would be very interesting as the last chapter clarified that the strain management of the SL-DBR relies on the diffusion-based TD bending and that this process should be influenced by the growth rate. This is of great interest as it might in this way be possible to control the relaxation process via the growth rate. In summary, it can be stated that the deposition of SL-DBR at higher growth rates is possible without compromising the crystal and interface quality. For precise process control, it is necessary to further investigate growth rates during the initial stages of layer growth.

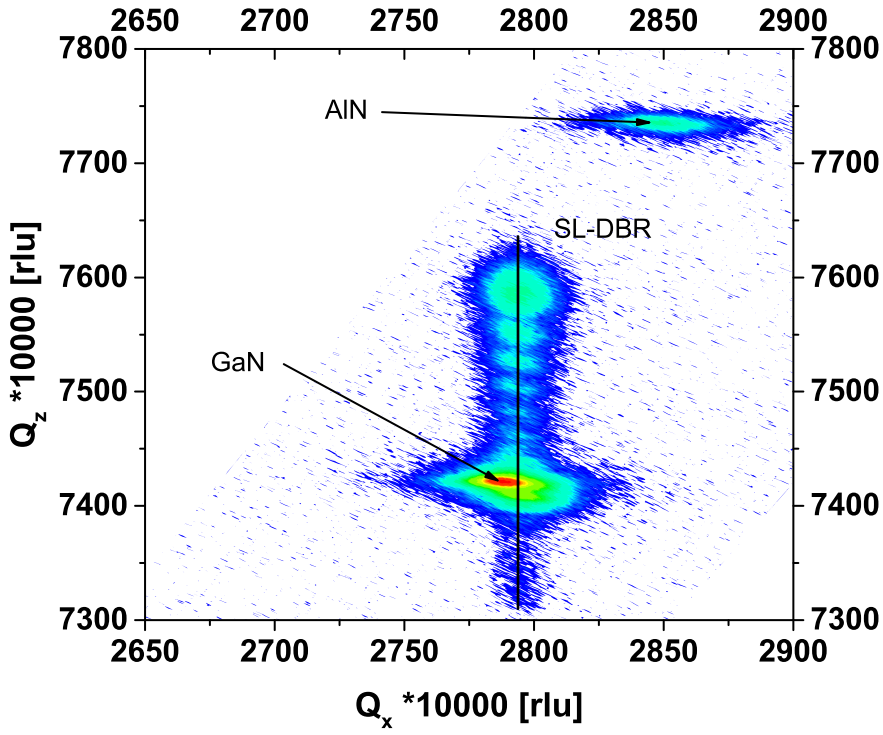

Figure 4.41: $(10\bar{1}5)$ *rsm of a 10-pair SL-DBR growth with 42 sccm (AlN) and 10 sccm (GaN). The vertical line marks the* Q_x *coordinate of the SL-DBR stack.* Q_x *values were modified to exclude measurement errors.*

4.3 Electro-optic Modulator Concept TuneDBR Based on SL-DBR

In the previous chapters, the concept of the SL-DBR which relies on the optical properties of the AlN/GaN-SL was elucidated. A possible influence of 2DEG on the optical properties of SL was found in chapter 4.2.3 in which a deviation of the refractive index and phase shift was presumed to explain the measured data. Chapter 4.1 presented the SL-HEMT. This device is based upon the electrical properties of 2DEG forming in AlN/GaN-SL. The current chapter now investigates the interplay of optical and electrical properties of AlN/GaN-SL and will introduce a novel electro-optic modulator based on AlN/GaN-SL called TuneDBR. The TuneDBR concept was invented by Ada Wille and Holger Kalisch at GaN Device Technology (RWTH Aachen University) and elected suitable for patenting by RWTH Aachen University. The German patent is pending ("Steuerbarer Bragg-Reflektor", Aktenzeichen: 10 2015 107 239.4, Dokumenten Referenz-Nr.: 2015050815272700DE8) with the priority date May 8th, 2015. In May, 2016, RWTH Aachen University decided to support a PCT application which is already submitted.

4.3.1 Working Principle of the Electro-Optic Modulator

Chapter 4.1 clarified that the thin AlN layer, which is part of the AlN/GaN-SL, is sufficient to induce 2DEG at every GaN-to-AlN heterointerface in the SL. These 2DEG were successfully implemented in multichannel transistors. Via the gate contact, it was possible to control the carrier concentration in the parallel configuration of multiple channels with frequencies up to 38.4 GHz (f_{max} for triple-channel device, cmp. fig. 4.13). All this still holds true if the SL is instead implemented in DBR. The depletion and accumulation of carriers in the 2DEG can be used to directly modulate the dielectric and optical properties of the SL as follows: If a single AlN/GaN-SL quarter wavelength layer in a SL-DBR is considered, every GaN-to-AlN interface poses a heterojunction at which a 2DEG can be formed. This implies that an AlN/GaN-SL contains free electrons. In the SL, the free electrons are confined into multiple, parallel 2DEG which translates the primarily 2D carrier concentration of a single GaN/AlN heterojunction into a quasi three-dimensional structure. By the systematic application of an electric field to the structure, the carrier concentration in the SL can be changed. The structure can be depleted or additional electrons can be accumulated in the SL. The changing carrier concentration in the multiple 2DEG structure affects the dielectric and optical properties (i.e. the refractive index) of the SL layer. This effect can be used to design a fast electro-optical modulator which can be implemented in a conventional DBR to switch the reflectivity (TuneDBR). This modulation principle is only limited by the RF properties of the system and no current flow in the structure is necessary. This enables ultra-fast and powerless electro-optic modulation.

In the following, a detailed explanation will be given how the changing carrier concentration can affect the dielectric and optical properties of a material. As this happens via several mechanisms, a general introduction to the topic will be given before the individual effects

of the changed carrier concentration are explained subsequently. The dielectric and optical properties are mainly determined by the complex dielectric function $\underline{\varepsilon}(\omega) = \varepsilon_1 + j\varepsilon_2$ of the material. This is a complex function consisting of the real and imaginary parts ε_1 and ε_2. The real and imaginary parts are connected via the Kramers-Kronig relations [61]:

$$\varepsilon_1(\omega) = \frac{1}{\pi}\mathcal{P}\int_{-\infty}^{\infty}\frac{\varepsilon_2(\omega')}{\omega' - \omega}d\omega' \tag{4.13}$$

and

$$\varepsilon_2(\omega) = -\frac{1}{\pi}\mathcal{P}\int_{-\infty}^{\infty}\frac{\varepsilon_1(\omega')}{\omega' - \omega}d\omega' \tag{4.14}$$

The integral over the whole frequency range in the formula is very important if the refractive index change, resulting from a change of the complex dielectric function, is considered. If a resonance at a certain frequency changes or vanishes from the dielectric function, both ε_1 and ε_2 are directly affected at this wavelength position of the spectrum. In addition to that, it follows from the Kramers-Kronig relation that a change of ε_1 at a specific frequency leads to a change of ε_2 for all values of ω and vice versa. This also means that the refractive index $\underline{n} = \sqrt{\underline{\varepsilon}(\omega)}$ is changed for the whole frequency range ω if a feature at a specific wavelength vanishes from the dielectric function. Therefore one has not only to consider effects which occur at frequencies in the spectral range of interest but also the effects at higher or lower frequencies. One of these effects is the change of the plasma resonance ω_p of the electrons which is generally in the infrared regime [123] If the carrier concentration N changes, the plasma resonance ω_p of the electrons is altered according to [61]:

$$\omega_p = \sqrt{\frac{Ne^2}{\varepsilon_0 m^*}} \tag{4.15}$$

with the elementary charge e, the vacuum permittivity ε_0 and the effective electron mass m^*. This also changes $\underline{\varepsilon}(\omega)$ and the resulting refractive index over the whole spectrum. If the spectral range of interest is considered in the near UV and visible spectrum, special attention has to be paid to effects concerning excitons close to the band gap energy for GaN-based devices. Excitons can interact with free carriers and create mixed states of excitons and carriers. Due to the fact that the carriers are confined into 2DEG, a quantization similar to an multi quantum well (MQW) structure occurs. In such structures, the wave function of excitons can be understood as a linear superposition of the eigenfunctions of all free carrier states. If the free carrier concentration increases, some of these states are occupied by free carriers and the eigenfunctions of theses states do not any longer contribute to the exciton wave function, which alters the exciton energy and therefore the dielectric function $\underline{\varepsilon}(\omega)$ [124].

For higher carrier concentrations, the dielectric function is also changed due to the quantum confined Stark effect (QCSE) and its effect on the band gap energy [104]. In the tilted quantum wells formed in the nitride SL, electrons and holes are spatially separated which reduces the

effective transition energy and the wavefunction overlap of electrons and holes. If an electric field is applied to the structure, this tilting can be compensated or enhanced depending on the direction of the electric field. For a compensated tilt, the transition energy and the overlap become higher. This is caused by the flat band edges in the quantum wells which blue-shifts the absorption edge. If the tilting is increased, the transition energy becomes even smaller, resulting in a red-shift of the absorption edge. At high carrier concentrations, the QCSE can be weakened by the electric field generated by the carriers in the quantum wells which counteracts the original electric field [125].

If the carrier concentration is even further increased, the average spacing of excitons can become smaller than the exciton radius. This tipping point is called the Mott density and the excitons dissociate into an electron-hole plasma. At this point, the exciton resonances vanish from the dielectric function and the electron-hole plasma resonance appears. This resonance also depends on the carrier concentration and is given by a formula similar to equation 4.15 but with the combined reduced effective mass of electron and hole instead of the reduced effective electron mass m^*. As the electron-hole plasma is lower in energy than the excitons, this resonance is likely to occur at lower frequencies [104]. For indirect semiconductors, a condensation of the electron-hole plasma into an electron-hole liquid can be observed which again changes the dielectric function but for direct semiconductors like GaN and AlN, this is unlikely to occur as carrier lifetimes are very short [104]. The origin of the exciton dissociation differs slightly for two-dimensional systems compared to conventional 3D systems. In the latter ones, exciton dissociation is dominated by Coulomb screening. In 2D systems, phase space filling dominates as electrical field lines threading through the barrier layers cannot be screened which makes Coulomb screening less effective. This can lead to the fact that not all exciton resonances vanish from the dielectric function at the same carrier concentration [104].

At very high carrier concentrations, the Burstein-Moss shift (BMS) comes into action. The semiconductor degenerates and an energy higher than the bang gap energy is needed to excite carriers from the valence band. This blue-shift of the band gap energy again relates to a change in the dielectric function [126], [127]. Bandgap renormalization (BGR) is also present and creates a red shift of the band gap energy via exchange interaction of electrons [128]. In 2D quantum well systems, bandgap renormalization is of less importance as the carriers are distributed into several subbands and the exchange interaction only occurs for carriers in the same subband [104].

The variety of effects related to an increase in carrier concentration make it very difficult to predict the actual change of the refractive index for a specific material which makes an experimental investigation necessary. Feneberg et al. showed that the imaginary part of the dielectric function of n-doped GaN is strongly influenced near the band edge by an increasing carrier concentration [128]. These results are very promising for the TuneDBR concept but a comparison with AlN/GaN-SL is difficult, as the carriers in the samples investigated by Feneberg et al. are not created by polarization but by dopands which can deteriorate crystal quality at high doping concentrations. This point is mentioned as a possible explanation for

the broadening of features in the dielectric function observed by Feneberg et al. Also the dimensionality of the carrier systems is different. This is of special importance because Feneberg et al. concluded the BGR to compensate the BMS up to carrier concentrations of $9 \cdot 10^{18}\ cm^{-3}$. If, for the samples discussed in this thesis, the BGR is reduced due to the lowered dimensionality of the 2DEGs as indicated in reference [104], the onset of the BMS might occur already at lower carrier concentrations. Also the exciton screening discussed by Feneberg et al. might be different for SL samples due to the same reasons as for the BGR.

The concept of using 2DEG/electrons to alter the optical properties of a material has not been exploited very often for group III nitrides but there are few publications which demonstrate the basic effect [128], [129]. In silicon, the change in refractive index due to carrier depletion is widely used as other modulation concepts via the Pockels or Franz-Keldysh effect are not possible [130], [131], [132], [133]. Also in group III arsenides and phosphides, the depletion and accumulation of free carriers in pin junctions has been investigated [134], [135]. In this context, the effect is called the free-carrier plasma effect [136]. While for silicon, the free-carrier plasma effect is still used in state-of-the-art ring modulators, it has not been pursued any farther in the case of arsenides and phosphides. For theses classical III-V materials, mostly Mach-Zehnder modulators are used [137]. Alping et al. reported a change in refractive index of $\Delta n = 0.4 \cdot 10^{-3}$ in a n-AlGaAs/n-GaAs/p-AlGaAs structure due to the free-carrier plasma effect [135].

4.3.2 Device Design of the Electro-Optic Modulator

After the origins of the electro-optic effects in SL have been discussed in the last paragraph, possible device geometries and materials are now investigated. The media surrounding the AlN/GaN-SL are examined via band structure simulations.

The schematic sample layout used in the simulation is depicted in figure 4.42. Synopsis TCAD simulations of the band structure of a SL layer sandwiched between two materials are shown in figure 4.43. The layer below the SL is always GaN. The top layer varies for the four graphs. The sample surface is located at 0 nm, which makes the position shown on the x-axis the distance from the surface. In figure 4.43a, the top layer is GaN (100 nm). This resembles the layer stack in a SL-DBR in which the SL is deposited alternatingly with $\lambda/4$ GaN. It can be observed that in this set up with no external electric field, only the lowest 2DEG near the underlying GaN are populated with electrons. Instead of depleting the few existent electrons, it seem more suitable to accumulate additional electrons in the upper 2DEG to gain a measurable change in refractive index. Figure 4.43b shows a layer stack in which an AlGaN barrier and an amorphous AlO_x film are investigated. Similar to the GaN top layer, this set up only populates the lower 2DEG. This structure should also show the largest change in refactive index if electrons are accumulated in the upper 2DEG. Such structures exhibit a behavior similar to a normally-off HFET. The two lower graphs c) and d) indicate that it is also possible to create layer designs in which electrons are already accumulated in every 2DEG at zero bias. This results in a structure in which the largest change in refractive index can be expected by electron depletion in analogy with a normally-on HFET. Figure 4.43c shows a layer stack with only amorphous AlO_x on top. All 2DEG are populated with zero external bias. Only the middle 2DEGs exhibit a slightly lower electron density. This could be compensated by n-type doping of the GaN layers in the SL. Figure 4.43d displays the simulated conduction band for this case. All 2DEG are now populated with similar carrier concentrations.

The SL needs to be implemented into a suitable device geometry to enable electro-optic modulation. One possible device is the tunable DBR which is also part of the TuneDBR patent application. For this device, one or multiple AlN/GaN-SL are incorporated into a DBR similar

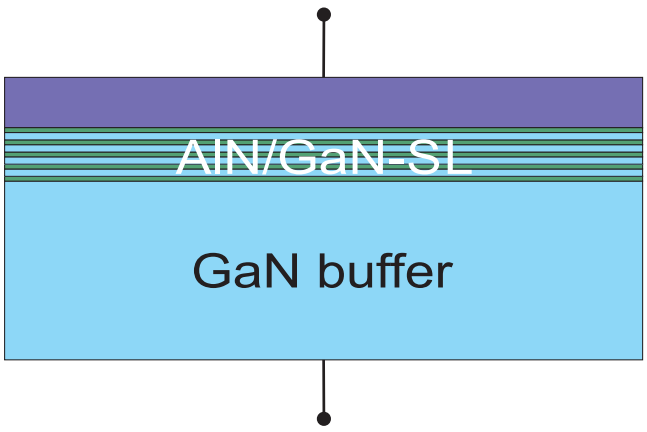

Figure 4.42: Schematic of the simulated SL layer stack. The layer material above the SL is varied in the simulation.

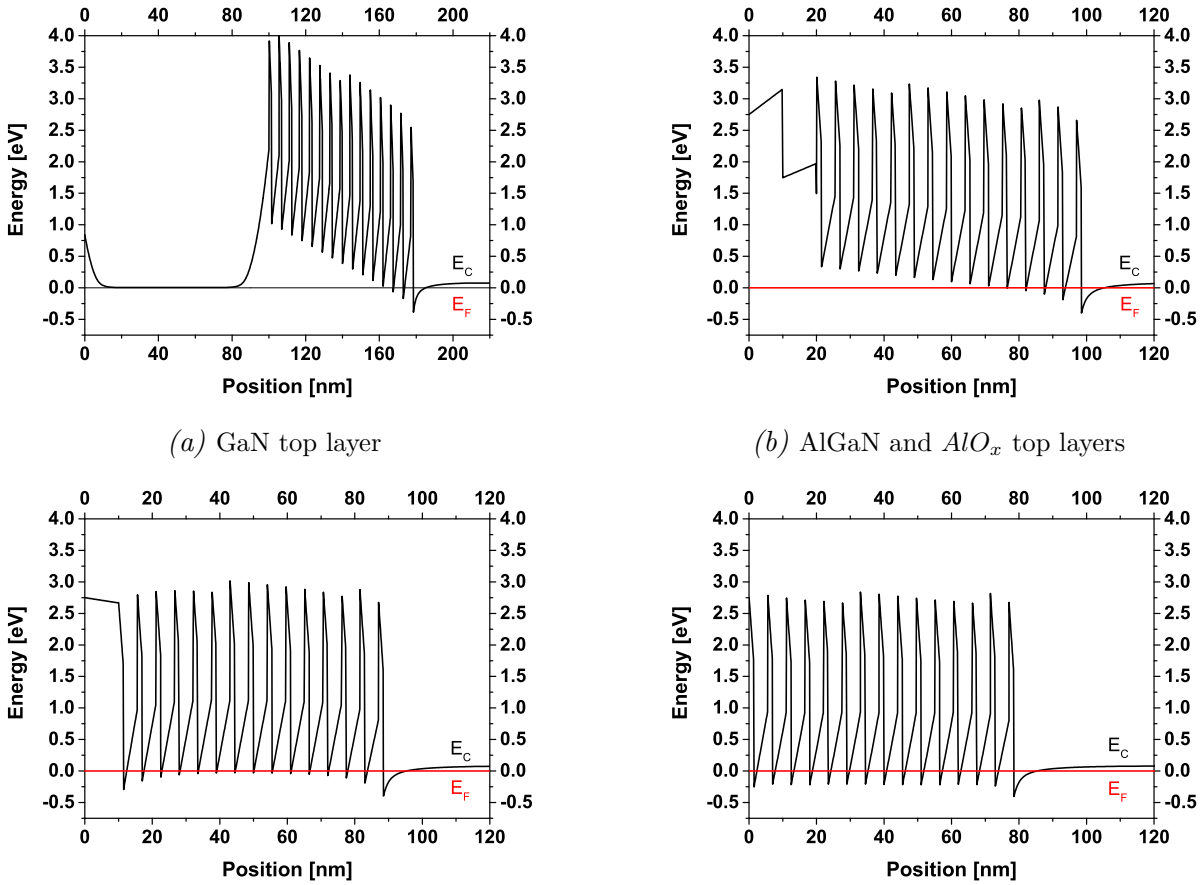

(a) GaN top layer

(b) AlGaN and AlO_x top layers

(c) AlO_x top layer

(d) Si-doped SL with AlN top layer

Figure 4.43: Synopsis TCAD simulations of the conduction band edge for 15-fold AlN/GaN-SL (1 nm AlN, 3 nm GaN) on GaN with different top materials. The sample surface is located at position 0 nm.

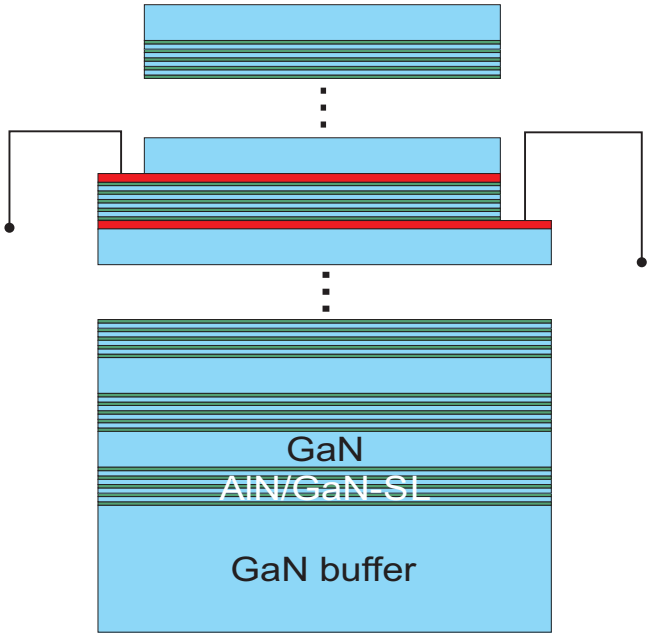

Figure 4.44: Schematic device geometry for a modulated DBR. The SL in the middle of the DBR is contacted via the layers in red to induce an electric field in the SL. The other low-index layers can also be SL (as shown here) but they do not contribute to the modulation effect.

to the SL-DBR shown before. But in contrast to the SL-DBR, the SL do not only constitute the low-index quarter wavelength layers. With a contact layer, an electric field can be applied to deplete or accumulate electrons in the SL. This changes the refractive index of the SL layer which detunes the DBR and decreases the reflectivity. Figure 4.44 shows a possible schematic layer design. The tunable SL with two contact layers is located in the middle of the DBR. For contact formation, two recess etches are necessary. With the first recess, the lower SL-GaN interface is exposed while the second recess, the upper SL-GaN interface is excavated. With appropriate interface layers and metal stacks, contact formation is now possible. The other low-index layers in figure 4.44 are depicted as SL stacks without contacts (i.e. passive SL layers). This is of course not necessary for the functioning of the modulator device. These layers can also be realized as standard AlGaN layers. The contact layers at the upper and lower interface of the active SL require a little more consideration as the light incidence generally is perpendicular to the SL-GaN interface planes which implies that the light also has to pass the contact layers without (severe) absorption. This can be realized either by using n- or p-doped nitride-based semiconductors as contact material or other conductive and transparent materials like ITO or conducting polymers. With the use of other than nitride materials, it might not be possible to maintain the monolithic deposition of the whole modulator stack. This is not necessarily a disadvantage. In this way, the material possessing the most suited properties could be selected and strain-related issued circumvented.

4.3.3 Fabrication and Characterization of Test Structures

To validate the concept of TuneDBR, the modulation of the optical properties via an applied electric field to the active modulator stack has to be investigated. For this purpose, a 15-fold AlN/GaN-SL was deposited on the standard GaN buffer stack (GaN on AlN on sapphire). On top of the SL, an AlGaN layer was grown to serve as a barrier layer similar to a conventional HFET. To minimize leakage additional AlO_x was deposited on top of the AlGaN barrier, forming an MIS structure.

Figure 4.45 shows the schematic layer stack and layout of the sample. The top contact is realized with a semitransparent Ni/Au Schottky stack to allow optical characterization of the SL. It is mechanically reinforced by an additional non-transparent Ni/Au stack in a circular shape at the mesa edge. The bottom contact consists of a Ti/Al/Ni/Au ohmic metal stack which is put to ground potential. Now the top contact can be biased with positive or negative potential to accumulate or deplete electrons in the SL. Due to the large active area of the device, realizing devices without strong leakage paths is challenging. Because of that, a first step including I-V and C-V measurements was conducted to test if the electron accumulation and depletion is possible in the device.

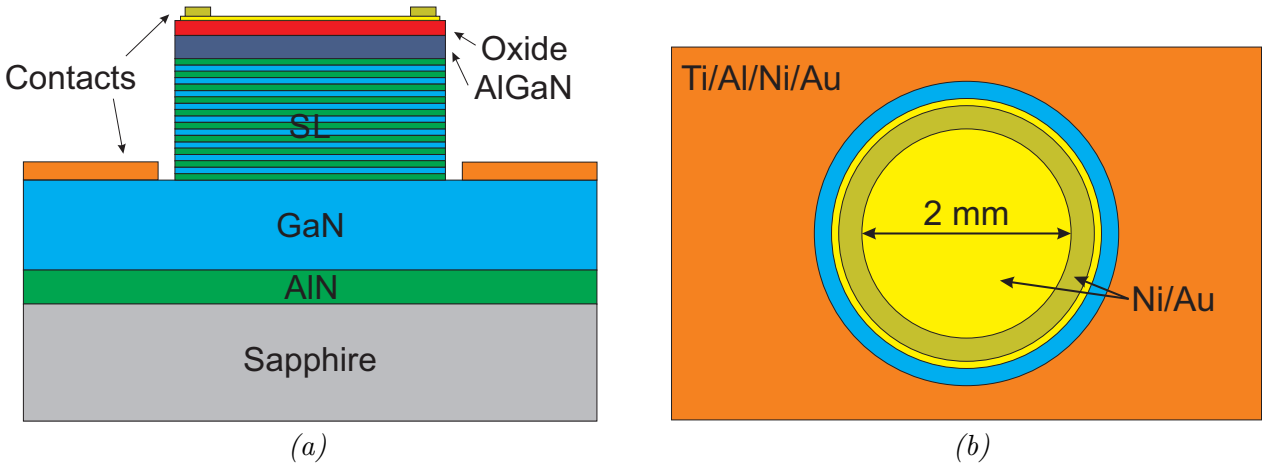

Figure 4.45: Side (left) and top view (right) of the TuneDBR test structure layer stack.

The C-V measurement is shown in figure 4.46. The overall shape of the C-V graph resembles a C-V graph obtained from HFET structures (cmp. chapter 4.1, fig. 4.11). The capacitance values are smaller than those of the multichannel HFET (fig. 4.11: $C_{pf,max}(double-channel) = 590\ nF/cm^2$, $C_{pf,max}(triple-channel) = 565\ nF/cm^2$) as the series connection of AlGaN barrier and oxide in the modulator test samples reduces the overall values.

At +5 V, the whole SL and the potential well forming at the oxide/AlGaN interface are populated with electrons. Calculated capacitance values match the measured values very well. The calculated capacitance for a populated oxide/AlGaN interface is 516 nF/cm^2 while the measured value is 520 nF/cm^2. At voltages higher than +5 V, the electron density at the oxide/AlGaN interface can be increased even further. Between 2.5 and 0 V, a steep drop in capacitance can be observed. This can be attributed to the depletion of the oxide/AlGaN interface (marked in red in figure 4.47). After the drop, the capacitance shows a plateau from

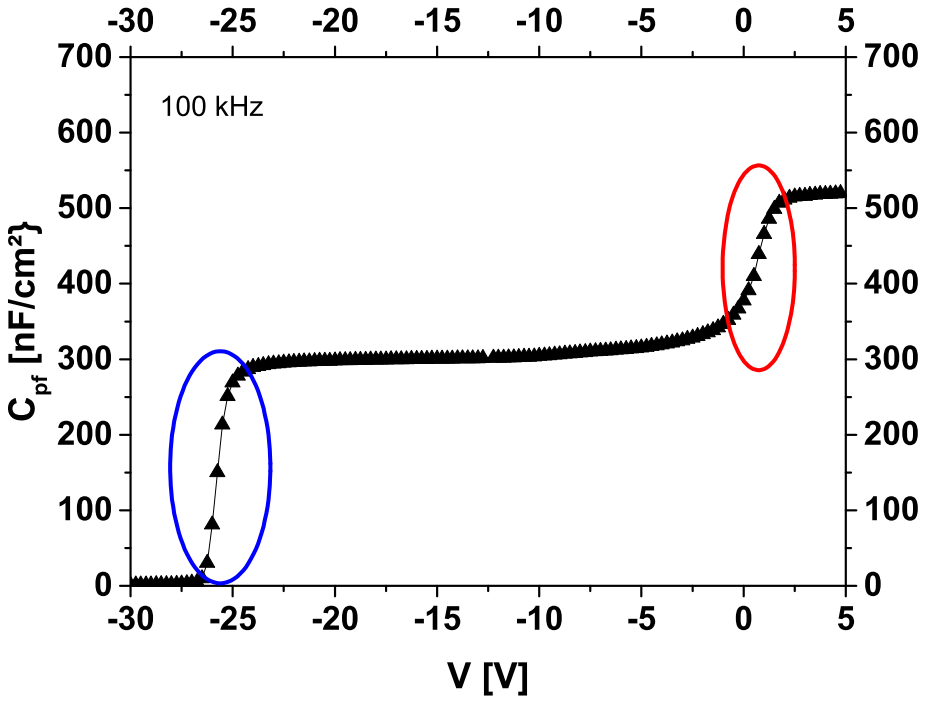

Figure 4.46: C-V results obtained from +5 to -30 V and 10 kHz from the test structure.

0 and -25 V at approximately 300 nF/cm^2. The calculated capacitance value for a depleted oxide/AlGaN interface and fully populated SL is 286 nF/cm^2 which again matches the measured data well (300 nF/cm^2). At approximately -25 V, a second capacitance step is observed which is caused by the simultaneous depletion of the 2DEG in the SL (marked in blue) similar to the simultaneous depletion of the upper and middle 2DEG in the triple-channel HFET C-V characteristic (cmp. chapter 4.1.3, fig. 4.11b).

Reflectivity measurements were carried out on this structure as described in chapter 2.3.3 at 0 and +8 V. Figure 4.48 shows the reflectivity measurement from 425 to 635 nm and a zoomed-in diagram around 450 nm is given in figure 4.49. The latter one clearly demonstrates an increased reflectivity of +0.5 % for 8 V in contrast to the reflectivity at zero bias. This reflectivity change is constant over the whole measured spectral range.

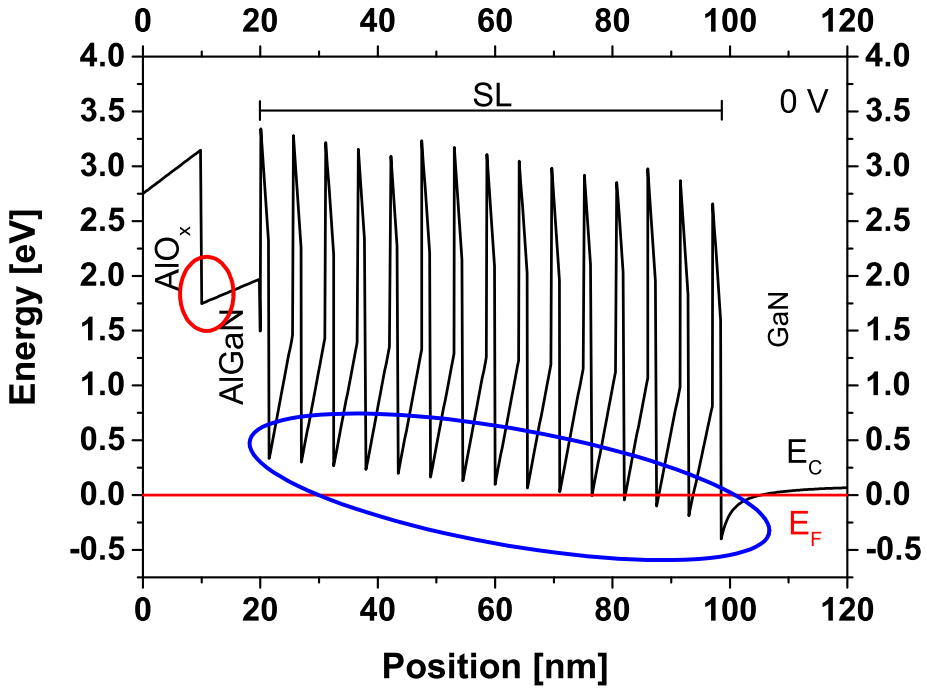

Figure 4.47: Simulated band diagramm of the test structure at zero bias. The circles approximately mark the corresponding capacitance drops from fig. 4.46.

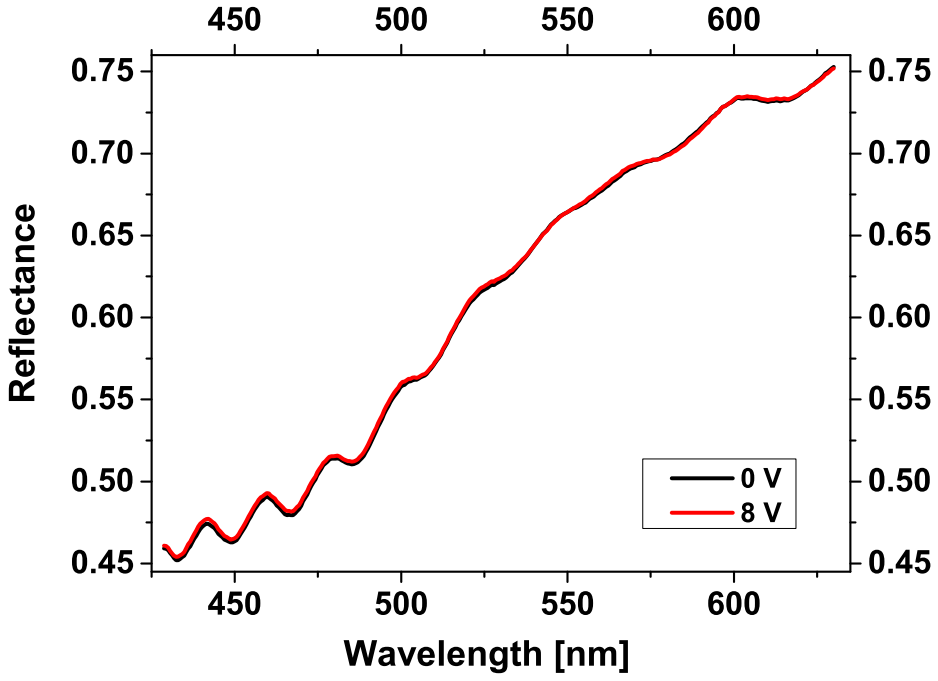

Figure 4.48: Reflectivity at normal incidence of the test structure at 0 V and +8 V from 425 to 635 nm. The whole reflectance spectrum is shifted to higher reflectivity values for +8 V.

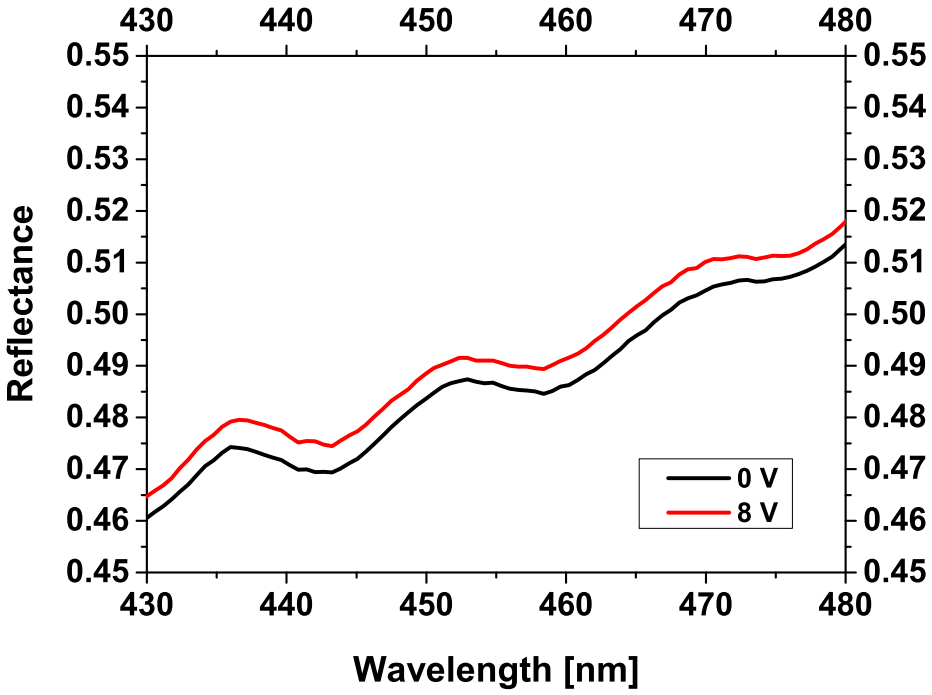

Figure 4.49: Zoomed reflectance spectra of the test structure at 0 V and +8 V. The reflectivity is increased about 0.5 % absolute at +8 V.

4.3.4 Simulation of the Electro-Optic Effect

To investigate the obtained results, the reflectance spectra of the test structure were also simulated with FreeSnell [118] and compared to the measured data. The successful simulation with FreeSnell of the SL-DBR was already presented in chapter 4.2.3. The same refractive index data are now used to simulate the reflectance spectra of the fabricated TuneDBR test structure described above. As carriers do change the complex refractive index, they can also introduce absorption (cmp. chapter 4.3.1). This implies that an extinction coefficient $k \neq 0$ has to be considered. The magnitude of the influence of the extinction coefficient on the absorption and reflectance is not as obvious as for the refractive index n. To clarify this, a single SL stack in air was considered and the absorption spectra for varying extinction coefficients k were simulated. For the real refractive index, a value of 2.41 was used which is the refractive index of $Al_{0.26}Ga_{0.74}N$ at 450 nm. The real refractive index was assumed to be constant over the whole simulated spectral range and for all extinction coefficients. The absorption spectra are depicted in figure 4.50. It can be seen that the absorption is approximately constant for all wavelengths and increases from 10 % for $k = 0.1$ (reflectance $r =$ 40 %) up to 60 % for $k = 1.5$ ($r =$ 35 %). If the extinction coefficient is further increased, the absorption decreases (35 % for $k = 4$, $r =$ 65 %) due to the increasing top reflectance of the layer, similar to a metallic mirror.

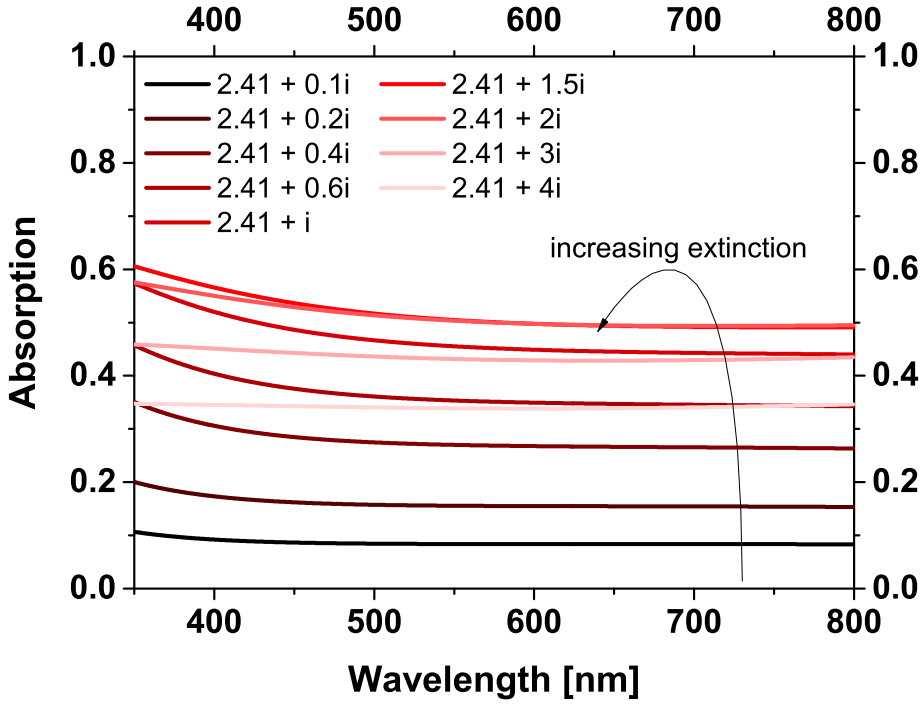

Figure 4.50: Absorption of a single SL in air for various extinction coefficients

In a second step, the complete layer stack of the test structure including substrate, buffer, oxide and semitransparent Schottky contact layers is employed in the simulation. To simulate the electro-optic effects, the complex refractive index of the SL layer was varied. Figure 4.51

shows the reflectance spectra for increasing extinction coefficients and the previously measured spectrum for comparison. The extinction coefficient was varied up to 2.5 which seems suitable if figure 4.50 is considered. In this way, the maximum variation of the absorption was investigated without reaching the regime of high reflectance at the upper SL interface which would prohibit light propagation through the SL (disadvantageous for the implementation of tunable SL into DBR). The refractive index was kept constant at 2.41. The black curve in figure 4.51 depicts the reflectance spectrum of the test structure without any absorption in the SL. Fabry-Perot oscillations are observed for the whole spectral range. The measured reflectance spectrum does not show oscillations in this extent. From figure 4.51 it can be directly derived that the oscillations can be quenched in the simulation by increasing the absorption in the SL (green graphs). The absorption also decreases the reflectance for wavelengths shorter than approximately 500 nm and increases the reflectance for wavelengths longer than 500 nm. If simulated and measured reflectance spectra of the test structure are compared, it can be derived that absorption seems already present in the test structure at zero bias because the spectra with absorption match the measured data better than the spectra without absorption. This also fits the results from C-V measurements (fig. 4.46), which showed that the 2DEG already contain carriers in the unbiased case which makes absorption likely to occur. A more thorough comparison of simulation and measurement shows that a simulation with lesser absorption fits the measured data better up to 500 nm and for wavelengths longer than 500 nm, a higher absorption is necessary to match the measurements. The oscillations in the measurement appear nearly completely quenched for long wavelengths while they are still present between 400 and 500 nm. From this is can be concluded that that the absorption in the SL is wavelength-dependent and increases for longer wavelengths. More advanced simulations of the effects described in chapter 4.3.1 could clarify if one of the effects described in there or a combination of them is able to generate the measured wavelength-dependent absorption.

Figure 4.52 illustrates the influence of a varied real refractive index with constant extinction coefficient on the reflectance of the test structure. As a value for the extinction coefficient, $k = 2$ was chosen because the simulation with $k = 2$ in figure 4.51 denotes the best fit of the measured data. The refractive index was varied from 2.3 to 2.55 including the value 2.41 used in the previous simulations which matched the reflectance spectra measured at zero bias. A change in refractive index shifts the reflectance spectrum upwards towards higher reflectivities for increased values of n and downwards for reduced ones. The shift is constant over the whole spectral range (not shown here) and in the same order of magnitude than the experimentally observed effect. The reflectance change in the simulation is indeed very similar to the one induced by the positive bias applied in the measurement (cmp. fig. 4.49). The change in reflectance of 0.5 % realized by biasing the test structure with +8 V can be reproduced in the simulation by increasing the refractive index of the SL from 2.41 to 2.5 while the extinction coefficient was kept constant. Therefore the measured reflectance change of the positively biased test structure can be attributed to a change in real refractive index and not in extinction coefficient (which would, according to the simulation, alter the shape of measured data and

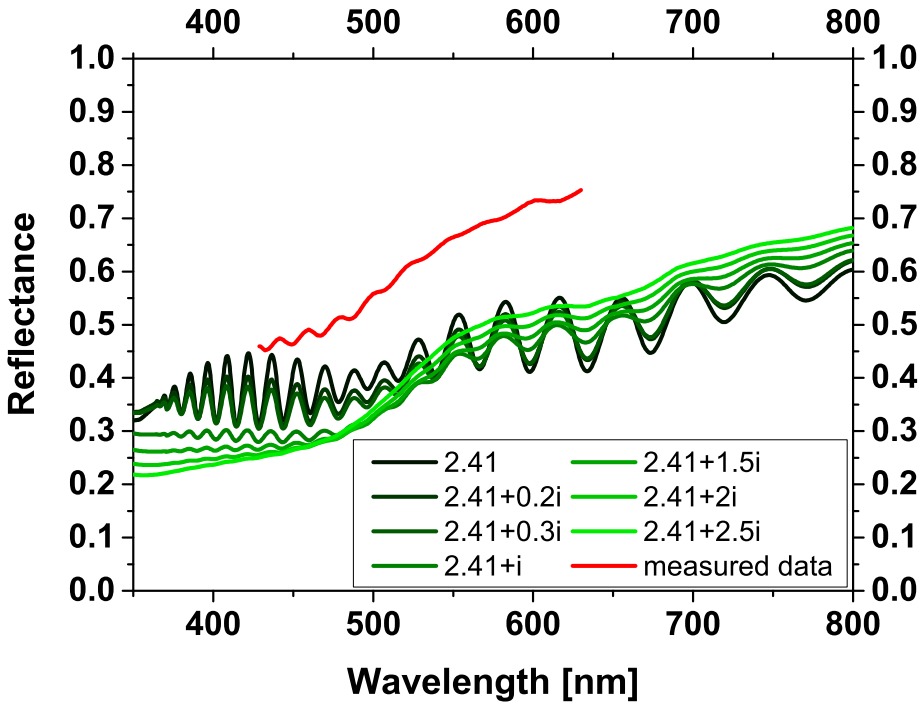

Figure 4.51: Simulated reflectance spectra of the fabricated test structure with varied absorption and the measured data (red) from fig. 4.48

further quench Fabry-Perot oscillations). Nevertheless, the absorption of a biased SL might still change if the structure is fully depleted of electrons an no absorption is possible. It was not possible to measure a reflectance spectrum of a fully depleted SL because the test structures were not able to withstand repeated cycling to negative voltages beyond -25 V. A change in refractive index of 0.09 (2.41 to 2.5) is very large compared to results obtained from other materials where only a change in refractive index of $0.4 \cdot 10^{-3}$ was observed (AlGaAs/GaAs) which is two orders of magnitudes smaller [135].

Simulation of the TuneDBR Structure

After the simulations of the test structure clarified that absorption seems present in the structure and that the measured electro-optical effect is presumably caused by a change in refractive index, theses findings can be used to simulate the final TuneDBR device in which the tunable SL denotes one quarter wavelength layer of a DBR. A 51-pair $Al_{0.26}Ga_{0.74}N/GaN$-DBR with a stopband at 450 nm was simulated placing the tunable SL layer in the middle of the DBR stack so that 25 DBR pairs are above and below this SL layer. With the previous results of the simulation a tuned and a detuned case of the DBR is modeled. For the tuned case, the refractive index of the tunable SL is assumed to be 2.41 with zero absorption which matches the quarter wavelength condition and creates a standard 51-pair DBR. This describes the case of a fully depleted SL. The simulated reflectance spectrum for this case is depicted in figure 4.53 by the black graph. The maximum reflectivity at the stopband wavelength is 94.3 %. For the detuned case, the refractive index and/or the extinction coefficient of the middle tunable

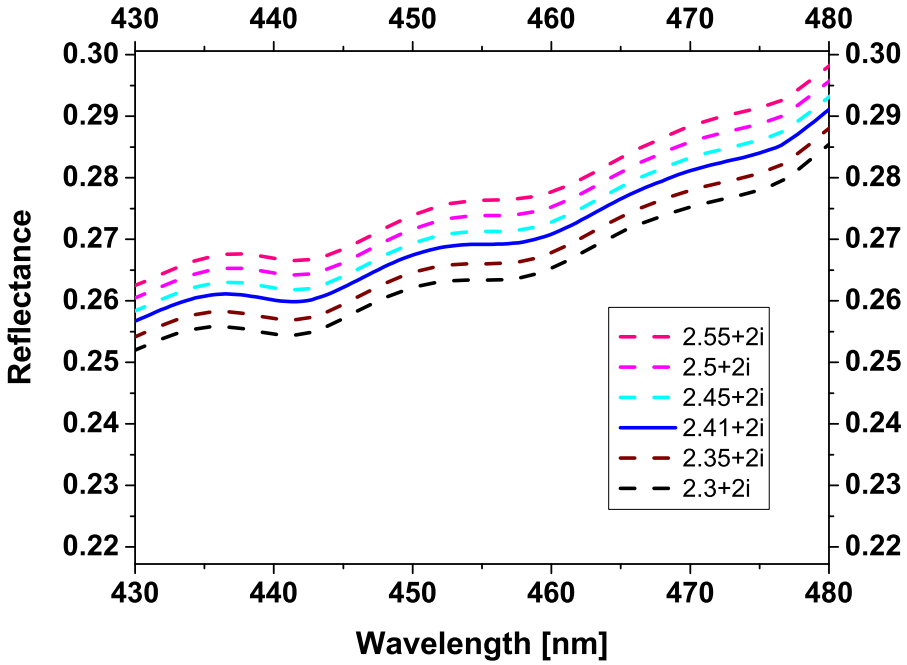

Figure 4.52: Reflectance spectra of the fabricated test structure with varied refractive index

SL are varied. An increase of the refractive index from 2.41 to 2.5 with no absorption (red graph) reduces the maximum reflectivity to 93.8 %.

For better visibility, figure 4.54 shows a zoomed image of the stopband region of the simulations in figure 4.53. If absorption is considered for the tunable SL, the reflectance spectrum is affected in a more severe way. The bright green graph in 4.53 shows the simulated reflectance spectrum for the complex refractive index of $\underline{n} = 2.41 + 2i$ which models the accumulation of carriers in the previously fully depleted SL. The maximum reflectivity is now reduced to 80.2 % and slightly shifted to 447 nm. This corresponds to a reduction in maximum reflectivity of 14.1 %. The overall shape of the reflectance spectrum also changed. The higher order peaks to the left and right of the stopband are greatly enhanced with the introduction of strong absorption. If the refractive index is now increased to 2.5 resulting in a complex refractive index of the tunable SL of $\underline{n} = 2.5 + 2i$ (blue graph), the change in the reflectance spectrum is similar to the change of refractive index without absorption (black and red graph). The maximum reflectivity is reduced to 79.5 %. The simulation of the absorption in a free-standing SL showed that an extinction coefficient of $k = 2$ already leads to an absorption around 55 %. This extinction coefficient fitted the measured data of the test structure best but nevertheless, an absorption of 55 % appears high. Therefore, it was investigated how the reflectance spectra are affected if an extinction coefficient of only $k = 0.2$ is assumed. $k = 0.2$ leads to an absorption of only 15 % in a single SL. Again both previously tested refractive indices for the SL of 2.41 and 2.5 were tested. The orange graph shows the simulated spectrum for a complex refractive index of $\underline{n} = 2.41 + 0.2i$, while the dark green curve denotes the simulation for $\underline{n} = 2.5 + 0.2i$. Both spectra resemble rather the case with zero absorption (black/red) than that with $k = 2$ (bright

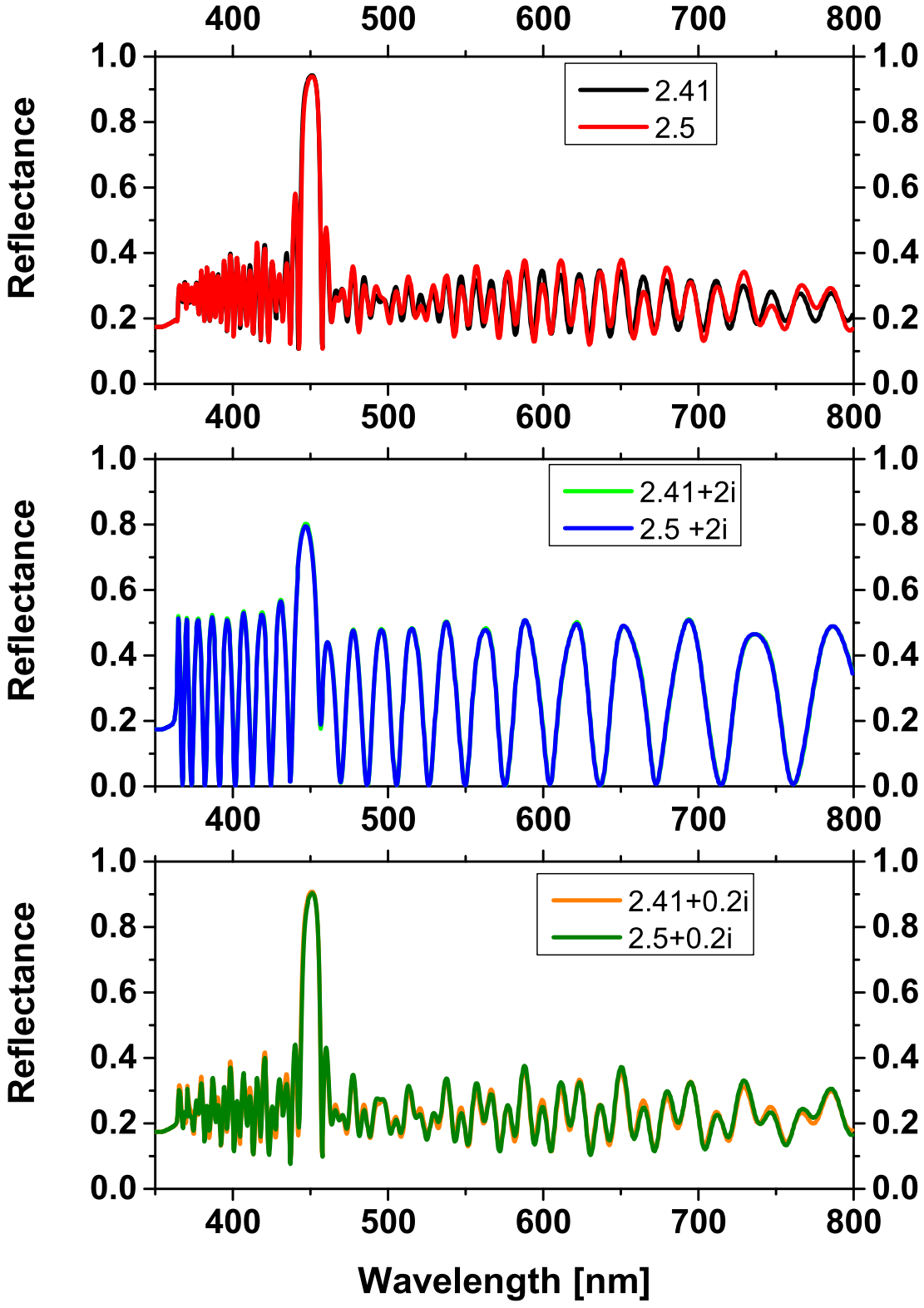

Figure 4.53: Reflectance spectra of a 51-pair SL-DBR with one tunable SL layer in the middle of the stack (26th pair). The complex refractive index of the 26th SL was varied to simulate the electro-optic effect.

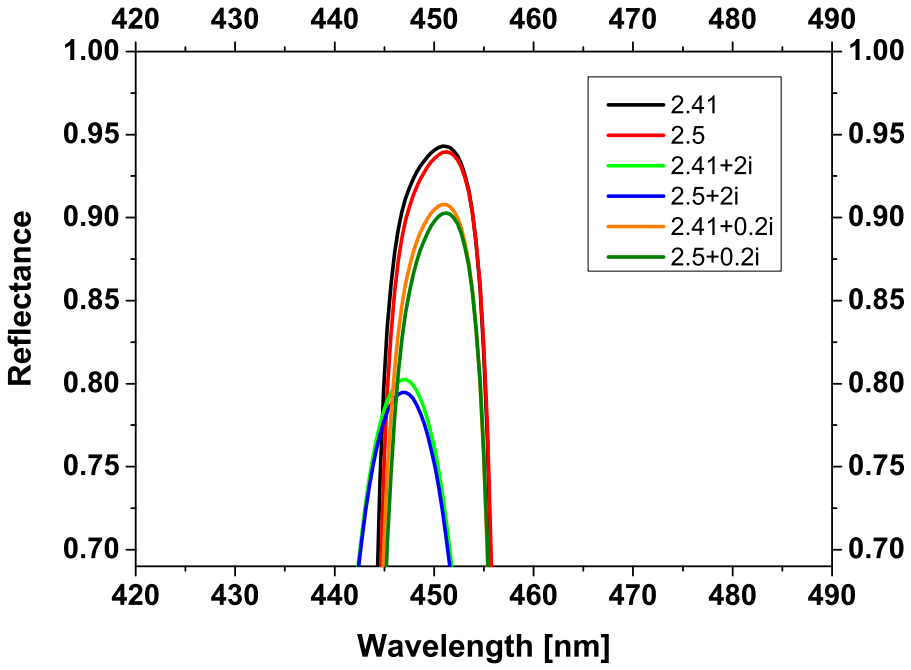

Figure 4.54: Merged image of the reflectance spectra in the stopband region of the simulated 51-pair SL-DBR with one tunable SL layer in the middle of the stack (26th pair) from fig 4.53.

green/blue). Still, the maximum reflectivity is reduced to 90.7 % ($\underline{n} = 2.41{+}0.2i$, orange graph) and 90.2 % ($\underline{n} = 2.5 + 0.2i$, dark green graph). Compared to the case with zero absorption ($\underline{n} = 2.41 + 0i$, black graph) the maximum reflectance is still changed about 4.1 % if a complex refractive index of $\underline{n} = 2.5 + 0.2i$ is considered.

In a last step, it is investigated at which position in the DBR the impact of a single detuned SL on the maximum reflectivity is largest. At first, a detuning of only the refractive index with no absorption onset has been investigated. Figure 4.55 shows the simulated reflectance spectra of 51-pair DBR in the stopband region. The position of the detuned SL layer was varied from the first pair (top, left) to the last pair (bottom, right). For comparison, the peak reflectance of the ideal static case is also shown (dashed grey line). To create a more pronounced effect in the spectra, a refractive index of 2.8 instead of the previously used 2.5 was used for the detuned layer. It can be seen that the peak reflectance increases at first if the position of the detuned SL moves downwards but then starts to decrease. The minimum reflectivity is reached if the detuned SL is positioned in the 49th DBR pair (i.e. with two passive pairs left below the detuned SL). This is most likely the position at which the partial wave amplitudes above and below the detuned SL are equal. This position is located near the bottom of the DBR stack because reflections at the buffer structure and the substrate are also considered in the simulation.

The situation changes if absorption is assumed to evolve. Figure 4.56 shows the same variation of position of the detuned SL, but in these simulations a complex refractive index of $\underline{n} = 2.5 + 0.2i$ is assumed for the detuned SL introducing absorption. Again, the position of the detuned SL is moved downwards from the first DBR pair (top, left) to the last pair

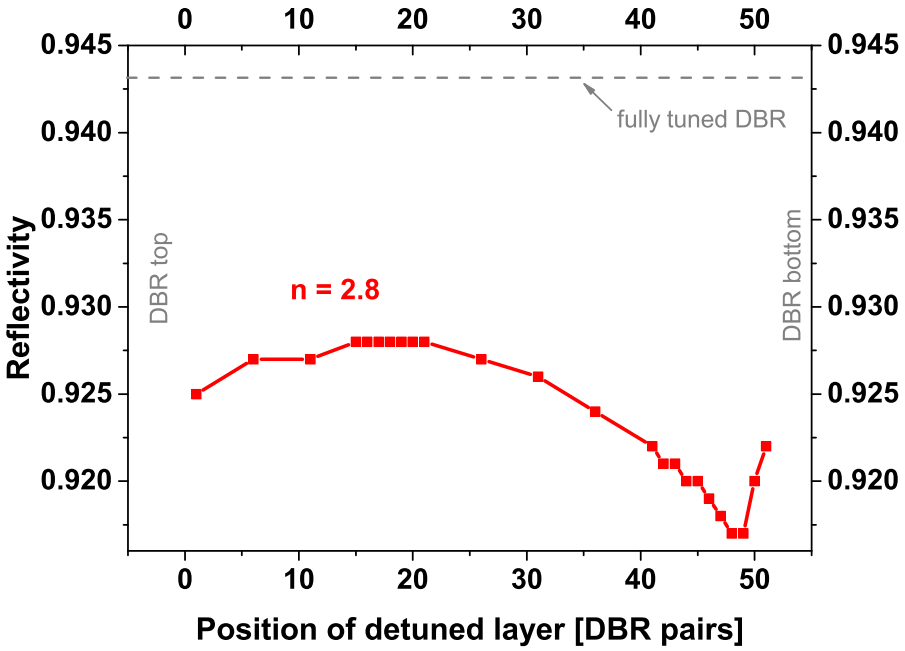

Figure 4.55: Peak reflectance of a 51 pair SL-DBR with varied position of one detuned SL layer from top to bottom with $n = 2.8$ and $k = 0$.

(bottom, right) and the grey line again denotes the peak reflectance of the ideal static DBR for comparison. With absorption present in the detuned SL, the peak reflectance increases if the SL is moved downwards in the DBR. The lowest reflectivity for the detuned case is realized at the top position (i.e. tunable SL located in the top DBR pair).

Figure 4.57 displays the same evaluation for a detuned refractive index of $\underline{n} = 2.5 + 2i$. The behavior of the peak reflectance is similar to the previously described case with $k = 0.2$. The peak reflectance increases if the detuned SL is moved downwards in the DBR stack. The lowest maximum reflectivity of 34.8 % is observed if the detuned SL is positioned in the second DBR pair (i.e. one passive pair is still located above the detuned one) but there is only a minute difference to the top position. If absorption is present in the detuned SL, a position near the DBR top surface seems more suitable to achieve the strongest modulation in the stopband reflectivity of a DBR. This seems reasonable as with absorption in the detuned SL, the part of the incident light transmitted into the tuned DBR part below is reduced. This lowers the contribution of ideal DBR pairs below the detuned SL to the overall reflectivity of the DBR. Therefore, the impact on the stopband reflectivity is largest if as many DBR pairs as possible are placed below the detuned and absorbing SL. If the extinction coefficient is further increased, the absorption is reduced again in favor of the reflectance (cmp. fig. 4.50). This might cause an increasing reflectance of the DBR if the detuned SL is positioned at the top position. Therefore, it seems more feasible to place the detuned layer slightly below the top DBR surface as the interfaces above the detuned SL are then able to reduce the increased reflectivity due to back reflection and phase shifts.

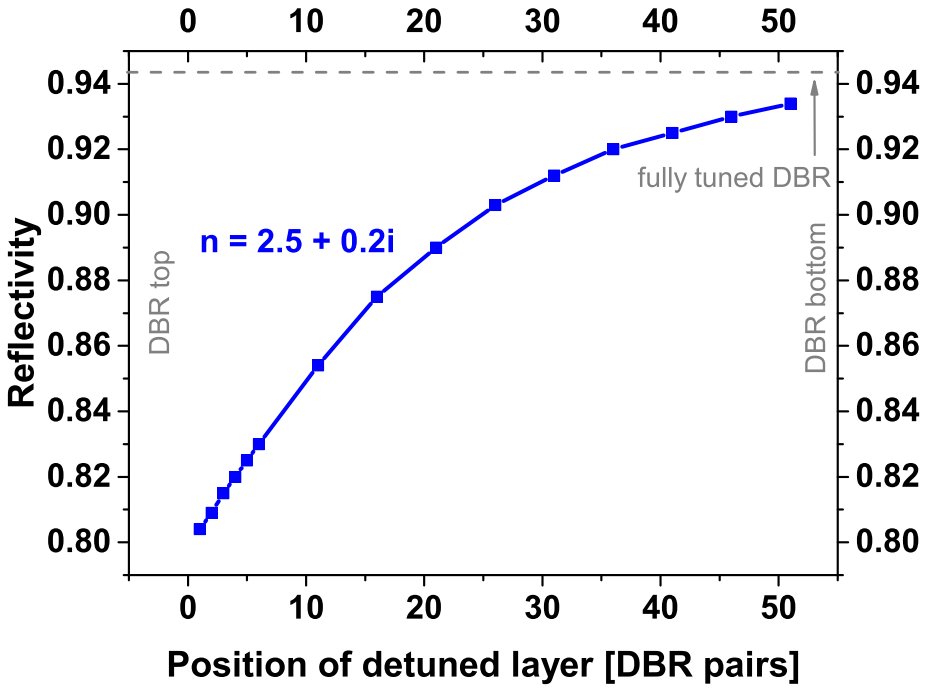

Figure 4.56: Peak reflectance of a 51 pair SL-DBR with varied position of one detuned SL layer from top to bottom with $n = 2.5$ and $k = 0.2$.

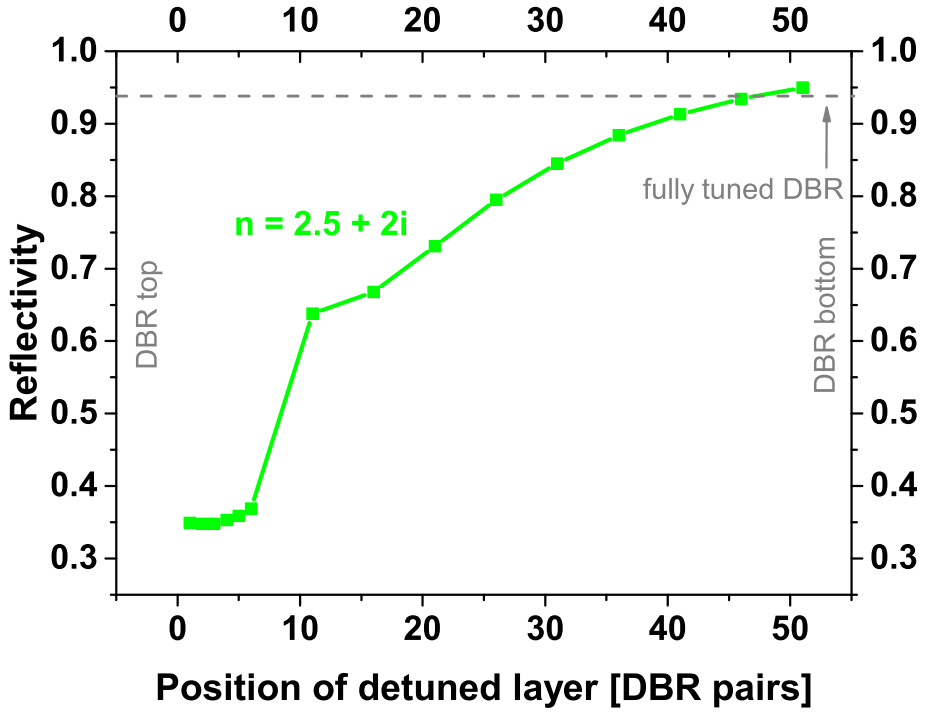

Figure 4.57: Peak reflectance of a 51 pair SL-DBR with varied position of one detuned SL layer from top to bottom with $n = 2.5$ and $k = 2$.

To summarize this analysis, the simulated stopband reflectivity of the ideal case ($\underline{n}(SL) = 2.41 + 0i$) without any absorption (fully depleted SL) is compared to the simulated stopband reflectivity of the detuned case with $\underline{n}(SL) = 2.5 + 2i$ (best fit of the measured test structure reflectance) which denotes a SL with accumulated electrons. The reflectivity at 450 nm is reduced from 94.3 % for the ideal case to 34.8 % for the detuned case. This denotes a reflectivity reduction of 59.5 %. The remaining reflectivity of 34.8 % is in the range of the GaN buffer reflectivity shown in figure 4.22. Therefore, it can be stated that according to the simulations, the DBR reflectivity can completely be destroyed by application of an appropriate voltage to a single tunable SL.

A more detailed interpretation of the measured and simulated reflectivity change and assignment of the responsible effects is very difficult at this point. All the electro-optic effects mentioned before can contribute to the observed modulation but there is only few to no data on the magnitude of these electro-optic effects in GaN or AlN. It has already been demonstrated that the depletion of a 2DEG can affect the reflectance of the sample (fig. 3 in [129]). This makes is seem likely that the observed change in reflectance can be attributed to the accumulation of carriers in SL 2DEG. To separate the influences of the concurring effects, a detailed analysis of the dielectric function of AlN/GaN-SL layers with subsequent modeling and simulations is necessary. Nevertheless, the pursued approach of electro-optic modulation via accumulation and depletion of 2DEG is a very promising one and could in general be demonstrated.

Chapter 5

Conclusion

The structure, morphology and growth behavior of AlN/GaN-SL as well as their applications to HFET, DBR and electro-optic modulators were successfully investigated.

First, growth conditions for AlN/GaN-SLs with high layer and interface quality were developed. The SL were found to be tensily strained and grown pseudomorphically on GaN buffer structures up to layer thicknesses of 79 nm for effective AlN contents in the SL of 31 %. For SL at or above this layer thickness, relaxation via micro crack formation occurred. Slight indications in the GaN XRD peak shape pointed towards MD generation at the SL/buffer interface accompanied by the introduction of compressive strain into the GaN wells of the SL prior to the occurrence of micro cracks. In comparison to homogeneous AlGaN alloys, the critical layer thickness was found to be about 20 nm higher for AlN/GaN-SL which was attributed to the presumably higher crack formation energy in unstrained or even slightly compressively strained GaN wells. The superior crystal and interface quality of the developed SL growth conditions was proven via a resonant tunneling diode which showed a negative differential resistance.

The principle of AlN/GaN-SL was then successfully implemented in HFET. The thin AlN barriers proved to induce sufficient polarization discontinuity in the multiple heterostructure to induce 2DEG at several interfaces and SL-HFET with up to four parallel 2DEG channels were realized. With the SL-HFET concept, it was possible to improve the carrier mobility from 1690 cm^2/Vs (single-channel) to 1900 cm^2/Vs (triple-channel) by reducing interface and phonon scattering in the high carrier concentration regime ($> 7 \cdot 10^{12}$ cm^{-2}) and by diminished impurity scattering via a backbarrier effect in the low carrier concentration regime ($< 7 \cdot 10^{12}$ cm^{-2}). The SL-HFET could be pinched off and individual depletion of the 2DEG was possible manifesting in local maxima in the transconductance characteristic. The depletion behavior was further analyzed by C-V measurements and well understood with additional simulations. Furthermore, the triple- and double-channel SL-HFET showed a wider transconductance profile allowing for linear amplification of larger input signals. The AC properties were also investigated and transit frequencies from 18.0 to 13.3 GHz were demonstrated. A decrease of f_T with increasing number of channels was attributed to a parasitic gate-drain capacitance generated by a parallel configuration of capacitances between the gate metal and the undepleted drain side part of the 2DEG which is not present in conventional single-channel

HFET. It was also shown that the linear DC characteristics of the SL-HFET translated into linear RF properties by a broader MAG profile for the triple-channel device in comparison to a single-channel HFET. This was affirmed by a higher degree of linearity in power amplification for the SL-HFET devices which makes an application for highly linear amplifiers feasible.

AlN/GaN-SL were also used in DBR for stress engineering. The AlN/GaN-SL replaced the low-index AlGaN layer in AlGaN/GaN DBR to control layer cracking. Crack-free SL-DBR with 10 pairs and a reflectivity of 79.5 % were realized with an effective AlN content of 26 % in the AlN/GaN-SL low-index layers. The reflectance spectrum of the SL-DBR was successfully simulated. It was found that for successful simulations of the reflectance, the optical thickness of an AlN/GaN-SL had to be assumed larger than for a homogeneous AlGaN layer with the same layer thickness effective AlN content which is most likely caused by absorption and/or a phase shift at the GaN/SL interface $\neq \pi$. Also the absorption onset of the SL seems to diverge from the one of homogenous AlGaN with the same effective AlN content caused by the GaN wells and/or 2DEG electrons present in the SL.

Pseudomorphic growth of the entire SL-DBR stack on the GaN buffer structure was ensured via an HR-XRD analysis. Relaxation occurred at elevated AlN contents in the low-index SL. In this case, the whole SL-DBR stack relaxed towards smaller in-plane lattice parameters relieving tensile strain in the AlN layers and introducing compressive strain in all GaN layers. In contrast to thicker SL stacks, no cracking occurred. Curvature measurements showed no additional strain for 10-pair SL-DBR stacks in comparison to thick SL stacks. This was attributed to a staircase movement of TD in the SL-DBR structure revealed by TEM. At every GaN/SL interface, the TD were found to incline into the $< 1\bar{1}00 >$ direction for a characteristic length followed by a return to their original $< 0001 >$ propagation. The diffusion-based process of dislocation climb was found responsible for the dislocation inclination. The inserted crystal half plane above the dislocation line was attributed to release a critical amount of tensile stress to ensure crack-free growth. Furthermore, higher growth rates were successfully tested on SL-DBR but the epitaxial process showed to become very sensitive to parameter fluctuations which made it difficult to precisely tailor the recipe to the aspired layer thicknesses.

After the successful realization of SL-HFET and SL-DBR, the concept of both devices was merged to create a novel electro-optic modulator. This invention was filed for patent by RWTH Aachen University (incl. PCT application). The modulation principle relied on depletion or accumulation of carriers in 2DEG via the change of presumably electron plasma resonance, exciton-carrier mixed states, QCSE, electron-hole plasma occurrence, BMS and BGR. Test structures were developed containing one single layer of the AlN/GaN-SL in a MIS structure. These test structures showed a voltage-dependent reflectivity with an increase of absolute +0.5 % for a bias variation from 0 to 8 V. With simulations, is was possible to remodel the reflectance spectra of the unbiased and biased case (+8 V). For both cases, it was necessary to introduce an extinction coefficient $\neq 0$ to the complex refractive index of the SL while the reflectance modulation could be modeled by an increase of the refractive index. The effect of a single tunable SL on the reflectance spectra of a DBR was also successfully simulated

with parameters extracted from the test structures. It was found that without absorption present in the detuned SL, the layer should be placed at a position in the DBR at which both partial wave amplitudes above and below the detuned SL are equal. With absorption, it was most advantageous to place the SL at the top of the DBR stack. With this design rule, the simulated stopband reflectivity of the DBR was reduced from 94.3 % for the ideal case to 34.8 % for the detuned case (51 DBR pairs) with a single detuned SL. This degraded the DBR reflectivity to the range of the underlying buffer structure without a DBR stack. In this manner, it was possible to completely "switch off" the DBR in the simulation with the novel electro-optic modulator concept.

With the gained results, a better understanding of the behavior of compositional SL in the nitride system has evolved and further device development can profit from these findings. Nonetheless, open questions remain and further research is necessary to fully understand the complicated strain evolution in AlN/GaN-SL. More detailed analysis should be directed to the SL/buffer interface of thick AlN/GaN-SL stacks to investigate whether MD are formed and clarify if compressive strain is induced in the GaN wells. Also other material combinations should be investigated regarding their relaxation mechanisms. Advanced concepts including device layouts are necessary to lower the increased gate-drain capacitance of the SL-HFET. The application of SL-HFET as linear amplifiers should also be examined. Recent simulation results also showed a possible implementation of SL-HFET for RF switches. Ongoing research should also be directed towards this possibility. For SL-DBR, a more detailed TEM analysis is desirable to clarify if the diffusion-based dislocation climb is affected by growth rate or growth temperature. The electro-optic modulator concept TuneDBR needs further validation and a thorough simulation analysis to fully understand the electro-refractive mechanisms accountable for the observed effect. Other device layouts based on different barrier materials or pin junctions instead of the MIS approach should also be evaluated. Especially, the pin junction seems promising in which the modulated SL is located in the i-region because the wide depletion region in p-GaN should be very effective to prohibit parasitic leakage currents. As the final step, the realization of a TuneDBR prototype consisting of a complete SL-DBR with a functionalized SL layer should be targeted to validate the results obtained by simulation.

Appendix A

Sample list

Chapter 3.1		
Series	Parameter varied	Sample number
Pressure	100 mbar	#3075
Pressure	125 mbar	#3076
Temperature	$1053°C$	#3181
Temperature	$1060°C$	#3235
Temperature	$1065°C$	#3168
Temperature	$1073°C$	#3165
V/III ratio	2130/1690	#2689
V/III ratio	1460/1270	#2690
V/III ratio	1310/1130	#2691
V/III ratio	1220/1015	#2693
Crit. thickness	7-fold	#2623
Crit. thickness	10-fold	#2635
Crit. thickness	15-fold	#2636
Crit. thickness	18-fold	#2649
Crit. thickness	20-fold	#2639
RTD	-	#2865

Chapter 4.1		
Series	Number of channels	Sample number
SL-HFET	1	#2805
SL-HFET	2	#2806
SL-HFET	3	#2807
SL-HFET	4	#2900

Chapter 4.2		
Series	Parameter varied	Sample number
Standard DBR	-	#2593
Pair series	10	#2633
Pair series	15	#2634
SL thickness	6-fold	#2593
SL thickness	7-fold	#2591
SL thickness	8-fold	#2527
More AlN	-	#2594
Curvature	GaN buffer	#3057
Curvature	10-fold SL	#3059
Curvature	15-fold SL	#3058
Curvature	23-fold SL	#3062
Curvature	SL-DBR	#2727
Growth rate	39/9	#2694
Growth rate	42/10	#2695
Chapter 4.3		
Series	Parameter varied	Sample number
TuneDBR	Test structure	#3036

Appendix B

Publications

- *First Polarization-engineered Compressively Strained AlInGAN Barrier Enhancement-mode MISHFET*, H. Hahn, B. Reuters, A. Wille, N. Ketteniss, F. Benkhelifa, O. Ambacher, H. Kalisch, A. Vescan, *Semicond. Sci. Technol.* **27**, 055004 (2012)
- *Growth Studies on Quarternary AlInGaN Layers for HEMT Application*, B. Reuters, A. Wille, B. Holländer, E. Sakalauskas, N. Ketteniss, C. Mauder, R. Goldhahn, M. Heuken, H. Kalisch, A. Vescan, *J. Elec. Mat.* **41**, 905-909 (2012)
- *Relaxation and Critical Strain for Maximum In Incorporation in AlInGaN on GaN Grown by Metal Organic Vapor Phase Epitaxy*, B. Reuters, M. Finken, A. Wille, B. Holländer, M. Heuken, H. Kalisch, A. Vescan, *J. Elec. Mat.* **41**, 905-909 (2012)
- *Polarization-Engineered Enhancement-Mode High-Electron-Mobility Transistors Using Quarternary AlInGaN Barrier Layers*, B. Reuters, A. Wille, N. Ketteniss, H. Hahn, B.+Holländer, M. Heuken, H. Kalisch, A. Vescan, *J. Elec. Mat.* **42**, 826-832 (2013)
- *Growth Properties and Electrochemical Characterization of InGaN Photoanodes with Different In Concentrations*, M. Finken, A. Wille, B. Reuters, B. Holländer, M. Heuken, H. Kalisch, A. Vescan, *Phys. Status Solidi C* **11**, 746-749 (2014)
- *Selective MOVPE of InGaN-based LED Structures on Non-planar Si(111) Facets of Patterned Si(100) Substrates*, B. Reuters, J. Strate, H. Hahn, M. Finken, A. Wille, M. Heuken, H. Kalisch, A. Vescan, *J. Cryst. Growth* **391**, 33-40 (2014)
- *Strain Relief Mechanisms and Growth Behavior of Superlattice Distributed Bragg Reflectors*, A. Wille, B. Reuters, M. Finken, F. Heyroth, G. Schmidt, M. Heuken, H. Kalisch, A. Vescan, *Phys. Status Solidi C* **11**, 758-761 (2014)
- *AlGaN/AlN-GaN SL HEMTs with Multiple 2DEG Channels*, A. Wille, H. Yacoub, A. Debald, H. Kalisch, A. Vescan, *J. Elec. Mat.* **44**, 1263-1267 (2015)
- *Investigations of the Electrochemical Stability of InGaN Photoanodes in Different Electrolytes*, M. Finken, A. Wille, B. Reuters, M. Heuken, H. Kalisch, A. Vescan, *Phys. Status Solidi B* **252**, 895-899 (2015)

- *Semi-polar* $\{1\bar{1}01\}$ *Blue and Green InGaN/GaN Light-emitting Diodes on Micro-Stripe Patterned Si(100)*, B. Reuters, J. Strate, A. Wille, M. Marx, G. Lükens, L. Heuken, M. Heuken, H. Kalisch, A. Vescan, *J. Phys. D: Appl. Phys.* **48**, 485103 (2015)

- *Steuerbarer Bragg-Reflektor*, A. Wille, H. Kalisch *Patentschrift*, Aktenzeichen: 10 2015 107 239.4, Dokumenten Referenz-Nr.: 2015050815272700DE8 (2015)

- *Effect of Stress Voltage on the Dynamic Buffer Response of GaN-on-Silicon Transistors*, H. Yacoub, D. Fahle, M. Eichelkamp, A. Wille, C. Mauder, M. Heuken, H. Kalisch, A. Vescan, *J. Appl. Phys.* **119**, 135704 (2016)

Appendix C

Conferences

- *Verspannungskontrolle mittels AlN/GaN-Übergitter in GaN-basierten Bragg-Reflektoren*, A. Wille, B. Reuters, M. Finken, M. Heuken, H. Kalisch, A. Vescan, *27. Treffen des Arbeitskreises „Epitaxie von III/V-Halbleitern" der Deutschen Gesellschaft für Kristallwachstum und Kristallzuüchtung e.V. (DGKK)*, Erlangen, Germany, 2012
- *Growth Studies on AlN/GaN Superlattices for Application in Distributed Bragg Reflector Structures*, A. Wille, B. Reuters, M. Finken, M. Heuken, H. Kalisch, A. Vescan, *XV.European Workshop on Metal-organic Vapor Phase Epitaxy (EWMOVPE)*, Aachen, Germany, 2013
- *Strain Relief Mechanisms and Growth Behavior of Superlattice Bragg Reflectors*, A. Wille, B. Reuters, M. Finken, F. Hexroth, G. Schmidt, M. Heuken, H. Kalisch, A. Vescan, *10th International Conference on Nitride Semiconductors (ICNS)*, Washington DC, USA, 2013
- *Verspannungsaufbau und Wachstumsverhalten von Übergitter-Bragg-Reflektoren*, A. Wille, B. Reuters, M. Finken, F. Heyroth, G. Schmidt, M. Heuken, H. Kalisch, A. Vescan, *28. Treffen des Arbeitskreises „Epitaxie von III/V-Halbleitern" der Deutschen Gesellschaft für Kristallwachstum und Kristallzuüchtung e.V. (DGKK)*, Ilmenau, Germany, 2013
- *AlGaN/AlN-GaN-SL HEMT with Multiple 2DEG Channels*, A. Wille, H. Yacoub, A. Debald, H. Kalisch, A. Vescan, *56th Electronic Materials Conference (EMC)*, Santa Barbara, USA, 2014
- *Multikanastrukturen zur Optimierung der Beweglichkeit in Gruppe III-Nitrid Feldeffekttransistoren*, A. Wille, H. Yacoub, A. Debald, H. Kalisch, A. Vescan, *29. Treffen des Arbeitskreises „Epitaxie von III/V-Halbleitern" der Deutschen Gesellschaft für Kristallwachstum und Kristallzuüchtung e.V. (DGKK)*, Magdeburg, Germany, 2014
- *HR-XRD Analysis of Multiple AlN/GaN Heterojunctions for Multichannel HEMT*, A. Wille, B. Reuters, M. Finken, H. Yacoub, M. Heuken, H. Kalisch, A. Vescan, *Worshop on X-ray Scattering for Thinfilm Characterization*, Prague, Czech Republic, 2014

- *Electro-optic Modulator Based on 2DEG-containing AlN/GaN Superlattice Structures*, A. Wille, H. Yacoub, S. Kotzea, G. Lükens, M. Heuken, H. Kalisch, A. Vescan, *30. Treffen des Arbeitskreises „Epitaxie von III/V-Halbleitern“ der Deutschen Gesellschaft für Kristallwachstum und Kristallzwüchtung e.V. (DGKK)*, Göttingen, Germany, 2015

Bibliography

[1] I. Akasaki, H. Amano, and S. Nakamura. Nobel prize in physics, 2014.

[2] O. Ambacher, J. Smart, J. R. Shealy, N. G. Weimann, K. Chu, M. Murphy, W. J. Schaff, L. F. Eastman, R. Dimitrov, L. Wittmer, M. Stutzmann, W. Rieger, and J. Hilsenbeck. Two-dimensional Electron Gases Induced by Spontaneous and Piezoelectric Polarization Charges in N- and Ga-face AlGaN/GaN Heterostructures. *J. Appl. Phys.*, 85, 1999.

[3] C. H. Oxley and M. J. Uren. Measurements of Unity Gain Cutoff Frequency and Saturation Velocity of a GaN HEMT Transistor. *IEEE Trans. Electron Devices*, 52, 2005.

[4] Y.-S. Liu, A. F. M. Saniul Haq, T.-T. Kao, K. Mehta, S.-C. Shen, T. Detchprohm, P. D. Yoder, R. D. Dupuis, H. Xie, and F. A. Ponce. Electrically Conducting n-type AlGaN/GaN Distributed Bragg Reflectors Grown by Metalorganic Chemical Vapor Deposition. *J. Crys. Growth*, 443, 2016.

[5] H. Mashiko, K. Oguri, T. Yamaguchi, A. Suda, and H. Gotoh. Petahertz Optical Drive with Wide-Bandgap Semiconductor. *Nature Physics*, 12, 2016.

[6] T. D. Germann, W. Hoffmann, A. M. Nadtochly, J.-H. Schulze, A. Mutig, A. Strittmatter, and D. Bimberg. Electro-Optical Resonance Modulation of Vertical-Cavity Surface-Emitting Lasers. *Optics Express*, 20, 2012.

[7] I. Vurgaftman and J. R. Meyer. Band Parameters for Nitrogen-containing Semiconductors. *J. Appl. Phys.*, 94, 2003.

[8] S. Adachi. GaAs, AlAs and $Al_xGa_{1-x}As$: Material Parameters for Use in Research and Device Applications. *J. Appl. Phys.*, 58, 1985.

[9] S. L. Chuang and C. S. Chang. Fundamental Chemistry and Modeling of Group-III Nitride MOVPE. *J. Crys. Growth*, 298, 2007.

[10] Y.-L-Tsai, C.-L. Wang, P.-H. Lin, W.-T. Liao, and J.-R. Gong. Obervation of Compositional Pulling Phenomenon in AlGaN Films Grown on (0001) Sapphire Substrates. *Appl. Phys. Lett.*, 82, 2003.

[11] S. Pereira, M. Correia, E. Pereira, K. O'Donnell, C. Trager-Cowan, F. Sweeney, and E. Alves. Compositional Pulling Effects in $In_xGa_{1-x}N/GaN$ layers: A Combined

Depth-resolved Cathodoluminescence and Rutherford Backscattering/Channeling Study. *Phys. Rev. B*, 64, 2001.

[12] E. Feltin, B. Beaumont, M Laügt, P. de Mierry, P. Vennéguès, M. Leroux, and P. Gibart. Crack-Free Thick GaN Layers on Silicon (111) by Metalorganic Vapor Phase Epitaxy. *Phys. Stat. Sol. (a)*, 188, 2001.

[13] S.-H. Jang and C.-R-Lee. High-quality GaN/Si(111) Epitaxial Layers Grown with Various $Al_{0.3}Ga_{0.7}N/GaN$ Superlattices as Intermediate Layer by MOCVD. *Phys. Stat. Sol. (a)*, 188, 2001.

[14] Y. Y. Zhang and Y. A. Yin. Performance Enhancement of Blue Light-Emitting Diodes with a Special Designed AlGaN/GaN Superlattice Electron-Blocking Layer. *Appl. Phys. Lett.*, 99, 2011.

[15] J. H. Park, D. Y. Kim, S. Hwang, D. Meyaard, E. F. Schubert, Y. D. Han, J. W. Choi, J. Cho, and J. K. Kim. Enhanced Overall Efficiency of GaInN-Based Light-Emitting Diodes with Reduced Efficiency Droop by Al-Composition-Graded AlGaN/GaN Superlattice Electron Blocking Layer. *Appl. Phys. Lett.*, 103, 2013.

[16] J.-K-Sheu, C.-C. Yang, S.-J. Tu, K.-H. Chang, M.-L. Lee, W.-C. Lai, and L.-C. Peng. Demonstration of GaN-based Solar Cells With GaN/InGaN Superlattice Absorption Layers. *IEEE Electr. Device Lett.*, 30, 2009.

[17] O. Ambacher. Growth and Applications of Group III-nitrides. *J. Phys. D: Appl. Phys.*, 31, 1998.

[18] O. Ambacher, J. Majewski, C. Miskys, A. Link, M. Hermann, M. Eikhoff, M. Stutzmann, F. Bernardini, V. Fiorentini, V. Tilak, B. Schaff, and L. F. Eastman. Pyroelectric Properties of Al(In)GaN/GaN Hetero- and Quantum Well Structures. *J. Phys.: Condesns. Matter*, 14, 2002.

[19] O. Ambacher, B. Foutz, J. Smart, J. R. Shealy, N. G. Weimann, K. Chu, M. Murphy A. J. Sierakowski, W. J. Schaff, L. F. Eastman, R. Dimitrov, A. Mitchell, and M. Stutzmann. Two-dimensional Electron Gases Induced by Spontaneous and Piezoelectric Polarization in undoped and doped AlGaN/GaN Heterostructures. *J. Appl. Phys.*, 87, 2000.

[20] H. P. Maruska and J. J. Tietjen. The Preparation and Properties of Vapor-deposited Single-crystalline GaN. *Appl. Phys. Lett.*, 15, 1969.

[21] N. Antoine-Vincent, F. Natali, M. Mihailovic, A. Vasson, J. Leymarie, P. Disseix, D. Byrne, F. Semond, and J. Massies. Determination of the Refractive Indices of AlN, GaN and $Al_xGa_{1-x}N$ Grown on (111)Si Substrates. *J. Appl. Phys.*, 93, 2003.

[22] G. M. Laws, E. C. Larkins, I. Harrison, C. Molloy, and D. Somerford. Improved Refractive Index Formulas for the $Al_xGa_{1-x}N$ and $In_yGa_{1-y}N$ Alloys. *J. Appl. Phys.*, 89, 2001.

[23] Q. Guo and O. Kato. Optical Constants of Indium Nitride. *Sol. State. Comm.*, 83, 1992.

[24] P. Hacke, H. Nakayama, T. Detchprohm, K. Hiramatsu, and N. Sawaki. Deep Levels in the Upper Band-gap Region of Lightly Mg-doped GaN. *Appl. Phys. Lett.*, 68, 1996.

[25] J. Neugebauer and C. G. Van de Walle. Role of Hydrogen in Doping of GaN. *Appl. Phys. Lett.*, 68, 1996.

[26] Y. Taniyasu, M. Kasu, and N. Kobayashi. Intentional Control of n-type Conduction for Si-doped AlN and $Al_xGa_{1-x}N$ $(0.42 \leq x < 1)$. *Appl. Phys. Lett*, 81, 2002.

[27] Y. Taniyasu, M. Kasu, and T. Makimoto. Electrical Conduction Properties of n-type Si-doped AlN with High Electron Mobility ($> 100cm^2V^{-1}s^{-1}$. *Appl. Phys. Lett*, 85, 2004.

[28] LayTec AG. www.laytec.de.

[29] R. J. Creighton, G. T. Wang, and M. E. Coltrin. $k \cdot p$ Method for Strained Wurtzite Semiconductors. *Phys. Rev. B*, 54, 1996.

[30] A. Dadgar, J. Bläsing, A. Diez, A. Alam, M. Heuken, and A. Krost. Metalorganic Chemical Vapor Phase Epitaxy of Crack-Free GaN on Si (111) Exceeding 1 μm in Thickness. *Jpn. J. Appl. Phys.*, 39, 2000.

[31] S. Zamir, B. Meyler, E. Zolotoyaboko, and J. Salzmann. The Effect of AlN Buffer Layer on GaN Grown on (111)-oriented Si Substrates by MOCVD. *J. Crys. Growth*, 218, 2000.

[32] A. Dadgar, M. Poschenrieder, J. Blsing, O. Contreras, F. Bertram, T. Riemann, M. Kunze, I. Daumiller, A. Krtschil, A. Diez, A. Kaluza, A. Modlich, M. Kamp, J. Christen, F. A. Ponce, E. Kohn, and A. Krost. MOVPE Growth of GaN on Si(111) Substrates. *J. Cryst. Growth*, 238, 2003.

[33] T. Mattila and R. M. Nieminen. Ab initio Study of Oxygen Point Defects in GaAs, GaN, and AlN. *Phys. Rev. B*, 54, 1996.

[34] C. Mavroidis, J. J. Harris, M. J. Kappers, N. Sharma, C. J. Humphreys, and E. J. Thrush. Observation of Thermally Activated Conduction at a GaN-Sapphire Interface. *Appl. Phys. Lett.*, 79, 2001.

[35] D. Fahle. *Investigation of HCl-assisted MOVPE of Group III Nitrides in a Planetary Hot-Wall System.* PhD thesis, RWTH Aachen University, 2014.

[36] R. Di Felice and J. E. Northrup. Energetics of AlN Thin Films on the $Al_2O_3(0001)$ Surface. *Appl. Phys. Lett.*, 73, 1998.

[37] H. Behmenburg. *Comprehensive Study on MOVPE of InAlN/GaN HEMT Structures and GaN Nanowires.* PhD thesis, RWTH Aachen University, 2013.

[38] D. Kapolnek, X. H. Wu, B. Heying, S. Keller, B. P. Keller, U. K. Mishra, S. P. DenBaars, and J. S. Speck. Structural Evolution in Epitaxial Metalorganic Chemical Vapor Deposition Grown GaN Films on Sapphire. *Appl. Phys. Lett.*, 67, 1995.

[39] K. Hiramatsu, S. Itoh, H. Amano, I. Akasaki, N Kuwano, T. Shiraishi, and K. Oki. Growth Mechanism of GaN Grown on Sapphire with AlN Buffer Layer by MOVPE. *J. Crys. Growth*, 115, 1991.

[40] C. G. Van de Walle and J. Neugebauer. First Principle Calculation for Defects and Impurities: Application to III-nitrides. *J. Appl. Phys.*, 95, 2004.

[41] J. L. Lyons, A. Janotti, and C. G. Van de Walle. Carbon Impurities and the Yellow Luminescence in GaN. *Appl. Phys. Lett.*, 97, 2010.

[42] G. Gottstein. *Physical Foundations of Materials Science*. Springer, 2004.

[43] M. A. Moram and M. E. Vickers. X-ray Diffraction of III-Nitrides. *Rep. Prog. Phys.*, 72, 2009.

[44] M. Hao, T. Sugahara, H. Sato, Y. Morishima, Y. Naoi, L. Romano, and S. Sakai. Study of Threading Dislocations in Wurtzite GaN Films Grown on Sapphire by Metalorganic Chemical Vapor Deposition. *Jpn. J. Appl. Phys.*, 37, 1998.

[45] J. Elsner, R. Jones, P. K. Sitch, V. D. Porezag, M. Elstner, T. Frauenheim, M. I. Heggie, S. Öberg, and P. R. Briddon. Theory of Threading Edge and Screw Dislocations in GaN. *Phys. Rev. Lett.*, 79, 1997.

[46] A. D. Bykhovski, B. L. Gelmont, and M. S. Shur. Elastic Strain Relaxation and Piezoeffect in GaN-AlN, GaN-AlGaN and GaN-InGaN Superlattices. *J. Appl. Phys.*, 81, 1997.

[47] D. M. Follstaedt, S. R. Lee, A. A. Allerman, and J. A. Floro. Strain Relaxation in AlGaN Multilayer Structures by Inclined Dislocations. *J. Appl. Phys.*, 105, 2009.

[48] S. Srinivasan, L Geng, R. Liu, F. A. Ponce, Y. Narukawa, and S. Tanaka. Slip Systems and Misfit Dislocations in InGaN Epilayers. *Appl. Phys. Lett.*, 83, 2003.

[49] J. Narayan, P. Pant, A. Chugh, H. Choi, and J. C. C. Fan. Characteristics of Nucleation Layer and Epitaxy in GaN/sapphire heterostructures. *J. Appl. Phys.*, 99, 2006.

[50] F. A. Ponce, J. S. Major Jr. and W. E. Plano, and D. F. Welch. Crystalline Structure of AlGaN Epitaxy on Sapphire Using AlN Buffer Layers. *J. Appl. Phys.*, 117, 1994.

[51] J. W. Matthews and A. E. Blakeslee. Defects in Epitaxial Multilayers. *J. Crys. Growth*, 27, 1974.

[52] J. W. Matthews. Defects Associated with the Accommodation of Misfit Between Crystals. *J. Vac. Sci. Technol.*, 12, 1975.

[53] Y. Taniyasu, M. Kasu, and T. Makimoto. Threading Dislocations in Heteroepitaxial AlN Layer Grown by MOVPE on SiC (0001) Substrate. *J. Crys. Growth*, 298, 2006.

[54] C. Stampfl and C. G. Van de Walle. Energetics and Electronic Structure of Stacking Faults in AlN, GaN and InN. *Phys. Rev. B*, 57, 1998.

[55] W. Liu, C. B. Soh, P. Chen, and S. J. Chua. Characterization of AlInGaN Quaternary Epilayers Grown by Metal Organic Chemical Vapor Deposition. *J. Crys. Growth*, 268, 2004.

[56] X. H. Wu, C. R. Elsass, A. Abara, M. Mack, S. Keller, P. M. Petroff, S. P. DenBaars, J. S. Speck, and S. J. Rosner. Structural Origin of V-Defects and Correlation With Localized Exitonic Centers in InGaN/GaN Multiple Quantum Wells. *Appl. Phys. Lett.*, 72, 1998.

[57] M. Shiojiri, C. C. Chuo, J. T. Hsu, J. R. Yang, and H. Saijo. Structure and Formation Mechanism of V defects in Multiple InGaN/GaN Quantum Well Layers. *J. Appl. Phys.*, 99, 2006.

[58] S. R. Lee, D. D. Koleske, K. C. Cross, J. A. Floro, K. E. Waldrip, A. T. Wise, and S. Mahajan. In Situ Measurements of the Critical Thickness for Strain Relaxation in AlGaN/GaN Heterostructures. *Appl. Phys. Lett.*, 85, 2004.

[59] A. Able, W. Wegscheider, K. Engl, and J. Zweck. Growth of Crack-free GaN on Si(111) with Graded AlGaN Buffer Layers. *J. Crys. Growth*, 276, 2005.

[60] A. E. Romanov and J. S. Speck. Stress Relaxation in Mismatched Layers due to Threading Dislocation Inclination. *Appl. Phys. Lett.*, 83, 2003.

[61] H. Ibach and H Lüth. *Festkörperphysik, Einführung in die Grundlagen*. Springer Verlag, 2009.

[62] L. Esaki and R. Tsu. Superlattice and Negative Differential Conductivity in Semiconductors. *IBM J. Res. Develop.*, 14, 1970.

[63] Y. Suzuki and H. Okamoto. Refractive Index of GaAs-AlAs Superlattice Grown by MBE. *J. Elec. Mat.*, 12, 1983.

[64] A. N. Westmeyer, S. Mahajan, K. K. Bajaj, J. Y. Lin, H. X. Jiang, D. D. Koleske, and R. T. Senger. Determination of Energy-band Offsets Between GaN and AlN Using Excitonic Luminescence Transitions in AlGaN Alloys. *J. Appl. Phys.*, 99, 2006.

[65] L. Hsu and W. Walukiewicz. Effect of Polarization Fields on Transport Properties in AlGaN/GaN Heterostructures. *J. Appl Phys.*, 89, 2001.

[66] S. Einfeld, H. Heinke, V. Kirchner, and D. Hommel. Strain Relaxation in AlGaN/GaN Superlattices Grown on GaN. *J. Appl. Phys.*, 89, 2001.

[67] P. K. Kandaswamy, C. Bougerol, D. Jalabert, P. Ruterana, and E. Monroy. Strain Relaxation in Short-period polar GaN/AlN Superlattices. *J. Appl. Phys.*, 106, 2009.

[68] P. D. Cherns, C. McAleese, M. J. Kappers, and C. J. Humphreys. Strain Relaxation in an AlGaN/GaN Quantum Well System. *Springer Proc. in Phys.*, 120, 2008.

[69] P. Kozodoy, Y. P. Smorchkova, M. Hansen, H. Xing, S. P. DenBaars, U. K. Mishra, A. W. Saxler, R. Perrin, and W. C. Mitchel. Polarization-Enhanced Mg Doping of AlGaN/GaN Superlattices. *Appl. Phys. Lett.*, 75, 1999.

[70] J. K. Kim, E. L. Waldron, Y.-L. Li, T. Gessmann, E. F. Schubert, H. W. Jang, and J.-L. Lee. P-type Conductivity in Bulk $Al_xGa_{1-x}N$ and $Al_xGa_{1-x}N/Al_yGa_{1-y}N$ Superlattices with Average Al Mole Fraction >20%. *Appl. Phys. Lett.*, 84, 2004.

[71] P. Chen, X. G. Tu, S. P. Li, J. C. Li, W. Lin, H. Y. Chen, D. Y. Liu, J. Y. Kang, Y. H Zuo amd L Zhao, S. W. Chen, Y. D. Yu, J. Z. Yu, and Q. M. Wang. Enhanced Pockels Effect in $GaN/Al_xGa_{1-x}N$ Superlattices Measured by Polarization-Maintaining Fiber Mach-Zehnder Interferometer. *Appl. Phys. Lett.*, 91, 2007.

[72] N. Sasaki, M. Tsukada, R. Tamura, K. Abe, and N. Sato. Dynamics of the Cantilever in Noncontact Atomic Force Microscopy. *Appl. Phys. A*, 66, 1998.

[73] A. E. Wickenden, D. D. Koleske, R. L. Henry, M. E. Twigg, and M. Fatemi. Resistivity Control in Unintentionally Doped GaN Films Grown by MOCVD. *J. Crys. Growth*, 260, 2003.

[74] A. V. Lobanova, K. M. Mazaev, R. A. Talalaev, M. Leys, S. Boeykens, K. Cheng, and S. Degroote. Effect of V/III ratio in AlN and AlGaN MOVPE. *J. Crys. Growth*, 267, 2006.

[75] A. Koukito, T. Taki, N. Takahashi, and H. Seki. Thermodynamic Study on the Role of Hydrogen During the MOVPE Growth of Group III Nitrides. *J. Crys. Growth*, 197, 1999.

[76] L. Vegard. Die Konstitution der Mischkristalle und die Raumfüllung der Atome. *Zeitschrift für Physik A: Hadrons and Nuclei*, 5:17–26, 1921.

[77] B. Gil. *III-Nitride Semiconductors and their Modern Devices.* Oxford University Press, 2013.

[78] G. Snider. 1d poisson. Version beta 8j1.

[79] D. Li, J. Shao, L. Tang, C. Edmunds, G. Gardner, M. J. Manfra, and O. Malis. Temperature-dependence of Negative Differential Resistance in GaN/AlGaN Resonant Tunneling Structures. *Semicond. Sci. Technol.*, 28, 2013.

[80] J. Encomendero, F. A. Faria, S. M. Islam, V. Protasenko, S. Rouvimov, P. Fay, D. Jena, and H. G. Xing. Repeatable Room Temperature Negative Differential Conductance in GaN/AlN Resonant Tunneling Diodes, 2016.

[81] C. Bayram, Z. Vashaei, and M. Razeghi. AlN/GaN Double-barrier Resonant Tunneling Diodes Grown by Metal-organic Chemical Vapor Deposition. *Appl. Phys. Lett.*, 96, 2010.

[82] M. Nagase and T. Tokizaki. Bistability Characteristics of GaN/AlN Resonant Tunneling Diodes Caused by Intersubband Transition and Electron Accumulation in Quantum Well. *IEEE Transac. Electr. Dev.*, 61, 2014.

[83] H. Hahn. *Threshold Voltage Engineering of GaN-based n-Channel and p-Channel Heterostructure Field Effect Transistors*. PhD thesis, RWTH Aachen University, 2014.

[84] M. N. Gurusinghe, S. K. Davidsson, and T. G. Andersson. Two-dimensional Electron Mobility Limitation Mechanisms in $Al_xGa_{1-x}N/GaN$ Heterostructures. *Phys. Rev. B*, 72, 2005.

[85] F. Stengel, S. N. Mohammad, and H. Morkoç. Theoretical Investigations of Electrical Characteristics of AlGaN/GaN Modulation Doped Field-effect Transistors. *Appl. Phys. Lett.*, 80, 1996.

[86] M. J. Manfra, K. E. Baldwin, A. M. Sergent, R. J. Molnar, and J. Caissie. Electron Mobility in Very Low Density GaN/AlGaN/GaN heterostructures. *Appl. Phys. Lett.*, 85, 2004.

[87] M. A. Littlejohn, J. R. Hauser, T. H. Glisson, D. K. Ferry, and J. W. Harrison. Alloy Scattering and High Field Transport in Ternary and Quaternary III-V Semiconductors. *Sol. St. Elec.*, 21, 1978.

[88] E. Bellotti, F. Bertazzi, and M. Goano. Alloy scattering in AlGaN and InGaN: A numerical study. *J. Appl. Phys.*, 101, 2007.

[89] E. Šermukšnis, J. Liberis, M. Ramonas, A. Matulionis, J. H. Leach, M. Wu, V. Avrutin, and H. Morkoç. Camelback channel for fast decay of LO phonons in GaN heterostructure field-effect transistor at high electron density. *Appl. Phys. Lett.*, 99, 2011.

[90] Y. Takeda and T. P. Pearsall. Failure of Matthiessen's Rule in the Calculation of Carrier Mobility and Alloy Scattering Effects in $Ga_{0.47}In_{0.53}As$. *Electronics Lett.*, 17, 1981.

[91] G. H. Jessen, Jr. and J. K. Gillespie R. C. Fitch, G. Via, A. Crespo, D. Langley, and Jr. and E. R. Heller D. J. Denninghoff anf M. Trejo. Short-Channel Effect Limitations on High-Frequency Operation of AlGaN/GaN HEMTs for T-Gate Devices. *IEEE Transac. Electr. Devices*, 54, 2007.

[92] M. S. Tyagi. *Introduction to Semiconductor Materials and Devices*. John Wiley and Sons, 1991.

[93] S. Zhang, M. C. Li, Z. H. Feng, B. Liu, J. Y. Yin, and L. C. Zhao. High Electron Mobility and Low Sheet Resistance in Lattice-matched AlInN/AlN/GaN/AlN/GaN Double-Channel Heterostructure. *Appl. Phys. Lett.*, 95, 2011.

[94] T. Palacios, A. Chini, D. Buttari, S. Heikman, A. Chakraborty, S. Keller, S. P. DenBaars, and U. K. Mishra. Use of Double-Channel Heterostructures to Improve the Access Resistance and Linearity in GaN-Based HEMTs. *IEEE Transac. Elec. Devices*, 53, 2060.

[95] R. Chu, Y. Zhou, J. Liu, D. Wang, K. J. Chen, and K. M. Lau. AlGaN-GaN Double-Channel HEMTs. *IEEE Trans. Elec. Devices*, 52, 2005.

[96] X.-D. Wang, W.-D. Hu, X.-S. Chen, and W. Lu. The Study of Self-Heating and Hot-Electron Effects for AlGaN/GaN Double-Channel HEMTs. *IEEE Transac. Electr. Devices*, 59, 2012.

[97] C. W. Farley and B. G. Streetman. The Schottky-gated Hall-effect Transistor and its Application to Carrier Concentration and Mobility Profiling in GaAs MESFET's. *IEEE Trans. Elec. Devices*, 34, 1987.

[98] K. Ismail, M. Arafa, F. Stern, J. Chu, and B. Meyerson. Gated hall effect measurements in high-mobility n-type si/sige modulation-doped heterostructures. *Appl. Phys. Lett.*, 66:842–844, 1995.

[99] A. Matulionis, J. Liberis, I. Matulionienė, M. Ramonas, E. Šermukšnis, J. H. Leach, M. Wu, X. Ni, X. Li, and H. Morkoç. Plamon-enhanced Heat Dissipation in GaN-based Two-dimensional Channels. *Appl. Phys. Lett.*, 95, 2009.

[100] R. A. Ferreyra, X. Li, F. Zhang, C. Zhu, N. Izyumskaya, C. Kayis, V. Avrutin, Ü. Özgür, and H. Morkoç. Microwave Performance of AlGaN/AlN/GaN-based Single and Coupled Channels HFETs. *Proc. of SPIE*, 8625, 2013.

[101] F. Bernardini and V. Fiorentini. Polarization-Based Calculation of the Dielectric Tensor of Polar Crystals. *Phys. Rev. Lett.*, 79, 1997.

[102] Linear Technology SPICE. 4.23i, 2016.

[103] W. W. Chow, S. W. Koch, and M. Sargent III. *Semiconductor-Laser Physics*. Springer, 1994.

[104] C. F. Klingshirn. *Semiconductor Optics*. Springer Verlag, 1995.

[105] C. Gerthsen, H. O. Kneser, and H. Vogel. *Physik*. Springer, 1989.

[106] C. J. R. Sheppard. Approximate calculation of the reflection coefficient from a stratified medium. *Pure Appl. Opt.*, 4, 1995.

[107] Z. P. Ling, T. Mueller, A. G. Aberle, and R. Stangl. Development of a Conductive Distributed Bragg Reflector for Heterojunction Solar Cells Using n-doped Microcystalline Silicon and Aluminum-doped Zinc Oxide Films. *IEEE J. Photovolt.*, 4, 2014.

[108] H. Chen, H. Guo, P. Zhang, X. Zhang, H. Liu, S. Wang, and Y. Cui. Enhanced Performance of GaN-based Light-emitting Diodes by Using Al Mirror and Atomic Layer Deposition-TiO_2/Al_2O_3 Distributed Bragg Reflector Backside Reflector with Patterned Sapphire Substrates. *Appl. Phys. Express*, 6, 2013.

[109] M. Cho, J.-H. Seo, D. Zhao, J. Lee, K. Xiong, X. Yin, Y. Liu, S.-C. Liu, M. Kim, T. J. Kim, X. Wang, W. Zhou, and Z. Ma. Amorphous Si/SiO_2 Distributed Bragg Reflectors with Transfer Printed Single-crystalline Si Nanomembranes. *J. Vac. Sci. Technol. B*, 34, 2016.

[110] Y.-H. Lin, C.-L. Wu, Y.-H. Pai, and G.-R. Lin. A 533-nm Self-luminescent Si-rich SiN_x/SiO_x Distributed Bragg Reflector. *Optics Express*, 19, 2011.

[111] J.-F. Carlin, J Dorsaz, R. Butté, N. Grandjean, M. Ilegems, and M. Laügt. Crack-free Fully Epitaxial Nitride Microcavity Using Highly Reflective AlInN/GaN Bragg Mirrors. *Appl. Phys. Lett.*, 86, 2005.

[112] K. E. Waldrip, J. Han, J. J. Figiel, H. Zhou, E. Makarona, and A. V. Nurmikko. Stress Engineering During Metalorganic Chemical Vapor Deposition of AlGaN/GaN Distributed Bragg Reflectors. *Appl. Phys. Lett.*, 78, 2001.

[113] C. M. Wu, B. P. Zhang abd J. Z. Shang, J. Y. Zhang, J. Z. yu, and Q. M. Wang. High-reflectivity AlN/GaN Distributed Bragg Reflectors Grown on Sapphire Substrates by MOCVD. *Semicond. Sci. Technol.*, 26, 2011.

[114] L. E. Rodak, J. Peacock, J. Justice, and D. Korakakis. AlN/GaN Distributed Bragg Reflectors Grown via Metal Organic Vapor Phase Epitaxy Using GaN Insertion Layers. *Mater. Res. Soc. Symp. Proc.*, 1396, 2012.

[115] M. Bass, C. DeCusatis, J. Enoch, V. Lakshminarayanan, G. Li, C. MacDonald, V. Mahajan, and E. Van Stryland. *Handbook of Optics, Third Edition Volume IV: Optical Properties of Materials, Nonlinear Optics, Quantum Optics.* McGraw Hill Professional, 2009.

[116] N. Nakada, H. Ishikawa, T. Egawa, and T. Jimbo. Suppression of Crack Generation in GaN/AlGaN Distributed Bragg Reflector on Sapphire by the Insertion of GaN/AlGaN Superlattice Grown by Metal-Organic Chemical Vapor Deposition. *Jpn. J. Appl. Phys.*, 42, 2003.

[117] G. S. Huang, T. C. Lu, H. H. Yao, H. C. Kuo, S. C. Wang, C.-W. Lin, and L. Chang. Crack-free GaN/AlN Distributed Bragg Reflectors Incorporated with GaN/AlN Superlattices Grown by Metalorganic Chemical Vapor Deposition. *Appl. Phys. Lett.*, 88, 2006.

[118] http://people.csail.mit.edu/jaffer/FreeSnell/.

[119] J. Pastrnak and L. Roskovcova. Refraction Index Measurements on AlN Single Crystals. *Phys. Stat. Sol.*, 14, 1966.

[120] S. Adachi. *Optical Constants of Crystalline and Amorphous Semiconductors*. Springer, 1999.

[121] A. S. Barker Jr. and M. Ilegems. Infrared Lattice Vibrations and Free-Electron Dispersion in GaN. *Phys. Rev. B*, 7, 1973.

[122] O. Ambacher, F. Freudenberg, R. Dimitrov, H. Angerer, and M. Stutzmann. Nitrogen Effusion and Self-Diffusion in $Ga^{14}N/Ga^{15}N$ Isotope Heterostructures. *Jpn. J. Appl. Phys.*, 37, 1998.

[123] P. Perlin, E. Litwin-Staszewska, B. Suchanek, W. Knap, J. Camassel, T. Suski, R. Piotrzkowski, I. Grzegora, S. Porowski, E. Kaminska, and J. C. Chervin. Determination of the Effective Mass of GaN from Infrared Reflectivity and Hall Effect. *Appl. Phys. Lett.*, 68, 1996.

[124] P. Bigenwald, A. Kavokin, B. Gil, and P. Lefebvre. Exclusion Principle and Screening of Excitons in $GaN/Al_xGa_{1-x}N$ Quantum Wells. *Phys. Rev. B*, 63, 2001.

[125] T. Takeuchi, S. Sota, M. Katsuragawa, M. Komori, H. Takeuchi, H. Amano, and I. Akasaki. Quantum-Confined Stark Effect Due to Piezoelectric Fields in GaInN Strained Quantum Wells. *Jap. J. Appl. Phys.*, 36, 1997.

[126] T. S. Moss. The Interpretation of the Properties of Indium Antimonide. *Proc. Phys. Soc. B*, 67, 1954.

[127] E. Burstein. Anomalous Absorption Limit in InSb. *Phys. Rev.*, 93, 1954.

[128] M. Feneberg, S. Osterburg, K. Lange, C. Lidig, B. Garke, R. Goldhahn, E. Richter, C. Netzel, M. D. Neumann, N. Esser, S. Fritze, H. Witte, J. Bläsing, A. Dadgar, and A. Krost. Band Gap Renormalization and Burstein-Moss Effect in Silicon- and Germanium-doped Wurtzite GaN up to $10^{20}cm^{-3}$. *Phys. Rev. B*, 90, 2014.

[129] D. Y. Lin, J. D. Wu, C. C. Hung, C. T. Lu, Y. S. Huang, C.-T. Liang, and N. C. Chen. Optical Investigation of an AlGaN/GaN interface with the Presence of a Two-dimensional Electron Gas. *Physica E*, 43, 2010.

[130] R. A. Soref and B. R. Bennett. Electrooptical Effects in Silicon. *IEEE J. Quantum Electronics*, QE-23, 1987.

[131] D. Marris-Morini, X. Le Roux, L. Vivien, E. Cassan, D. Pascal, M. Halbwax, S. Maine, and S. Laval. Opticla Modulation by Carrier Depletion in a Silicon PIN Diode. *Optics Express*, 14, 2006.

[132] A. Liu, L. Liao, D. Rubin, H. Nguyen, B. Ciftciogle, Y. Chetrit, N. Izhaky, and M. Paniccia. High-speed Optical Modulation Based on Carrier Depletion in a Silicon Waveguide. *Optics Express*, 15, 2007.

[133] R. Wu, C.-H. Chen, J.-M. Fedeli, M. Fournier, K.-T. Cheng, and R. G. Beausoleil. Compact Model for Carrier-injection Silicon Microring Modulators. *Optics Express*, 23, 2015.

[134] F. Ito, M. Matsuura, and T. Tanifuji. A Carrier Injection Type Optical Switch in GaAs Using Free Carrier Plasma Dispersion with Wavelength Range from 1.06 to 1.55 μ m. *IEEE J. Quantum Elec.*, 25, 1989.

[135] A. Alping, X. S. Wu, T. R. Hausken, and L. A. Coldren. Highly Efficient Waveguide Phase Modulator for Integrated Optoelectronics. *Appl. Phys. Lett*, 48, 1987.

[136] B. R. Bennett amd R. A. Soref and J. A. Del Alamo. Carrier-Induced Change in Refractive Index of InP, GaAs and InGaAsP. *IEEE J. Quantum Elec.*, 26, 1990.

[137] P. C. Schindler, D. Korn, C. Stamatiadis, M. F. O'Keefe, L. Stampoulidis, R. Schmorgrow, P. Zakynthinos, R. Palmer, N. Cameron, Y. Zhou, R. G. Walker, E. Kahayas, S. Ben-Ezra, I. Tomkps, L. Zimmermann, K. Petermann, W. Freude, C. Koos, and J. Leuthold. Monolithis GaAs Electro-optic IQ Modulator Demonstrated at 150 Gbit/s With 64QAM. *J. Lightwave Tech.*, 32, 2014.

[138] A. I. Alhassan, R. M. Farrell, B. Saifaddin, A. Mughal, F. Wu, S. P. DenBaars, S. Nakamura, and J. S. Speck. High Luminous Efficacy Green Light-emitting Diodes with AlGaN Cap Layer. *Optics Express*, 24, 2016.

[139] S. Hearne, E. Chason, J. Han, J. A. Floro, J. Figiel, J. Hunter, H. Amano, and I. S. T. Tsong. Stress Evolution During Metalorganic Chemical Vapor Deposition of GaN. *Appl. Phys. Lett.*, 74, 1998.

[140] G. S. Higashi, R. S. Becker, Y. J. Chabal, and A. J. Becker. Comparison of Si(111) Surfaces Prepared Using Aqueous Solutions of NH4F versus HF. *Appl. Phys. Lett*, 58, 1991.

[141] J. Kinoshita, Y. Ikeda, and Y. Takeda. Speckle-free Phosphor-Scattered Blue Light Emitted out of InGaN/GaN Laser Diode with Broadened Spectral Behavior for High Luminance White Lamp Applications. *IEICE Trans. Electron.*, E96-C, 2013.

[142] C. Lee, C. Zhang, M. Cantore, R. M .Farrell, S. H. Oh, T. Margalith, J. S. Speck, S. Nakamura, J. E. Bowers, and S. P. DenBaars. 4 Gbps Direct Modulation of 450 nm GaN Laser for High-speed Visible Light Communication. *Optics Express*, 23, 2015.

[143] I. Ratschinski. *Versetzungsaktivität und Rissbildung in GaAs und GaN.* PhD thesis, Martin-Luther Universität Halle, 2015.

[144] B. Reuters. *Polarization-optimized Heterostructures with Quarternary AlInGaN Layers for Novel Group III Nitride Devices*. PhD thesis, RWTH Aachen University, 2015.

[145] S. Takagi, Y. Enya, T. Kyono, M. Adachi, Y. Yoshizumi, T. Sumitomo, Y. Yamanaka, T. Kumano, S. Tokuyama, K. Sumiyoshi, N. Saga, M. Ueno, K. Katayama, T. Ikegami, T. Nakamura, K. Yanashima, H. Nakajima, K. Tasai, K. Naganuma, N. Fuutagawa, Y. Takiguchi, T. Hamaguchi, and M. Ikeda. High-Power (over 100 mW) Green Laser Diodes on Semipolar {2021} GaN Substrates Operating at Wavelengths beyond 530 nm. *Appl. Phys. Expr.*, 5, 2012.

[146] C. Wetzel, D. Volm, B. K. Meyer, K. Pressel, S. Nilsson, E. N. Mokhov, and P. G. Baranov. GaN Epitaxial Layers Grown on 6H-SiC by the Sublimation Sandwich Technique. *Appl. Phys. Lett.*, 65, 1994.

Acknowledgements

This work was only possible with the help and support of many people. I would like to express my thanks to:

Prof. Andrei Vescan for giving me the opportunity to work under his supervision with continuous encouragement and support,

Prof. Rainer Waser for kindly accepting to referee this work,

Dr. Holger Kalisch for fruitful discussions, support at the MOVPE system and extensive proofreading,

Ben Reuters, *Matthias Marx*, *Carsten Beckmann* and the *whole epiteam* for splendid team work, helpful discussions and support,

Frank Jessen, *Gerrit Kuivenhoven* and *Jan Gruis* for their technological support at the MOVPE system, fast help and commitment to always find a solution,

Hady Yacoub for the processing and measurements of the SL-HFET including detailed discussion and great support,

Simon Kotzea, *Gerrit Lükens*, *Sonja Buchholz-Trappe* and *Gabi Noguiera-Glenski* for processing of the TuneDBR test structures,

Dr. Frank Heyroth and *Prof. Georg Schmidt* from the Martin-Luther University in Halle and *Koji Yoshitsugu* in the group of Prof. Uraoka from Nara Institute of Science and Technology in Japan for the TEM images of the SL-DBR,

all my colleagues at GaN Device Technology for the superb working atmosphere and helping hands,

all students for their committed work,

Arnis for his absolute support and steady encouragement,

my family who made all this possible and supported me at all times.